THE UNIVERSITY
of EDINBURGH

Development and validation of direct contact gas liquid heat exchange for energy storage

Daniel Howard McKinley

Doctor of Philosophy
Institute for Energy Systems
College of Science and Engineering
University of Edinburgh
2020

Abstract

Decarbonisation of the electrical grid, necessitated by international targets to limit further global warming, will require a steadily increasing penetration of non-dispatchable intermittent renewable electricity generation sources. Energy storage has the potential to substantially increase the grid's ability to accept greater quantities of renewables while maintaining stability. Pumped-Heat Energy Storage (PHES) is a form of electrical energy storage targeted to provide storage on the order of days or weeks, as opposed to short durations of storage currently available through battery technologies. PHES systems could be utilised at substations across the country to help the grid endure diurnal load fluctuations and periods of low wind and solar resource. This system is based upon the Joule-Brayton cycle, which operates in the reverse direction to store exergy and the forward direction to generate electricity. An inert gas is the cycle working fluid, and a liquid is used to transfer heat to and from thermal exergy stores. Exergy is stored as temperature differences from ambient in balanced hot and cold stores.

PHES development at the University of Edinburgh has iteratively explored different system architectures, and focused on increasing confidence in components within these architectures where there is uncertainty with regard to performance. Early work concentrated on gas-liquid mixing within the cylinder of a compressor/expander machine, while current work has eliminated such mixing and instead proposes the use of large scale, direct-contact heat exchangers. Such exchangers suffer from significant uncertainty for this application owing to the lack of existing experimental correlations with which to predict their behaviour at the proposed operating pressure and temperature. As a result, gas liquid surface interactions and heat-transfer between gas and liquid streams are largely unknown, hindering system development.

Two experimental campaigns were conducted to verify components in both the early and current system iterations. The first demonstrated a novel in-cylinder gas-liquid mixing device and quantified device behaviour against the no-mix condition. The second campaign demonstrated operation of a scaled pilot packed-column direct contact heat exchanger, where gas and liquid comingled to exchange heat. Existing experimental correlations for high pressure packed column flooding were verified against experimental results, and the overall heat exchange coefficient was calculated. Results were used to validate a finite volume heat transfer model based upon previous correlations. Successful gas-liquid heat exchange in the temperature and pressure range of interest was demonstrated, advancing PHES development and informing future iterations of the system.

Lay Summary

In order to limit further global warming, the electrical grid will require a steadily increasing amount of wind, solar, and marine electricity generation. Energy storage has the potential to substantially increase the grid's ability to accept greater quantities of these renewable generation sources while maintaining grid stability. Pumped-Heat Energy Storage (PHES) is a form of electrical energy storage in development at the University of Edinburgh which could provide the electricity storage that the grid needs. This system is based upon the Joule-Brayton thermodynamic cycle, and stores energy as hot and cold in balanced thermal stores. An inert gas is the cycle working fluid, and a liquid is used to transfer heat to and from the gas to the thermal energy stores.

PHES development at the University of Edinburgh has iteratively explored different system architectures, and focused on increasing confidence in components within these architectures where there is uncertainty with regard to performance. Early work concentrated on gas-liquid mixing within the cylinder of a compressor/expander machine, while current work has eliminated such mixing and instead proposes the use of large scale, direct-contact heat exchangers. Such exchangers suffer from significant uncertainty for this application owing to the lack of existing models with which to predict their behaviour at the proposed operating pressure and temperature. As a result, direct-contact heat exchanger performance cannot be confidently predicted, hindering system development.

Two experiments were conducted to verify components in both the early and current system iterations. The first demonstrated a novel in-cylinder gas-liquid mixing device and quantified device behaviour against the no-mix condition. The second experiment demonstrated operation of a scaled pilot packed-column direct contact heat exchanger, where gas and liquid directly exchange heat. Results were compared with a finite volume heat exchange model and the model was validated by experimental results. Successful gas-liquid heat exchange in the temperature and pressure range of interest was demonstrated, advancing PHES development and informing future iterations of the system.

Acknowledgements

I'd first like to thank my supervisor Win Rampen for the guidance he provided throughout the course of my degree. Without his enthusiasm and hands-on attitude, the work presented here would not have been possible. I don't know of another supervisor at the University who would weld 3 metres atop a scaffold or oxy-fuel cut steel beams for their PhD student! Your dedication to the project truly provided me with a fulfilling experience, and your supervision is sincerely appreciated.

Thanks are due to the entire team at SynchroStor for the supportive environment they provided: Amy, Daniel, Jim, and Martin - you'll be missed. Rick, many thanks for your guidance on numerical modelling and for reminding me to keep an eye on the big picture. Carn, thanks for expanding my thinking of engineering design and teaching me to iterate (and fail!) to achieve results. I must also thank Akhilesh Singhal and Pramath Srikanth, two visiting summer researchers from Bangalore, India, for their assistance in numerous experimental commissioning steps.

Thanks are also due to my PhD and MSc colleagues, both those within IES and without. I enlisted a fair number of you throughout the years to help me move bulky or heavy equipment, freeing you from your desk-based work, and I thank you for cooperating. No PhD can take place in isolation, and I thank those of you who helped me find time to unwind.

Many thanks are due to the following groups for their contributions to the packed-column experimental apparatus: Sulzer Chemical, for donating structured packing, Paratherm Ltd., for donating the thermal heat transfer oil, and Sun Hydraulics, for donating rectification manifolds. I must thank all the technical staff who supported me along the way, including Steve Gourlay for design and pressure vessel certification advice. The assistance of the mechanical engineering teaching workshop was particularly invaluable, and I'm very grateful that Andrew Brown and Callum Melrose tolerated my frequent appearances to borrow tools. I'm additionally grateful to Mark Partington and the engineering structures lab with assistance in hydrostatic proof testing.

I'd like to thank my entire family for their constant encouragement, and my mother and father for interesting me in the fields of engineering and science.

Finally, I must especially thank my partner, Michaela Klímová, for her unwavering patience and support throughout the course of my degree. I acknowledge my experiments took much longer than expected and the company of a harried researcher must have been trying towards the end; I take comfort in the fact that you'll conclude your own PhD journey in a few years and I look forward to supporting you then.

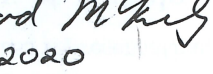

2020

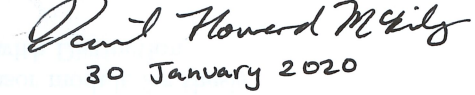

30 January 2020

2020

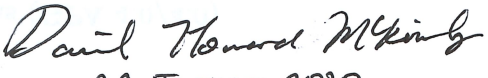

29 January 2020

29 January 2020

31 January 2020

29 January 2020

Howard McKinley

Table of Contents

Chapter 1

Introduction

1.1 Climate & Changing Grid Needs

The modern electrical grid is broadly based on the principle that large generators, often remote from population centres, supply electrical energy to the grid in a manner which follows the loads placed upon the grid by end users. This is the result of decades of debate, invention, and standardisation which chose high-voltage Alternating Current (AC) as a means of energy transmission, and chose to centralise generation in few large stations in order to minimise costs. Although the early electrical grid operated on the same principles that apply today, the value that electrical energy storage could provide was realised early on. The first grid-scale energy storage was built in 1930, and the reasons for doing so were largely the same as they are today (Paus, 1930) - to compensate for peak energy demands, and to smooth variations in renewable energy (at the time, water availability for hydro power). This was a pumped-hydro energy storage plant, a system that stores energy by moving water between two reservoirs of different height. Water is pumped to the upper reservoir when electricity supply exceeds demand, and is released to the lower reservoir to drive a turbine-generator when needed. The UK began to construct pumped hydro storage facilities in response to the nuclear power boom of the 1960s and 1970s. Nuclear generators, unlike their fossil fuelled counterparts, were unable to readily vary output power to match demand and policy makers of the time saw pumped hydro as a method to deal with excess generation, particularly during the night (Gardner et al., 2016).

The electrical grid has evolved significantly since the 1970s, and the rapid introduction of variable and non-dispatchable solar and wind generation in the past 15 years has given renewed importance to the field of energy storage. MacKay (2010) considers

a scenario where the UK has 33 GW of wind, generating 10 GW of power on average. To cope with a 5 day lull in wind production, he calculates that the UK would need 1200 GWh of storage. The UK currently has about 27 GWh of pumped hydro storage split between four facilities (two in Scotland and two in Wales), and about 120 GWh of additional pumped hydro storage in planning or proposed (Gardner et al., 2016). Other forms of energy storage do not significantly contribute to this figure, although they are in use on the UK network providing ancillary services. MacKay (2010) estimates that the UK could feasibly raise its pumped hydro storage capacity to 400 GWh by constructing dozens of facilities across Scotland and Wales, falling well short of the 1200 GWh needed if pumped hydro alone were to cover this hypothetical (but instructive) lull in wind production. To put these numbers in perspective, the UK currently has 18.5 GW of wind power installed (BEIS, 2018) and only 27 GWh of storage, so clearly the grid adapts to wind's lulls with minimal storage at the present. This is primarily accomplished with load-following Combined-Cycle Gas Turbine (CCGT) generation, supplemented with Open-Cycle Gas Turbines (OCGT) and coal. These fossil-fuel technologies, in addition to providing a large quantity of baseload power, can adjust their output according to renewable energy production and grid demands. Although effective at maintaining grid stability, it is the stated policy of the UK government, in order to comply with the Greenhouse Gas (GHG) reductions set out in the Paris Agreement, to gradually decarbonise the electricity sector by phasing out fossil fuel generation (United Nations Framework Convention on Climate Change, 2016).

In a future where the principles of the Paris agreement are adhered to in the UK, standalone coal, CCGT, and OCGT would all be gradually phased out and replaced with a mix of wind, solar, marine, and CCGT with carbon capture and storage (CCS). Nuclear power is slated to remain on the grid providing baseload power, but unless investment and planning processes are rapidly sped up in the next 5 years, it appears that new builds will only serve to replace the existing capacity which is due to begin phased retirements beginning in 2023 (World Nuclear Association, 2017). Significant questions remain over the economic feasibility of large scale CCS, the political palatability of nuclear, and the high capital costs of both. Accordingly, the future UK electrical grid will most likely have a substantial amount of variable and non-dispatchable renewables, necessitating large scale electrical energy storage (National Grid plc, 2018).

1.2 Electrical Energy Storage Technologies

Given the political will that exists at present to follow the Paris agreement, the need for technical solutions to provide large scale energy storage in the UK is clear. As MacKay (2010) discussed, there is a significant amount of additional pumped-hydro capacity in planning or proposed, but these new builds face a trio of challenges: high environmental impacts, remoteness from population centres, and high capital costs. The environmental impacts and capital costs could be mitigated to an extent with supportive legislation and government financing, but the long transmission distances necessitated by locating pumped-storage in remote locations deals a harsh penalty to storage systems. Unless co-located with generation, a storage system far from demand and generation incurs a double efficiency penalty: transmission losses affect both energy stored and energy generated. Figure 1.1 illustrates the problem in the context of the UK, and lists storage capacities for existing systems. For example, the 440 MW Cruachan station connects to Glasgow via a 275kV transmission line approximately 115 km in length (Robert Currie et al., 2002). One way electrical transmission losses could reasonably be estimated to be 4.2% (American Electric Power, 2011), and assuming energy is generated nearby the city, stored at Cruachan, and consumed in the city, the total transmission losses would amount to double the one way loss, 8.4%. The 120GWh of pumped-hydro storage in planning is a combination of expansions to these systems and new storage in similar areas of the UK. While it is likely that some of this planned pumped-hydro storage will be built, additional technologies will be needed to meet future grid demands. In addition to balancing supply and demand, energy storage provides several other benefits to the grid, as highlighted by Brandon et al. (2016):

- Enhancing the grid's ability to absorb renewable generation, thereby reducing renewable curtailments. Depending on local grid topology, renewable generators may be forced to curtail output due to transmission constraints. Co-locating storage and renewables can store energy when transmission is constrained.

- Reducing generation investments by increasing the security of supply of existing generation. By providing reserve capacity, storage can allow generation upgrades to be deferred.

- Offsetting investment in interconnection and transmission. Similar to the previous two points, storage can allow for transmission upgrades to be deferred in lieu of local storage providing peak electricity demand.

- Reducing the need for distribution network reinforcement driven by the electrification of heat and transport. Although these trends are not discussed further in this thesis, they have the potential to place significant loads on the grid which could be mitigated in part by storage.

Energy storage systems beyond pumped-hydro are slowly emerging; perhaps the most widespread to date are lithium-ion battery storage systems which have been introduced to provide ancillary services and small scale arbitrage. While they are a quick responding, scalable, and geographically independent form of energy storage, examining their costs reveals that it is unlikely they will provide GWh scale storage in the foreseeable future. To properly compare storage technologies on price, both the incremental cost of storage in $/kWh and capital cost in $/kW must be considered. Consider pumped-hydro, which has an incremental cost of storage of $10 - $15 per kWh and a capital cost of $600 - $1000 per kW (Tester et al., 2012). Although the capital costs are high (as expected for a large civil works project) the incremental cost of storage is low and it is financially advantageous to build a large installation. Lithium-ion batteries differ sharply in value characteristics, with an incremental cost of storage of $150 - $300 per kWh and a capital cost of $200 - $400 per kW (Tester et al., 2012). While they can't compete for large scale arbitrage at these prices, there are no economic barriers to small-scale installations. To put current lithium-ion development in perspective with previously discussed grid needs, consider that in the UK the largest lithium-ion battery storage facility as of writing is 50MW/50MWh (George, 2018), and the largest worldwide is 100MW/129MWh in Southern Australia (Parkinson, 2017). Although the available power from these installations is not inconsequential, the stored energy is orders of magnitude less than predicted demands and current pumped-hydro installations.

Other battery technologies are far less widespread and are at varying Technology Readiness Levels (TRL); flow batteries encompass a wide range of chemistries and the largest demonstrated to date is 15MW/60MWh (Mancheva, 2016), although permitted plans call for a substantially larger installation of 120MW/700MWh by the early 2020s (Bucker, 2017). Sodium-Sulphur batteries have been demonstrated at scales up to 50MW/300MWh (Brown, 2016), and incremental improvements are expected in these technologies in the near future. Current costs are around $500 per kWh, with capital costs similar to lithium-ion (IRENA, 2017). Although these battery technologies compare favourably with lithium-ion on metrics of energy and cost per kWh, there is still a large technological void to be filled.

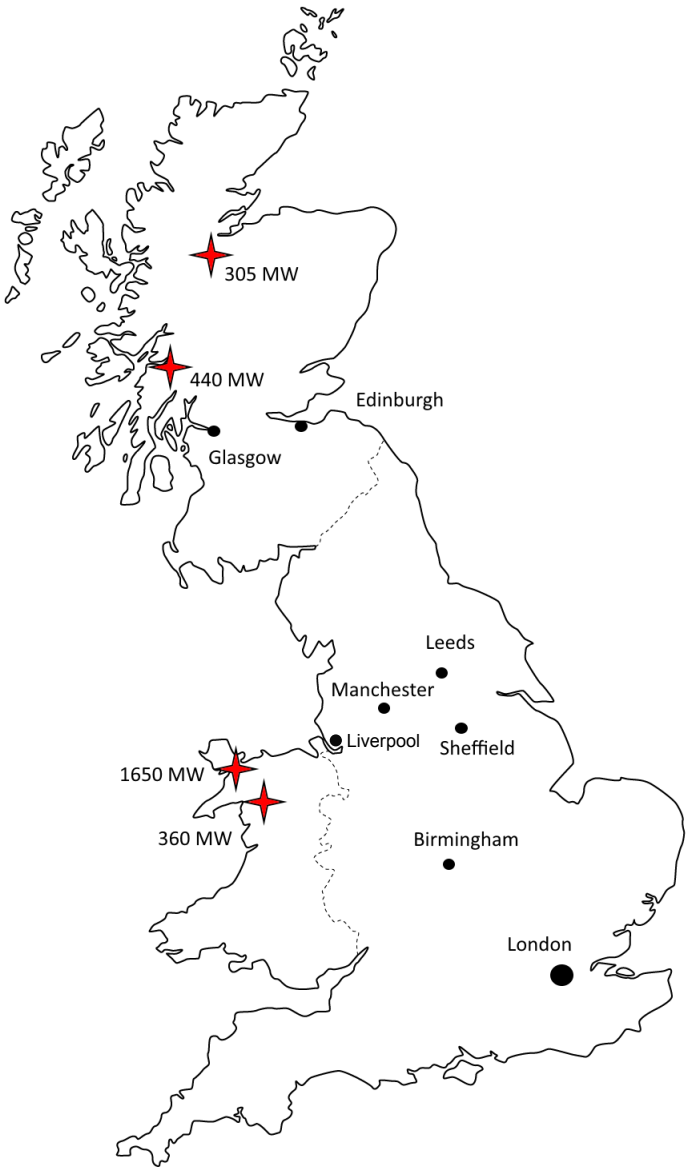

Figure 1.1: Distribution of pumped-hydro storage (red crosses), remote from UK population centres. Note that additional storage is likely to be constructed in similar locations.

Compressed Air Energy Storage (CAES) is one technology that might bridge the gap between batteries and pumped-hydro; the technology stores energy as compressed air in underground caverns and has been demonstrated at larger scales than batteries (one at 290MW/580MWh, another at 110MW/2860MWh). These installations are examples of diabatic CAES, which combust methane to operate in a manner similar to a gas turbine. Efficiency comparisons of these systems to other storage technologies are not straightforward due to their methane consumption, multiple approaches are discussed by Elmegaard and Brix (2011) and summarised here. The first is plant energy

efficiency, which compares the plant input energy to the work it produces:

$$\eta_{cc} = \frac{W_t}{Q_f + W_c} \tag{1.1}$$

where W_t is the output turbine work, Q_f is the fuel energy input, and W_c is the compressor work. This measure of efficiency ignores the exergetic differences of fuel and electricity, and doesn't clearly address the notion that the fuel is burnt to recover stored energy, not to generate electricity independently. Using this metric for the 110MW/2860MWh CAES plant in McIntosh, Alabama, USA gives a plant energy efficiency of 56% (Elmegaard and Brix, 2011). This efficiency measure can be adapted to give the primary energy efficiency of a system:

$$\eta_{pc} = \frac{W_t}{\eta_{sys} Q_f + W_c} \tag{1.2}$$

where the η_{sys} is the efficiency of electricity production in the energy system. While this metric describes the primary energy consumption of a CAES plant relative to its output, it still does not provide a basis for comparison with other storage systems. For the same McIntosh plant, the primary energy efficiency is 29%. A comprehensive storage efficiency value based upon an exergetic analysis of the CAES process is presented by Elmegaard and Brix (2011) and is briefly reproduced here:

$$\eta_{sc} = \eta_{charging}\eta_{storage}\eta_{discharging} = \eta_{x,c}\eta_{x,stor}\eta_{x,t} \tag{1.3}$$

where $\eta_{x,c}$ is the exergetic efficiency of the compressor, $\eta_{x,stor}$ is the exergetic efficiency of storage, and $\eta_{x,t}$ is the exergetic efficiency of the turbine. This analysis produces a storage efficiency of 36% for the McIntosh system. Storage efficiency addresses the exergetic differences between the input methane and the stored electricity, and provides a robust comparison to other energy storage systems. The McIntosh storage efficiency is representative of diabatic CAES systems in operation today, placing them significantly behind pumped-hydro and batteries. These systems have similar cost characteristics to pumped-hydro, with a low incremental cost of storage of $10 - $15 per kWh and a high capital cost of $500 - $1000 per kW. Adiabatic CAES systems, which store heat generated during air compression instead of burning natural gas to replace this heat, promise significantly higher efficiencies of 70% (IRENA, 2017) and the first demonstration plant was commissioned by General Compression at a scale of 2MW/500MWh (Gaiser, 2016). The plant encountered operational difficulties, and it appears to have ceased operation several years ago at the time of writing. Additionally constant-pressure CAES, which use underwater flexible storage vessels rather than salt

caverns, have been tested on a small scale with similar efficiencies to adiabatic CAES, with a 750kW/1.5MWh pilot plant currently operational and others planned (Pimm and Garvey, 2016). Costs of these adiabatic systems could reasonably be assumed to be similar to that of diabatic systems, albeit with a slightly higher incremental cost of storage due to the required thermal stores.

Other technologies which are less widespread include potential energy based storage developed by Gravatricity (Flaig, 2019) which stores energy by moving large masses to different heights with cranes, and storage by Advanced Rail Energy Storage (Massey, 2014) which operates on the same principle using rail track, hoppers, and electric locomotives. Neither have progressed sufficiently to provide accurate cost metrics. Flywheels, which store kinetic energy in a rotating mass, have been used for grid support, the largest of which is operated by Beacon Power at 20MW/5MWh (Beacon Power, 2010). Costs tend to be high, with an incremental cost of storage of $100 - $800 per kWh and capital costs of $200 - $500 per kW. Hydrogen is an often-touted electrical energy storage technology, as it promises long duration storage with little to no time-dependent losses. The technology operates on the premise that cheap, off-peak, or otherwise 'unwanted' electricity would be used to electrolyise water to produce hydrogen, which would be stored either as a gas in a tank or underground cavern, or as a liquid or slush. The hydrogen would be extracted and either burned in a gas-turbine or used in a fuel-cell to produce electricity. No grid-scale demonstrations of this approach have been built, likely because the overall efficiency of the process is less than 55% (Breeze, 2018) and capital costs are high; ALK-type electrolysers alone are around $750 per kW. Of the remaining technologies, no prototypes have been built of gravity-based technologies, and flywheels are practically constrained to short-duration storage. Although CAES is likely the technology with the highest TRL for large scale energy storage other than pumped-hydro at the moment, it carries the same fundamental drawback as pumped hydro: the need for a very specific geography, whether it be a salt cavern or deep water. This is disadvantageous for two reasons: first, the aforementioned transmission efficiency penalty, and second, dependence on specific site geography introduces a significant amount of risk into project development since there is a possibility that the site is later found to be unsuitable.

While there clearly are a number of medium scale energy storage technologies proposed, in development, and in demonstration which could address the UK's energy storage needs of the future, no system has yet emerged as a clear winner. A system which could provide energy storage at a similar incremental cost of storage to

pumped hydro or CAES without geographic restriction would likely find that there is ample space in the energy storage market to support it. A comprehensive albeit dated overview of energy storage technologies is presented by Dincer and Rosen (2011) which provides greater depth to the information presented here.

1.3 Pumped-Heat Energy Storage

A technology proposed to fill the void of geographically-independent energy storage systems is a reversible heat-pump/heat-engine based upon the Joule-Brayton cycle, termed Pumped-Heat Energy Storage (PHES). This system was first presented in published literature by Desrues et al. (2010), although a patent by Isentropic Ltd., an early developer of this technology, precedes publication by several years (Howes and Macnaghten, 2007). Desrues describes what can simplistically be described as a 'heat battery'. The battery is charged by running the cycle in the forward direction, heating one thermal store and cooling another by drawing electrical power from the grid. The battery is discharged by running the cycle in the reverse direction, converting stored heat and coolth to electricity to return to the grid. The conversion from electricity to heat (or coolth) is made by compressing or expanding a single-phase gaseous working fluid; a compressed gas heats up and an expanded gas cools down. A simplified system diagram is shown in Figure 1.2.

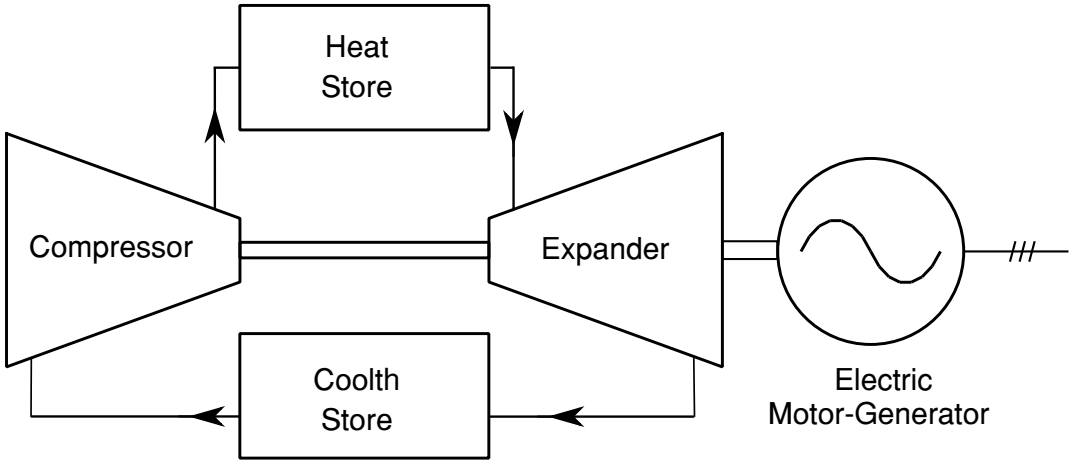

Figure 1.2: Simplified diagram of a PHES system, shown in charging mode.

Isentropic's development of a PHES system began around 2005 with patents covering an air-source heat pump (MacNaghten and Howes, 2007), and it secured funding from the Carbon Trust and other investors beginning in 2010 to further system

development (MacNaghten, 2010). In mid 2012, Isentropic was selected to build a 1.5MW/6MWh demonstration plant at an electricity substation in the Midlands as part of a five year plan to prove the feasibility of its technology (Robinson, 2012). A demonstration plant was constructed and the company released positive results of thermal storage testing showing that the stores performed adequately, but publicly provided little other information on system performance. In early 2016 the company went into administration and its assets were purchased by Newcastle University and incorporated into the Sir Joseph Swan centre for energy research. A press release issued by the centre in early 2019 provided an update on the system, claiming a rated power of 150kW and storage of 600kWh with efficiencies of 60-65% (Centaur Media, 2019). If confirmed, these figures paint a bleak picture of system performance as both rated power and storage capacity are an order of magnitude less than originally planned. Although little is publicly known about the reasons for the failure of the Isentropic Ltd., industry observers have speculated that the decision to set the cycle's cold pressure at ambient atmospheric pressure resulted in excessively large swept volumes, rendering the system unable to meet desired power ratings. This speculation appears to be confirmed by Newcastle's system performance data. The company's choice to set the cycle cold-side pressure to ambient pressure was tied to the choice to use a pressurised heat store and an ambient pressure coolth store, which incurred a significant cost premium for the hot store compared to ambient pressure storage.

Garvey et al. (2015) proposed a wind-turbine power take-off and transmission system based upon the Joule-Brayton cycle, noting earlier work done by Isentropic. This system incorporated energy storage in several of its operational modes, and suggested two critical improvements to previous work. First, it proposed raising the cycle cold-side pressure above ambient pressure to improve power density by reducing compressor swept volume. Second, it planned to decouple the pressure inside the gas compression/expansion loop with the pressure in the thermal stores. As noted above, Isentropic was tied to using the hot-side pressure for its hot thermal store, and the cold-side pressure for its cold thermal store, necessitating expensive pressure vessels for its hot thermal store. Decoupling was accomplished by utilising gas-air heat exchangers on both the hot and cold sides of the cycle. Air was to be heated or cooled by the exchanger, then circulated through the thermal store at ambient pressure, eliminating the need for pressure vessels and drastically reducing thermal store cost. Garvey et al. (2015) also proposed that the system utilise a wind-turbine nacelle mounted radial gas compressor, similar in nature to Artemis Digital Displacement (DDP) hydrualic pump-

motor technology. Both this literature and Isentropic's demonstration system provided inspiration for the PHES system in this thesis based on the same basic thermodynamic principles. Notably, since the commencement of the work which will shortly be described, a substantial number of entities seeking to commercialise PHES in one variant or another have emerged, including Malta Inc. (Burke, 2018) which uses molten salts and turbomachinery, Stiesdal A/S (Stiesdal, 2019) which proposes a system similar to what is described here for offshore applications, and WindTP (WindTP, 2019) which is developing wind driven heat-pump/heat-engines, as described by Garvey et al. (2015). Although relevant to a comprehensive discussion of this technology, these competitors were unknown to the author or the wider public until after the majority of work presented in this thesis was carried out.

The work detailed in this thesis was undertaken as part of the ongoing development of a PHES system by Prof. Win Rampen and SynchroStor Ltd. at the University of Edinburgh. Similar to previous technologies, the goal of this system is to provide grid-scale electrical energy storage based upon the Joule-Brayton cycle which is modular, affordable, and without significant geographic restrictions. Incorporating lessons-learned from Isentropic Ltd. and proposals by Garvey et al. (2015), this system will operate at an elevated cold-side low pressure of 20 bar and decouple pressure within the gas-loop from the pressure within the thermal energy store.

Development began when Prof. Rampen accepted the Chair of Energy Storage at the University of Edinburgh in the autumn of 2014, with a goal of applying Artemis DDP hydraulics to the field of energy storage. A research group was formed consisting of Prof. Rampen, research associate Dr. Rick Jefferys, design engineer Mr. Carn Gibson, and the author. This group later evolved into SynchroStor Ltd. with the addition of several employees, and seeks to commercialise the system. Initial work funded in part by Innovate UK examined a large diameter, slow speed, reciprocating piston compressor/expander system which incorporated gas-liquid mixing in-cylinder. The liquid was used to limit high and low temperatures in the compressor/expander, and to decouple the thermal stores from the gas loop. Development of this initial (v1) system included performance modelling, costing, and the construction of an experimental reciprocating piston-cylinder compressor/expander incorporating liquid mixing. System evolution continued, and partially due to the results of the experimental apparatus, a second (v2) system was developed to replace the large, linear reciprocating pistons with a smaller, faster, radial reciprocating compressor/expander derived from Artemis technology. This second iteration introduced a direct-contact heat exchanger to trans-

system	v1	v2
gas	argon	nitrogen
liquid	Paratherm HR thermal oil	Paratherm HR thermal oil
compressor style	linear	radial
piston stroke	3000 mm	15 mm
piston speed	0.5 m/s	1.2 m/s
heat exchanger	in-cylinder	G-L direct contact

Table 1.1: Summary of PHES design evolution. Note that 'G-L' refers to gas-liquid heat exchange.

fer heat between the gas and liquids, as liquid mixing within the compression chamber was not possible with the radial compressor/expander design. The direct-contact heat exchanger is the subject of study for the majority of this thesis. Development work continued as SynchroStor was incorporated, and a third evolution (v3) system is currently in design, partially based upon the results of the direct-contact heat exchanger experiments. All three evolutions have a pressure-ratio of 10, yielding a hot-side high pressure of 200 bar with a cold-side low pressure of 20 bar. These pressures were selected after system modelling and optimisation, to which the author contributed. The aim of this modelling was to produce a system with sufficient power density which operated within temperature and pressure regimes for which components and sensors are commonly available. Further discussion of these trade-offs is made in the following chapter. System evolution is catalogued in Table 1.1 and in Figures 1.3 and 1.4. Detailed information on the third evolution has been omitted owing to intellectual property concerns, and is not relevant to this thesis. As of writing, SynchroStor continues work on the radial compressor/expander and the v3 system design as part of an effort to develop a demonstration plant as part of the UK Government's Business, Energy, and Industrial Strategy (BEIS) Low Cost Storage programme.

1.4 Chapter Summary

This thesis contains eight chapters, as summarised below.

Chapter 2 provides a review of literature regarding the proposed energy storage system. The Joule-Brayton cycle is discussed in greater depth, as is the performance of PHES systems built upon it. Irreversibility, heat transfer, and process heat exchange

are examined in the context of the PHES system, while an overview of packed columns and gas-liquid mixing is given.

Chapter 3 discusses the experimental process of verifying the performance of an in-cylinder gas-liquid mixing device as necessitated by v1 of the PHES system. It sets out the experiment goals, defines the experimental setup and methods, and details the preliminary results. Results are presented using high speed photography and by examining the changing nature of the pressure-volume (p-V) curve of the compression and expansion processes as experiment parameters are varied.

Chapter 4 describes the basis for the primary body of work in the thesis. A MATLAB model is constructed to simulate a direct-contact heat exchanger, necessitating experimental work to verify the heat-transfer coefficient correlation used. An examination of pilot to full-size column heat exchanger scaling is made, and the basic parameters (diameter, length, packing size, temperatures, pressure) of an experimental exchanger are defined.

Chapter 5 describes the direct-contact heat exchanger experimental design, how experiment variables are quantified, desired operational modes, and the experimental campaign. The selection of data-acquisition hardware to meet experimental needs is also discussed.

Chapter 6 chronicles the direct-contact heat exchanger experimental apparatus detailed design, including component sourcing, manufacturing, and assembly.

In Chapter 7, the results of the direct-contact heat exchanger apparatus experiments are analysed. Apparatus performance is appraised, and the Log-Mean Temperature Difference method is used to determine an approximate overall heat transfer coefficient of each column in the apparatus under varying conditions. Column performance is then compared with the finite volume heat transfer MATLAB model, and measurements of column flooding are compared with existing models.

Chapter 8 summarises the results of both experiments and discusses the performance of the experimental apparatus and the models. Opportunities for further work on the packed-column experimental apparatus and the PHES system are discussed.

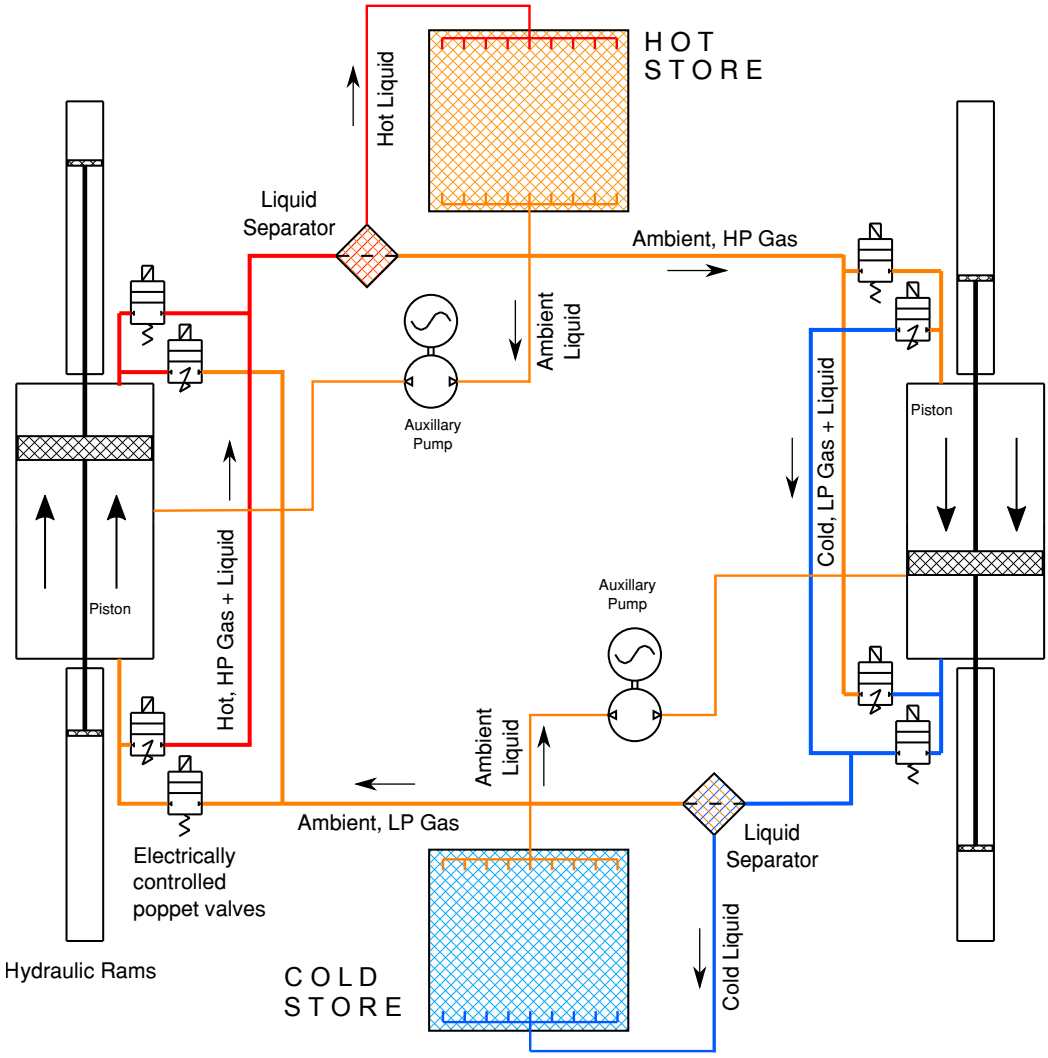

Figure 1.3: The first iteration of the SynchroStor PHES system, shown in storage mode. Hydraulic rams are driven by Artemis DDP pump/motors to compress and expand the gaseous working fluid in large, slow speed linear piston-cylinders. Liquid is injected into the cylinders during compression and expansion, and removed from the pressure envelop to transfer heat and coolth to thermal energy stores. In-cylinder gas-liquid mixing is examined in Chapter 3.

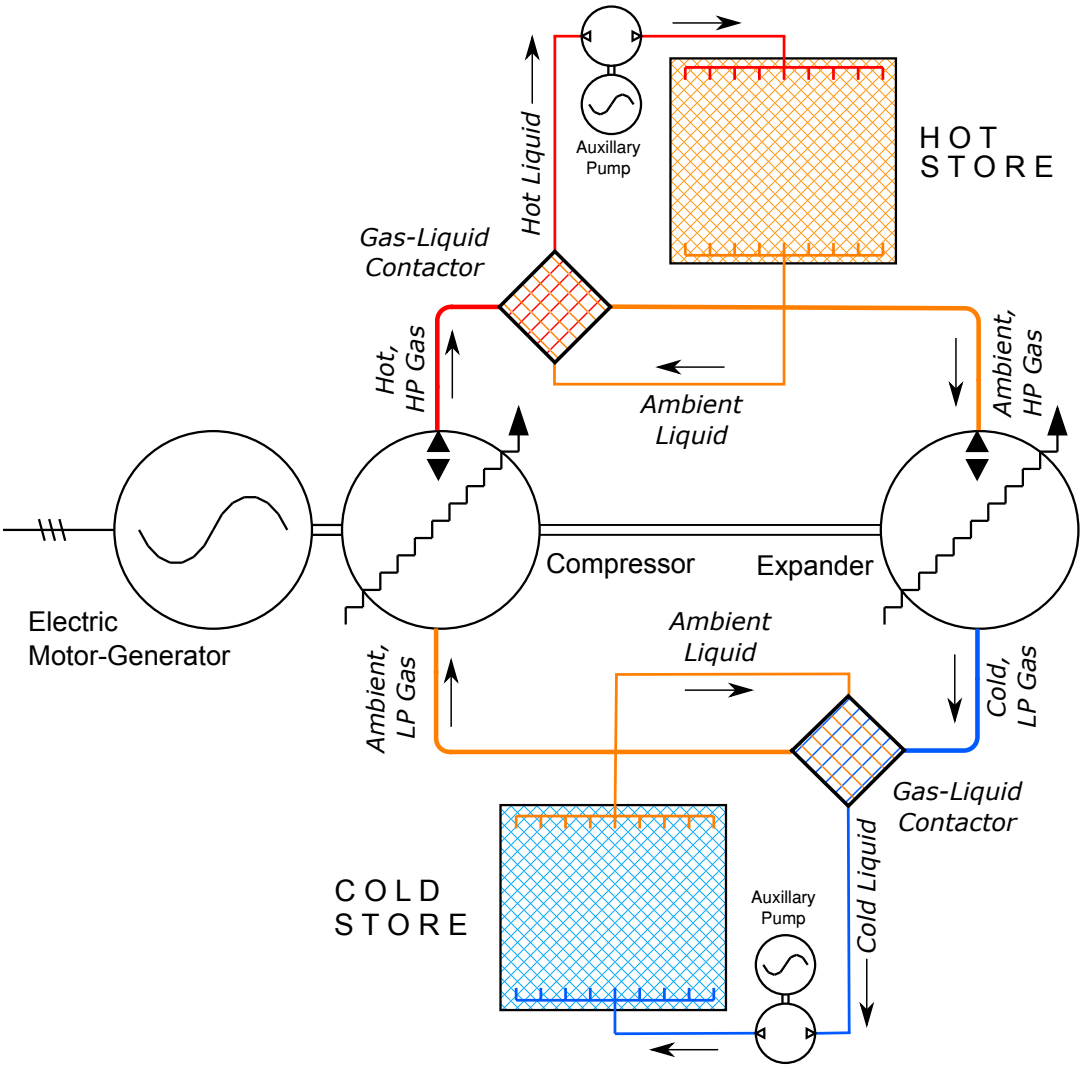

Figure 1.4: The second iteration of the SynchroStor PHES system, shown in storage mode. Artemis-derived high-speed radial compressor/expanders replace the previous linear design, and in-cylinder liquid injection is eliminated. A gas-liquid contactor is introduced to transfer heat from the gaseous working fluid to a separate liquid loop for each thermal store. The gas-liquid contactors are examined in Chapters 4,5,6 and 7.

Chapter 2

Background & Literature Review

This chapter provides a review of literature regarding the proposed electrical energy storage system. The Joule-Brayton cycle is discussed in greater depth, as is the performance of PHES systems built upon it. Irreversibility, heat transfer, and process heat exchange are examined in the context of the PHES system, while an overview of packed columns and gas-liquid mixing is given.

2.1 The Joule-Brayton Cycle

The Joule-Brayton cycle is the foundation of the PHES system, and although introduced briefly in Chapter 1, is explored in greater depth here. Sometimes referred to as the Brayton Cycle or (when reversed) the gas refrigeration cycle, it is an idealised steady-state thermodynamic power cycle with two isentropic (constant-entropy) and two isobaric (constant-pressure) processes utilising a single-phase gaseous working fluid (Borgnakke and Sonntag, 2014b). The isentropic processes are compression and expansion, and the isobaric processes are heating and cooling. When the cycle is run in a manner which generates a net output of work it is said to be running in the forward direction, and an apparatus operating on it is known as a heat engine. When the cycle is run in a manner which consumes a net input of work it is said to be running in the reverse direction and an apparatus operating on it is known as a heat pump. The forward and reverse directions of the cycle move the gasesous working fluid in opposite direction to one another, and heat flows in opposite directions. An instructive pressure (p) versus volume (V) and temperature (T) vs entropy (S) diagram for the forward cycle is shown in Fig. 2.1 for a hypothetical heat engine. Step 1-2 shows isentropic compression, 2-3 isobaric heating, 3-4 isentropic expansion, and 4-1 isobaric cooling.

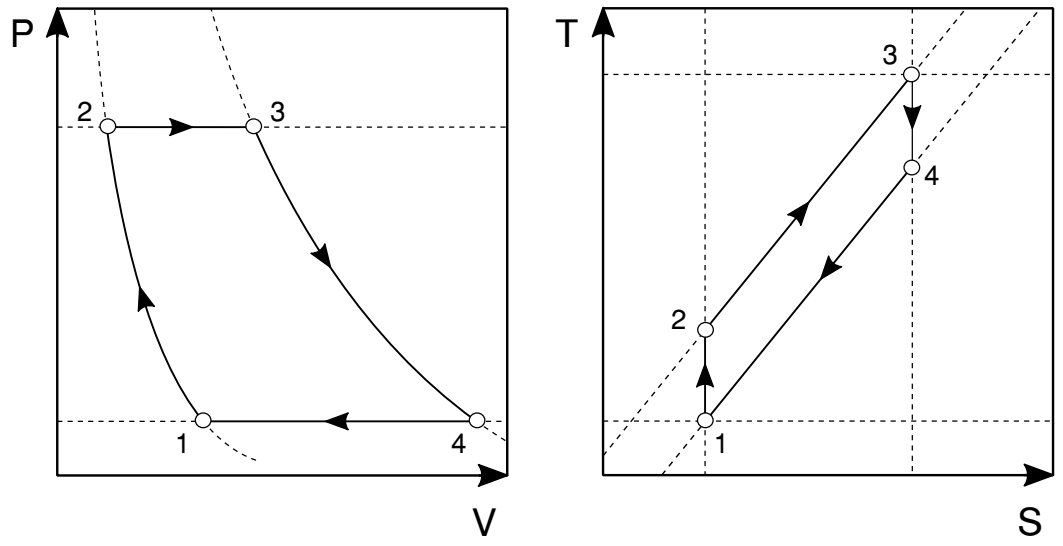

Figure 2.1: Instructive pressure versus volume (*p*-*V*) and temperature versure entropy (Ts) diagrams for the forward Brayton cycle. Points show 1-2 isentropic compression, 2-3 isobaric heating 3-4 isentropic expansion, and 4-1 isobaric cooling. Adapted from Kolin (1998).

The area enclosed by the *p*-*V* curve represents the net work done by the cycle, and the area enclosed by the *T*-*S* curve represents the net heat added by the cycle.

A heat engine based on the Joule-Brayton cycle was first described in a patent by John Barber in 1791, in which he characterised a reciprocating gas compressor (isentropic compression), a combustion chamber (isobaric heating), and a crude turbine (isentropic expansion) (Davey, 1914). The isobaric cooling process was proposed to take place at atmospheric pressure, as the system was open to the atmosphere and used ambient air as its working fluid. Barber's invention was never built, and the next development of the cycle came approximately 40 years later in 1833 when John Ericsson constructed his first heat engine operating on the cycle, although instead of using combustion for isobaric heating, he utilised an external supply of heat (Kolin, 1998). Ericsson used a reciprocating piston-cylinder design for his apparatus, and created several different versions of this engine, some which were open to the atmosphere and some which were closed and recirculated their working fluids. Ericsson was a prolific inventor and created many variations on his first engine; one of his many variations operated on a different cycle with two constant temperature (isothermal) and two isobaric processes and a single-phase gaseous working fluid. This is what is commonly known as the Ericsson cycle today. James Joule continued development in 1852 with heat

engines that largely replicated Ericsson's (Kolin, 1998), and in 1872 George Brayton developed a heat engine based on the same cycle, but using internal combustion rather than external heating as Ericsson and Joule had (Butterman, 2012). It was Brayton's reciprocating engine that later evolved into modern gas turbines; perhaps this is why his name is solely attached to the cycle today in a great deal of literature. This thesis will exclusively use the terminology 'Joule-Brayton cycle', which at least partially credits work which preceded Brayton and is used widely in international literature. MacNaghten (2010) and Isentropic Ltd. have termed the cycle 'the first Ericsson cycle', and while it rightly credits the engineer who first demonstrated the cycle, its use is not widespread.

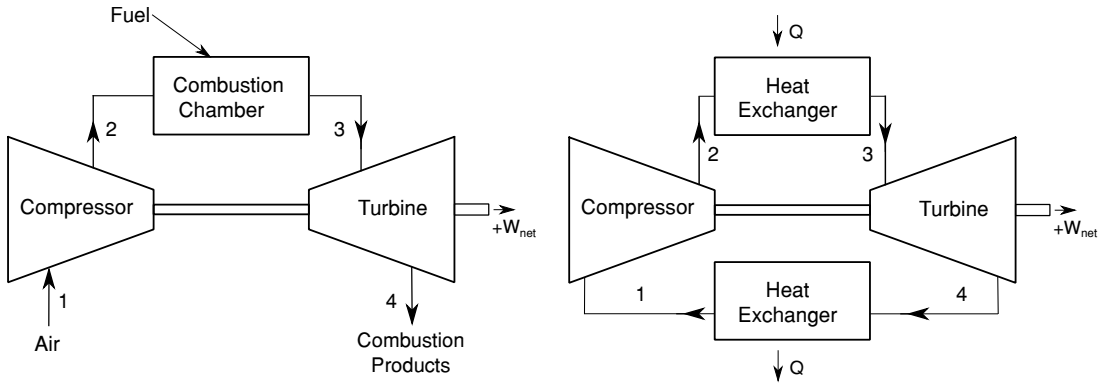

Figure 2.2: The forward Joule-Brayton Cycle, showing both open (left) and closed (right) variants. Adapted from Borgnakke and Sonntag (2014b).

A distinction is made in literature between Joule-Brayton cycle heat engines with and without internal combustion; engines with internal combustion are commonly known as 'open' because they inlet and exhaust to the atmosphere, and engines without internal combustion as 'closed'. This terminology is a slight misnomer because early iterations of Ericsson and Joule's engines were open to the atmosphere and did not utilise internal combustion; however due to their lower power densities and air-only working fluid, these engines were quickly replaced with closed variants. Figure 2.2 compares the two types of engines, and should be cross referenced with the *p*-*V* and *T*-*S* diagrams in Figure 2.1 as points 1,2,3, and 4 correspond between figures. Although the open variant of the cycle is by far the most widespread in modern times and several examples are discussed here, the closed variant is the subject of study for the remainder of the thesis. Therefore, the distinction between open and closed cycle will be omitted outwith this section and the reader should assume that the closed cycle is referred to unless otherwise stated. Heat engines operating on the open Joule-Brayton

cycle today include open cycle gas turbines and some air-fed jet engines, and engines which operate on the closed cycle include closed cycle gas turbines. Neither the closed nor open examples given meaningfully instruct the work presented here, as all involve internal combustion.

The history of heat-pumps based upon the same cycle is significantly briefer, with the first patent for a reverse Joule-Brayton cycle air refrigeration machine issued to Joseph Coleman in 1877, and installed by Scottish shipping agents John Bell & Sons for transoceanic meat shipping in 1879 (Wilkins, 1989). For this reason the reverse Joule-Brayton cycle is sometimes referred to as the Bell-Coleman cycle, or the air refrigeration cycle. Although Coleman's machines fell out of favour for refrigeration purposes by the early 1910s due to the higher efficiency of vapour compression alternatives and the poor reliability of his slow-moving reciprocating design (Hundy et al., 2016), many heat pumps operate on the cycle today for other applications. Small and medium scale liquefied natural gas (LNG) production plants sometimes utilise the cycle, owing to its cheap construction, simple operation, and reduced hydrocarbon inventory when compared with traditional methods of LNG production (Roberts et al., 2015). Some aircraft pressurisation and cooling systems and air liquefaction plants also operate on the cycle (Borgnakke and Sonntag, 2014a). The LNG applications of the cycle are particularly instructive for the desired PHES system, as the cold temperatures of the two applications are quite close.

2.2 Applications to PHES

The first (and to date, only) commerical apparatus operating on the Joule-Brayton cycle as both a heat-pump and heat-engine is the PHES system developed by Isentropic Ltd. discussed in Chapter 1. While other systems operating in a similar manner have been described in previously discussed published literature, none have been built. A simplified schematic of the system built by Isentropic is shown in Figure 2.3, showing both storage (heat-pump) and generation (heat-engine) modes of operation. This schematic broadly also applies to the PHES system which is in development by SynchroStor Ltd. and is the subject of this thesis, with modifications discussed later. A synchronous motor-generator drives or is driven by a compressor and expander on a common shaft, which sequentially compresses then expands a gas. When operating as a heat-pump (storage mode, Figure 2.3), the system is in storage mode and draws electricity from the grid. The gaseous working fluid is isentropically compressed from

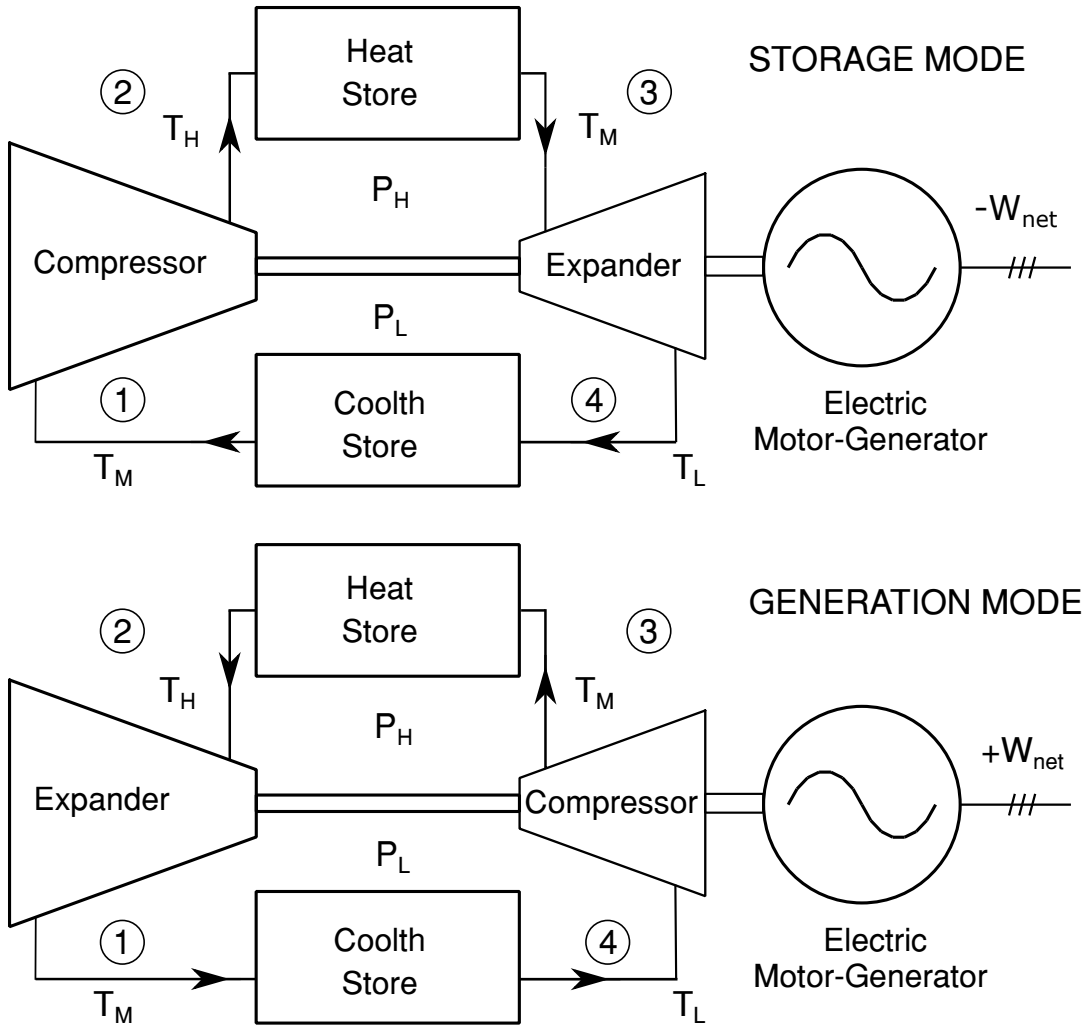

Figure 2.3: A generalised schematic of PHES operation, showing both storage and generation modes.

low pressure p_L and middle temperature T_M at point 1 to high pressure p_H and high temperature T_H at point 2. The working fluid travels through the heat store and isobarically rejects heat filling the store, arriving at point 3 at middle temperature T_M. The fluid is then expanded from p_H and T_M to p_L and low temperature T_L at point 4. It then passes through the coolth store and absorbs heat filling the store, returning to T_M at point 1. Exergy is stored as a temperature difference from ambient temperature in both stores. The opposite cycle occurs when the apparatus is switched to operate as a heat engine (generation mode, Figure 2.3). The compressor and expander machines switch function, producing a net work output which drives the motor-generator to return electricity to the grid. The working fluid flows in the opposite direction, and fluid at middle temperature T_M and low pressure p_L at point 1 is passed through the coolth

stage	temperature	pressure
1	$T_M = 30°C$	$p_L = 20\,bar$
2	$T_H = 400°C$	$p_H = 200\,bar$
3	$T_M = 30°C$	$p_H = 200\,bar$
4	$T_L = -120°C$	$p_L = 20\,bar$

Table 2.1: Summary of PHES Joule-Brayton cycle parameters.

store, isobarically rejecting heat to arrive at T_L at point 4. The fluid is then compressed to high pressure p_H and middle temperature T_M at point 3, before travelling through the hot store and absorbing heat to reach T_H at point 2. The fluid is then expanded to low pressure p_L and middle temperature T_M at point 1, completing the cycle. When the heat and coolth within the stores are degraded to the point at which output temperatures T_L and T_H cannot be reached, the apparatus can no longer function and the stores must be recharged by running the system in storage mode. A summary of the chosen cycle values is given in Table 2.1, which reflect the results of system modelling and optimisation undertaken outside the scope of this thesis.

Throughout the discussion of the thermal stores of the PHES system, the term 'exergy' is used in preference to 'energy' on the basis that exergy is a more rigorous metric than energy because it quantifies the usefulness of a system, not just the energy which it contains. Exergy is the maximum useful work that can be obtained from the energy in a system at a specified state (Cengel and Boles, 2011). Work is a function of a system's initial state, process path, and a final state; therefore exergy is a property dependent on a system, a reversible process, and the system's environment. A system is said to be in a dead state when it is in thermodynamic equilibrium with its environment, at this point the exergy of the system is zero. Therefore, both the hot and cold thermal stores contain non-zero, positive quantities of exergy. Exergy properly captures the usefulness of the thermal stores in the PHES system, while an analysis based purely on energy could wrongly dismiss the coolth store as unnecessary.

The real-world utility of the Joule-Brayton cycle to effectively store and return energy is highly dependent upon the pressures, temperatures, and working fluid selected. Pressures must be chosen which are both realistic for compressor and expander machinery, while having a high enough ratio between them to generate or store the desired power. Temperatures must not violate fluid or apparatus thermal limits, both at T_H and T_L. Each variable has an effect upon the other, and the selection of p_H and p_L are

perhaps the most influential, as they ultimately determine T_H, T_L, and the power rating of the system. T_L and T_H are primarily constrained by material selection, as a portion of the apparatus must be economically built to contain the working fluid at T_H and p_H, as well as at T_L and p_L. The strength of common carbon steels are detrimentally affected by high temperatures; creep must be considered at temperatures above 370°C and strength parameters must be derated (European Committee for Standardization, 2014). Additionally, impact and ductility concerns can arise below -50°C, requiring careful engineering to produce a safe design at the desired working temperatures. In both cases, engineering concerns can be assuaged with material choices beyond carbon steel, at additional expense.

Making the simplifying assumption that the working fluid is an ideal gas, the relation between pressure and temperature for isentropic expansion or compression is given by Equation 2.1, where γ is the heat capacity ratio of the gaseous working fluid.

$$\frac{T_2}{T_1} = \left(\frac{p_H}{p_L}\right)^{\frac{\gamma-1}{\gamma}} \tag{2.1}$$

For a chosen p_H and p_L and a known T_M, both T_H and T_L can be calculated from this equation. To calculate T_H, substitute it for T_2 and T_M for T_1. To calculate T_L, substitute it for T_1 and T_M for T_2. T_M is a function of the high and low temperatures, and is calculated as the geometric mean of T_H and T_L, given in Equation 2.2 (Garvey et al., 2015).

$$T_M = \sqrt{T_L \cdot T_H} \tag{2.2}$$

The selection of a working fluid affects performance through variation in γ, the specific heat capacity ratio. Two commonly available industrial gases, Nitrogen ($\gamma = 1.4$) and Argon ($\gamma = 1.67$) are widely discussed (Garvey et al. (2015), Desrues et al. (2010)) as suitable gaseous working fluids for a PHES system, noting that Equation 2.1 shows that for a given pressure ratio, the higher the γ the greater the temperature rise. Air is not considered a viable working fluid owing to its oxygen content, which could support combustion within the apparatus when combined with certain liquids. Nitrogen was ultimately chosen over Argon owing to its lower freezing point, higher c_p, lower γ, and lower price. The overall power rating of the system can be determined by calculating the work done by each isentropic process, and multiplying it by the mass-flow rate of the working fluid. For an isentropic process, work is calculated by:

$$W = h_2 - h_1 = c_p(T_2 - T_1) \tag{2.3}$$

where h is the enthalpy of the fluid at states 1 and 2. Because analysis up to this point considers only ideal, reversible processes, the equation can be further simplified in terms of specific heat and temperatures. Substituting into this equation the points in the PHES system previously described yields:

$$Storage: \quad W_{net} = \dot{m}\Big(c_p(T_M - T_H) + c_p(T_M - T_C)\Big) \tag{2.4}$$

$$Generation: \quad W_{net} = \dot{m}\Big(c_p(T_H - T_M) + c_p(T_C - T_M)\Big) \tag{2.5}$$

where $\dot{m}$ is the mass-flow rate of the working fluid, and c_p is the average specific heat of the working fluid over the given temperature range. $\dot{m}$ can be chosen to give the apparatus a desired power rating, noting that lower values of p_L will require higher volume-flow rates $\dot{V}$ for the same $\dot{m}$. This relation helps to describe the performance issues experienced by Isentropic Ltd. alluded to in Chapter 1. Although Isentropic's selection of the ratio between p_L and p_H produced suitable storage temperatures and power, due to their choice of a low p_L they required large volume-flow rates of working fluid, necessitating large machinery moving at high speeds. In storage mode (when the apparatus acts as a heat-pump), W_{net} is negative, following the convention that energy transferred to the electrical grid is positive. In the ideal scenario considered so far, W_{net} for storage is the negative of W_{net} for generation. To obtain a more realistic estimate of system performance irreversibilities, non-ideal gases, and non-constant c_p values must be accounted for.

2.3 Irreversibility

The Joule-Brayton cycle is an idealised cycle, and the degree to which this idealised cycle can be followed in practice is critical to the success of the PHES system. The Joule-Brayton cycle describes two isobaric and two isentropic processes; isobaric processes are not idealised and therefore can be performed with real-world equipment. Isentropic processes, which cannot be performed in actuality, can also be defined as processes which are both adiabatic and fully reversible. No real-world processes are fully reversible due to the presence of irreversibilities, which include friction, heat transfer, unrestrained expansion, mixing of two fluids, and chemical reactions (Cengel and Boles, 2011). Therefore, the Joule-Brayton cycle is in practice a cycle with two isobaric and two adiabatic processes. Although no process can be fully reversible, an apparatus designed to minimise irreversibilities (both within the gas cycle and without)

will operate as close to the isentropic ideal as possible, and return the greatest proportion of the electrical energy taken from the electrical grid. This proportion is termed *overall system efficiency*, and in order for the SynchroStor PHES system to have an efficiency on par with pumped-hydro storage it is desired that this value is above 70%. Sources of irreversibility in the system include:

- Friction and heat transfer within the compressor and expander
- Heat transfer, friction and fluid mixing within the gas-liquid contactor (in the second iteration)
- Fluid mixing within the compressor and expander cylinder (in the first iteration)
- Friction losses in pipework and electrical machines
- Heat transfer from the thermal stores to the environment

The task of any technology developer is to drive down uncertainty in order to quantify device feasibility, performance and cost. In the case of the SynchroStor PHES system, quantifying the overall system efficiency is a critical part of the development in order to ensure that the system is economically feasible. This task begins by quantifying the irreversibility in all parts of the proposed system. Unlike pure heat-engines or heat-pumps which suffer one-way irreversibility losses, the PHES system suffers losses both charging and discharging the system, effectively doubling the impact an irreversibility has on the overall system efficiency. Consider a heat store where heat is transferred from the gas loop to the store with an efficiency of η. This efficiency impacts the system both charging and discharging, making the total impact to system efficiency of η^2. A full analysis of how irreversibilities affect the performance of the gas cycle and previously discussed system parameter equations is not presented here, however work by Desrues et al. (2010) thoroughly examines the effect of irreversibilities on a Joule-Brayton cycle energy storage system. In short, irreversibilities most prominently affect the cycle performance by altering the exit temperatures of the working fluid from the thermal stores. Compared to an ideal storage cycle, the real-world cycle shows higher hot thermal store exit temperatures, and higher cold thermal store exit temperatures. Each indicate that heat transfer between the gas and thermal store was not reversible, and affect the compression or expansion process that follows. One important departure from the work presented by Desrues et al. (2010) regarding the PHES system presented here is the use of a liquid to transfer heat from the cycle

working gas to the heat stores, this choice introduces pumping losses as liquid must be pumped across the system pressure boundary to exchange heat with the gas. Work can be recovered from the liquid as it exits the pressure boundary, one way to accomplish this would be to add a pump and turbine on a common shaft. Net power loss P can be quantified by:

$$P_{loss,pumping} = P_{pump,in} - P_{turbine,out} \tag{2.6}$$

A preliminary system costing exercise conducted by the author in collaboration with SynchroStor Ltd. concludes that energy losses to the environment from pipework, pumping, and thermal stores can be cost-effectively reduced to negligible amounts; similarly pipes can be sized to minimise fluid-flow friction losses. Of much greater concern, and the subject of the majority of this thesis, is the irreversibility in gas-liquid heat exchange, both in the first iteration cylinder and in the second interation direct-contact heat exchanger, which is discussed presently.

2.4 Heat Transfer

Heat transfer is the physical process by which energy in the form of heat flows from high to low temperature in three modes: conduction, convection, and radiation. Conduction is the transfer of energy from more to less energetic particles of a substance with no bulk or macroscopic motion of the substance (Incropera, 2007). One-dimensional heat transfer by conduction along an axis x is described by the rate equation:

$$q_x = -k\frac{dT}{dx} \tag{2.7}$$

where q is the heat flux in W/m^2, dT/dx is the temperature gradient, and k is a property of the substance known as thermal conductivity having units $W/(m \cdot K)$. Convection is energy transfer from more to less energetic particles of a substance with macroscopic motion of the substance. Heat transfer by convection from a fluid to a surface is defined by Newton's law of cooling:

$$q = h(T_s - T_\infty) \tag{2.8}$$

where T_s and T_∞ are the surface and fluid temperatures respectively, h is the convective heat transfer coefficient with units W/m^2K, and q is the heat flux. Radiation is energy emitted as electromagnetic waves from a body at a non-zero absolute temperature due to changes in electron configuration (Incropera, 2007). One common radiative heat transfer scenario can be quantified by:

$$q = \varepsilon\sigma(T_s^4 - T_{surr}^4) \tag{2.9}$$

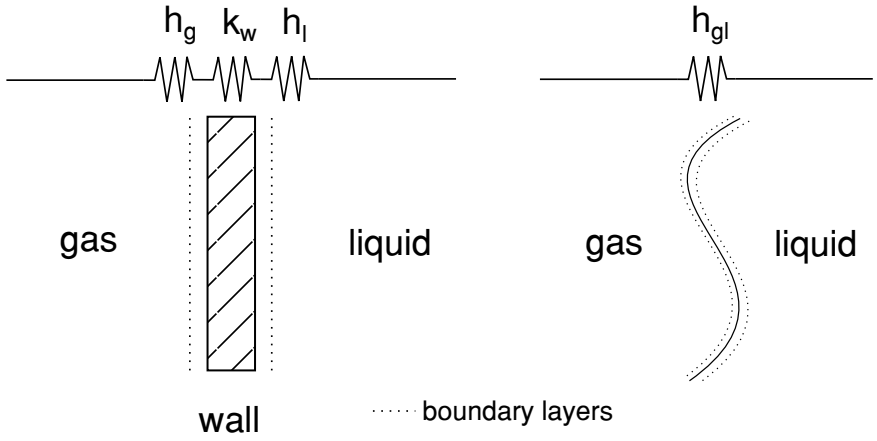

Figure 2.4: Heat transfer in (left) a traditional heat exchanger which separates fluids by a wall and (right) a direct-contact heat exchanger.

where ε is the substance emissivity, σ is the Stefan-Boltzmann constant, T_s is the absolute surface temperature of the substance, and T_{surr} is the absolute temperature of the surroundings. Radiation is neglected in this thesis because when compared to conduction and convection in heat transfer process with low temperature differences between bodies, it is often negligible. Heat conduction is considered throughout the thesis, however it is well defined in literature for conditions found in these experiments and therefore not the primary subject of study. Convection, although well defined for a multitude of situations, is a flow and geometry specific form of heat transfer which is not well-defined in existing literature for the conditions in the heat exchanger described in this thesis. The convective heat transfer coefficient depends not only on fluid properties such as specific heat, thermal conductivity, viscosity, and density, but also on fluid flow conditions and surface geometry. Variations in these parameters vary the fluid flow and thermal boundary layers, the latter of which primarily defines the convective heat transfer coefficient (Incropera, 2007). The thermal boundary layer is characterised by a temperature gradient, at the surface its temperature is equal to that of the surface, while at the edge of the boundary its temperature is equal to that of the free-stream fluid.

To illustrate the problem of convective heat transfer coefficient uncertainty, consider two different heat exchangers shown in Figure 2.4, both exchanging heat between a gas and a liquid at different temperatures. The exchanger on the left shows heat exchange between fluids through a wall, as would be found in a shell and tube heat exchanger. The exchanger on the right shows direct contact heat exchange. Estimating the performance of either exchanger requires estimation of both convective

heat transfer coefficients h, but in the case of the traditional heat exchanger these estimations can follow well established correlations. If gas were the tube-side fluid of the shell and tube exchanger, flow conditions in the tube could be readily calculated using existing correlations and the gas mass-flow; these flow conditions combined with average values of fluid properties would readily produce a reliable estimate of h_g. The liquid convective heat transfer coefficient h_l could be calculated in a similar manner, and k_w is easily looked up from property tables. This process is readily completed because the geometry and flow conditions are common and well documented; the specific interaction between the liquid and gas does not need to be known, only the interactions between the gas and liquid and the wall. In the direct-contact exchanger, the interaction of the two fluids is critical, and existing literature provides little reliable information which covers the scenario discussed in this thesis. An estimation of h_{gl} is made in Chapter 4, but the drawbacks of this estimation prevent the parameter from producing confident results.

2.5 Process Heat Exchange

Heat transfer across a finite temperature difference incurs an irreversibility penalty as dictated by the first law of thermodynamics; heat transferred from high to low temperature will not return to high temperature without an input of work. Efficient heat transfer (defined as heat transfer which minimises irreversibilities) minimises the temperature difference dT between the two bodies exchanging heat. As dT approaches zero, the rate of heat transfer also approaches zero; if dT could reach zero with a non-zero rate of heat transfer then the process would be fully reversible. dT can be minimised by reducing the thermal resistance between fluids, and by ensuring that process streams have similar heat capacity rate C, defined as $c_p \cdot \dot{m}$.

In the second version of the PHES system where two liquid loops are used to transfer heat from the primary gas loop to the hot and cold stores, an examination of the most efficient method of exchanging heat between the gas and liquids was needed. Although heat exchanger design, sizing, and performance estimation is a well-studied topic and off-the-shelf heat exchangers exist for nearly all applications, the unique challenges of the PHES system necessitated deviation from the normal practice. Specifically, the PHES system required a heat exchanger which could operate at high pressures, operate with a high efficiency, and yield low dT values between the fluid streams across the whole range of heat exchange temperatures. One method of categorising heat ex-

UniSim STE R440.0 - DESIGN

Geometric details						
Shell type / series / parallel	AEL		1		1	
Shell diam / tube length / total area	1118	mm	6096	mm	531.19	m²
No of passes / no of plain tubes	1		1456			
Tube id / od / pitch (pattern)	14.83	mm	19.05	mm	25.4(90)	mm
No of baffles / pitch / cut	36		152.4	mm		%
Process details						
Total mass flowrates shell / tube	9326.3	kg/h	13536.0	kg/h		
Inlet temperature shell / tube	20.0	°C	400.0	°C		
Outlet temperature shell / tube	360.0	°C	60.0	°C		
Inlet / outlet quality shell / tube	0.0 / 0.0		1.0 / 1.0			
Results						
Total pressure drop shell / tube	0.1043	bar	0.315	bar		
Velocity highest shell xflow / tube		m/s	0.16	m/s		
Coefficients shell / tube / wall	1000	W/m² K	779	W/m² K	7067	W/m² K
Fouling coeff shell / tube		W/m² K		W/m² K		
Overall coefficient clean / dirty / service	412.2	W/m² K	412.2	W/m² K	388.1	W/m² K
Heat load / eff wtd mtd	1501.71	kW	8.24	°C		
Area ratio (act/req)	1.062					
Weight bundle / dry / full	10738	kg	47801	kg	54989	kg

Figure 2.5: Summary of shell and tube heat exchanger sizing. 200 bar N_2 is the tube-side fluid, Dowtherm A thermal oil is the shell-side fluid.

changers divides them into indirect-contact heat exchangers which do not allow their fluid streams to come into contact with another and direct-contact exchangers which do. Indirect heat exchangers are the industry standard for the exchange of sensible heat, with commonly available types including plate exchangers, shell and tube exchangers, and spiral heat exchangers (Incropera, 2007). The proposed high system operating pressure p_H of 200 bar discussed in Chapter 1 narrows these choices to a specific geometry of shell and tube heat exchanger. A sizing exercise for a shell and tube heat exchanger suitable for the hot heat exchange process in a proposed 633 kW SynchroStor PHES pilot plant was undertaken using the commercially available heat exchanger design software UniSim Shell & Tube Exchanger (STE) R440. PHES system modelling completed by Dr. Rick Jefferys concluded that a mass-flow of 3.7 kg/s (13536 kg/h) of gaseous N_2 was required for the plant to operate; this parameter and properties of the thermal oil Dowtherm A were used to size a shell and tube exchanger. The results are summarised in Figure 2.5 and included in full in Appendix A3. Note that even for the relatively small pilot plant size, the required shell and tube heat exchanger is excessively large and carries high costs due to the large pressurised volume and complicated internal geometry. Because the proposed working fluids, gaseous N_2 and thermal heat transfer oil, are minimally miscible and not chemically incompatible, direct-contact

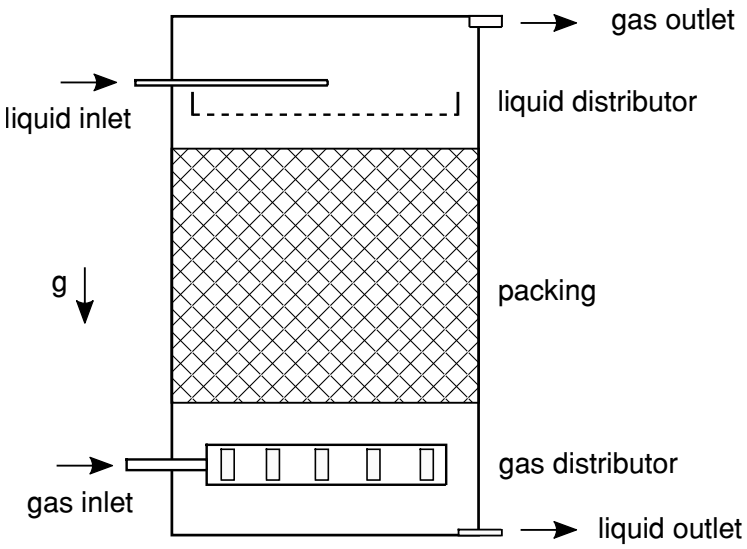

Figure 2.6: Principal components of a packed column operating with gas as the continuous media travelling upwards and liquid flowing through the influence of gravity in the opposite direction

exchangers were considered as a viable alternative. This type of exchanger has several advantages over indirect-contact exchangers including much higher heat transfer rates, simplified geometry, lower cost, and little to no fouling potential (Shah and Sekulić, 2003). Traditionally, direct-contact exchangers are used for phase change or mass-transfer applications and are rarely used for only the exchange of sensible heat. This is likely due to two factors; first, the needs of most processes can be met with commonly available indirect heat exchangers, and second many processes cannot permit their fluids to co-mingle, either for chemical compatibility, safety, or hygiene reasons. The primary disadvantage of direct-contact exchangers is their propensity to exhibit 'flooding' in certain conditions, where one fluid forces the other backwards in the exchanger causing a collapse of heat exchange (Kolev, 2006). This phenomenon is discussed at length in later chapters. The high system operating pressure, high desired heat transfer rate, and potential cost savings all made direct-contact heat exchangers worthy of thorough investigation.

The most widespread and easily constructed form of a direct-contact heat exchanger is a packed column, a cylindrical vessel providing contact area for two counter-current or co-current flows, and is commonly used in the process industry. Only a counter-current flow is considered here, as co-current flows exhibit large dT values which undesirably cause highly irreversible heat transfer. These columns vary in design based upon which fluid is the continuous media, the fluid which occupies the

majority of internal volume. This fluid is most often gas, however liquid is sometimes used and in this case the column can be referred to as a bubble column. Gas is the continuous media for the proposed PHES column due to its lower C value and the high cost of the liquid. The internal layout of a generic process column is shown in Figure 2.6, describing the principal components. Liquid is input at the top of the column through a liquid distributor, which evenly disperses it across the cylindrical cross section of the packing material. Packing materials are materials designed to have a high specific surface area (m^2/m^3), are generally constructed of plastic or stainless steel, and are manufactured either as structured elements with repeated patterns, or random individual elements which are poured into the column (Kolev, 2006). Liquid travels down the packing material under the influence of gravity, wetting-out across the packing surface. Gas is pumped in at the bottom of the column through a gas distributor, and travels up through the packing. Heat and mass are exchanged between the two fluids owing to the intimate nature of their contact, after which the gas exits the column at the top and the liquid at the bottom. These columns are used for a myriad of process industry components such as distillation towers, chemical reactors, and scrubbers. Columns used exclusively for heat exchange commonly involve water and air for either water cooling or air humidification, and typically 90% of the energy transferred is through mass transfer from phase change (Shah and Sekulić, 2003). These air-water heat exchange columns are poor models with which to inform work on the PHES system as they involve both phase change (which is not desired in the proposed system) and very low pressure (usually ambient) operation. Accordingly, a survey of existing columns focuses on those which operate at or near PHES system high pressure p_H and high temperature T_H.

A wealth of information on the topic of column design is available owing to the widespread history of use amongst the process industries, with a text by Kolev (2006) presenting a comprehensive overview of the subject discussed at length in Chapter 5. The general design methodology for an industrial packed column involves sizing a column to meet a series of hydrodynamic and performance goals through the use of experimentally verified equation coefficients. In the early days of packed columns, it was general practice to construct a pilot column to confirm expected operation whenever a new process, packing, or pressure range was introduced owing to complex nature of fluid interactions. As past work accumulated, engineers were able to rely less on pilot columns and could draw on previous experimental knowledge. If existing knowledge were suitable, a pilot column could be avoided for the PHES system. Un-

fortunately, a survey of existing literature revealed no columns designed exclusively for heat-exchange at or above the proposed operating pressure p_H, although many high pressure mass-transfer process industry applications exist such as CO_2 absorption (Hairul et al., 2017). A pilot column for the hot, high pressure gas liquid-heat exchange would not only verify the expected full-scale column performance, but also make an original contribution to existing work. Krehenwinkel and Knapp (1987) provides useful correlations for column performance in the pressure range of 20 to 100 bar at temperatures up to 300K. Stockfleth and Brunner (2001) finds hydrodynamic correlations for a supercritical CO_2 countercurrent column from 80-300 bar between 313 and 373K, and discusses why low pressure column hydrodynamic models yield poor results when applied to high pressure columns. In short, high pressure columns generally have a much smaller density difference between countercurrent fluid streams, greatly increasing the range of operating conditions under which the liquid could cause the gas to flow in the opposite direction (known as flooding).

Design methodologies for packed columns have historically relied heavily on empirical coefficients as computer modelling lacked the capabilities to accurately represent these systems. Computational fluid dynamics (CFD) are commonly used today to evaluate flows through packing structures, but often this is only applied to a representative packing unit cell, the results of which are then scaled up and hoped to represent full column behaviour (Baker et al., 2014). CFD is conducted by initially dividing the packing geometry into either finite elements or finite volumes, a process known as meshing. Meshing can be very computationally intensive, and the accuracy of the simulation results are highly sensitive to how faithfully the mesh represents the physical geometry. Column packing geometries are often complex and contain many thin walls, sometimes posing numerical difficulties for solving software. Additionally, columns using random packings require the use of statistical models to create a representative geometry for analysis, introducing another step into the analysis process which must be verifiable. Recent work by Zhang et al. (2018) successfully demonstrates CFD modelling of an entire gas-solid column including wall effects, but this work is at the forefront of CFD development, and does not include liquids. Any model to predict the behaviour of the packed columns proposed for the PHES system requires two qualities: first, it must produce results which have a high degree of confidence, and second it must be technically achievable. Accordingly, the author chose not to employ CFD methods to model column behaviour as the effort and time required to construct a CFD model which would produce results with a high level of confidence exceeded the time

and resources available. Instead, work focused on existing empirical correlations and design methods. Without suitable experimental correlations to draw upon, and without practical and trustworthy CFD, the author chose to construct a pilot column to meet desired PHES parameters. This process is documented in Chapter 5.

2.6 In-Cylinder Mixing

The first version of the PHES system intended to utilise in-cylinder gas-liquid mixing in order to limit the maximum high temperature of the compressed gas, and allow for the heat in the gas loop to be easily extracted. This version of the system did not use a packed column; instead gas-liquid separation equipment was used to extract the liquid from the gas loop, to then transfer heat or coolth into the stores. The overarching objective of this mixing was to maximise the contact area between the gas and liquid phases throughout the entirety of the compression or expansion stroke, to ensure that heat from compression was evenly distributed throughout the mixture. The most common form of in-cylinder gas-liquid mixing today is found in direct-injection diesel and petrol engines, where mixing is accomplished by pumping the liquid fuel through an atomiser or orifice to create a mist which mixes with air within the cylinder. These spray nozzles must operate at pressures up to 350 bar (Delphi Technologies, 2019) at high temperatures, so they likely could be made robustly enough to operate in the proposed PHES compression cylinder. Atomisers with feed pressures of up to 700 bar are commercially available today (Evaporator Dryer Technologies, Inc., 2016), although it must be noted that the liquid pressure behind the nozzle must be significantly higher than the pressure within the chamber into which the nozzle outlets, and most are designed to operate into chambers of ambient or low pressure. Accordingly, it is not likely that an off-the-shelf solution is viable for this application. Another notable characteristic of atomisation is its highly irreversible nature (Petela, 1984), which is undesirable due to system efficiency targets. Although the application of spray nozzles was considered for the PHES cylinder, they were ultimately rejected on the basis of these concerns and on concerns of liquid de-entrainment. While mists remain in suspension for common piston stroke timings for diesel and petrol engines, the proposed PHES cylinder averages around 6 seconds per stroke, a significantly longer time. If liquid were sprayed into the cylinder at the beginning of the compression stroke, it would likely wet-out cylinder surfaces and fall out of suspension well before the stroke was complete McBride et al. (2013).

Another method of creating large surface areas between gases and liquids is foaming, a process whereby the gas is vigorously bubbled through the liquid to create a foam. This foam is either moved into the cylinder in bulk, or generated within the cylinder. It provides a large range of possible gas-liquid surface areas depending on bubble size, and will generally break down on the order of tens of seconds. McBride et al. (2013) discusses an isothermal expander operating from 200 to 20 bar utilising gas-liquid mixing via foaming, and points out that for lower frequency compression, foaming presents several advantages over sprays. Although encouraging because the described process is very similar to the desired in-cylinder mixing, foaming was not utilised in the proposed cylinder due to concerns over full liquid evacuation from the cylinder after each stroke, and breakdown of the foam further in the heat exchange loop.

Middleton (1992) provides a comprehensive overview of gas-liquid mixing in the process industry, which while instructive does not immediately suggest a solution for mixing within a compressor or expander, as most mixing in the process industry is performed in a dedicated device. The majority of devices involve the use of a turbulent gas to either bubble through or otherwise disperse a liquid, but most contain stationary geometries which are ill-suited for the inside of a compression chamber. Scraped film mixing devices shown in Figure 2.7, particularly the dynamic in-line mixer and rotating disk contactor are most similar to the proposed PHES mixing device, although neither in their established forms can be contained within a compression or expansion cylinder (Middleton, 1992). Ultimately neither spraying nor bubbling was chosen for the PHES system, and instead a novel in-cylinder mixing device was proposed, drawing on elements of scraped film devices.

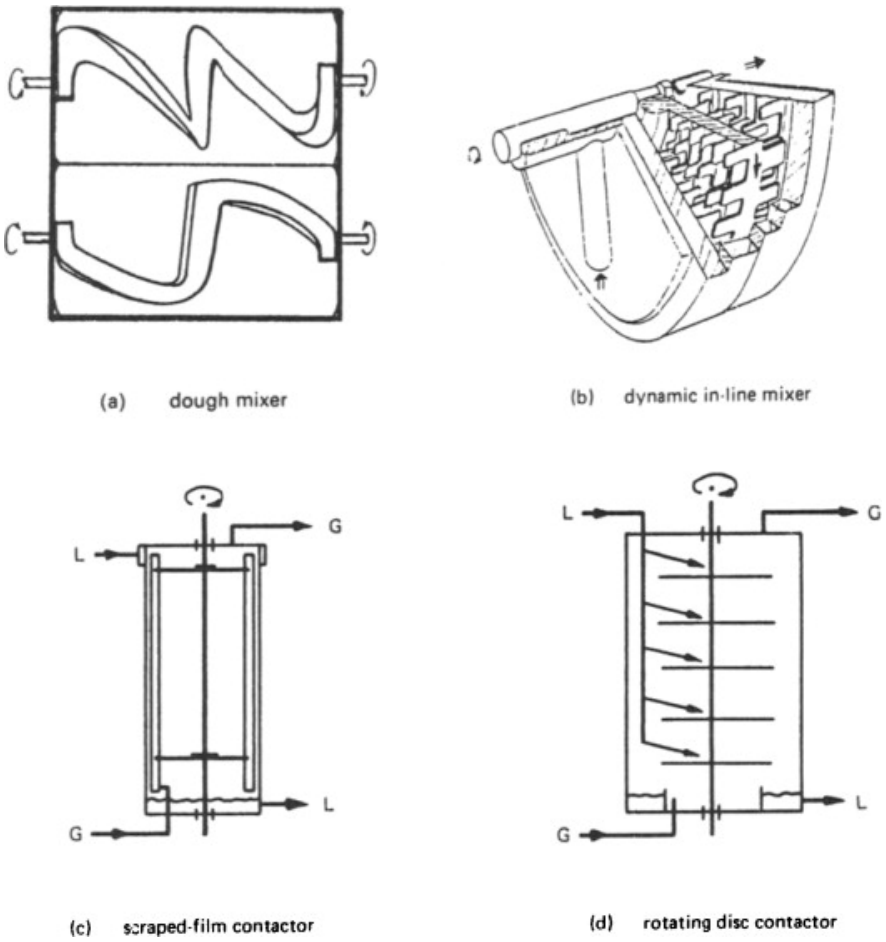

Figure 2.7: Four types of scraped film gas liquid mixers commonly used in the process industry. Clockwise from top left: (a) dough mixer, (b) dynamic in-line mixer, (c) scraped-film contactor, (d) roating disc contactor. Reprinted from *Mixing in the Process Industries*, 2nd edition, J. Middleton, Gas liquid dispersion and mixing, Pages 322-363, ©1992, with permission from Elsevier.

Chapter 3

Reciprocating Gas Compression Experiments

This chapter discusses the experimental process of verifying the performance of an in-cylinder gas-liquid mixing device as necessitated by the first iteration of the PHES system. It sets out the experiment goals, defines the experimental setup and methods, and details the preliminary results. Results are presented using high speed photography and by examining the changing nature of the pressure-volume (p-V) curve of the compression and expansion processes as experiment parameters are varied.

3.1 Background

The first iteration (v1) of the PHES system was designed to use large reciprocating piston compressor/expanders, as it was assumed they would pair well with high efficiency hydraulics and have a higher overall efficiency than turbomachinery. A full scale energy storage system was envisioned based upon a large reciprocating piston-cylinder design, but significant uncertainty existed regarding one aspect of the design, a desire to mix gas and liquid within the cylinder and maintain the mixture throughout the compression or expansion process. Injecting a well-dispersed liquid into the cylinder would allow the PHES system to operate at a higher pressure ratio without violating fluid thermal limits. Additionally, injecting liquid removed the need for a dedicated gas/liquid heat exchanger later in the thermodynamic cycle, theoretically simplifying the system design. This chapter documents an experimental apparatus designed to test a gas piston-cylinder containing a mixing-device. It is worth noting the complexity of the desired mixing process in the decision to pursue an experimental apparatus to

validate the mixing-device concept; creating a multi-physics model to incorporate two phase flow in a complex 3D dynamic environment is extremely challenging. Creation of such a model was deemed by the author to have a greater time commitment and lower degree of confidence when compared to constructing an experimental apparatus.

This chapter encompasses experiment design, commissioning, and presents preliminary results. After the apparatus showed difficulties in gas-liquid mixing in early results, the PHES research group revised the system design to incorporate a smaller higher speed reciprocating compressor/expander without in-cylinder mixing. This decision was also based upon expected fabrication difficulties and projected high costs. As a result of these decisions, the experiments were concluded; all results are documented here.

3.2 Experimental Aim

The experiment was designed to validate a novel in-cylinder mixing-device which was proposed to be used in the reciprocating piston of v1 of the PHES system. During PHES operation gas and liquid would separately be drawn into the cylinder, the liquid mixed with the gas, and the mixture compressed before being expelled. The movement of gas and liquids into and out of the cylinder was not a design concern, nor would have been gas liquid mixing if it occurred in a dedicated process. However, as gas liquid mixing needed to take place within the cylinder during compression, validation of the novel mixing-device was necessary. Because gas and liquid flow into and out of the cylinder was not the subject of inquiry, it was decided that an apparatus to test the mixing-device could be manually 'charged' with a set quantity of gas and liquid before compression began. Similar in nature to the PHES system, a single horizontal cylinder would be used, within which it was expected liquid would form a pool along the bottom surface which would be dispersed using the mixing-device. Validation of gas-liquid mixing was intended to be accomplished by two means:

Qualitatively, by high speed photography to verify liquid droplet propagation from the bottom of the horizontal cylinder to the remainder of the internal cylinder surface and across the surfaces of the mixing-device, during both compression and expansion. Results which indicate effective gas liquid mixing would show uniform liquid distribution across the internal surface of the cylinder both axially and radially. Additionally, liquid should visibly propagate across the surface of mixing device in order to maximise available heat transfer surface.

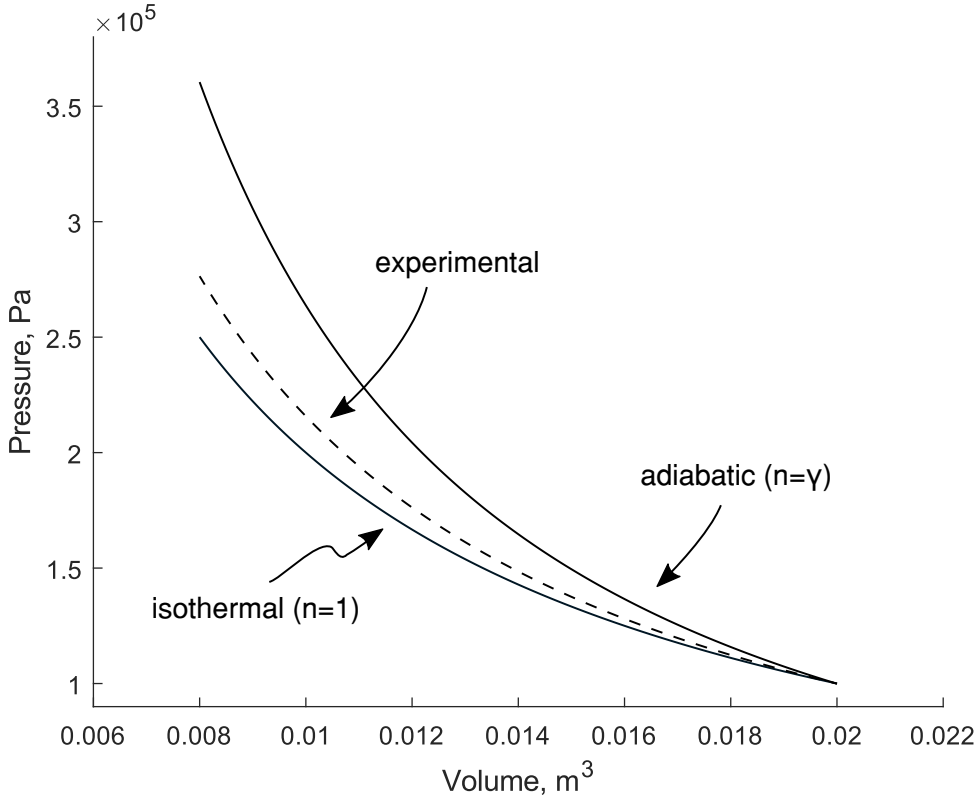

Figure 3.1: Pressure Volume (PV) plot showing differing polytropic compression curves for an ideal gas, with experimental results expected to fall between the isothermal and adiabatic cases. NB the volumes shown correspond to the experimental apparatus.

Quantitatively, by pressure and volume measurements to evaluate the modification of the dry pressure-volume (p-V) curve caused by the addition of liquid to the compression/expansion process. As shown in Figure 3.1, it was expected that this dry experimental curve would follow a process somewhere between the isothermal and adiabatic case. An effective mixing device would intimately mix the gas and the liquid, modifying the dry p-V curve to be closer to the isothermal case. Differing degrees of curve modification can be quantified with the polytropic exponent n from the equation $PV^n = C$ where P and V are pressure and volume, n is the polytropic index, and C is a constant. Poorly mixed gas and liquid are expected to show minimal difference from the dry air condition, while well mixed gas and liquid are expected to show a significant difference from the dry air condition. Additionally, measurements of the p-V curve with the quantity of liquid systematically manipulated would be compared with the dry air base case.

3.3 Experimental Design

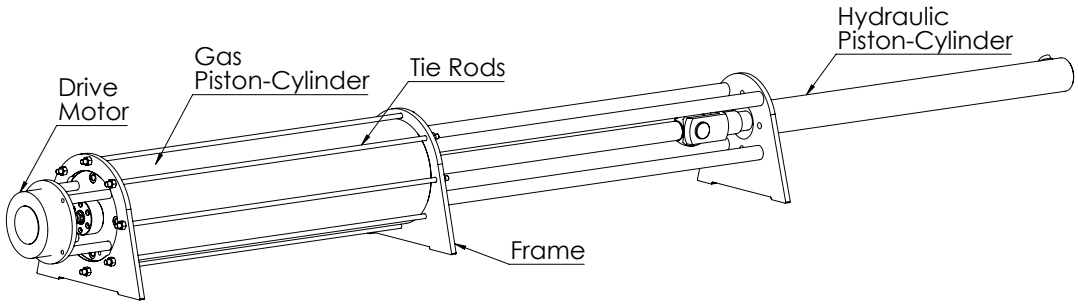

Figure 3.2: External view of experimental apparatus.

Working in conjunction with Mr. Carn Gibson, a design engineer on the PHES project, an experimental apparatus was designed to achieve the listed aims. The apparatus consisted of a single hydraulically driven reciprocating piston-cylinder with an internal liquid mixing device, into which liquid could be incrementally added (see Figure 3.2). Mr. Gibson designed and sourced the piston, cylinders, mixing device, and frame, while the author designed and sourced the sensors, motor & controller, and software. The author performed 90% of the initial assembly and all of the subsequent commissioning and testing.

The gas cylinder has a 190mm bore with a 800mm stroke; there are two interchangeable cylinders, one made of E355 steel with a wall thickness of 15mm for tests up to 5.0 bar, and one made of clear acrylic with a wall thickness of 5mm for tests up to 2.0 bar to allow for high-speed photography. Two aluminium end caps seal either end of the cylinder, and are held in place by frame plates and tie rods. A gas-liquid mixing device consisting of 0.2mm thick spot welded circular 1.4310 (X10CrNi18-8) stainless steel disks was mounted internally to the cylinder on a guide rod, and expanded and contracted with the motion of the piston similar in manner to an accordion (see Figures 3.3 and 3.4). The mixing device was spun at the drive motor end of the cylinder using a Kollmorgen ServoDisc U12M4 24V D.C. permanent magnet motor driven by a H-bridge controller with a PID speed control loop. The piston was driven forwards and backwards by a hydraulic piston-cylinder, which was in turn driven by a 3kW Artemis DDP hydraulic power pack. Piston displacement was measured with a string potentiometer, mixing device drive motor speed with a D.C. Tachogenerator, gas pressure with a 0-10 bar, 0-10V Telemecanique OsiSense XMLP pressure transducer, and internal temperature with a K-type thermocouple. Hydraulic oil pressure was monitored internally by the Artemis power pack.

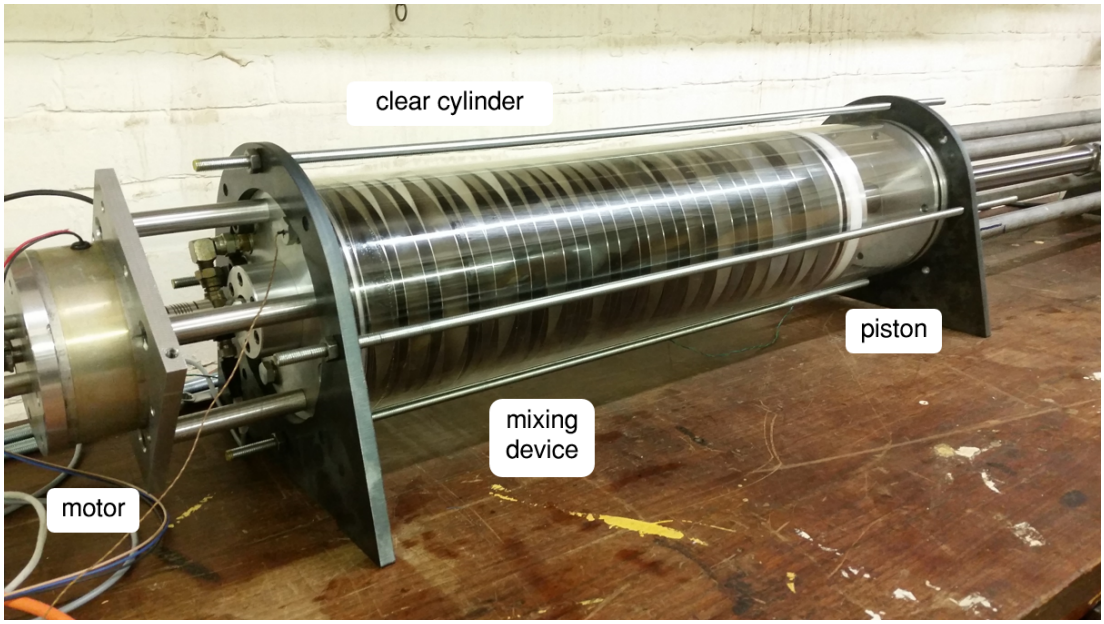

Figure 3.3: Apparatus with acrylic cylinder showing fully extended mixing device

Standard fluid ports (G 1/4) were added to the front and rear end caps of the gas cylinder to mount sensors and allow for the addition of liquid. Although originally envisioned to operate using welding-grade N_2 and DOW Syltherm 800 heat transfer fluid to mimic conditions found in the PHES system, experimental trials were initiated using air and a non-corrosive machine coolant liquid to provide preliminary results without the handling requirements incurred by compressed gasses and synthetic heat transfer fluids.

A Labview Virtual Instrument (VI) was created to manage experiment operation; it interfaced with an Arduino Uno which ran the PID loop to control the mixing-device motor via a H-bridge controller. The VI recorded all sensor data using a Labview USB-6001 data acquisition device (DAQ), and commanded the Artemis power pack to provide flow when needed using a 0-10V analogue output on the DAQ. The direction of hydraulic flow was controlled by a solenoid driven by a MOSFET controlled by a DAQ digital output. The experiment was operated from a control room via Windows Remote Desktop to reduce operator risk, and the VI was programmed to drive the hydraulic pump forward to compress the cylinder until a specified gas pressure was reached and then reverse direction and return to its starting position. Liquid was added in 15mL increments between trials by the operator who was required to enter the lab, remove a G 1/4 hex plug on the drive motor end of the piston, and pour in the liquid through a funnel. Both a software maximum displacement limit and a hard-

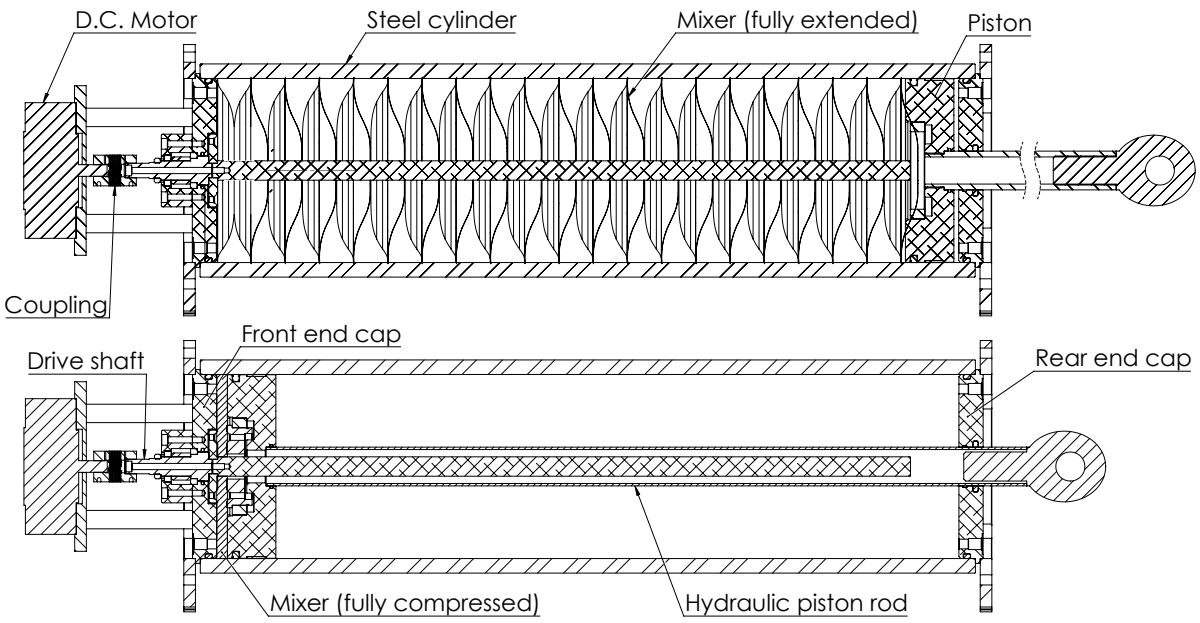

Figure 3.4: Cross section of experimental apparatus, at bottom dead-centre (top image) and top dead-centre (bottom image).

ware hydraulic pressure relief valve ensured safe operation. All sensor measurements were recorded into a Labview TDMS database at 1000Hz sampling frequency. Data was extracted from this database using a TDMS MATLAB plug-in and segmented into compression and expansion strokes for analysis. Post-processing was performed in MATLAB to apply calibrations to sensor inputs and organise data for analysis. High speed photography was performed using a Point Grey Grasshopper camera (GRAS-03D2M-C) which recorded mono video at 640x480 resolution and 200 frames per second. Matte white board was placed beneath and behind the acyrlic cylinder during recording, and photography lights with diffusers were used to ensure sufficient illumination.

Considering the experimental objectives laid out in Section 3.2, two questions were used to formulate the proper manipulation of variables in the experimental trials:

1. Is there a significant difference in the PV curve when the mixer is spinning versus when it is stationary?

2. Does the addition of liquid result in a significant effect on the PV curve, and if so how does this effect vary with the amount of liquid?

It is possible to observe a significant effect in both criteria highlighted above, however this does not necessarily mean the proper variation of variables was achieved. The

trial	mixing speed (rev/min)	piston speed (mm/s)
1	0	28
2	0	45
3	0	76
4	400	28
5	400	45
6	400	76

Table 3.1: Configuration of trials for each liquid quantity, normally completed twice at each liquid quantity.

desired outcome is an interaction of the two variables such that the effects on the PV curve are greater with the addition of liquid with a spinning, as opposed to stationary, mixer.

Bearing in mind these questions, experimental trials were designed to provide sufficient variation of the independent variables of the experiment (mixing device rotational speed, piston velocity, maximum pressure, and the quantity of liquid added to the cylinder) such that the previous questions could be rigorously answered without interference from non-relevant independent variables. This resulted in trials which:

- Operated with a constant mixing-device rotational speed optimised for liquid mixing.
- Sequentially varied piston speed between low (28mm/s), medium (45mm/s), and high (76mm/s) at each liquid quantity.
- Began at 0 barg and and reached top-dead-centre (TDC) at 3 barg.
- Equally varied mixing-device operation between rotating and stationary at each liquid quantity.

Table 3.3 shows the sequence of trials carried out at each liquid quantity. The objective of varying compression/expansion speeds was to cancel out any effect differing speeds had on the results. Varying mixing device activation was used to answer the experimental questions.

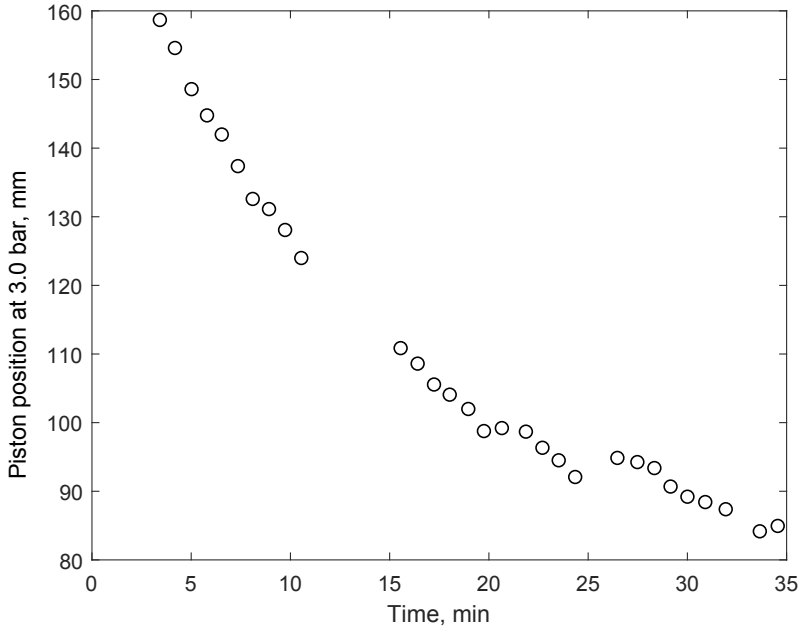

Figure 3.5: Piston position when a pressure of 3.0 bar is reached over several trials. Position decreases over time as a vacuum is drawn and greater displacement is required to reach 3.0 bar.

3.4 Commissioning Challenges

During initial testing to compress the gas up to 3 bar, a problem was encountered where each trial required a progressively larger piston displacement to reach the same top pressure; see Figure 3.5. Additionally, after a series of trials were completed, a vacuum was noted within the cylinder. This behaviour indicated that gas was leaving the control volume during the compression stroke, and an equivalent quantity of gas was not drawn back into the control volume during the expansion stroke. The vacuum was difficult to initially detect as the pressure sensor was unable to measure pressures less than 1 atm. The problem was resolved by identifying leaks with a soap solution, and then either tightening the fitting, adding thread seal, or adding bonded seals. The custom built thermocouple assembly (a thermocouple protruding though a resin seal in a hex plug) was replaced with a stainless steel sheathed thermocouple and a compression fitting.

Temperature measurements across experimental trials were also examined during commissioning, and showed an upward trend over time when the mixing device was used. Temperature of the apparatus before use was 22°C, and rose to 26°C after approximately 25 minutes. These measurements were compared with an equivalent length of experimental time where the mixing device was inactive and a clear differ-

ence was noted; without the mixing device active no upward temperature trend was present. The D.C. motor driving the mixing device reached approximately 40°C while in use, and was mounted with aluminium spacers to the cylinder end plate within which the temperature probe was mounted. Because aluminium has a high thermal conductivity of 204 $W/m \cdot K$ (Karwa, 2017), heat was conducted through the spacer at a high enough rate to cause the observed heating trend. These spacers were replaced with a machined Nylon version with a thermal conductivity of 0.25 $W/m \cdot K$ (Engineering ToolBox, 2011), nearly two orders of magnitude less than the aluminium. The self-heating effect was reduced to the extent that it no longer significantly affected temperature measurements.

3.5 High-Speed Photography

The apparatus was initially assembled with the clear cylinder so that commissioning could take place with the mixing device visible. This allowed clearance between the mixing device and the cylinder to be verified during operation, as well as observation of liquid movement within the cylinder. Visual inspection of the mixing device in operation verified the efficacy of the mixing device at different rotational speeds, at low speeds very little liquid was moved from the pool along the bottom of the cylinder. At higher speeds, the liquid appeared to be pulled up the side of the cylinder to the top of the cylinder, before falling down the back wall of the cylinder. For optimal performance the liquid should also wet-out across the disks of the mixing-device, however only minimal wet-out was observed. Additionally, a banding effect was witnessed where sections of the cylinder would exhibit sufficient liquid mixing, while other sections showed minimal mixing. These effects are qualified in this section.

High speed photography initially focused on the effect of mixer rotational speed. Figure 3.6 shows the difference in liquid distribution between low speed (200 RPM), medium speed (400 RPM), and high speed (600 RPM). At low speeds most liquid remained pooled at the bottom of the cylinder and wide peaks formed on some disks which generally did not reach the top of the cylinder. At medium speeds, a greater amount of pooled liquid was pulled up to form peaks, and these peaks were generally thinner and taller than those at low speeds. In some areas, peaks combined to form continuous films between disks. A small proportion of the liquid was moved over the top of the mixing device and down the back side of the cylinder. At high speeds, liquid was pulled into well-defined channels which formed a continuous ring around

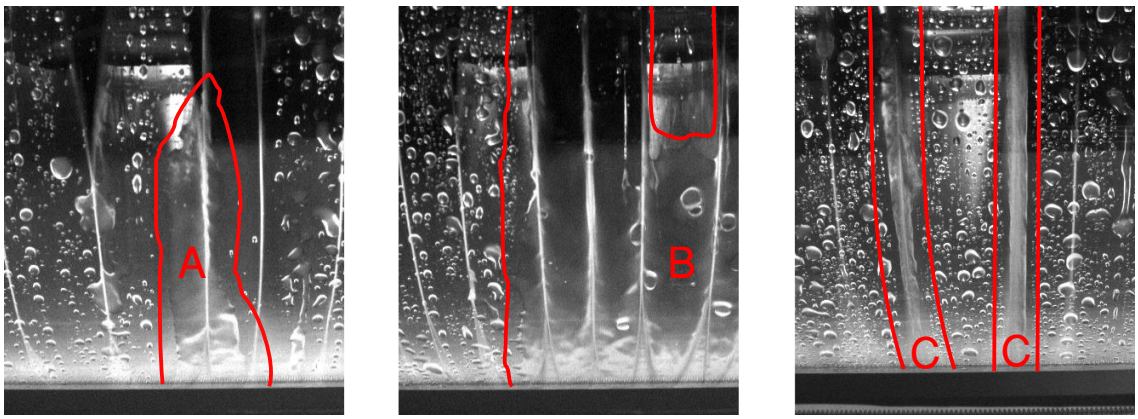

Figure 3.6: Variation of liquid mixing as a function of rotational speed; distributed liquid is bounded in red markings. A: slow rotational speed yielding a single central liquid tendril. B: medium rotational speed with well distributed liquid. C: high rotational speed with narrow liquid banding.

the whole cylinder. Notably, the liquid in these channels was significantly more aerated than liquids mixing at low or medium speeds. Because the medium spinning speed distributed the liquid over the widest cylinder surface area, 400 RPM was selected as the constant speed for higher-pressure compression tests with the steel cylinder.

Photography also documented liquid 'bunching', whereby liquid was collected in one portion of the cylinder; in trials where only liquid mixing was tested and the gas was not compressed, this occurred randomly along the axis of the cylinder. Most likely this banding was caused by variations in the clearance between the mixing device and the cylinder, with areas of less clearance more effectively mixing the liquid. In trials where the gas was compressed, the liquid had a tendency to collect at the piston. A degree of bunching was expected, as the piston collects liquid as it compresses. Interestingly, as the piston retracted, the liquid tended to follow the piston, as shown in Figure 3.7. This behaviour is undesirable, as it minimises gas-liquid contact areas for heat transfer to take place.

Both naked-eye and high speed observations highlighted the challenges the mixing device encountered distributing the liquid. Due to the thinness of the disks (0.2mm) the contact area between the spinning disk edge and the liquid pool was not sufficiently large to facilitate proper liquid distribution. Potential improvements to the mixing device disks might be made by cutting and bending tabs around the periphery of each disk to increase the surface area. Additionally, the observed failure of the liquid to wet-out across the mixer surfaces and propagate towards the centre of the mixer was

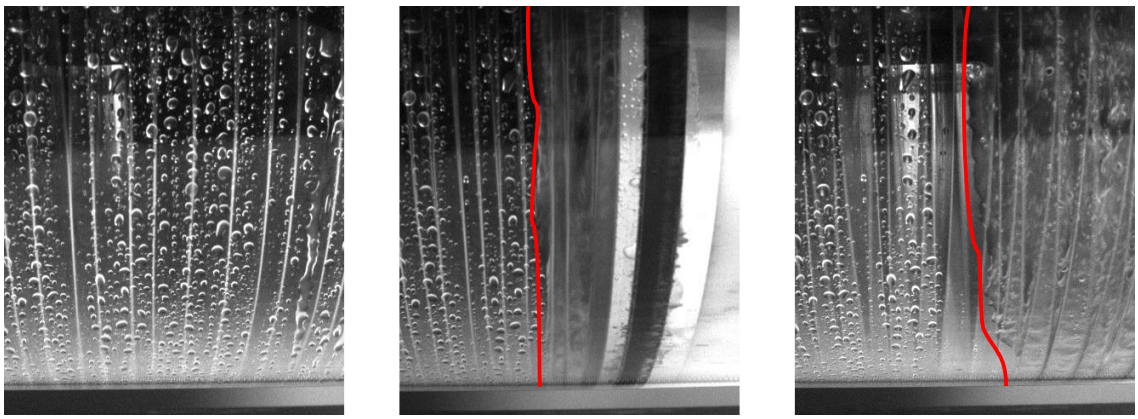

Figure 3.7: Three photos at the same position showing a slug of liquid which travels with the piston. Left: Before piston has reached TDC. Middle: Piston at TDC with liquid slug bounded by a red line. Right: Piston retracted and liquid remains, bounded by a red line.

most likely due to the force on liquid droplets from the rotation of the mixer. A system to inject liquid into the cylinder via the central guide rod would use the rotation of the mixer to assist with liquid distribution, and would likely significantly improve the mixing process.

Completion of this section of the experimental objectives allowed an optimal mixing speed of 400 RPM to be selected for the remaining trials utilising the metal cylinder. This section also provided qualitative observations on mixing device performance and given further experimental incentive these observations would have formed the basis for improvements.

3.6 PV Curve Analysis

Polytropic index	Process
$n = 0$	isobaric
$n = 1$	isothermal
$1 < n < \gamma$	heat and work flow in opposite directions
$n = \gamma$	adiabatic

Table 3.2: Variation of the polytropic index n by process. NB γ is the heat capacity ratio.

Compression and expansion p-V curves were extracted in MATLAB by plotting

pressure as a function of time, selecting points at the beginning of compression, at maximum pressure, and at the end of expansion and grouping all data in this time range into two curves - one for compression and the other for expansion. Pressure data was calibrated to eliminate zero-offset error, and converted from gauge pressure to absolute pressure by adding 1 standard atmosphere. Piston cylinder chamber volume was calculated as a function of piston position, accounting for the volume of the mixing device. Pressure was then plotted against volume, and a non-linear least squares fit to the equation $P = C/V^n$ was performed, see Figure 3.8. This equation is the rearranged form of $PV^n = C$, where P and V are pressure and volume in consistent units, n is the Polytropic index, and C is a constant. As discussed in Chapter 2, this equation applies to all processes which are polytropic.

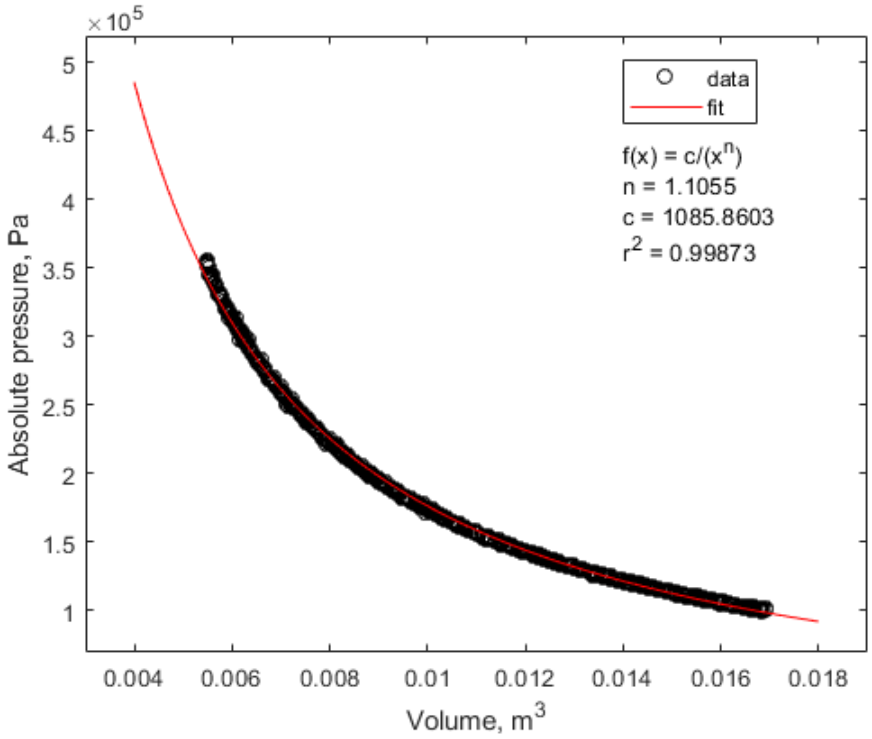

Figure 3.8: PV plot for typical compression curve where piston speed is 76mm/s, mixing-device speed is 400 RPM, and 200mL of liquid is present in the cylinder. A good fit to the equation $P = C/V^n$ is shown.

The polytropic index n varies according to the nature of the process, and if the ideal gas law applies the value of n can be interpreted with Table 3.2. In the case of these experimental trials, only the dry trials (air with no added liquid) can be considered to follow the ideal gas law. However, results from trials with liquid can still be compared with those from dry trials, allowing for discussion of the extent to which the results

material	mass (kg)	heat capacity (kJ/K)
gas	0.027	0.027
liquid	0.20	0.836
mixer	2.69	1.35
cylinder	60.67	30.5

Table 3.3: Heat capacity of several apparatus components

have been modified. Curve fitting yielded polytropic indices which were averaged across varying conditions to answer the experimental questions presented in Section 3.3. Rather surprisingly, the commissioning process revealed that the dry air n value was much closer to the isothermal value of $n = 1$ than the expected value corresponding to an adiabatic process, $n = \gamma = 1.4$. An adiabatic process was anticipated before experimental trials began due to the limited number of heat transfer paths within the apparatus when no liquid is added, however the large thermal mass of the mixing-device relative to that of the gas coupled with its large surface area provided a large thermal sink and made the process more isothermal. The heat capacities of key parts of the apparatus are shown in Table 3.3; note that the steel cylinder also provides a large thermal sink. This unintended consequence of mixing-device design points to potential improvements that a future apparatus could incorporate, namely constructing the mixing-device out of less thermally conductive materials with a lower specific heat.

The mean values of polytropic index n were taken across different experimental variables, with an interpretation given here. Note that all calculated indices are subject to an experimental uncertainty of $n \pm 0.006$. The experimental uncertainty was primarily driven by the pressure sensor which has an accuracy of $\pm 0.5\%$ of the sensor's full scale range. Comparisons between groups of trials organised to show an effect were made using T-tests. This statistic tests to see if a significant difference between the means of two groups exists (Porta and Last, 2018). The results of these tests, if a significant difference between means was found, were compared with the experimental uncertainty value. A significant difference between groups was declared only if the difference in means between groups exceeded the uncertainty value.

It is best to begin discussion of the results with Table 3.4, which compiles n values averaged across differing experimental trials, with a focus on how piston speed affects n. Note that each row represents a subset of experimental data, and the n value listed is an average across this data subset. These average n values are further averaged across

avg. n	n	piston speed (mm/s)	mixing-device speed (RPM)	liquid (mL)
	1.112	28	400	0
1.120	1.125	28	400	15-200
	1.123	28	400	0-200
	1.121	45	400	0
1.125	1.127	45	400	15-200
	1.127	45	400	0-200
	1.119	76	400	0
1.124	1.127	76	400	15-200
	1.126	76	400	0-200

Table 3.4: n as a function of piston speed, compared across trials with no liquid, trials with 15-200mL of liquid, and trials with both no and varying quantities of liquid (0-200mL).

0 mL liquid		15-200 mL liquid	
n	mixing-device speed (RPM)	n	mixing-device speed (RPM)
1.124	400	1.122	400
1.101	0	1.132	0
1.113	0 & 400	1.127	0 & 400

Table 3.5: Matrix of average polytropic indices by experimental configuration

piston speeds in the column *avg. n*. Experimental trials were designed to balance piston speed across differing conditions, however an examination of the data has merit if future experiments are to be conducted with the same apparatus. Rows 1-3 show results at 28 mm/s, rows 4-6 at 45 mm/s, and rows 7-9 at 76 mm/s. Accounting for the experimental uncertainty of $n \pm 0.006$, there is no significant difference between these average n values. Therefore, piston speed did not have a significant effect on the results and if further experiments were conducted piston speed would not necessarily need to be varied. Note that within constant piston speed groups significant variations do exist, an effect which is discussed presently.

Table 3.5 examines mixing-device operation and liquid effect on n. A subset of trials where no liquid is added are presented on the left, and a subset where varying quantities of liquid (between 15 and 200 mL) are added are presented on the right.

Within these subsets, average n values of trials with the mixing-device rotating at 400 RPM, trials with the mixing-device stationary, and of both sets of trials combined are presented. Consider first the last row of results in the table. The average n value between trials with liquid and those without is significantly different, but this difference doesn't follow logically with the expected effect of adding liquid to a compression or expansion process. The lower the n value, the more isothermal a process is. A process with added liquid was expected to have greater heat transfer from the gas to its surroundings (liquid, mixing-device, piston, cylinder) and therefore be more isothermal, but these results show that adding liquid *increases* the n value.

Separating the results into categories based on liquid mixing (rows 1 & 2) doesn't provide additional clarity. First, note that across row 1 there is no significant difference between mixed trials with and without liquid. Across row 2, there is a significant difference between unmixed trials with and without liquid, but the direction of the difference again doesn't agree with the expected notion that a process with liquid in it would be more isothermal than one without. Finally, compare row 1 with row 2. When liquid is present, spinning the mixing-device appears to lower n as expected. However, when liquid is not present, spinning the mixing device appears to raise n. These results as presented reflect the total number of trials segregated by operating condition, however investigating the results on a more segmented basis reveals additional trends.

Figure 3.9 shows the 290 experimental trials in the order in which they were conducted, where each trial is a compression and expansion stroke from 0 barg to 3 barg to 0 barg. The amount of liquid added is shown on the right axis. At first glance a curve with a distinct peak is obvious, but this curve should be viewed with caution by the reader. First, note the wide distribution of values at 0mL of added liquid. This distribution encompassed a significant portion of the subsequent points on the curve, potentially indicating that if more data points were collected at each liquid quantity the curve would take a different shape. Focusing on the left hand side of the plot, note that as the number of trials increases and liquid is added to sequentially reach volumes of 15, 30, 45 and 60 mL, the average n value decreases in a manner consistent with a process becoming more isothermal, as expected. As trials continue and more liquid is added, an increase in n value can be observed which then eventually decreases. Although no upward temperature trend was observed across all trials at the thermocouple, heat nonetheless may have accumulated in the mixing device, liquid and cylinder walls across subsequent trials, which were continuously conducted across several hours. This accumulation could potentially inflate the polytropic index

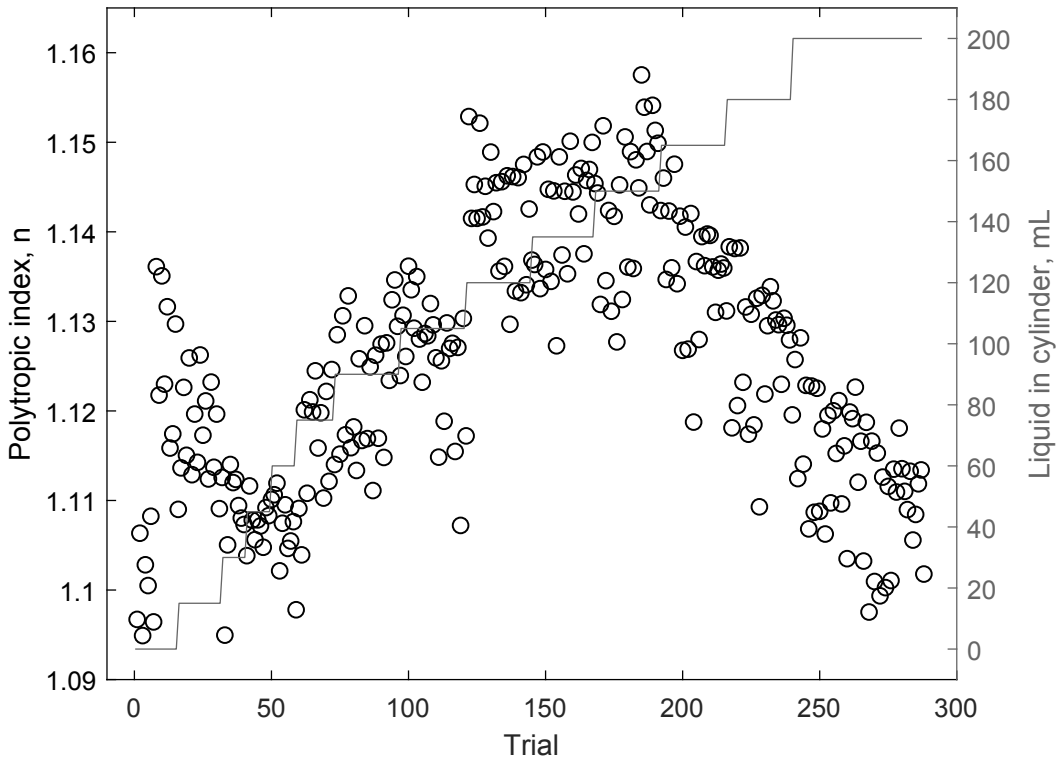

Figure 3.9: Average n values across experimental trials, with quantity of added liquid overlaid.

by reducing the rate of heat transfer between the gas and the liquid, mixing device, and cylinder. Unfortunately, temperature measurements across the presented data are highly unreliable due to an instrumentation failure and are unable to confirm or refute this potential source of experimental error. These results make it difficult to conclude the experimental apparatus's success with regards to its original aims.

The first experimental design question in Section 3.3 states: *Is there a significant difference between trials where the mixer is spinning versus trials where it is stationary?* There is a statistically significant difference in the value of the polytropic exponent between trials which spun the mixing device and trials which did not. The mixed trials have a lower value of n than the unmixed trials when liquid is present, but when liquid is not present the unmixed trials have a lower value of n. As these results contradict one another this question cannot be answered from the experimental trials presented in this chapter. The second experimental design question states: *Is there a significant difference between trials with liquid versus those without?* There is a statistically significant difference in the value of the polytropic exponent between trials

where liquid was used versus those without. Trials with liquid had a higher n value, indicating that the use of liquid within the cylinder did not provide the desired effect. The second part of this question, which examines the incremental effect of adding liquid, also is not definitively answered from these experimental trials. As previously discussed, the results presented in Figure 3.9 are most likely due to heat accumulation inside the cylinder as a result of the decision to run trials sequentially.

Given impetus to do so, these questions could be much more robustly answered through revisions to data acquisition equipment and a greater number of experimental trials.

3.7 Conclusion

The overall PHES system architecture eventually evolved past a large reciprocating design with liquid injection, the design this experimental apparatus was designed to evaluate, due to several factors:

- Adjustments to the compression ratio based upon numerical modelling performed by the PHES group to eliminate the need to use liquid to limit the top temperature of compression (or the bottom temperature of expansion).
- Naked-eye and high-speed photography visuals collected by these experiments to evaluate gas liquid mixing effectiveness.
- Expected difficulties in PHES fabrication and operation, particularly with regard to scaling up piston seals.

In addition to the contribution these experiments made to the system architecture evolution, they also provided valuable experience in instrumentation, experimental design, and data analysis which were applied to the second set of experiments. These experiments provide insight into basic gas-liquid mixing, and the high-speed photography results provide a clear route towards potential improvements in the mixing device. However, they also highlighted problems with uniform liquid dispersal within the cylinder, and pointed to a number of challenges that would need to be overcome to utilise a reciprocating piston design in a pilot PHES plant. p-V curve analysis may have been hindered by the large thermal mass of the apparatus, and could have benefited from a mechanism to ensure equal liquid distribution along the length of the compression

chamber prior to each compression stroke. Temperature measurements proved unreliable, however even with more reliable equipment it would have been very difficult to measure anything other than bulk temperature at the end of the piston.

Around the time that preliminary experimental trials concluded, the decision was made to modify the PHES architecture to eliminate reciprocating piston compressor/expanders and replace them with an smaller reciprocating design which omitted in-cylinder mixing. Therefore, the full breadth of this experiment was not explored although fundamental questions regarding this particular experimental setup were partially answered. Given impetus to do so, the experiment could be improved by testing multiple mixing device designs, adding multiple angles to the high speed photography, and by varying the gas and liquid used.

These experiments gave valuable experience in experimental design, data instrumentation, data analysis, and control methods, all of which fed into a significantly more robust data acquisition scheme for the next phase of experiments. Additionally, working through the experimental process from conception to results on the modest scale of this apparatus proved to be a valuable learning experience for the much larger experiment to follow.

Chapter 4

Packed Column Design

This chapter describes the basis for the primary body of work in the thesis. A MATLAB *model is constructed to simulate a direct-contact heat exchanger, necessitating experimental work to verify the heat-transfer coefficient correlation used. An examination of pilot to full-size column heat exchanger scaling is made, and the basic parameters of an experimental exchanger are defined.*

4.1 Full Scale Packed Column

Following the decision to eliminate the reciprocating piston compressor/expanders marking the transition from the first to the second iteration of the PHES system, a new method of exchanging heat between the Joule-Brayton cycle gaseous working fluid (Nitrogen) and the heat transfer liquid was needed, as liquid was no longer to be injected into the cylinder. The large, linear, slow-moving piston compressor/expander from the first iteration was replaced with a fast-moving, Artemis-derived radial compressor/expander, into which it was deemed undesirable to directly inject liquid in order to simplify compressor design. A dedicated heat exchanger was proposed, and a design study was performed on heat exchangers which could operate at the proposed pressures and temperatures, with a particular focus on counter-current shell and tube heat exchangers. This study is discussed further in Chapter 2. Costs were higher than desired to meet system targets, and exchangers were large and complex, almost certainly requiring a long and involved fabrication process. Additionally, there was concern about the greater irreversibility of gas-liquid heat exchange found in a conventional heat exchanger compared to the previous method of direct cylinder injection. A packed-column was selected to exchange sensible heat between the gaseous working

fluid and the liquid in direct-contact with on another; more detail on packed columns is also provided in Chapter 2. Sizing the packed column to the proposed heat exchange process is a more complicated exercise than sizing for shell and tube heat exchangers, as shell and tube exchangers are prolific and a number of commercial software packages are available to size them. Additionally, the lack of direct contact between process fluids in traditional heat exchangers significantly simplifies the number of heat exchange coefficients which must be tabulated; in order to simulate a direct-contact exchanger the engineer must have knowledge of how two particular fluids interact with one another, while in a traditional exchanger the engineer only needs to know how each fluid interacts with the exchanger geometry. Two heat exchangers are needed for the PHES system to operate, one to exchange heat between T_H and T_M and another to exchange heat between T_M and T_L. Each heat exchanger must operate with a different 'hot' fluid depending on system operation; in storage mode hot gas at T_H is cooled by liquid at T_M, while in generation mode hot liquid at T_H is cooled by gas at T_M. A similar reversal of 'hot' fluid takes place in the cold heat exchanger, and the packed column must be designed to accommodate this.

PHES system modelling produced by Dr. Rick Jefferys indicated that when using Nitrogen (N_2) as the working fluid for a proposed 633kW full-scale PHES plant, a gas massflow ($\dot{m}_{g,f}$) of 3.67 kg/s would be required. This model reflected system temperatures which were primarily driven by the chosen liquids: low temperature T_L was set to -120°C, just above the freezing point of 1-Propanol, high temperature T_H was set to 370°C, just below the maximum recommended operating temperature of the thermal oil Paratherm HR, and system middle temperature T_M is the geometric mean of the two, as discussed in Chapter 2. The liquids were selected by SynchroStor on the basis of chemical compatibility with one another and with Nitrogen, freezing and boiling points, toxicity, and cost. The fluid properties, gas massflow, and chosen T_L, T_M and T_H values, fully define the heat exchange problem. A method of sizing a packed-column heat exchanger to fit these requirements was needed, and given no off-the-shelf sizing solution the author, collaborating with Dr. Jefferys, set out to develop one.

4.2 Basic Simulation

As discussed in Chapter 2, a CFD model was deemed an infeasible tool for the design of a packed column within the scope of the PHES project, owing to the extremely complex hydrodynamics of such a simulation and the comparatively low confidence

such a model would produce. Instead, a MATLAB one-dimensional finite volume heat exchange model was constructed to simulate column performance. A one dimensional packed column model was deemed adequate by the author owing to the absence of bulk fluid movement in the radial direction, a consequence of the gas and liquid distributors which ensure even distribution of the fluids across the column cross section. With a uniform fluid distribution, no radial thermal dispersion would be expected unless the column wall provided a thermal sink or source. As columns considered for this application will be well insulated and have a low thermal mass, no significant heat sink or source is present and the 1-D assumption is taken to be valid. One important consequence of this simplification is that the model would not capture instabilities caused by fluid flows which are not radially uniform, such as the effects of viscous fingering on packings in multiphase heat transfer described by (Davenne et al., 2018). This phenomena can cause thermal 'tunnelling' where non-uniform thermal fronts develop, and while it is significant in packed beds used for energy storage which (unlike packed columns) have a non-stationary and steep thermocline, the author judged that its effects would not be significant enough in a packed column to warrant a two dimensional analysis. In addition to modelling heat transfer between the gas, liquid, and packing materials, this model evaluated hydrodynamic conditions within the column against several packed-column performance metrics available in literature. Evaluation of these metrics allowed the comparison of the packed column against others commonly found in industry, and allowed for calculation of the flooding point, a critical measure past which expected column behaviour breaks down. Kolev (2006) summarises these metrics:

1. Liquid Superficial Velocity, (m^3/m^2h). Also known as the liquid loading or capacity factor, the average liquid volume flow-rate for the column divided by its void cross section. Common values range between 2 and 300 m^3/m^2h.

2. Flooding Point (%). The flooding point is the gas flow-rate at which the liquid can no longer flow down the packing material and is instead entrained in the gas and carried back up the column. Manufacturers usually recommend operating at 80% of this value, too low and the process is inefficient, too high the process floods. It is highly dependent on the packing.

3. Gas load F-factor ($Pa^{0.5}$). A measure of gas loading of a column. This simplified term, also known as the gas capacity factor, discounts changes in liquid density but is widely used. It is the gas superficial velocity times the square-root of gas density . Common values are less than 5 $Pa^{0.5}$.

4. Column Diameter (mm). The smallest diameter experimental column described by Kolev is 100mm, standard commercial columns start at about 300mm, and go up to at least 5000mm.

The model considers a finite volume consisting of a cylindrical section k of the proposed packed column, with the diameter of the volume equal to the inner diameter of the packed column d_c, and an cylinder thickness dH. As shown in Figure 4.1, each volume contains a mass of packing material, a mass-flow of liquid travelling downward with gravity, and a counter-current mass-flow of gas. Each element packing mass had an independently varying temperature, with elements labelled *k*, *k-1*, and *k+1*. Elements are linked to one another by liquid and gas flows, and conduction or radiation between elements is not considered. The liquid is assumed to fully wet the packing material, covering the packing with a thin film. This allows for several simplifications, first, the surface area of the liquid is approximately equal to that of the packing, and second, no heat exchange takes place directly between the gas and the packing. The dominant mode of heat exchange is convection between the gas and liquid. Convection between the packing and liquid is considered although its effects are expected to be transitory once the packing and liquid reach thermal equilibrium. Derivation of the differential equations which describe the change in temperature with respect to time of the packing, liquid, and gas masses within the volume are presented here in abbreviated form. For each mass within the volume, derivation begins with the first law of thermodynamics:

$$\Delta E = E_{in} - E_{out} \tag{4.1}$$

where ΔE is the change in total energy of a system, and E_{in} and E_{out} are the total energy added and removed from the system. The left side of this equation is defined as:

$$\Delta E = \Delta U + \Delta KE + \Delta PE \tag{4.2}$$

where U, KE, and PE represent internal energy, kinetic energy, and potential energy respectively. For calculations involving the packing material kinetic and potential energy changes are zero, and for gas and liquids they are considered to be negligible inside a packed column. Changes in fluid kinetic energy across the column are assumed to be negligible on the basis that no substantial changes in fluid velocity take place, while changes in fluid potential energy are negligible relative to changes in internal energy due to changes in temperature. Therefore it is assumed that $\Delta E = \Delta U$. The right side of Equation 4.1 can be expanded as:

$$E_{in} - E_{out} = (Q_{in} - Q_{out}) + (W_{in} - W_{out}) + (E_{mass,in} - E_{mass,out}) \tag{4.3}$$

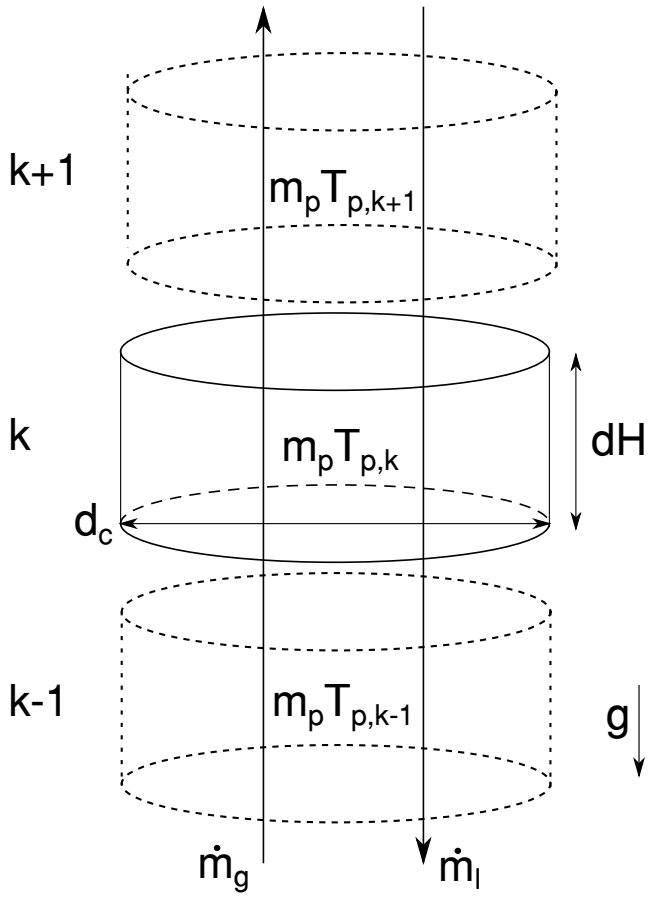

Figure 4.1: The finite volume arrangement used within the column performance MATLAB model, where $\dot{m}_g$ is gaseous mass-flow, $\dot{m}_l$ is liquid mass-flow, m_p is the mass of packing within the volume, T_p is the temperature of the packing mass, g is gravity, dH is the height of the cylindrical volume, and d_c is the diameter of the volume, set equal to the internal diameter of the column. The elements are indexed as k (the element being analysed), and k-1 and k+1, the elements before and after this element.

where Q is heat, W is work, and E_{mass} is the total energy in a mass which crosses the boundary of the volume, also simplified to U. There is no work transfer between any of the masses, so W can be eliminated. Combining this equation with the simplification of Equation 4.2:

$$\Delta U = (Q_{in} - Q_{out}) + (U_{mass,in} - U_{mass,out}) \tag{4.4}$$

Where Q and E_{mass} terms can be simplified to net terms. This equation can be differentiated with respect to time to yield, for a given mass m:

$$\frac{dU}{dt} = \frac{dQ}{dt} + \frac{dU_{mass}}{dt} \tag{4.5}$$

Equation 4.5 forms the basis of the mass specific differential equations which are solved in MATLAB. Beginning with the packing mass within the volume, the change in internal energy ΔU for an incompressible substance from an arbitrary state 1 to 2 is:

$$\Delta U = \int_1^2 c_p(T)dT \cong mc_{p,avg}(T_2 - T_1) = mc_p\Delta T \tag{4.6}$$

Defining vf as the volume fraction of each mass within the volume, vf_p is the fraction of volume within the finite volume that is packing material. This value, along with the packing material density ρ_p and volume, is substituted for m.

$$\Delta U = \rho_p \pi (d_c/2)^2 vf_p \cdot c_{p,p} \cdot \Delta T \tag{4.7}$$

which can then be differentiated with respect to time, filling the left side of Equation 4.5.

$$\frac{dU_p}{dt} = \rho_p \pi (d_c/2)^2 vf_p c_p \frac{dT}{dt} \tag{4.8}$$

The right side of Equation 4.5 can be simplified because the packing material is stationary; no packing mass crosses volume boundaries so dU_{mass}/dt can be set to zero. Additionally, it is assumed that the packing mass is thin enough so that there is always a uniform temperature throughout the mass. dQ/dt describes heat transferred between the packing mass and other fluids. As it is assumed that the liquid fully wets the packing material and radiation is neglected, the only heat transfer mode is convection between the packing and the liquid. Heat transfer from convection is defined as:

$$\frac{dQ}{dt} = h_{lp}A_p(T_l - T_p) \tag{4.9}$$

where h_{lp} is the convective heat transfer coefficient between the liquid and packing, A_p is the heat transfer surface area, and T_l and T_p are the liquid and packing temperatures respectively. Note that axial conduction between packing volumes is not considered,

owing to the poor thermal conductivity of the packing material, low contact area between adjacent packing pieces, and negligible heat transfer magnitude relative to the bulk fluid movements. A_p is found by multiplying the packing manufacturer provided specific surface area a_p by the finite volume volume:

$$A_p = a_p \cdot \pi (d_c/2)^2 \cdot dH \tag{4.10}$$

A_p is substituted into Equation 4.9 and combined with the definitions of $\frac{dQ}{dt}$ and $\frac{dU}{dt}$ in Equation 4.5 to yield:

$$\rho_p \cdot \pi (d_c/2)^2 \cdot vf_p \cdot c_p \frac{dT}{dt} = h_{lp} \cdot a_p \cdot (d_c/2)^2 \cdot dH (T_l - T_p) \tag{4.11}$$

which, when solved for $\frac{dT}{dt}$ and simplified gives:

$$\frac{dT_p}{dt} = \frac{h_{lp} \cdot a_p (T_l - T_p)}{\rho_p \cdot \pi \cdot vf_p \cdot c_p} \tag{4.12}$$

This equation defines the change in temperature with respect to time of the packing mass, and is one of three differential equations which must be simultaneously solved to model column performance. Derivation of the liquid mass equation is more complex, as it must account for liquid entering and leaving the volume boundary, as well as convection between both the gas and the packing material. Beginning once again with Equation 4.5, dQ/dT is similar to that for the packing, except it must account for two convection terms: convection between the liquid and packing, and convection between the liquid and gas.

$$\frac{dQ}{dT_l} = h_{lp} \cdot A_l (T_p - T_l) + h_{lg} \cdot A_l (T_g - T_l) \tag{4.13}$$

where h_{lp} and h_{lg} are the convective heat transfer coefficients between the liquid and packing and liquid and gas respectively. A_l, the surface area of the liquid, is assumed to be the same of that of the packing. Substituting in A_p for A_l yields:

$$\frac{dQ}{dT} = a_p \pi (d_c/2)^2 dH \left[h_{lp} (T_p - T_l) + h_{lg} (T_g - T_l) \right] \tag{4.14}$$

Liquid dU/dT is very similar to the previously derived equation for packing dU/dT:

$$\frac{dU}{dt} = \rho_l \cdot \pi (d_c/2)^2 dH \cdot vf_l \cdot c_{p,l} \frac{dT_l}{dt} \tag{4.15}$$

With subscripts changed from p to l, noting that ρ and $c_{p,l}$ are functions of temperature. dU_{mass}/dT is defined by:

$$\frac{dU_{mass}}{dT} = \dot{m}_l (u_{l,in} - u_{l,out}) \tag{4.16}$$

where u is the specific internal energy calculated from a custom MATLAB function. The internal energy is calculated by the integral of the polynomial fit to the fluid specific heat variation as a function of temperature. Combining these three equations for dQ, dU and dU_{mass} in Equation 4.5 and solving for dT/dt and simplifying produces:

$$\frac{dT_l}{dt} = \frac{a_p(h_{lp}(T_l - T_p) + h_{lg}(T_g - T_l))}{\rho_l \cdot vf_l \cdot c_{p,l}} + \frac{\dot{m}_l(u_{l,in} - u_{l,out})}{\pi(d_c/2)^2 dH \cdot \rho_l \cdot vf_l \cdot c_{p,l}} \tag{4.17}$$

which is the second of three differential equations needed for the model. The derivation for the gaseous equation is omitted, as it is very similar to the liquid derivation with the exception that there is no convection between the gas and the packing. This equation is:

$$\frac{dT_g}{dt} = \frac{h_{lg}a_p\pi(d_c/2)^2 dH(T_l - T_g) + \dot{m}_g(u_{g,in} - u_{g,out})}{\rho_l\pi(d_c/2)^2 dH \cdot vf_g \cdot c_{p,g}} \tag{4.18}$$

Equations 4.12, 4.17 and 4.18 are combined in a MATLAB function which is solved as a system of differential equations by ODE45, a common ordinary differential equation solver. The assumptions made in forming these equations are summarised as follows:

- The packing mass is thermally thin, and therefore lumped capacitance is valid.
- No bulk fluid movement or thermal conduction in the radial direction, allowing for a one dimensional model.
- Axial conduction is negligible.
- Negligible kinetic and potential energy changes.
- Perfect insulation at the column wall.
- The liquid fully wets out the packing.
- Radiation is negligible.
- Steady state gas and liquid flow-rates.
- Constant, average, packing properties across each volume.

Initially, it is assumed that a uniform temperature of T_M exists in the packing, liquid, and gas. Furthermore, it is assumed that in generation mode the liquid input is at T_H or T_L, and in storage mode the gas input is at T_H or T_L. These temperatures are used as the initial condition for the system of ODEs as it approximates cold start-up conditions of the exchangers, providing a reasonable starting point for analysis. Boundary conditions are set as follows:

- The liquid mass within the volume on the end of the column where liquid is input is fixed to the liquid input temperature.
- The gas mass within the volume on the end of the column where gas is input is fixed to the gas inlet temperature.
- The packing mass within the volume on the end of the column where liquid is input is fixed to the liquid inlet temperature.

Utilising these boundary and initial conditions, the system of ODEs can be solved by MATLAB to produce results which detail the temperatures of the masses throughout the column. Specific heat, density, and viscosity of all fluids were computed using several custom functions which evaluated fluid properties at a given temperature and pressure. Polynomials were fit to property tables from (NIST, 2018) for Nitrogen, (Mikhail and Kimel, 1963) and (van Miltenburg and van den Berg, 2004) for 1-Propanol, and (Paratherm, 2018) for Paratherm HR. Packing specific heat and density were considered to be constant with temperature, and an average value of each property was calculated for each volume. Column packings were varied between 15 and 25mm stainless steel Pall rings, Rashig Super Rings, Sulzer Metallapak 752.Y, and Berl saddles; packings were selected on the basis of commonality, high and low temperature performance, and cost. Column size (both diameter and height) were sequentially varied until a column which could produce the desired performance was produced. Model convergence was checked by plotting column temperatures as a function of time to ensure that a steady state was reached.

The model also evaluated the packed column performance metrics at each configuration, to ensure that the proposed column wouldn't flood and didn't exceed common industry values. The flooding point was calculated using a pressure drop and capacity model for gas/liquid packed columns developed by Stichlmair et al. (1989). Calculation of this parameter is not straightforward, as it relies heavily on experimental correlations and requires iterative calculations to produce a result. The full procedure is not reproduced here, however Appendix A of the cited publication provides a detailed example calculation.

4.3 Simulation Results

Variations on column performance led the author to select a packed column notionally of a diameter d_c = 1600mm, a height h = 1700mm, and a packing material of 25mm

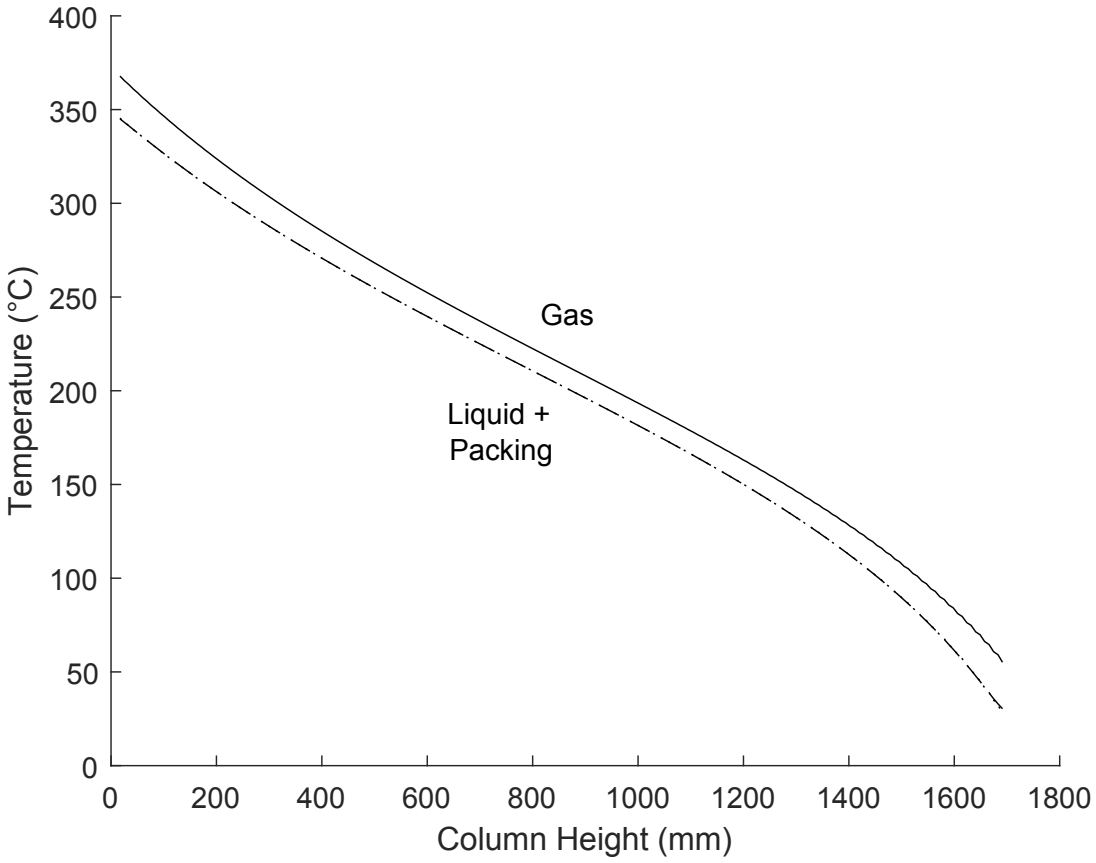

Figure 4.2: Results of finite volume model showing packed column gas, liquid, and packing temperatures. Note that the liquid inlet ($h = 1700mm$) and the gas inlet ($h = 0mm$) are set to T_H and T_M respectively. The liquid and packing profiles fall on top of one another.

stainless steel Pall rings for the proposed 633kW PHES pilot plant. Pall rings were selected for their low cost and ease of installation, and the height of the column was chosen to ensure the column length would be sufficient for heat exchange but remain feasible for small scale construction. The column was discretised into 200 volumes giving a $dH = 8.5mm$, this value was chosen to minimise property variation across volumes to provide a more accurate simulation. Variations on dH were tested (at twice and half the final selected value) but produced no significantly different column temperature profiles and therefore are not included here.

Figure 4.2 shows the simulated temperatures of the internal masses within the described packed column; the liquid and packing temperatures are nearly identical owing to the intimate nature of their contact and high convective heat transfer coefficient. The figure shows the hot exchanger in storage mode, so liquid at T_M absorbs heat from the gas at T_H, and therefore its temperature trails that of the gas by a finite dT. This dT is

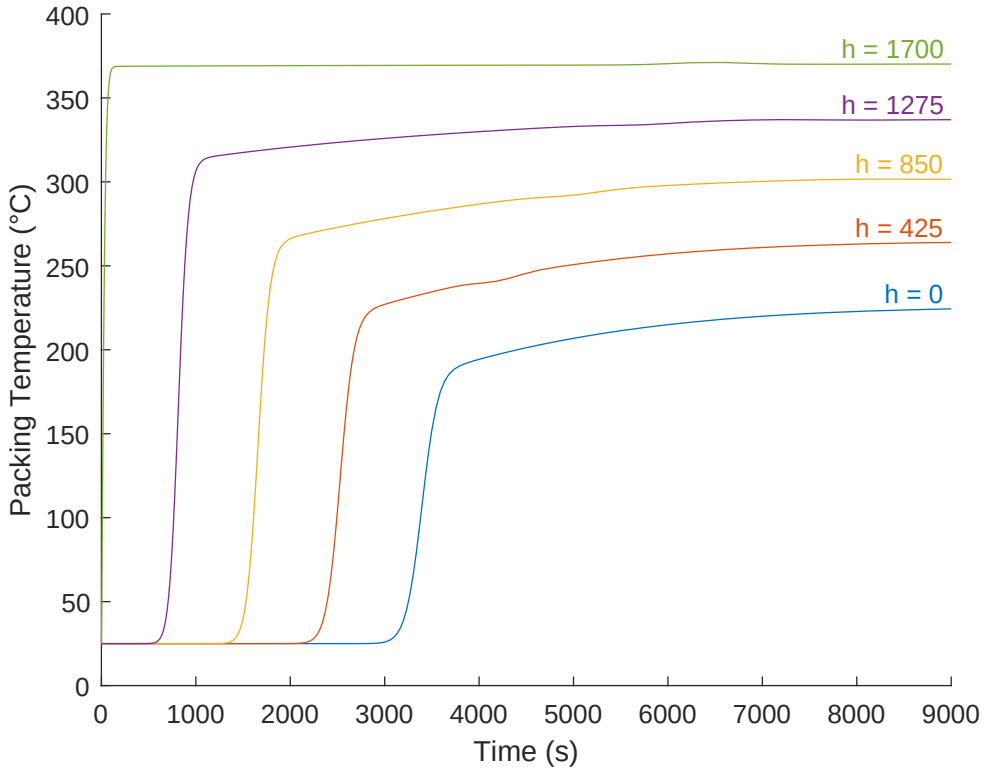

Figure 4.3: Time-dependent packing temperatures at various column heights h (mm).

non-constant owing to fluid changes with temperature including specific heat and density. Time varying results are shown in Figure 4.3, which plots a selection of column packing temperatures and shows how the model initial conditions transition to steady state. All temperatures reflect steady state conditions by $t = 9000s$, with significant transients subsiding by $t = 5000s$. Although effective in simulating the heat transfer characteristics of a packed column, the model is heavily dependent upon the chosen convective heat transfer coefficients h_{lp} and h_{lg}. h_{lp}, convection between the liquid and packing, is assumed to be similar to oil in free convection and a value of 50 W/m^2K is used (Engineers Edge, 2000), while h_{lg}, convection between the liquid and gas, is calculated according to the definition of the Stanton number:

$$St = \frac{h}{\rho \cdot v_g \cdot c_p} = \frac{Nu}{Re \cdot Pr} \tag{4.19}$$

Although the gas density ρ_g, gas superficial velocity v_g, and gas specific heat $c_{p,g}$ are all well known parameters, if h is to be calculated from first the definition of the Stanton number then the Stanton number itself for the fluid flow must be known. Defining it in terms of the Nusselt, Reynolds and Prandtl numbers allows for an estimation, as for a packed bed (Dwivedi and Upadhyay, 1977):

$$Re = \frac{\rho_g \cdot v_g \cdot d}{\mu_g} \tag{4.20}$$

where d is the characteristic diameter of the particle in the packed bed, and μ_g is the gas dynamic viscosity. Correlations between the Reynolds and Nusselt number are available in literature for gas-solid packed beds (Balakrishnan and Pei, 1979), but no available literature provided correlations for gas-liquid packed beds. Assuming a gas-solid system with a void fraction of 0.63 and a high sphericity of packing material, a Nusselt number of 150 is a reasonable estimate for the gas within the hot packed bed (Singh et al., 2006). The Prandtl number does not depend on any characteristic dimension as both the Reynolds and Nusselt numbers do, and therefore is widely available in property tables. Across our temperature ranges, the Prandtl number for N_2 is between 0.724-0.848 (Wischenewski, 2016). Calculating the Stanton number based upon these dimensionless numbers yields a plausible value, albeit without a high degree of confidence. Calculation of the Reynolds number is based upon a packed column with spherical particles and no liquid, a highly approximate representation of our situation. The Nusselt number is similarly based upon assumptions which only approximately describe the packed column discussed here, notable sources of error include differing sphericity and correlation with the Reynolds number.

Confidence in the finite volume model could be increased significantly by experimentally determining the convective heat transfer coefficient h_{gl} and using it to re-run the described model. An experimental apparatus to determine h_{gl} for the fluids and flow conditions of the proposed full scale packed column would be specialised and unable to demonstrate packed column operation or provide insights into hydrodynamic performance; one such apparatus is described by Jiang et al. (2014). An alternative approach to increase confidence in the finite volume model would be to experimentally determine heat transfer rates and column temperature profiles and compare them with the results generated by the finite volume model for the same column. The author chose to pursue an experimental apparatus that would yield these results and a value of U_h, the overall heat transfer coefficient, so that the packed columns could be easily compared with other heat exchangers. The self evident way forward was to design and test a pilot packed column; a smaller and more easily constructed packed column to prove operational performance before a large amount of resources are invested into a full scale column. In addition to providing data needed to validate the model described here, a pilot column allows for a full demonstration of the proposed heat exchange process, validating a design which is dependent on a vast number of parameters not all of which are necessarily adequately captured in the model. The process of scaling down the proposed full scale column for the 633kW plant presented as a result of this finite volume analysis is now outlined.

4.4 Pilot Column Scaling

Given the widespread use of pilot columns to verify a packed column's performance before full scale construction, there are a multitude of resources which provide guides on how to undertake this process. Johnstone (1957) gives a comprehensive overview of the topic, and provides several scaling rules to ensure that a pilot column performs faithfully to the full scale version. He notes that the foundation for a successful pilot column is one which is homologous with respect to the full scale version, meaning that it uses the same fluids at the same temperatures, pressures, and proportions. This is a significant experimental burden, as the design of a pressure vessel to contain a column operating at a T_H of 370°C and p_H of 200 bar is non-trivial, especially if the same column is also desired to later demonstrate operation at a T_L of -120°C and p_L of 20 bar. However, the effort is necessary to produce reliable results, as both the gaseous working fluid and the liquids exhibit significant property variations with temperature

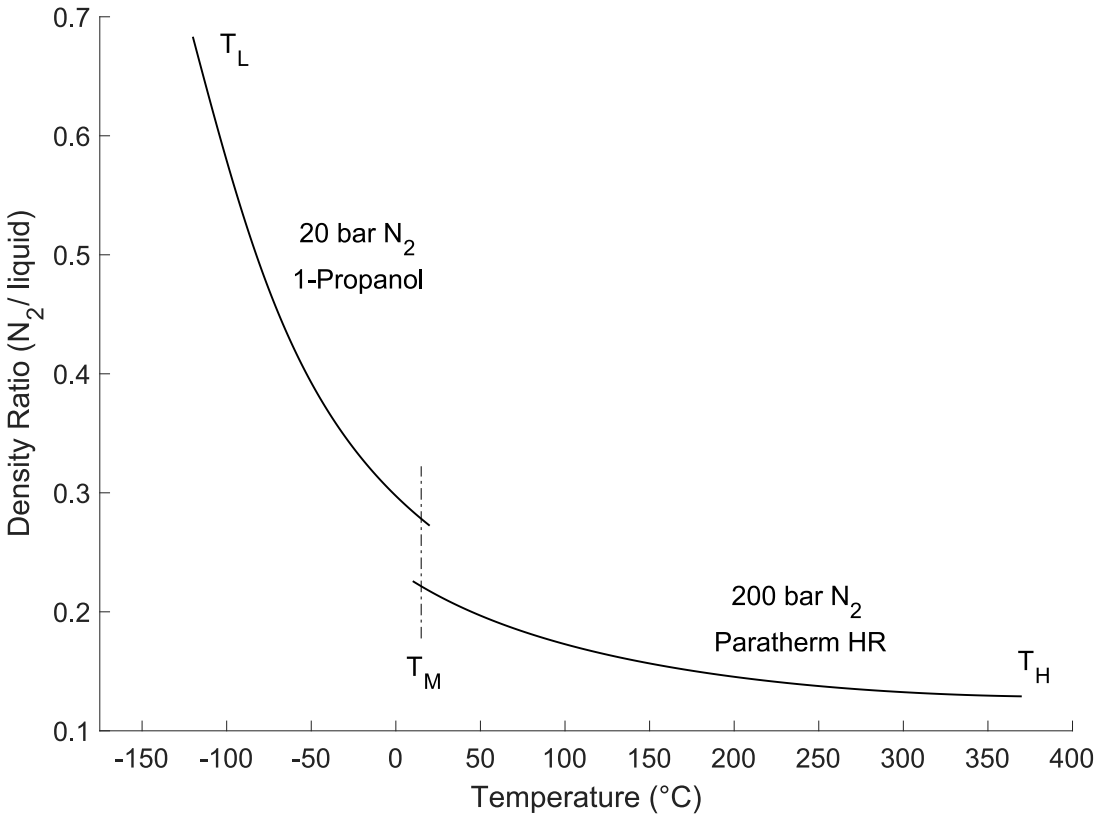

Figure 4.4: Variation in the density ratio between the gaseous working fluid N_2 and the liquid working fluid in both the cold (T_L-T_M) and hot (T_M-T_H) heat exchange processes.

and pressure. For the gaseous working fluid, density, specific heat, and viscosity are all functions of both pressure and temperature, while in the liquid these properties are only considered to be functions of temperature for this analysis. Variations of these properties have a considerable effect on the hydrodynamics of the fluid flows and their heat capacities C, affecting heat transfer to varying extents along the length of the column. Physical manifestations of these property changes within the column are varying temperature differences dT between the fluid according to changes in their C values, and varying liquid holdup, a hydrodynamic interaction whereby liquid droplets are entrained in the gaseous working fluid and either stop flowing downward under the influence of gravity or do so much slower. Consider Figure 4.4, which shows the relative densities of the two fluids and their changes with temperature. Relative fluid density is key metric which affects holdup, as the greater the gas density is with respect to the liquid, the greater its propensity to blow back the liquid at a given gas velocity. Changes in c_p and μ are also non-trivial over both the hot and cold temperature ranges considered, further reinforcing the need for a homologous pilot column.

In addition to this homologous condition, Johnstone (1957) (J) sets out several additional similarity conditions between a pilot and full scale column, as does Coulson (1999) (C) which are summarised here.

1. (J) To avoid the domination of viscous forces in hydrodynamic effects, packing diameter d should be greater than 12.5mm, preferably 19mm.

2. (J) The diameter of the packed column should not be less than eight times the packing diameter, preferably fifteen times.

3. (J) The scale ratio of the pilot to full scale packing diameter should be less than three, preferably less than two.

4. (C) For a column with less than 300mm diameter, the packing diameter d should be less than 25mm.

5. (C) The minimum wetting rate for random packings is in the range of 1.2-4.8 m^3/m^2h

Neither Johnstone nor Coulson specifically comment upon the length of a pilot column in relation to its full scale length, although any column should be of sufficient length to demonstrate the required heat or mass transfer process. In the case of the PHES pilot column, it was desired to produce as near a temperature profile to the full scale column within the pilot as possible. The proposed full-scale column was 1700mm long, and if the pilot was to reproduce this temperature profile, a similar dT of the masses per unit height dH is needed, suggesting that the pilot height should be the same as that of the full scale packed column.

Based upon the 633kW full scale packed column set out previously in this chapter, the homologus condition, equal heights between columns, and these scaling rules, a pilot column size was selected. Although detailed design was not yet underway, consideration was given to common column packing sizes and common carbon steel tube availability, the inner diameter of which would form the diameter of the packed column. A MATLAB script was written to evaluate user selected packing and column diameter against these scaling rules, which the author utilised to test common sizes in an iterative fashion until a pilot size was agreed upon. The final pilot size was selected primarily with the intention to construct the smallest pilot column which would produce reliable results. The optimal pilot column was determined to be one containing 15mm stainless steel Pall rings, having a diameter of 150mm and a height of 1700mm. This column, and its performance against the scaling rules, is tabulated in Table 4.1.

Scaling Rule	Expression	Evaluation	Result
J1	$d_p > 12.5$ mm	d_p=15	Pass
J2	$D > 8$*d	$150 > 8$*15=120	Pass
J3	d_p / $d_f < 3$	15/25=1.6<3	Pass
C4	For D<0.3, d<25	15 mm <25	Pass
C5	LL $> 1.2 m^3/m^2h$	12 m^3/m^2h	Pass

Table 4.1: Evaluation of pilot column parameters against scaling rules provided by Johnstone (1957) and Coulson (1999).

The remainder of this thesis focuses on work undertaken by the author to fabricate, instrument, test, and analyse this pilot column.

Chapter 5

Experiment Design

This chapter describes the direct-contact heat exchanger experimental design, the quantification of experiment variables, and the experimental campaign. The selection of data-acquisition hardware to meet experimental needs is also discussed.

5.1 Apparatus Conception

With the pilot column size and characteristics fully defined, attention now fell to how an experimental apparatus would be designed to support this pilot column operation. As discussed previously, there are four gas-liquid heat exchange processes in the PHES system which must be performed with minimal irreversibility:

- In storage mode, hot gaseous working fluid at T_H must heat the liquid at T_M.
- In storage mode, cold gaseous working fluid at T_L must cool the liquid at T_M.
- In generation mode, hot liquid at T_H must heat the gaseous working fluid at T_M.
- In generation mode, cold liquid at T_L must cool the gaseous working fluid at T_M.

The storage and generation processes are performed in the same heat exchangers, with one exchanger dedicated to the hot processes and the other to the cold. How these processes result from changing the directions of the Joule-Brayton cycle is show in Figure 5.1 for clarity. When the system switches from generation to storage or vice-versa, the exchangers reverse direction. An apparatus to test both the hot and cold exchangers simultaneously (in either operational mode) would require either construction of an entire pilot PHES plant, or the use of high capacity heating and chilling equipment to change fluid temperatures from ambient to T_H and T_L at the required experimental

flow-rate. The construction of a pilot PHES plant, while an objective of SynchroStor Ltd, was not a feasible means of testing the proposed pilot columns owing to the uncertainty that existed within other system components in development. The use of high capacity heating and chilling equipment was considered, but particularly with regard to chilling equipment to generate T_L, options were sparse and costly for the power required to meet pilot column flow-rates. Testing each process in a packed column individually was also considered, however high capacity heating or cooling equipment would still be needed to meet desired input temperatures and fluid flow-rates; similarly, fluid thermal reservoirs with low capacity heating and chilling equipment and transient column operation were rejected as any experimental column was desired to be able to demonstrate steady-state operation like that which would be found in a PHES pilot plant. Instead, the author, in collaboration with Mr. Carn Gibson, proposed to design an experimental apparatus which tested the hot and cold exchangers separately but regeneratively; the apparatus would consist of two packed columns, one performing the storage and the other the generation heat transfer process for a given temperature range. Switching apparatus operation between T_H and T_L would necessitate fully draining the apparatus and replacing the liquid with the appropriate liquid for the desired mode of operation. When the apparatus is demonstrating hot operation, the hot gas would sequentially be heated by the liquid then heat it, in the case of cold operation the cold gas would sequentially be cooled by the liquid then cool it. The advantage of this approach is twofold; first, a lower power heater or chiller can be used to slowly reach T_H or T_L, and second, compared with transient methods, it allows for long-duration study of the heat exchange processes.

Figure 5.2 provides a high-level overview of such a regenerative apparatus, this design is the basis for the experimental apparatus whose construction is outlined in the following chapter. Note that for each operational mode, two heat sources/sinks are needed: one primary heat source/sink either at T_H or T_L, and another secondary heat source/sink at T_M. The primary source or sink heats or chills the liquid at a fraction of the power which is exchanged in either exchanger, building up a temperature difference from ambient in the fluids and apparatus mass over a period of several hours as the system operates. The secondary heat sink ensures proper apparatus operation in the event that either column heat exchange process is incomplete; an expected situation given that no real-world processes are fully reversible. Consider hot operation, where it is likely that liquid leaving the bottom column will not have been completely cooled to T_M from its entry temperature of T_H; the secondary heat sink ensures that the liquid

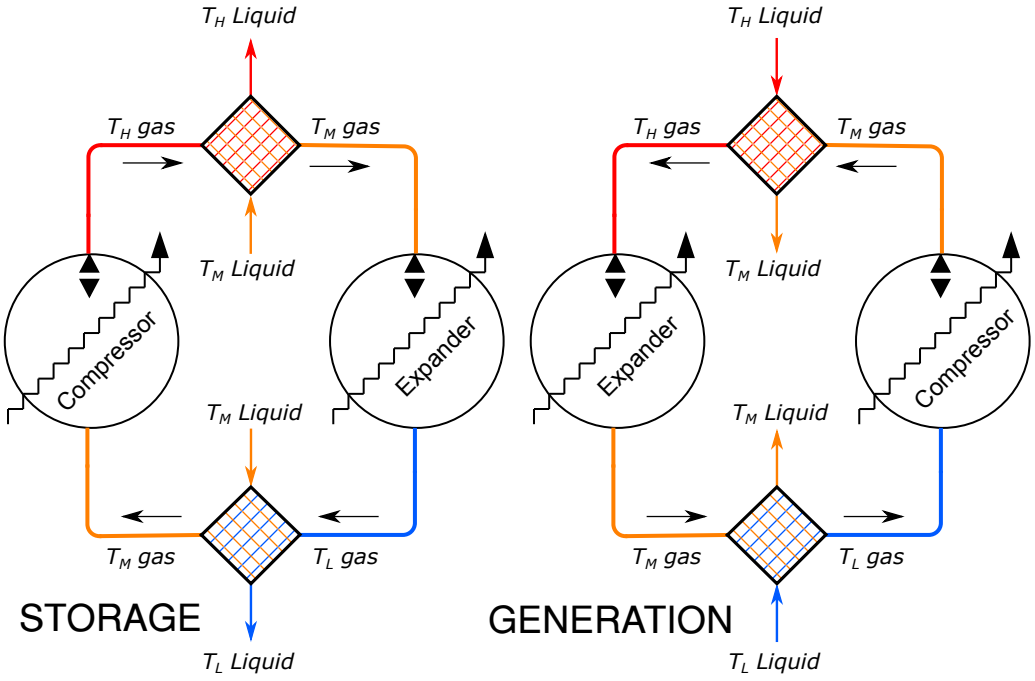

Figure 5.1: Variation in heat exchange processes in the PHES system owing to operational mode. Storage mode runs the reverse Joule-Brayton cycle, while generation mode runs the forward Joule-Brayton cycle.

reaches T_M before it is fed back into the top column. The choice of siting both the primary and secondary heat sinks/sources on the liquid pipework reflected the author's intuition that heat exchange with the liquid would have a higher convective heat transfer coefficient h than with the gas. In retrospect, given the fluid velocities and chosen pipe sizes, it might have been more effective to have placed the heat source/sinks on the gas pipework as it had a turbulent flow. An electrical resistance heater was proposed as the heat source operating at T_H, consisting of a temperature controlled thermal mass, inlets and outlets for the liquid, and a turbulation device to increase the turbulence of the liquid flow. The heat sink operating at T_L is proposed to be a low-temperature chiller or a liquid nitrogen drip heat exchanger, and a water-jacket style exchanger using mains water is proposed to be the T_M heat sink. Two positive displacement pumps circulate the working fluids, one for the liquid and another for the gas. Liquid flows through the columns in the direction of gravity, so unlike the gas flowrate, the actual liquid flowrate in the columns is not necessarily equal to the rate at which it is pumped. Ideally this is the case, however if the liquid is pumped at too high a rate it could accumulate within the columns. A design consequence of this packed column arrangement is that one column must be positioned vertically above the other and there must be

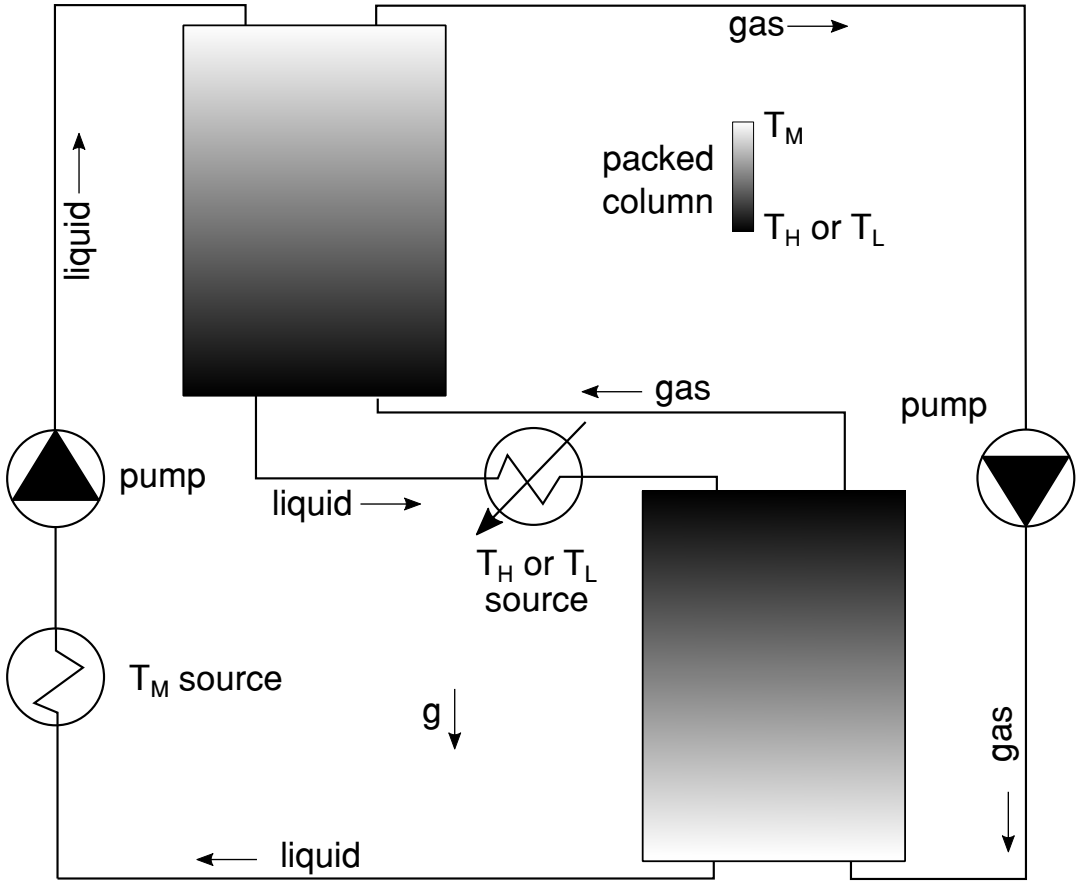

Figure 5.2: Process diagram for regenerative packed-column heat exchange apparatus. The gradation within the packed columns shows temperature difference from mid temperature T_M, towards either T_H or T_L depending on operational mode. Although not to scale, the relative position of the columns and their orientation with respect to gravity is critical.

sufficient fall in liquid tubing between the columns to ensure liquid flow between the top and bottom column. Considering the 1.7m long pilot column described previously, the proposed apparatus presents non-trivial structural engineering challenges.

A further design consequence of the regenerative apparatus design presented here is the full re-circulation of the working fluids. Although the chosen liquids and gas are chemically compatible with one another and do not exhibit significant degradation over the proposed operating conditions and lifespan, care must be taken to ensure proper apparatus pressure given fluctuating temperatures in a closed system. In order for desired operating conditions to be reached, the quantity of gas initially added to the apparatus must be carefully calculated, owing to the linked nature of pressure and tem-

perature for gases. Considering the gas to be ideal, this relationship can be calculated from the ideal gas law:

$$\frac{P_1 V_1}{n_1 T_1} = \frac{P_2 V_2}{n_2 T_2} \tag{5.1}$$

where P, V, n, and T are the pressure, volume, quantity, and temperature of the gas at two differing states 1 and 2. In the case of the described apparatus, it is filled with gas at state 1, when the apparatus and the gas are at an ambient temperature. The apparatus reaches state 2 after a heating or cooling period. Apparatus volume V and gas quantity n are unchanged between states 1 and 2, allowing for cancellation to yield the relation:

$$P_2 = P_1 \left(\frac{T_2}{T_1} \right) \tag{5.2}$$

which can be used to calculate the final apparatus pressure based upon an initial pressure, indicating how much gas ought to be added before an experiment begins. Notably for hot operation, the initial pressure will be lower than the operational pressure, while for cold operation the initial pressure will be higher than operational pressure. With a high-level overview of the proposed apparatus in place, thought is now given to its experimental use.

5.2 Experimental Campaign

As discussed in Chapter 4, the primary objective of the experimental apparatus is to generate column temperature profiles and verify the overall heat transfer coefficient U_h of the exchangers. Temperature profiles can be used to compare packed-column performance against the previously discussed MATLAB model allowing it to be verified or modified as necessary, and U_h can be compared with other heat exchangers. A secondary objective of the apparatus is to experimentally verify the flooding point of the packed-column against the empirical flooding model developed by Stichlmair et al. (1989). The primary objective is accomplished whenever the apparatus is demonstrating steady-state operation at the desired temperature and pressure, while the secondary objective requires a calculated experimental plan.

Operation of the apparatus was intended to be divided into discrete experimental trials which begin and end with the entire apparatus at the ambient temperature of the lab. Each trial would begin with a fixed quantity of gas and liquid in the apparatus; it is envisioned that the entire apparatus need not be purged of gas and liquid in-between trials, only that appropriate quantities are present. Likely this would entail the liquid

remaining within the apparatus over several trials, with gas added to the apparatus between trials to increase apparatus pressure as needed. The initial gas pressure in the apparatus would be calculated using the previously set out equations depending on desired experimental conditions. Following the addition of the gas, the primary heat sink/source at T_H or T_L is enabled along with the gas and liquid pumps and the T_M heat sink. The hot or cold heat source or sink would progressively heat or chill its thermal mass to temperatures closer to T_H or T_L, eventually reaching a final value. The reason for this progression is to avoid sudden, uneven temperature change in connections near by the heat source/sink which could cause joint failure. Final apparatus operating conditions would be reached after a heating or cooling period of several hours during which the gas and liquids would gradually approach the set T_H or T_L. During this time gas-liquid heat exchange would be demonstrated within each column, albeit at lower temperatures and pressures than found after the period were complete. This heating/cooling period is the result of large thermal masses within the apparatus, and the significant temperature swings that parts of the apparatus must undergo.

In practice, gas and liquid mass-flows are set within the apparatus by adjusting pumping volume flow-rates at known temperatures. Because both the gas and liquid pumps are purposefully positioned outside of the section of the apparatus which will experience T_H or T_L, less robust pumps are needed and flow conditions can be calculated using constant ambient temperature fluid properties. To convert mass-flow to volume-flow, gas and liquid densities are calculated at T_M and the respective mass-flow is divided by this density. Initial gas and liquid flow-rates were calculated by scaling full-scale column flows as discussed in Chapter 4 to satisfy the primary requirement of equal fluid heat capacities C within each column. Given that C is calculated by multiplying the mass-flow $\dot{m}$ by specific heat c_p, the required mass-flow to match heat capacities between fluids can only be approximated owing to the large variation in specific heats of both fluids across the packed columns. Accordingly, selected mass-flows for apparatus heat/cooling period reflected balanced heat capacities between fluids.

Calculation of U_h requires only knowledge of the gas and liquid entry and exit temperatures, as well as the mass-flow rate of the fluids. This calculation is intended to take place at several points in time during each experimental trial, and is averaged across trials with similar operating conditions. Therefore, if calculation of U_h was the only objective of the apparatus it would be operated in steady-state conditions following start-up for a fixed period of time, then shut down. However, the secondary objective, the calculation of packed column flooding point, provides impetus to vary appara-

tus behaviour to establish this parameter. Establishing the flooding point requires the development of test criteria to establish its onset and evaluation of this metric under differing conditions. Metrics used elsewhere in literature include:

- Visual observation of the packed column to note the establishment of a standing front which entrains liquid and inhibits liquid flow out of the bottom of the column (Elgin and Weiss, 1939). Over time, liquid may accumulate in column.
- Pressure measurements to quantify a step-change increase in pressure drop across a packed column indicating that flooding has occured and the passage of the gas upwards has been restricted by this flooding (Jiřičný et al., 2001).

Visual observation is not considered feasible for the apparatus discussed here owing to the desired operating pressure of 200 bar; no transparent or translucent materials exist with which a column could be practically constructed to contain this pressure. Small viewing ports of transparent material as are sometimes utilised in high pressure apparatus, however the desire to insulate the packed-column from the pressure vessel precludes the use of such ports in this application. Thermal isolation of the experimental apparatus from its surroundings is discussed in greater detail in Chapter 6, however its purpose is to avoid axial thermal conduction along the packed column which would distort experimental results. Quantifying the flooding point using pressure measurements was considered, however pressure transducers (differential or otherwise) available to operate at 200 bar with the required precision to detect flooding were deemed too costly for this application. Temperature measurements to quantify the onset of flooding are therefore proposed to be used as the flooding metric for this experimental apparatus, as the required instrumentation was already necessary to fulfil the primary objective of the apparatus. Similar to the significant decrease in separation efficiency in distillation columns which occurs under flooding conditions measured by Cahill (2012), temperature measurements are thought to show a breakdown in the heat transfer process between gas and liquid under flooding conditions. Although this assumption is accepted as-is for the subsequent analysis, one way to verify this temperature breakdown in future work would be to carry out a gas-liquid heat transfer process in a low pressure transparent column which is systematically flooded, and observe the column temperature profiles relative to the onset of flooding. A secondary flooding metric which may be used is the formation of a non-linear temperature distribution within the column due to the convergence of temperatures in the lower sections of columns, potentially indicating an accumulation of liquid.

Operation of the apparatus is intended to take place in a series of trials to repeatedly quantify the flooding point of the packed columns at differing pressures. Although the homologous condition between the pilot columns tested in this apparatus and the proposed full-scale system discussed previously dictates that both columns operate at the full system operating pressure of 200 bar, the author felt it relevant to obtain heat transfer and hydrodynamic performance results of the columns across a variety of pressures. The reason is twofold; first the full-scale apparatus could be desired to operate at a lower pressure and packed-column performance in this case is valuable to quantify, and second, the author wanted to verify the existing empirical relationship between pressure and flooding at apparatus pressures. The flooding point would be quantified by sequentially increasing gas mass-flow, after the start-up period had been completed, until a non-linear temperature gradient developed to indicate the onset of flooding. Liquid flow is intended to remain unchanged across all trials; given that the gas is the continuous media within the column its velocity can be much more precisely controlled. Following the observation of flooding, the apparatus would be allowed to cool before additional trials were undertaken to allow for the addition of gas as needed. The overall experimental campaign therefore would follow the procedure:

1. Fill apparatus to desired liquid quantity and gas pressure. Begin trials at an operating pressure of 5 bar.

2. Begin start-up procedure by engaging heater/chiller, T_M heat sink, and gas and liquid pumps.

3. Once equilibrium is reached (indicating start-up is complete), incrementally increase gas flow-rate until flooding point is found.

4. Disable heater/chiller, allow apparatus to fully cool, disable pumps and T_M heat sink.

5. Add incremental quantity of gas such that operating pressure is 10 bar.

6. Repeat steps 2-5 adding 5 bar each iteration until full system operation pressure of 200 bar is reached.

In addition to the flooding point, the overall heat transfer coefficient will be calculated at each operating pressure, and these results will be used to further verify the model discussed in Chapter 4. The selection and placement of hardware to allow these calculations to take place is now discussed.

5.3 Experimental Variables and DAQ Hardware

The primary experimental objective of calculating the heat transfer coefficient, U_h, is accomplished through knowledge of inlet and outlet packed column temperatures, fluid mass-flow rates, and fluid specific heats. These temperatures are used with the *Log Mean Temperature Difference* (LMTD) method to calculate U_h. Therefore, the temperatures of the gas and liquid must be independently measured at the inlets and outlets of both columns. In addition to these temperatures, the author chose to quantify the temperature profile within the packed columns, both to verify that it agreed with the profile generated by the experimental model and for the detection of flooding. This necessitated measuring internal packed-column temperature at several points along each column; the author chose to do this at ten points along each column in the apparatus. In the pipework surrounding the columns where the fluids flow separately it is possible to measure the temperature of the fluids independently, while within the column itself differentiation between the gas and liquid temperature was not deemed feasible. If it were, localised heat-transfer coefficients could be calculated for the apparatus, further improving the model. However, any contact-based temperature sensor would be unable to differentiate between gas, liquid, and packing, and the approach used in a similar packed column study by Halkarni et al. (2016) to embed select temperature sensors within packing material is not possible for the selected Pall ring packing owing to its geometry. Such an approach also would not resolve the most critical issue, differentiation between gas and liquid temperatures. Non-contact temperature sensors including ultrasonic (Industrial Measurement Systems, 2019) and infrared (Omega Engineering, 2018) sensors were also considered, but none were able to selectively identify liquid, gas, and packing temperatures. Contact temperature sensor technologies considered were thermocouples, resistance temperature detectors (RTDs), and thermistors. All are widely available in packages readily applied to the process industries and are usually supplied as tip-sensitive stainless steel probes. These probes are inserted into apparatus pipework by means of a compression fitting, which provides a gas-tight seal. Of the three technologies, thermistors are readily dismissed from consideration for this application due to their limited temperature range of -50°C - 250°C, a result of the exponential nature of their output at high temperatures (Ametherm Inc, 2015). RTDs have a high temperature of 600°C and thermocouples 1150°C, and both have a low temperature of -200°C, so they are adequate for the proposed operating ranges of the apparatus. Accuracy between the two technologies differs significantly, with RTDs

generally in the range of $\pm$ 0.1 - 1°C and thermocouples $\pm$ 1 - 5°C (Ametherm Inc, 2015). Additionally, thermocouples are known to suffer from drift over long time periods, a phenomenon which could potentially hinder comparisons between trials spaced months apart (Scervini, 2009). Although such a long duration of testing is not planned for the experiments discussed in this thesis, the author wanted to ensure continuity in temperature probe performance across the lifetime of the apparatus, expected to be several years. This factor, combined with the greater accuracy, led to the selection of RTDs as the temperature probes for this apparatus.

Although not utilised directly to calculate U_h or the flooding point, knowledge of apparatus pressure is essential to ensuring operation at desired conditions. Measurement of the gas differential pressure across the columns was also desired in order to estimate system pumping losses. The author therefore chose to include two pressure transducers in the apparatus, one above the top column and the other below the bottom column. Measurements at both of these transducers would yield the total column pressure drop, and additionally allow for an average apparatus pressure to be calculated. An overview of temperature and pressure probe placement is given in Figure 5.3, a modified version of Figure 5.2. A comprehensive examination of pressure sensing technologies is not presented here owing to the breadth of the field; focus in the design of this apparatus was on commonly available process pressure transducers. An accuracy of $\pm$ 1 bar was deemed acceptable to ensure that the apparatus was reasonably operating near set pressures. Individual column pressure drop was expected to be on the order of 0.1 bar based upon column flooding correlations utilised in flooding calculations as set out in Chapter 4, but quantifying this value was not a primary objective in the experiment. Balancing available resources with transducers readily available from common suppliers, a 0-250 barg Gems Sensors pressure transducer part number 3100B0250S01B000 was selected. An accuracy value provided by the manufacturer is $\pm$ 0.625 bar, sufficient for general operation but not for quantification of column pressure drops. Differential pressure sensors were considered to compliment the chosen transducers for calculation of the pressure drop, however discussions with several vendors failed to produce components which would satisfy budgetary and performance constraints.

Measurements of gas and liquid flow-rates were needed to ensure that the apparatus was operating under the correct experimental conditions. A wide variety of volume flow sensors are available, although the high apparatus operating pressure limited the selection. The author investigated various options, however ultimately the selection

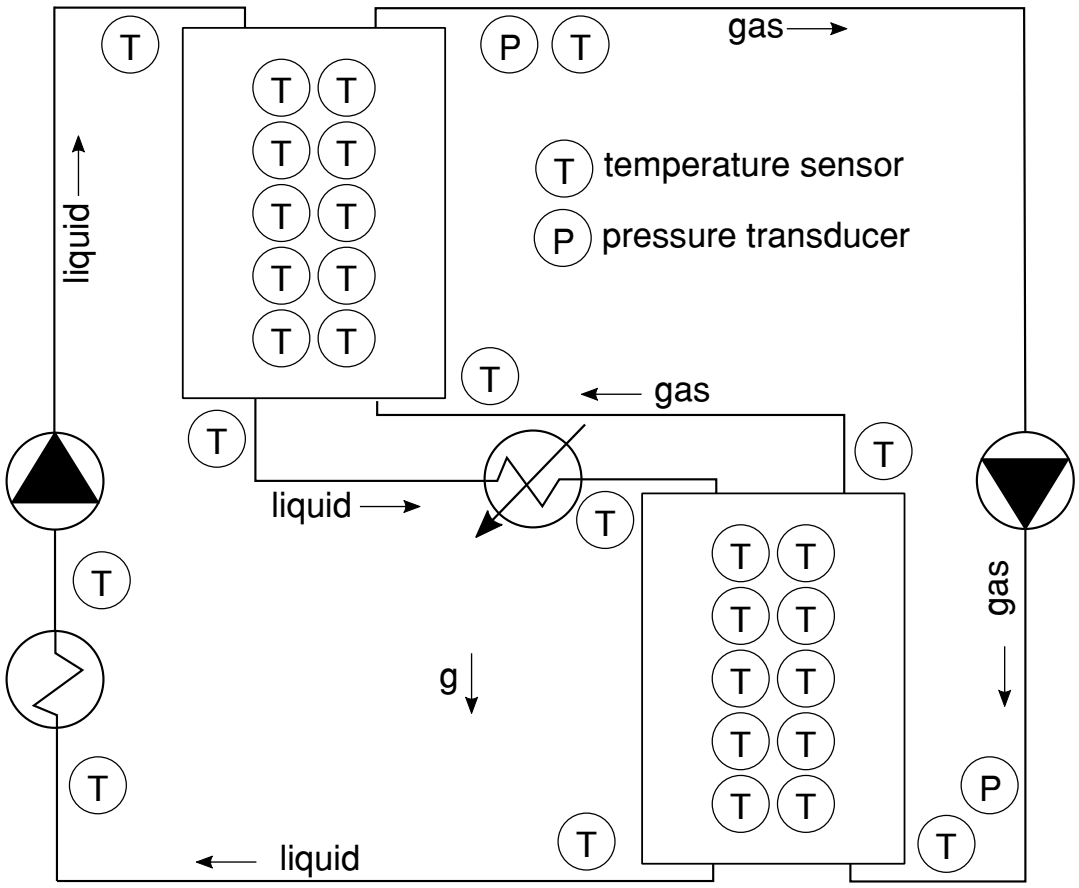

Figure 5.3: Position of temperature and pressure sensors within experimental apparatus. Note that this figure is a modification of Figure 5.2.

of positive displacement gas and liquid pumping technology averted the need to incorporate dedicated flow metering devices in the apparatus. Discussed further in the following chapter, positive displacement pumps were chosen which by nature of their operation move a quantity of fluid exactly in proportion to their operational speed. No fluid may bypass the pumps, so the fluid flowrates can be calculated based upon pump speed. With experiment method and operation now laid out, focus turned to the fabrication, installation, and commissioning of the apparatus.

Chapter 6

Apparatus Detailed Design and Construction

This chapter describes the direct-contact heat exchanger experimental apparatus detailed design, including component sourcing, manufacturing, and assembly. The author worked collaboratively with Mr. Carn Gibson, a SynchroStor employee, to complete the detailed design according to the author's packed column experimental design laid out in previous chapters. Mr. Gibson and the author jointly completed approximately 60% of the detailed design, after which the author concluded the detailed design, sourced all components, and assembled and commissioned the experiment.

6.1 Packed Columns

As the value of the results produced by the apparatus depend heavily on the design of the packed columns, great care was taken to ensure that they produced appropriate experimental conditions. In order to achieve good thermal characteristics, it was decided that the column should only be used to contain the packed column internals, and not serve dual function as a pressure vessel. Therefore, the packed column assembly would be composed of a column and a separate pressure vessel. Detailed conceptual design initially focused on the pressure vessels which contain the packed columns, as they were anticipated to be the longest lead-time items due to their specialised nature. Pilot column dimensions set out in Chapter 4, as a result of scaling the full size PHES plant, specify a 150mm diameter column 1.7m in length. In order to minimise radial heat conduction from the interior of the packed column into the steel of the pressure vessel, an insulating layer was incorporated as a way to thermally decouple the pressure

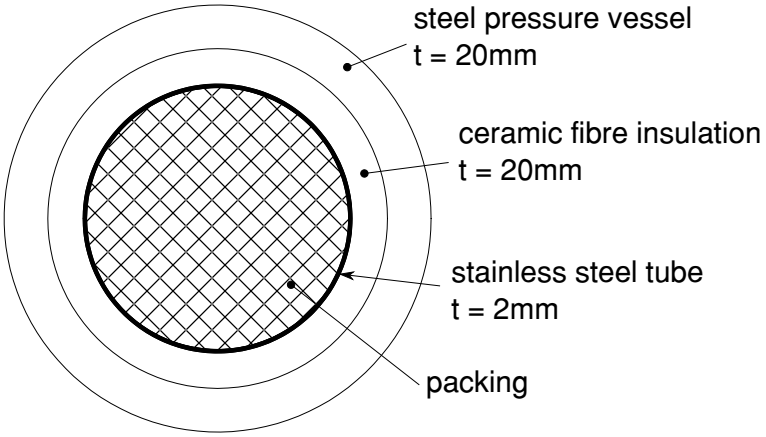

Figure 6.1: Cross section of packed column assembly showing the pressure vessel, insulation, containment tube, and packing.

vessel from the packed column. Without this layer, there would be a large steady-state heat loss to the pressure vessel, drastically increasing either the heating/cooling start-up period or the required heating or cooling power. A further benefit of the insulation layer was to reduce axial conduction along the pressure vessel length, a phenomenon which would jeopardise the integrity of the proposed experimental plan. If a significant quantity of heat were allowed to conduct along the axis of the column, the experimental results would show a temperature profile attributable to conduction rather than gas liquid heat transfer. Each packed column assembly would therefore consist of a thin-walled, non-pressure bearing 150mm diameter 1.4401 stainless steel tube making up the packed column, a layer of 128 kg/m^3 bio-soluble ceramic fibre blanket insulation, and a steel pressure vessel. This column component arrangement is shown in Figure 6.1, noting that the design thoroughly thermally isolates the pressure vessel from the packed column. The choice to insulate the column in this way had two critical effects upon subsequent design: first, it prohibited the use of viewing ports in the columns, and second it required temperature probes to be inserted into the columns axially, rather than radially penetrating the insulation. Manufacturing and statutory pressure vessel certification of the column pressure vessels was contracted to Hystat Ltd. of Huddersfield, England, who worked to design columns which could meet apparatus pressure and temperature requirements. A key issue in the manufacturing process was selecting a material which had sufficient strength at high temperature T_H and did not become too brittle at low temperature T_L. Stainless steel was the company's first material choice to meet these requirements but the cost would have exceeded available resources, so it was instead determined that the columns would be made of P355N carbon steel and

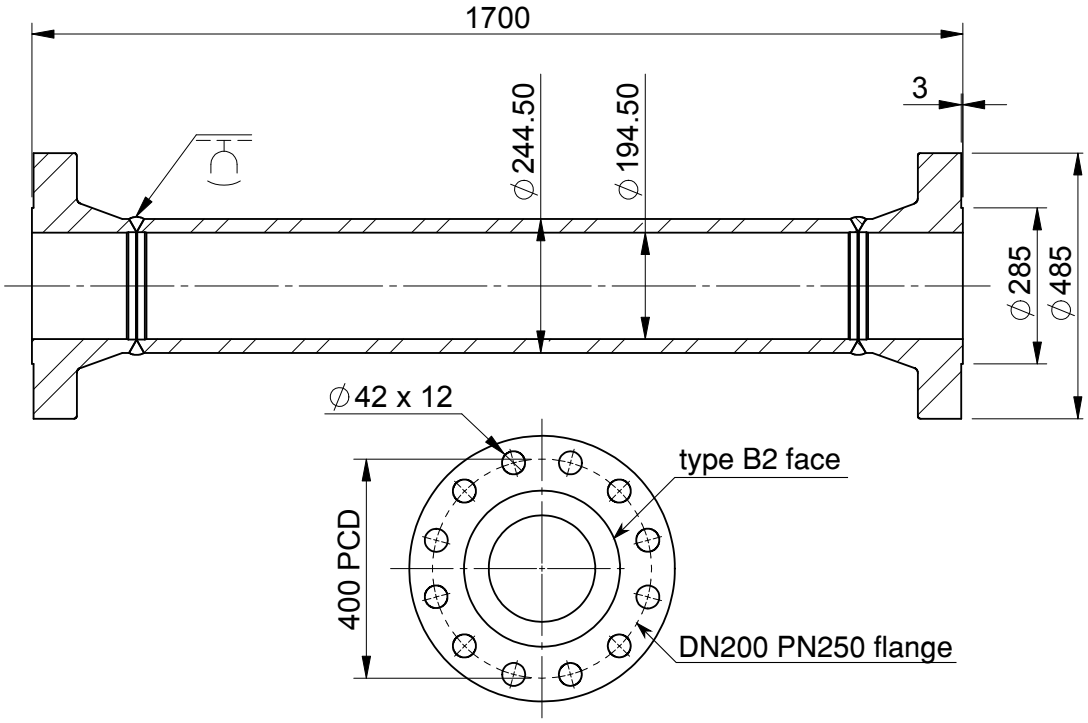

Figure 6.2: Packed column pressure vessel manufactured from P355N steel. All dimensions are given in millimetres.

have a design pressure of 200 bar with a temperature range of -50°C to a T_H of 400°C. This design was a compromise which prohibited operation at the desired T_L of -120°C due to brittle fracture concerns for P355N steel at 200 bar. Existing legislation does not permit a pressure vessel to be certified for multiple pressures under differing temperature conditions, even though brittle fracture was not a concern for the operational conditions of cold operation: T_L and 20 bar. As a consequence of this compromise, the author agreed to re-certify the vessels for 20 bar and T_L operation before cold experiments began. Two column pressure vessels were subsequently fabricated having type B2 DN200 PN250 flanges according to EN1092-1, a wall thickness of 20mm, and a length from flange to flange of 1700mm. The provision of standard flanges allowed for the author to separately procure components to attach to these columns to facilitate sensors, gas and liquid pipework, and other packed column components. Critically, the pressure vessels were delivered fully tested and certified, a non-trivial task for gas containing vessels of this size and pressure.

With the provision of the primary column components complete as outlined, attention now fell to the column internals: pipework connections for gas and liquid inlets and outlets, gas and liquid distributors, gas and liquid separation, packing, and sensors.

Recall Figure 2.6 which details the internal components of a packed column assembly; one liquid distributor must be located at the top of each column, while one gas distributor must be located at the bottom of each column. Packing must be contained within the column to allow for a void in the bottom of both columns, and to prevent packing from being driven upward under high gas loads. Similar to the approach taken for the column, the author was guided by the principle that any large thermal masses ought to be decoupled to the greatest extent possible from fluids at elevated or depressed temperatures. The rationale was to limit heat transfer to or from the thermal masses in order to limit the time needed to heat or cool large thermal masses. In all areas of the apparatus, this approach required insulation on the interior of the pressure bearing components. In the column itself, this was accomplished with the ceramic fibre blanket previously discussed. After testing the insulation, it was found that it lost structural integrity when it absorbs liquid, restricting its use in areas where it could be directly exposed to liquids. Given the porous nature of the insulation, it also loses insulating value. As a result, in addition to the above described column internals, two additional features were required in the column assembly. First, a system to ensure that the column insulation was kept dry was needed, and second, an additional type of insulation material to thermally decouple areas of the apparatus having direct contact with the liquid or gas was required.

To accommodate all column peripherals, Mr. Gibson and the author proposed a semi-modular system of plates to attach to both ends of each column to provide internal volume for packed column components and fluid ports for pipework connections. The number and orientation of plates varies based upon the needs at each location, and the plates have the same standard flange as had been designed into the column pressure vessels. All flange connections are made using spiral-wound graphite gaskets sized to match the standard flange chosen. These gaskets are compressed by twelve M39 bolts in each flange, which forms a robust gas-tight seal. Three plates were designed: one to facilitate the gas or liquid distributor and gas pipework (gas plate), another to facilitate liquid pipework and temperature probes (liquid plate), and a third to act as a spacer and provide greater internal volume (spacer plate). All three plates would attach to the bottom of both columns, while only the gas plate and the liquid plate would be used at the top of each column. The arrangement of these plates is shown in Figure 6.3, noting that the rotational orientation of the liquid plate varies throughout the apparatus to accommodate liquid pipe routing.

The liquid plate is addressed first; in addition to providing connection ports for

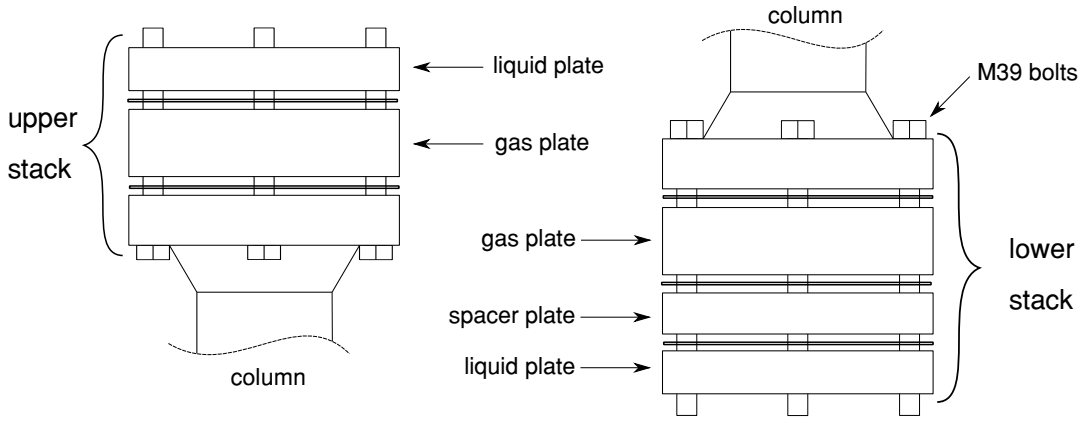

Figure 6.3: Plate attachment configuration to the flange of both ends of both columns.

sensors and the liquid pipework, it also served as a cap to both ends of the column assembly. A series of fluid ports of the tapered British Standard Pipe (BSPT) form are specified on the face of this plate, providing attachment points for RTD temperature probe compression fittings. All but one of these ports passes fully through the plate so that the RTDs can measure the column interior temperature. One additional port is reserved to measure the incoming or outgoing liquid temperature. One larger fluid port of the same form was provided on the plate face for use as a liquid drain, and two more ports were provided on the circumference of the plate for liquid and gas connections. The rationale in the duplicate provision of liquid piping connections is that the plate used at the bottom of the bottom column would be able to fully drain all liquid from the apparatus, while liquid plates in other positions would be better served by side connections for liquid pipework. The design decision to create one multi-purpose plate to be used in four different positions in the apparatus reflected industry experience that the overall cost of manufacture of four slightly more complex identical parts would be less than the manufacture of four simpler yet unique parts. An overview of the liquid plate is provided in Figure 6.4, the full manufacturing drawings for this part and other components are provided in the appendices.

The spacer plate is next addressed, and is significantly simpler than the other plates. It has no fluid connections, only two flanges of the previously described standard on both faces and a hollow cavity in the middle; it is essentially a ring. Two spacer plates were required, both serve as liquid sumps at the bottom of both columns.

The gas plate is the most complex of the three as it was designed to accommodate either the liquid or the gas distributor depending on its location in the apparatus. Before providing detail on this plate, it is helpful to first review the gas and liquid distributor

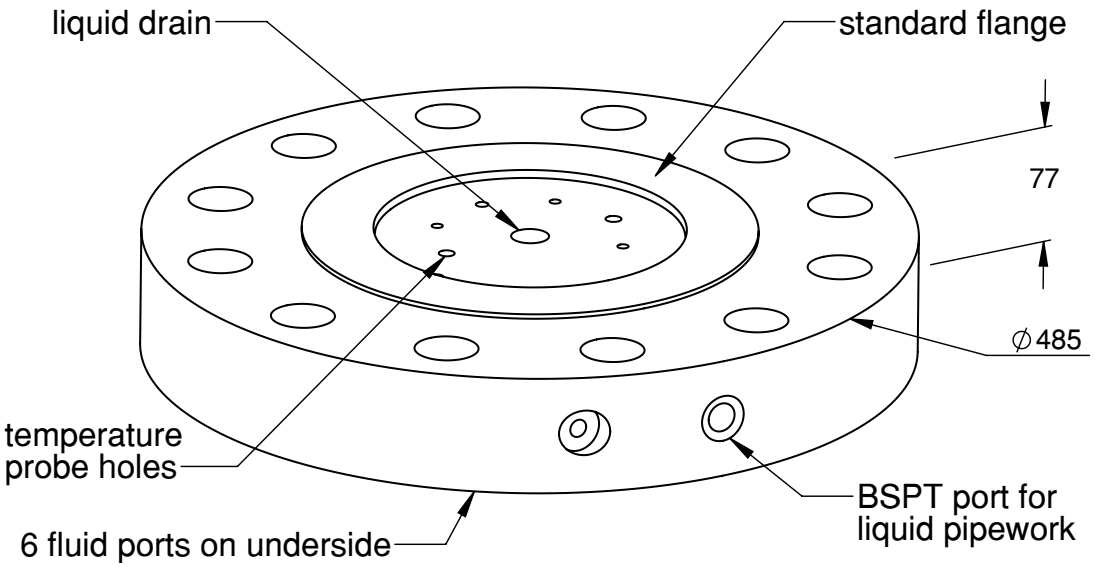

Figure 6.4: Liquid plate which acts as a cap for both ends of both columns. It facilities temperature probe mounts and liquid pipework connections.

geometry.

Kolev (2006) provides an overview of the internals of packed columns, and includes great detail on the design of gas and liquid distributors. A multitude of designs exist to serve different combinations of column diameter, packing material and fluids, but only a few are applicable to the size of column in this apparatus. For the liquid, a shower head type distributor was selected owing to its widespread use in experimental columns of similar sizes (Miyahara et al., 1992) and recommendation by Kolev. A liquid distributor ensures an even distribution of liquid at the top of each column by providing a small reservoir for liquid to accumulate and bossed holes of even height for the liquid to over-top and distribute across the packing. Liquid within a packed column tends to propagate outward towards column edges (Kolev, 2006), necessitating liquid re-distributors at fixed heights in large commercial columns. To account for this liquid propagation, the shower head distributor designed for this apparatus is a smaller diameter than the column itself to allow for the outward spread of the liquid. A distributor designed by the author and fabricated from aluminium by the Edinburgh School of Engineering workshop is shown in Figure 6.5; the distributor was fitted on a lip on the inner diameter of the gas plate at the top of each column. Note that the distributor also provides holes for the passage of gas and RTD temperature probes around its outer circumference.

The gas distributor is similarly based upon established experimental practice and

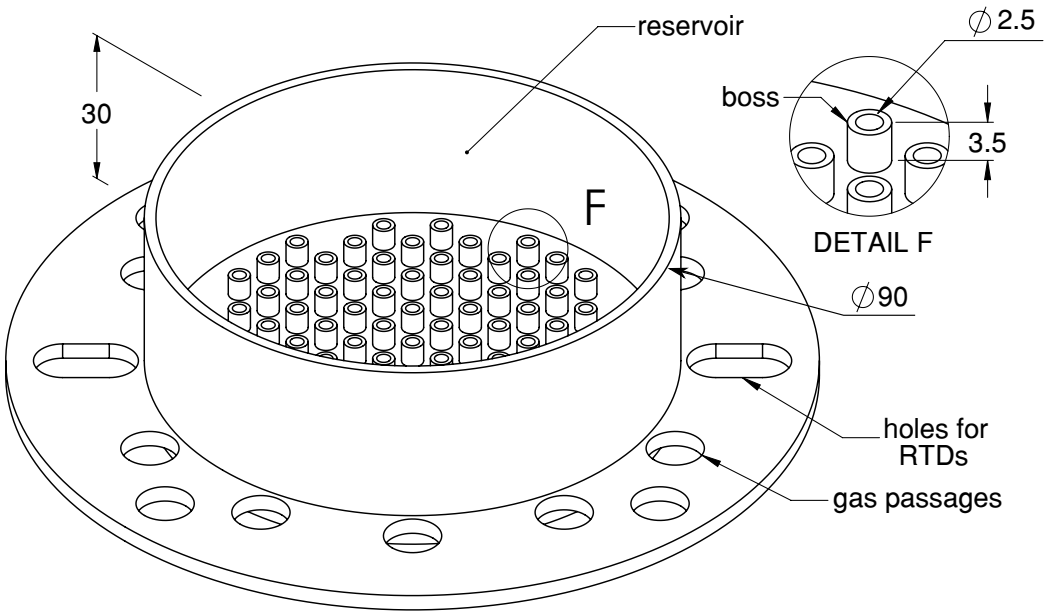

Figure 6.5: The shower head style liquid distributor designed for the apparatus.

has a similar function: to evenly distribute the incoming gas across the cross-section of the column packing. The distributor design chosen for this apparatus was a stainless steel tube which fit concentrically inside the gas inlet hole in the gas plate. A majority of the tube protrudes into the internal volume, and there are holes on the underside of the tube to allow the gas to escape. Two gas distributors are mounted at the bottom of each column in the apparatus. The gas plate, which houses both distributors, is shown in Figure 6.6. It is similar in construction to the spacer plate in its ring-like geometry, however it has a gas inlet drilled radially to allow for the passage of gas and to hold the gas distributor. There are a series of mounting lips on the inner edge of the ring to both hold the liquid distributor (at the top of the column) and to hold a packing retaining sheet (at the bottom of the column). Where the gas inlet meets the outer plate circumference a polished flat surface with tapped holes was specified to accommodate the connection of sensor blocks. The purpose of the block is to facilitate fluid ports for pressure and temperature measurement of the gas stream as it enters and exits the columns. All three column plates were specified to be manufactured of P355GH steel, and machining was subcontracted to Hughes Engineering of Glasgow. In a decision that would later have negative schedule implications, pressure vessel certification of the parts was not undertaken concurrently with manufacture.

A detailed description of the sensor blocks is not provided owing to their relatively simple design. Each block provided three fluid ports for sensor connections at the

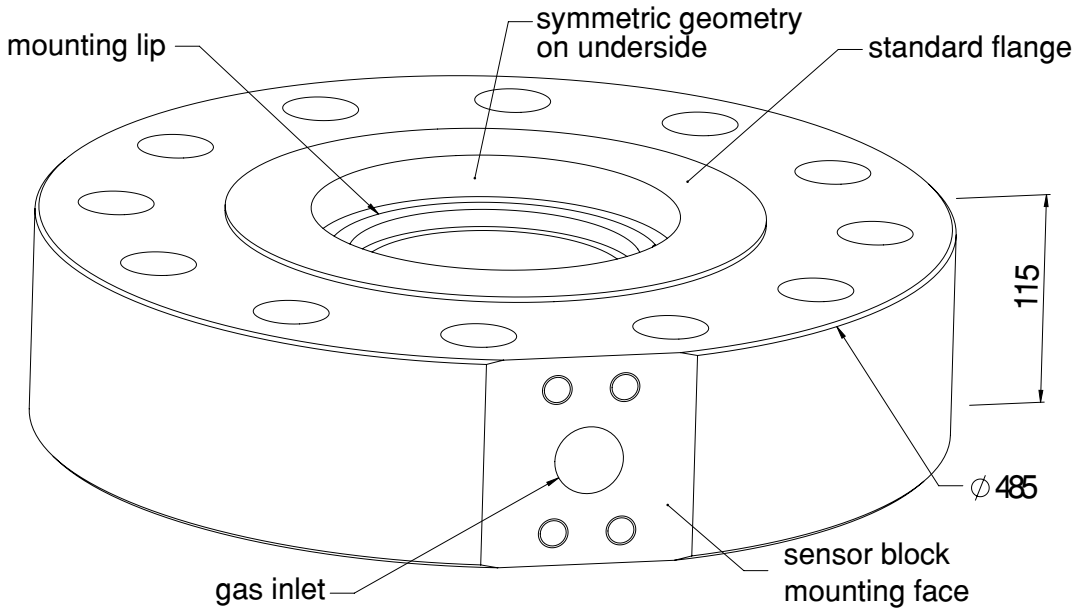

Figure 6.6: Gas plate which facilitates the connection of the sensor block and provides additional internal volume.

gas passage and a large fluid port for a gas pipework connection. A seal is made between the sensor block and the machined mounting face on the gas plate using metal c-ring seals, a challenging arrangement necessitated by the high gas temperatures. Four sensor blocks were fabricated by Chesser Engineering of Edinburgh from P355NL2 steel.

With the majority of column components described, the remaining components to be addressed are gas and liquid separation, packing, and insulation. A substantial design challenge for the apparatus was to ensure that the gas and liquid were properly separated after they had passed through the columns. Minimal liquid should be drawn out of each column through the gas piping at the top of the columns, and minimal gas should enter the liquid piping at the bottom of both columns. Two solutions were proposed to address each problem, both shown in Figure 6.7. This figure is a cross sectional view of the top and bottom of the columns, and shows most internal components. In the top of the columns, several gas passages around the perimeter of the liquid distributor allow gas to easily flow to the gas outlet, while the reservoir of the liquid distributor and the liquid input is purposefully isolated from the gas outlet in an attempt to discourage gas from flowing through the outlets of the liquid distributor. In the bottom of the columns, the gas distributor is oriented such that gas exists from the underside of the distributor pipe, and liquid collects in a sump below this pipe providing the liquid with no easy path to enter the gas distributor to reach the gas piping. In

both the top and bottom of the columns, attention is given to providing a passage for dry gas to enter and exit the ceramic fibre insulation blanket in the column. Dry gas is supplied from the gas input at the top of the upper column, and piped independent of the main gas piping to various points along both columns. These gas passages are intended to allow any liquid which becomes entrained in the column insulation to be dried, and to prevent a pressure difference across the thin-walled experimental tube.

Stainless steel 16mm Pall ring random packing was selected as the heat transfer surface for the columns, as it was widely available, easy to install, and performed well in column performance simulations set out in Chapter 4. It is pictured in Figure 6.11. Initially it was envisioned that both a structured packing and a random packing would be tested, as both were considered for a full scale column. Structured packing is usually easier to model using CFD or finite volume methods owing to its consistent, repeatable geometry. Given that CFD multi-physics analysis was considered for future work, structured packing, with its well defined geometry, was an obviously favoured choice - as the experimental work could later be used for validation. Additionally, structured packing generally have a greater specific surface area than random packings, allowing for more heat transfer per unit volume of packed column. A sample of Sulzer Metallapak 752.Y structured packing was provided by the Sulzer Ltd. for use in the apparatus, however adapting the packing to allow for the passage of 6.0mm RTDs proved very challenging and time and resource limits resulted in the packing not being used. The Pall rings used in this apparatus were movable enough after installation that the RTDs could be inserted through the packing bulk.

The final component of the column assemblies is an insulating material capable of decoupling the thermal mass of the plates from the liquids and gases they contain. Selection of an insulation capable of withstanding 200 bar pressure and temperatures between -120°C and 400°C was very challenging, and the author tested several materials before selecting Superwool 607 fibre insulation board. Hollow insulating cylinders were constructed by the author from layers of this board to provide a thermal break on the internal surfaces of the gas and spacer plates, and an insulating board with holes for the RTD probes fit the flat surface of the liquid plate. Insulating sheets were glued together and coated with refractory mortar to prevent disintegration when submersed in liquid.

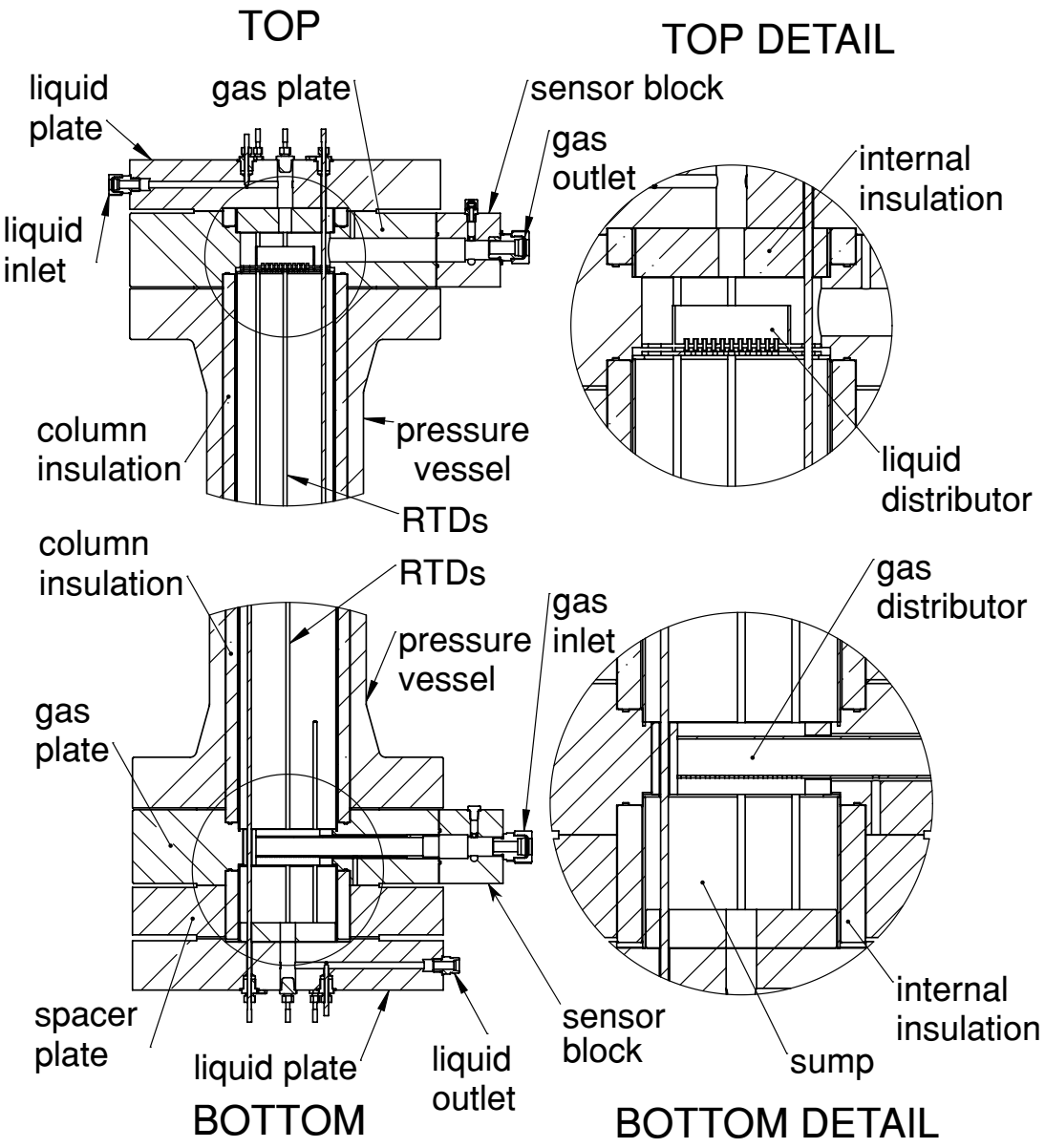

Figure 6.7: Cross-sectional view of top and bottom of column assembly showing gas and liquid distributors, Superwool internal insulation, and RTDs.

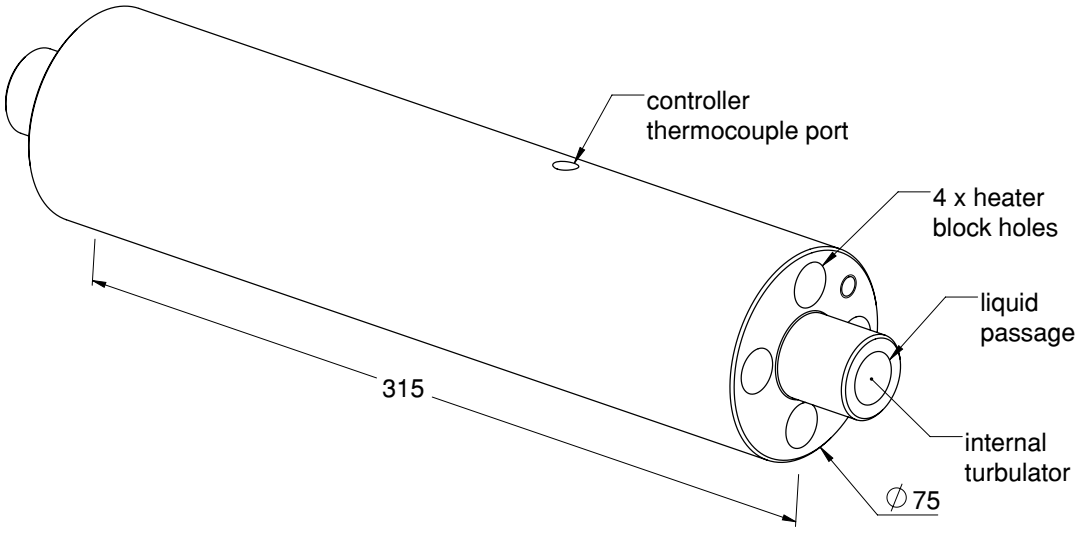

Figure 6.8: The liquid heater.

6.2 Heat Sources and Sinks

Two of the three heat sources/sinks proposed in the previous chapter were built as part of the experimental apparatus: a heater and the T_M heat sink, a mains water-jacket style heat exchanger. Although preliminary design work for a chiller to provide a heat sink at the T_L of -120°C was undertaken, the author chose to limit the scope of the initial experiments to consider only the forward and reverse processes of the hot exchanger. Because the hot exchanger operates at 200 bar while the cold only operates at 20 bar, the hot operation is currently less well described in existing literature than the cold operation. It was envisioned that after the hot experiments were complete, a chiller would be procured for cold operation.

The T_H heat source, an electrical resistance heater, was fabricated from a 75mm diameter round of X12CrS13 stainless steel. A central passage for liquid was bored through the middle, and four holes for heater cartridges were reamed at 90° to one another radially offset from the central passage. Four 16mm x 1 kW cartridge heaters were inserted into the round and controlled by a Proportional, Integral, Derivative (PID) temperature controller, which took measurements of heater temperature with a K-type thermocouple probe in contact with one of the cartridges. The primary heater body, manufactured by the author, is shown in Figure 6.8. A liquid turbulation device consisting of a stainless steel strip bent into a helix was inserted into the liquid passage.

The T_M heat sink, a co-current co-axial heat exchanger, was constructed by placing

22mm copper water piping concentrically around a 3m vertical section of 16mm liquid piping, with a water inlet at the bottom and outlet at the top of the section. The copper pipe inlet was attached to the mains water supply via a ball valve and a rotameter, which allowed flow control between zero and two litres per minute. The outlet was connected to a drain, and an identical turbulation device to the one used within the heater was added within the liquid piping for the length of the exchanger.

6.3 Gas and Liquid Pumps

Selection of pumps to circulate gas and liquid within the apparatus was challenging due to the high internal pressure of 200 bar and the desired gas and liquid flowrates. A gear pump, one of the few off-the-shelf pumps available in the operating pressure range, was considered for the liquid however was found to be cost prohibitive. The selection of gas pumps was particularly limited, likely due to the difficulties in sealing a rotating shaft against high pressure gas. A linear actuator was made available to the author as surplus from another lab, so a reciprocating cylinder style pump was designed incorporating this actuator. The pump consists of a double acting hydraulic cylinder driven by the linear actuator; unidirectional fluid flow accomplished through the use of a hydraulic rectification circuit in a manifold. Hydraulics are commonly used at higher pressures than 200 bar, so suitable hydraulic piston-cylinder-rod assemblies are readily available at low cost. Low-friction Viton seals were used in both assemblies. Two pumps were designed, one to pump the liquid and another to pump the gas. The gas pump is shown in Figure 6.9, and was mounted vertically on the apparatus frame; note that the pipework and the rectification manifold are omitted in this figure. This location ensured that the pumps did not experience significantly elevated or depressed temperatures. Cylinder dimensions and stroke were determined by working backward from the desired maximum fluid flow rate. For this flow rate, a rod and bore were chosen which balanced the force limits of the actuator with its speed limits. Too large a bore and the actuator would not be able to move the cylinder, while too small a bore and the actuator would have to move too fast to reach desired flow rates. Cylinder stroke was determined by balancing actuator length, cylinder fabrication cost, and a desire not too require the actuators to change direction at high frequency. Available mounting space for the cylinders was also an important consideration. The gas pump cylinder has a geometry of 120mm bore, a 50mm rod, and 500mm stroke, while the liquid pump has a 45mm bore, 16mm rod, and 400mm stroke. A smaller and less

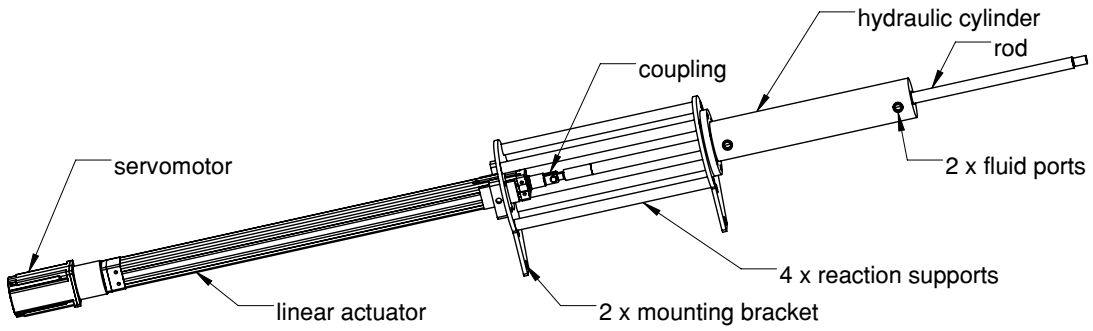

Figure 6.9: Gas pump composed of servo-motor driven linear actuator, hydraulic piston cylinder, and framework. Rectification manifold not shown.

powerful linear actuator was acquired for the liquid pump, as significantly smaller liquid flow rates were needed. In addition to cost, the advantage of this approach to gas and liquid pumping is that it is positive displacement pumping. Piston displacement dictates flow, so the quantity of fluid to pass through the pump is known by virtue of its operation. Given cylinder dimensions and the linear actuator velocity profile, the gas or liquid volume flowrate is readily determined, eliminating the need for separate fluid flowrate instrumentation.

6.4 Pipework

Pipework and fittings were selected for suitability at apparatus temperature and pressures, necessitating the use of 1.4401 stainless steel pipework. Gas piping was 25mm outer diameter by 3.0mm wall thickness seamless pipe, while liquid piping was 16mm outer diameter by 2.0mm wall thickness seamless pipe; both are common sizes for hydraulic applications. A larger gas pipe size would be required in a full PHES demonstration plant to reduce pumping losses for the gas, however the size chosen for this apparatus was the largest for which the author could install fittings without the use of costly hydraulic swaging equipment. As pumping losses are not a concern in this apparatus, the given sizes were deemed acceptable. Twin-ferrule 1.4401 stainless steel compression fittings were used at all unions, tees, elbows, and bulkhead fittings, while single-ferrule compression fittings were used for the RTD probes. Pipes were preferentially bent to avoid the use of elbows, and pipe routes were chosen to minimise the total length of pipe.

Pipework between pumps and rectifying manifolds was routed such that the output of the gas manifold was connected to the bottom of the lower column, and the output of

the liquid manifold was connected to the top of the upper column. The input of the gas pump therefore connected to the top of the upper column, while the input of the liquid pump connected to the bottom of the lower column. Gas pipework directly connected the columns to one another at the midpoint of the apparatus, while liquid pipework connected the columns together via the heater block. All liquid pipework was fit to maintain a descending gradient so that gravity would ensure the liquid travelled to the bottom of the apparatus. This piping arrangement is shown in Figure 6.10. Pipework between the two columns was insulated using foil faced mineral wool pipe lagging, as was the heater block. The pipework outwith this section was not insulated, as these pipes would act as additional heat sinks to keep fluid temperatures near T_M. Liquid was stored in a holding tank outside of the apparatus pressure envelope when not in use. When the apparatus was unpressurised liquid could be pumped into the bottom of the apparatus using a diesel fuel transfer pump to provide the required liquid fill. This tank also provided for Nitrogen blanketing of the Paratherm HR liquid when not in use, as recommended by the manufacturer. In order to ensure safe apparatus operation, a pressure relief and emergency vent were provided. A pressure relief valve set at 200 bar was designed to connect to the gas pipework of the apparatus and vent excess pressure via the holding tank to the exterior of the lab. An external vent was installed for this purpose.

Nitrogen blanketing of the holding tank and apparatus pressurisation were provided via a 300 bar Nitrogen cylinder piped into the lab from an external cage. Supply pressure was controlled from an in-lab regulator, and routed to the apparatus via 6.0mm stainless steel pipework. Two ball valves controlled the direction of gas flow between apparatus and holding tank. A full process diagram for the apparatus and associated pipework is given in Figure 6.10.

6.5 Control and Data Acquisition

The author had two primary goals in apparatus control and data acquisition; first, the instrumentation of as many experiment parameters as possible for later analysis, and second, to ensure operator safety. Whilst pressurised liquids contain relatively small amounts of stored energy, stored gases contain considerably more energy. A quick literature search reveals a plethora of deaths and serious accidents due to sudden releases of gas pressure, including from mundane, relatively low pressure, items such as car tyres (Bowman, 2018). As a result of the inherent danger of elevated pressure gasses,

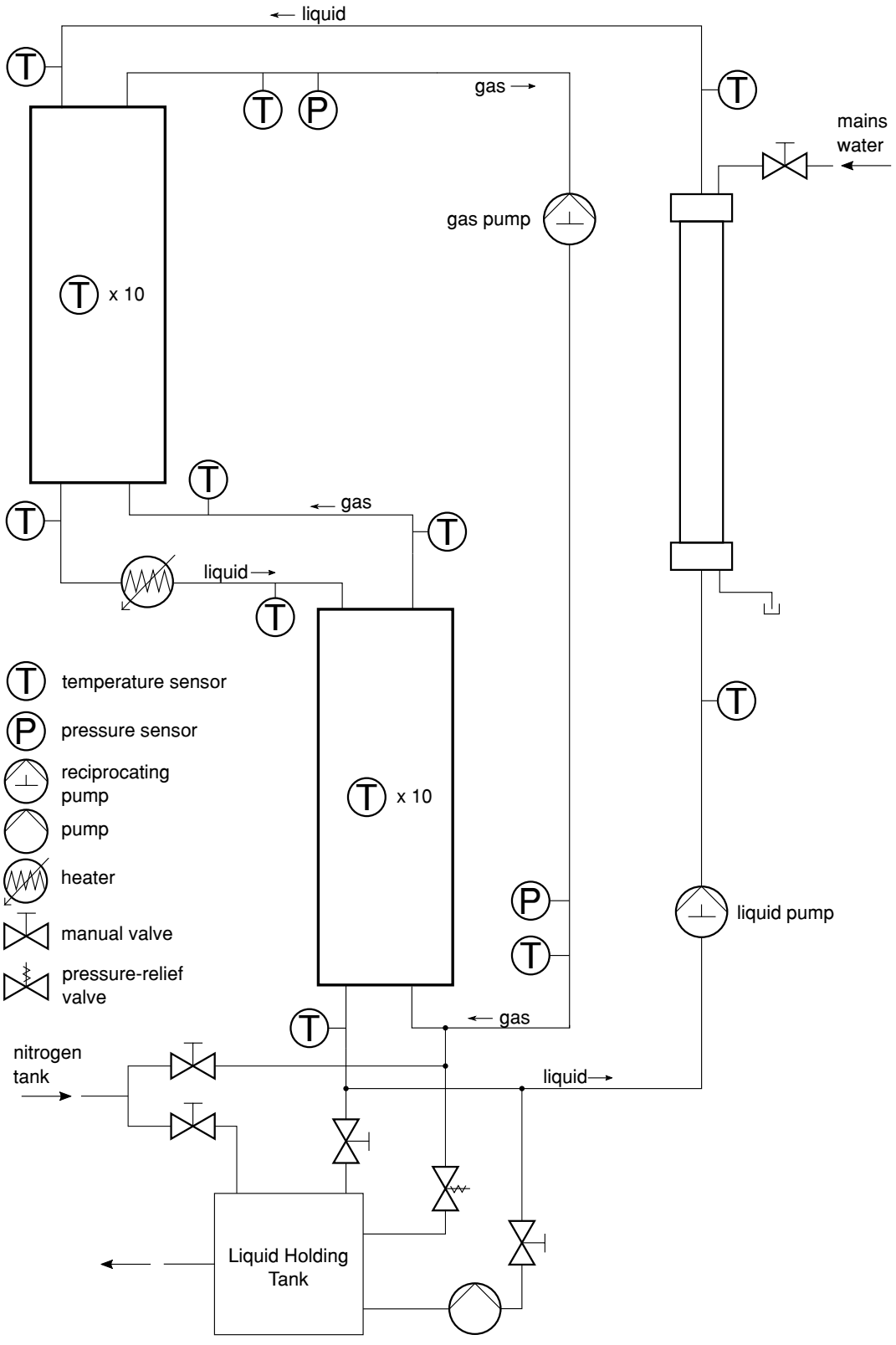

Figure 6.10: Apparatus process diagram showing connecting pipework, valves, holding tank, water-jacket, and vents.

pressure vessel legislation within the European Union strictly regulates pressure vessels which contain gas with the Pressure Equipment Directive (PED). All components used in the apparatus were either purchased certified for pressure use or certified by the author for such use. However, further caution was warranted by the author due to the unique nature of the apparatus. Notably, the heat transfer liquid Paratherm HR used here has severe negative health consequences if it is both hot (above 150°C) and in the form of a mist or spray. Conceivably such a mist could be formed by a leaking joint at high temperature and pressure, and indeed this was observed during commissioning. As a result of these hazards, remote monitoring and control was deemed critical for this apparatus.

Instrumentation and control for the apparatus was built around the Labview system, which provided the author with a graphical user interface to control apparatus operation and record sensor measurements. The operator could view column temperatures and pressures, adjust pump speeds, and vary heater temperature. Modbus over RS-485, a common industrial communication protocol, was used to network ADAM data acquisition modules which provided RTD inputs, pressure sensor inputs, and digital in/out channels. The PID heater controller and an Industruino micro-controller driving the liquid pump linear actuator were on the same RS-485 network, and all data was recorded by Labview at 10 Hz using a USB to RS-485 interface and stored in a Labview database. The thermal inertia of the apparatus prevented rapid fluctuations in temperature, so the low frequency of recording necessitated by the data acquistion hardware was more than adequate. The RS-485 network allowed for sufficiently fast Labview control of the Industruino, which ran a dedicated real-time control loop to dictate liquid actuator operation. The gas pump linear actuator operated on a separate network of Modbus over TC/IP, and was similarly updated by Labview and controlled servomotor positioning independently. Emergency stops and software based over-pressure and over-temperature alarms were also incorporated. The Labview control software was operated on a dedicated PC from a room adjacent to the lab with a viewing window.

6.6 Assembly and Commissioning

Apparatus assembly and commissioning was a multi-month process which began with the delivery of the column pressure vessels and plates. Before apparatus assembly could begin, components which were neither exempt from the pressure regulation PED such as the pipework and fittings nor delivered with certifications needed to be certified

before use. Accordingly, the author certified the plates and the heater block with the design by analysis route of EN-13445, the unified European unfired pressure vessel design code. It necessitates material evaluations, proof testing, and five design checks: gross plastic deformation, progressive plastic deformation, instability and buckling, cyclic fatigue failure, and static equilibrium. Representative documentation of this process is included in the appendices for the gas plate. Hydrostatic proof testing the plates required covering the plate openings with blanking plates which were provided by the column pressure vessel manufacturer after they had been used to hydrostatically test the column pressure vessels. Each plate was filled with hydraulic oil and pressurised to 300 bar, the code specified test pressure for an operational pressure of 200 bar. University insurers validated component testing and certifications but upon inspection of the hydraulic cylinder assemblies for the gas and liquid pump refused to give permission for them to be put into service. Although these components were meant to have arrived certified and ready for use, the manufacturer hadn't marked them correctly and upon further investigation hadn't used a design code in their manufacture, instead relying upon "industry experience". The author was able to partially correct this error by completing analysis of the components according to EN-13445, however owing to missing weld qualifications and material data the insurer only allowed them to be operated up to a pressure of 42.5 bar. The only solution to allow higher pressure operation accepted by the insurer was full replacement of both hydraulic cylinder assemblies, which neither time nor resources allowed. As a result of these restrictions the apparatus was unable to be operated at full 200 bar pressure, impacting the results presented in the following chapter. Following hydrostatic testing and documentation, apparatus assembly began.

Apparatus assembly started with the erection of a support gantry, which was designed by the author, fabricated off-site, and assembled by the author with assistance. The gantry is composed of two universal columns and a universal beam connecting the two columns at the top of the structure. Large angle iron was used to reinforce the structure and provide mounting points for the column pressure vessel assemblies which attached via tapped M20 holes in the liquid plate at the top of each column. A chain hoist on a movable beam clamp was attached to the top beam to raise and lower the pressure vessels, and the gantry was attached to the lab floor with 8 M20 anchor bolts. Given the mass of each column assembly (approximately 840 kg), the height of each column, and the restricted lab space, the design and erection of the gantry was challenging.

Assembly of the individual columns began by wrapping the insulating ceramic fibre blanket around the stainless steel column sleeve and inserting the sleeve into the column pressure vessel. The bottom stack of plates of the top column were next attached to the column pressure vessel; all internals including gas distributor, packing support, and internal insulation were in place. The twelve M39 bolts in the plate stack and flange assembly were torqued according to the flange standard using a heavy duty torque wrench, after which the column was tilted to near vertical, RTDs were inserted from the bottom of the column, and the packing material poured into the column interior. The top column top stack of plates were then added to the column assembly with all internals, and the top set of bolts similarly torqued to the code specified value. The top RTDs were then inserted into the column, shifting packing out of their path in the process. Notably, some radial positioning error in the RTDs undoubtedly occurred owing to the flexible nature of the 6.0mm RTDs, the longest of which was 1150mm. The column is designed to provide radially uniform flow and thermal conditions (a prerequisite to the use of the 1-D finite volume model discussed in Chapter 4), so the potential radial positioning error is not considered to be significant unless a probe were in contact with the column wall. If column wall contact occurred, the measured temperature for a given axial position would likely be slightly below bulk gas and liquid temperatures owing to conduction along the column wall. It is not likely that extensive wall contact occurred as probes were positioned sufficiently far from the column wall to account for positioning uncertainty. Limited axial positioning errors could have occurred owing to radial displacement. For example, a 100mm deviation from vertical in the 1150mm probe would result in an axial positioning error of 5mm, which is not significant relative to the column length and therefore these errors are not subsequently considered. The column assembly was next lifted to the top of the apparatus gantry, and the column was secured to the gantry with four M20 bolts. The assembly process was repeated for the bottom column. Gas and liquid pumps, the heater, pipework and water-jacket were all subsequently installed.

Commissioning initially focused on the calibration of the gas and liquid pumps. Piston motion profiles were programmed into linear actuator motor controllers, and this motion profile was translated into a fluid flow rate for control and data recording purposes. The average liquid pump flow was verified at atmospheric pressure by disconnecting tubing from the pump and directing the liquid flow into a container; by measuring the liquid volume and timing the test, and average liquid flow was produced which agreed with the predicted flow. All RTDs and pressure sensors were

connected and tested, and were used to verify fluid flow within the apparatus. All tapered threaded joints were painted with a heat-curing high-temperature thread sealant and baked to cure, necessitating the use of temporary heaters. A detailed leak check was performed on the apparatus, first utilising a hydrogen tracer gas and later using a soap-bubble method. A significant number of leaks were initially encountered owing to faulty high temperature thread sealant, likely expired or improperly stored. A slightly less robust but room temperature curing sealant was used to replace the failed joints, requiring fitting removal and laborious cleaning on half of apparatus joints. This introduced some delay to the commissioning process. Heater control was tested and the PID loop was tuned, and the water-jacket was leak tested. With the experimental apparatus operational, the experimental campaign began and is documented in the next chapter. Several photos of column components and the fully assembled apparatus are shown in Figures 6.11, 6.12, 6.13, 6.14, 6.15, and 6.16. Further design drawings are provided in the appendices.

Figure 6.11: 16mm stainless steel Pall ring random packing used in both columns.

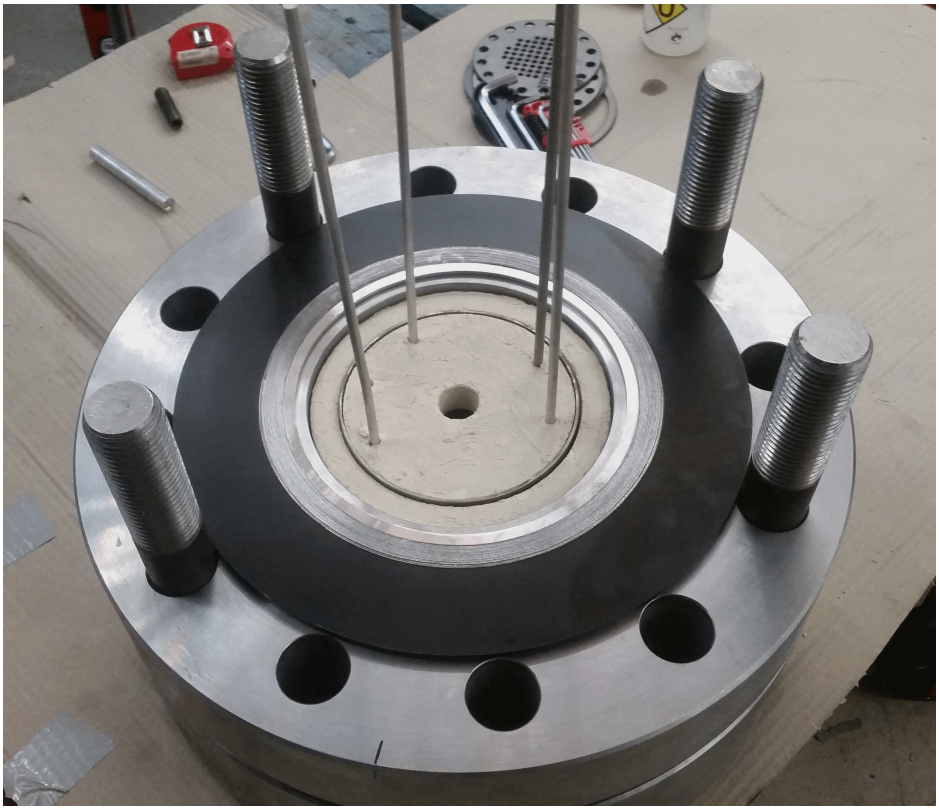

Figure 6.12: Partially assembled plate stack showing internal insulation with holes for RTDs, graphite spiral wound gasket and four M39 bolts.

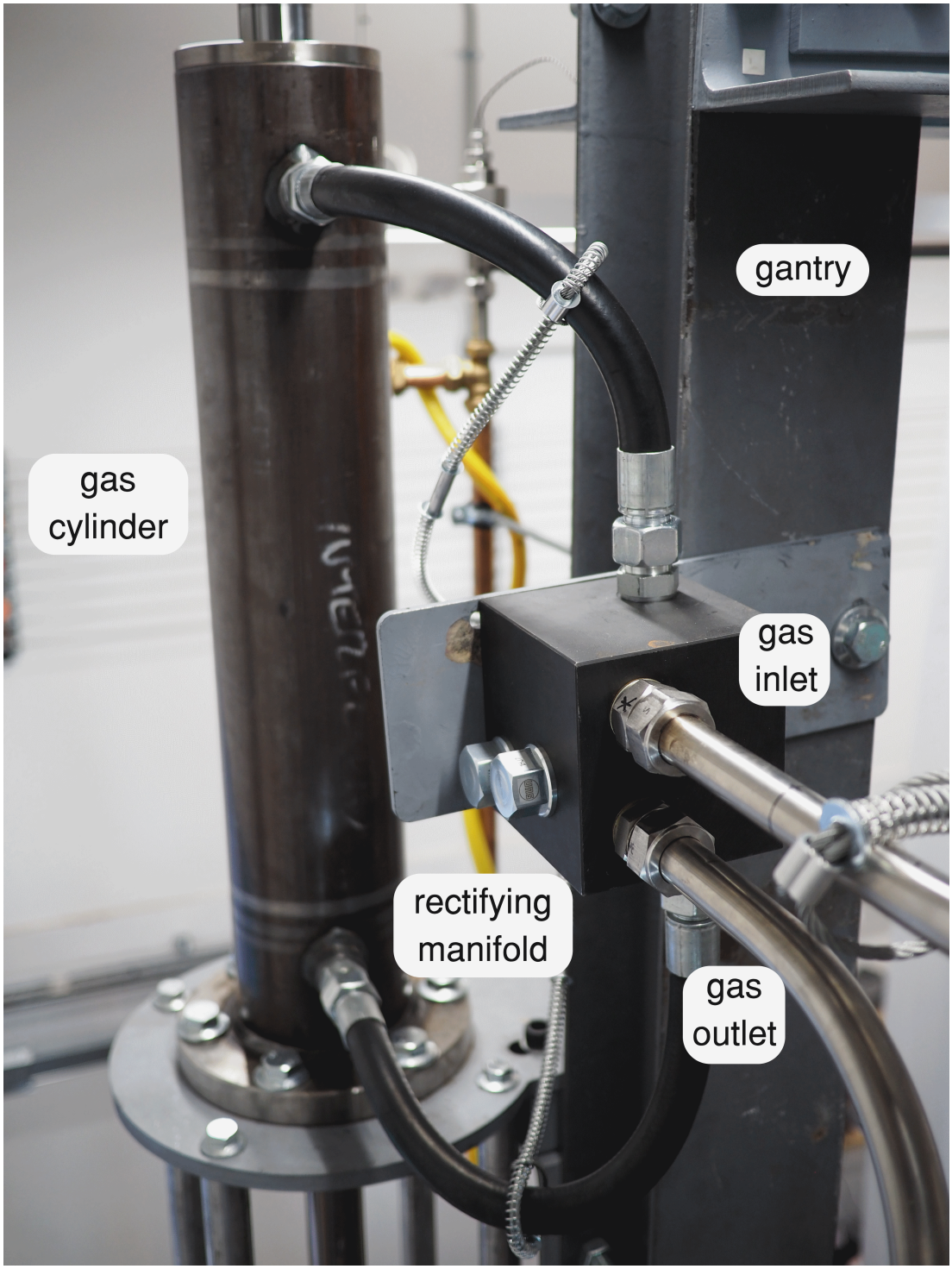

Figure 6.13: Positive displacement gas pump, showing gas cylinder, rectifying manifold, and connecting pipework. Linear actuator and servomotor are not shown but are visible in Figure 6.16. Hoses connect the manifold to the cylinder owing to the tight geometry.

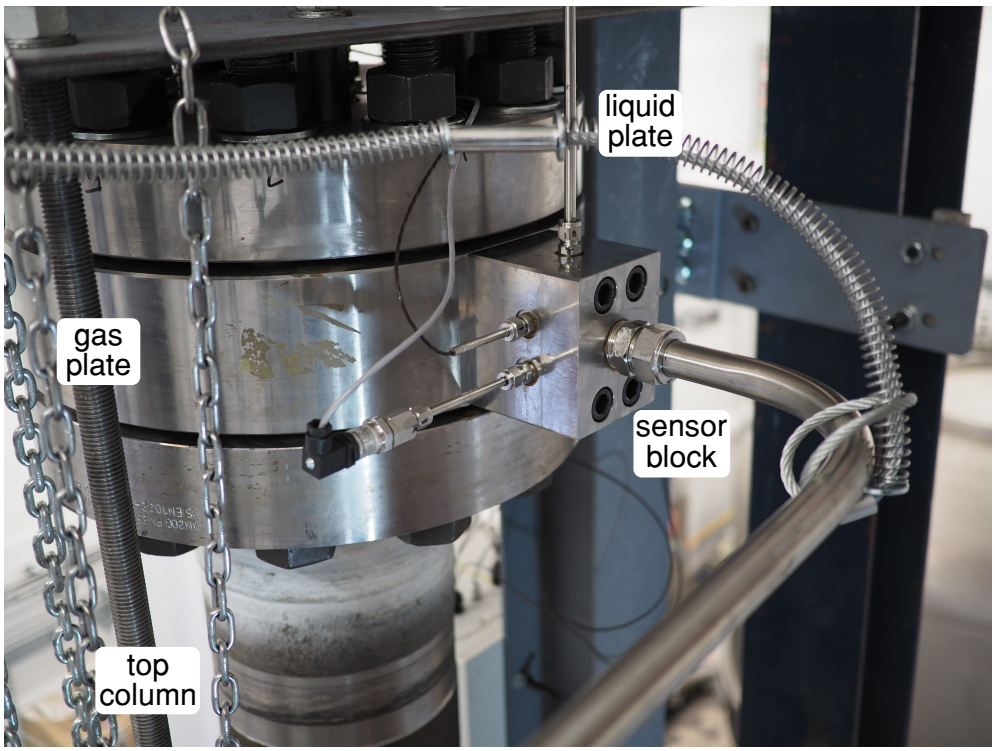

Figure 6.14: Top of top column, showing liquid plate, gas plate, sensor block, and column. Pressure and temperatures sensors are visible in the sensor block.

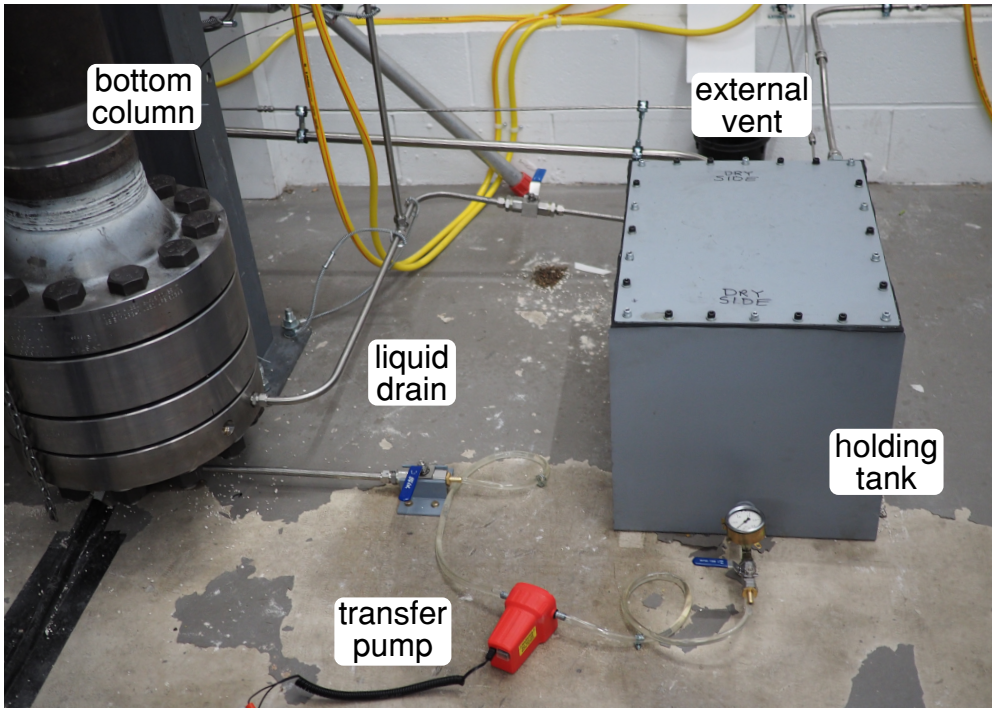

Figure 6.15: Apparatus support components including liquid holding tank, transfer pump, and external vent.

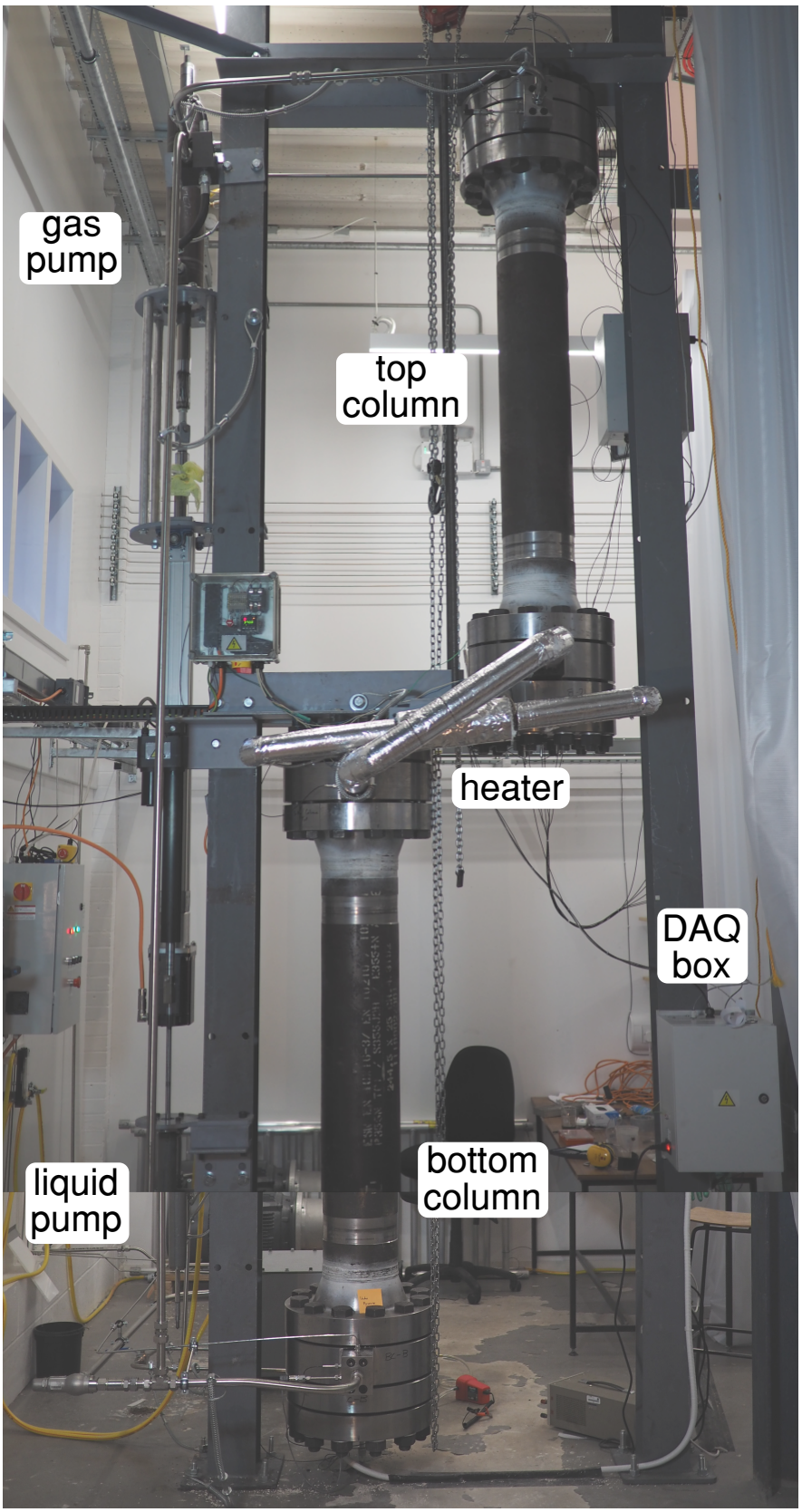

Figure 6.16: Composite image of the fully assembled experimental apparatus showing both columns, insulated pipework and heater between the columns, the gas and liquid pumps, and several data acquisition boxes. The water-jacket is obscured by the left gantry column.

Chapter 7

Experimental Results

In this chapter, the results of the direct-contact heat exchanger apparatus experiments are analysed. Apparatus performance is appraised, and the Log-Mean Temperature Difference method is used to determine an approximate overall heat transfer coefficient of each column in the apparatus under varying conditions. Column performance is then compared with the finite volume heat transfer MATLAB model, and measurements of column flooding are compared with existing models.

7.1 Data Collection

Experimental trials using the pilot column apparatus described in the previous chapter were conducted by the author to fulfil the objectives set out in the experimental design: quantification of column overall heat transfer coefficients U_h, measurement of column temperature profiles, and quantification of column flooding points. Eight trials with an average duration of nine hours each were conducted, including an approximately three hour start-up phase and excluding a cool-down phase which was not recorded. Several additional trials were conducted but are excluded from the data examined here owing to interruptions in data recording or apparatus leaks. Before a detailed analysis of the experimental results to determine U_h and the flooding point are presented, the apparatus performance is assessed over the course of one typical experimental trial. The purpose of this assessment is to evaluate apparatus performance to provide context for the data which it has produced. In the typical trial considered the apparatus is pressurised to 15 bar, heated until it achieves steady state gas and liquid temperatures, and then the gas volume flow-rate is progressively increased until flooding is detected. This was the same procedure performed on all trials, and column temperatures, trial length, and

gas flow-rates are similar between trials. The liquid flow rate is the same across all trials, and was chosen from the pilot column scaling procedure outlined in Chapter 4. This procedure follows the experimental plan set out in the previous chapter. Figure 7.1 shows column temperature data for both the top and the bottom column over the course of the 15 bar trial. Ten probes are axially spaced in equal increments throughout each column, and four are used to individually measure incoming and outgoing fluid temperatures, two at the top and two at the bottom of each column.

The plot in Figure 7.1 shows the time history of the temperatures in both columns as they are first heated, tested at a sequence of increasing gas flow rates until flooding occurs, then cooled back to ambient. There are three distinct phases of operation visible, beginning with a start-up phase during which top and bottom column temperatures progressively increase while gas flow-rates are constant. In the next phase, the gas flow-rate was progressively increased, leaving the apparatus to operate for about 45 minutes after each flow-rate increase. This settling period was implemented by the author after initial trials showed the large amount of thermal inertia in the apparatus, and is characterised by temperatures asymptoting to constant values. In this trial the gas flow rate has been squentially increased five times in increments of about 1.5L/min; on the fifth increase the apparatus exhibits flooding and this flow rate is recorded as the flooding flow rate for the experimental trial. The temperature trends presented in the figure are readily observable when examined on a time scale of hours, however it proved difficult for the author to determine when flooding occurred in real time owing to the slow change of temperatures in the columns. Accordingly, all trials include further gas flow-rate increases after what would later be determined to be the flooding point. Once column temperatures declined for at least 45 minutes in both columns the onset of flooding was considered to be definitively captured in experimental data, further gas flow-rate increases stopped, and the experiment was concluded. This 45 minute period was validated after examination of the data from initial trials. The difficulty in determining apparatus behaviour during experiment operation was further complicated by transient temperature instabilities after each gas flow rate change, likely a result of the momentary pause in gas pump operation required to change speed. These instabilities are manifested in experimental data as small surges or dips in column temperatures; note the spikes in temperature at each gas volume flow-rate increase. The final phase of each trial was cool-down: the heater was switched off but the gas and liquid pumps were kept in operation to maintain flow through the columns, allowing the water-jacket and steady state heat loss to cool the apparatus back to ambient temperature. The first

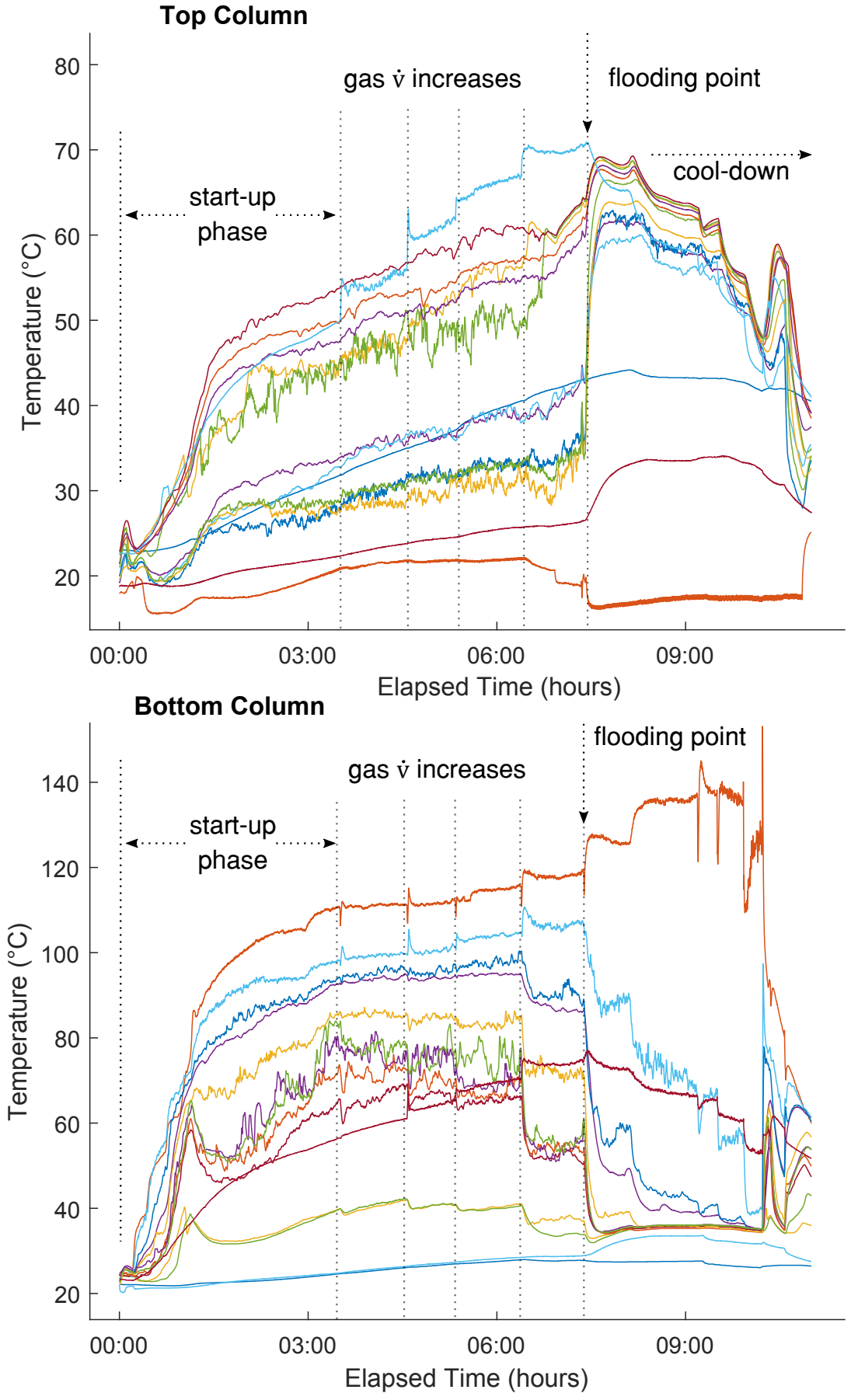

Figure 7.1: Plot of column internal temperatures measured by 14 RTD temperature probes in each column assembly. This trial was conducted at 15 bar and start up, gas volume flow ($\dot{v}$) increases, and flooding are shown.

hour of the cool down phase was generally recorded, after which all pumps and systems were shut down and the apparatus finished cooling overnight.

Although Figure 7.1 shows expected column temperature trends under varying experimental conditions, the magnitude of temperatures within the columns were lower than the experiment design temperature by a significant margin. In this trial, the hottest temperature in the bottom column reached around 120°C, and the hottest in the top column reached around 70°C. Both are a significant distance away from the design temperature T_H of 370°C. Temperatures in the bottom column increase slightly above 120°C after the onset of flooding due to restrictions in liquid flow through the heater, but this is not experimentally helpful. The low column temperatures were likely the result of two factors: high steady-state heat losses and inadequate heater performance. Heat was lost to the lab environment both directly through exposed piping and indirectly through the large thermal masses of the apparatus pressure vessels. Relative to the thermal capacity of the gas and liquids contained in the apparatus, the thermal capacity of pressure vessels are several orders of magnitude greater. As discussed in Chapter 6, the gas and liquid flows within the columns were insulated from the pressure vessels using custom fabricated internal insulation. The operational performance of this insulation could not be ascertained by the author without apparatus disassembly, however significant temperature increases were observed in several pressure-bearing components that had been designed to remain thermally isolated from the process fluids. Heat losses to both the lab and to the pressure components are shown in Figure 7.2, where elevated temperatures can be observed in the column pressure vessel, bolts, sensor block, and liquid pipework. If the internal insulation had performed adequately, it is likely that the magnitude of these elevated surface temperatures would be less. The majority of heat leakage appears to have occurred at the ends of the columns rather than along the column length, indicating that the main heat loss source was the Super-Wool internal insulation, rather than the ceramic fibre blanket which runs the length of the column. The exposed pipework shown was the result of insulation removed during commissioning to diagnose a joint leakage which had caused a high temperature Paratherm mist to form. The insulation was left off for all experimental trials to ensure any leaks could quickly be observed. Uninsulated pipework was calculated to contribute about 100W of heat loss, making this small section of exposed piping an insignificant heat sink.

Steady-state thermal losses, although clearly a significant factor in apparatus performance, do not alone explain the low column temperatures. The liquid heater perfor-

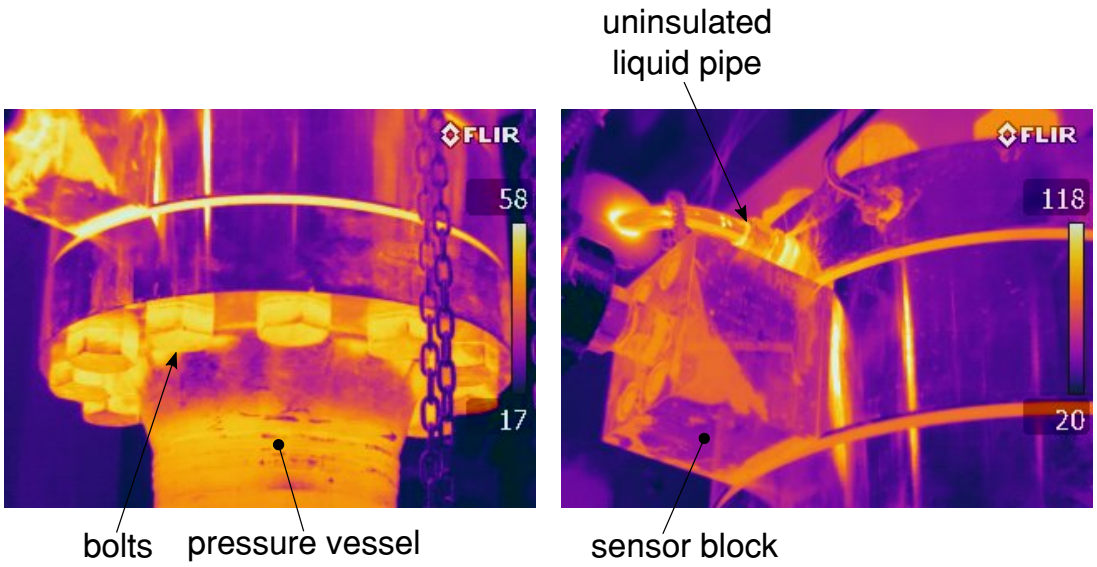

Figure 7.2: Two thermal images of the apparatus in operation; note differing scales in degrees Celsius. On the left, elevated bolt and pressure vessel temperatures are shown. On the right, an un-insulated liquid pipe and sensor block are visible. Vertical banding on plates are reflections.

mance is next examined; its operational performance during the 15 bar trial is shown in Figure 7.3. Note that the experiment milestones correspond to those shown in Figure 7.1. The heater mass, a round of stainless steel, is able to maintain a constant temperature at T_H after the start-up phase is complete. The liquid outlet temperature does not exceed approximately 120°C throughout the trial, and the liquid inlet temperature shows a slow increase in temperature, likely due to apparatus heating. Several conclusions about the heater can be drawn from this data. First, the heater mass is maintained at its set temperature of 370°C without significant deviation throughout the trial, indicating that the liquid heating demand never exceeded the available power of 4kW. This conclusion is confirmed by examining the Labview control data for the heater: it had a load-factor of around 35% during the trial, excepting the cool-down period. This indicates that the average heating demand was about 1.4kW during this trial. The relatively constant temperature difference between the liquid inlet and outlet indicate that the heating load was steady throughout the trial. These temperature profiles show that for the liquid flow-rate, heater size, and steady state losses, the convective heat transfer coefficient between liquid and heater was too low to effectively transfer the full heater power available. Steady-state thermal losses would be expected to increase with increasing apparatus temperature so it is difficult to predict if the full

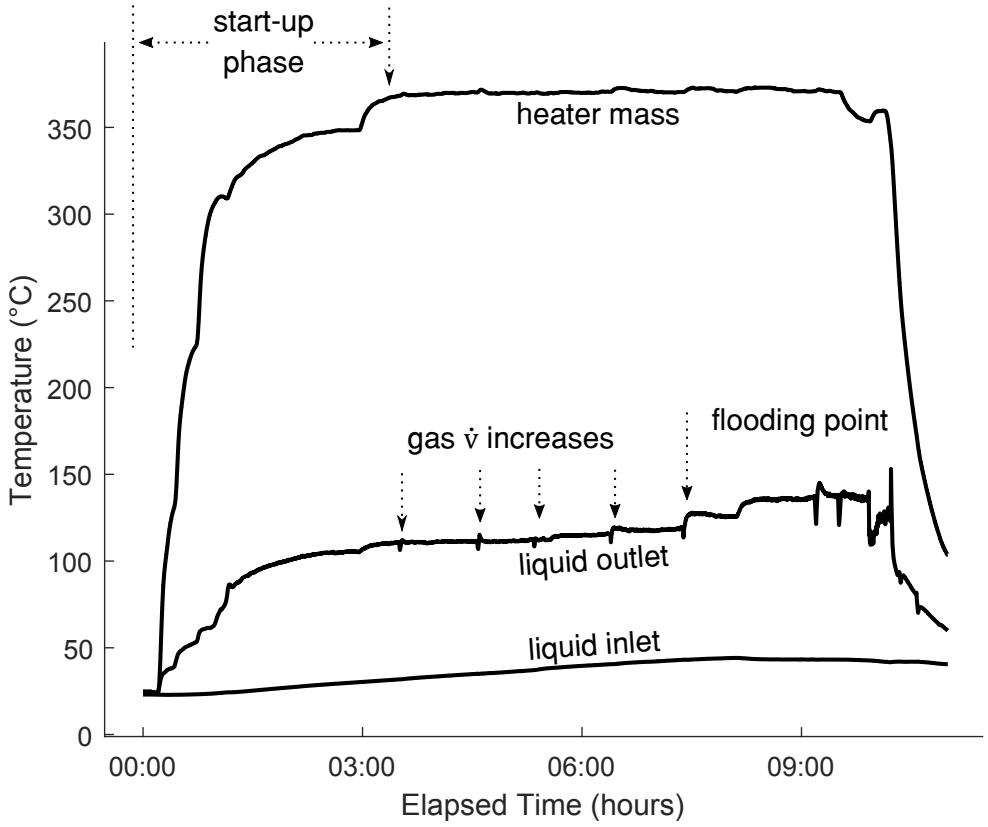

Figure 7.3: Electrical resistance heater performance in the selected experimental trial.

4kW of heater performance would be enough to heat the liquid to T_H, but reaching full heater utilisation would be a first step in improving performance. The Log-Mean Temperature Difference (LMTD) method, discussed in detail in the following section to quantify column performance, can also be used to analyse the heater. Utilising this method yields an average overall heat transfer coefficient of the heater $U_{h,H}$ of 150 W/m^2K for this trial, which is at the low end of the range for a liquid heat exchanger: 150-1200 W/m^2K (Roetzel and Spang, 2010). Assuming a 100°C temperature rise across the heater (which is currently shown in experimental results), if a liquid output temperature approaching T_H was desired, the heater would need a $U_{h,H}$ approaching 1750 W/m^2K for its size. Overall heat transfer coefficients of this magnitude are generally found in phase-change or direct contact exchangers, so in practice if a new heater were to be fabricated to provide a higher rate of heat transfer, it would require a larger heat transfer surface area such that more power could be transferred with little to no increase in $U_{h,H}$. Although no changes to the heater or insulation were made over the course of the trials presented here, evaluation of these components explains apparatus behaviour and informs future work.

Apparatus pressure control throughout the trial including initial pressurisation, experimental operation, and depressurisation were carried out generally in line with the experimental plan set out in Chapter 5. Apparatus pressure increased with temperature according to the ideal gas equations as was expected, although pressure rises were initially below expecations because the bulk of the gas within the apparatus did not reach the heater temperature of T_H, 370°C, or even the heater liquid outlet temperature of 120°C. Initial calculations had expected a pressure rise proportionate to a bulk gas temperature equal to that of the heater liquid outlet temperature; once this calculation was adjusted to use a temperature probe at the midpoint of the top column it provided good agreement with measured pressures. The assumption that Nitrogen within the apparatus behaves as an ideal gas for the purposes of this calculation is therefore likely valid; the apparatus volume is relatively large, pressures are not excessively high and temperatures are above ambient. Commissioning testing lead the author to forgo these calculations in favour of a simpler method. The initial (unheated) apparatus pressure for each trial was set about 0.5 bar below the target pressure and this kept apparatus pressure within approximately 2 bar of the intended trial pressure. Strict pressure regulation using either ideal gas initial pressure calculations or selective gas venting during operation was not deemed necessary, as the analysis presented in the remainder of this chapter easily accounts for variations in pressure. Several leaks were visually detected during operation; in each case when this occurred the trial was ended, the data discounted from analysis, and the leak repaired. Although apparatus pressure was not as precisely regulated as originally envisioned, it had no negative effects on the experimental results.

The final aspect of apparatus performance to be examined is the water-jacket T_M heat sink, which used cold mains water to cool the liquid exiting the bottom column as it was pumped back into the top of the top column. This exchanger was designed to prevent liquid from entering the top column at temperatures above T_M; this condition could occur if liquid left the bottom column at an elevated temperature due to incomplete gas-liquid heat transfer. Several insights are obtained from the plot of the co-current water-jacket heat exchanger in Figure 7.4. First, the inlet water temperature varies over the course of the trial, likely due to mains water supply temperature variations. The water outlet temperature follows the inlet temperature with a relatively constant temperature difference, indicating that an approximately constant 95W is removed by the water-jacket exchanger throughout the trial. The liquid inlet temperature steadily increases from the beginning of the trial until the flooding point, indicating that

liquid circulation is disrupted when flooding occurs. The steady temperature increase in the liquid inlet temperature shows that under normal operation heat accumulates within the apparatus, an expected condition that the water-jacket addresses. The liquid outlet temperature fluctuates according to the water inlet temperature, and stays between 15°C and 25°C, an acceptable T_M range. The final point of interest in Figure 7.4 is the oscillation of the liquid outlet temperature visible from 7 hours and 30 minutes elapsed time onwards. When these oscillations were examined on a finer time scale, it was found that the period of the oscillations was identical to that of the reciprocating motion of the liquid pump. It is likely that as the apparatus operates, liquid accumulates within the packing material and internal insulation. Under flooding conditions, even more liquid becomes entrained in the columns. When this occurs, the liquid pump may not have a large enough reservoir of liquid to draw upon at the bottom of the apparatus, causing it to intermittently pump gas. The liquid outlet temperature probe is located at one of the highest points in the apparatus, and under these conditions would only transiently be exposed to the liquid after each pump stroke, causing the temperature oscillation. This oscillation does not appear within the columns themselves, probably due to the secondary liquid reservoir that the liquid distributor provides at the top of each column. These post-flooding oscillations do not affect the analysis of U_h or the flooding point, and given that the water-jacket liquid outlet temperatures were within acceptable margins throughout the trial, the water jacket is considered to have operated without fault.

While an initial review of the apparatus indicates areas where improvements could be made (particularly with regard to the heater), the author was obliged to continue the experimental campaign as-is in order to produce preliminary results within the time and resources allotted. The apparatus was therefore operated with the lower temperature ranges described, and at pressures up to 42.5 bar instead of full 200 bar pressure due to insurer restrictions discussed in Chapter 6. An analysis of the heat transfer within the columns is now presented.

7.2 Overall Heat Transfer Coefficient

As initially set out in Chapter 4, it was desired to quantify column behaviour for easy comparison with other heat exchangers. Either the column volumetric heat transfer coefficient with units of W/m^3K or the overall heat transfer coefficient U_h with units W/m^2K can be calculated. The volumetric heat transfer coefficient evaluates heat

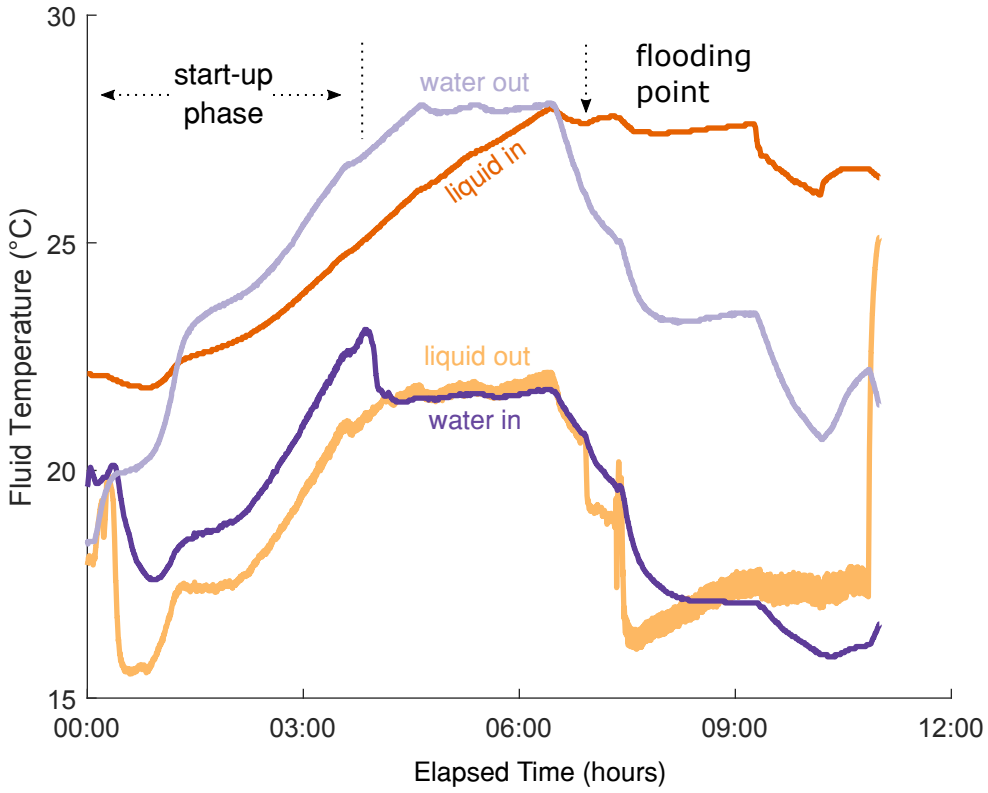

Figure 7.4: Water-jacket heat exchange performance in the 15 bar experimental trial. Note the exchanger operates cocurrently.

transfer against the internal volume of heat exchanger and is sometimes used in literature to evaluate direct-contact exchangers, while the overall heat transfer coefficient evaluates heat transfer against total heat exchange surface area and is widely used for most types of heat exchanger. The overall heat transfer coefficient is used in this analysis owing to its standardised use. The LMTD temperature difference method provides the basis for the calculation of U_h used here, and relies upon several important assumptions. First, it is assumed that the heat exchanger is fully insulated from its surroundings and axial conduction along the exchanger is negligible. Initial testing revealed heat leakage into pressure vessel components, however as shown in Figure 7.2 this heat loss is primarily concentrated in the column plates and ends of the columns, meaning it is reasonable to assume negligible heat loss along the length of the columns. Axial thermal conduction along the column is likely non-zero, but column temperature profiles in Figure 7.1 do not suggest that it is a dominant mode of heat transfer. If axial conduction were a dominate mode of heat transfer, spatially disparate temperature probes along the axis of each column would have very similar temperature profiles, while Figure 7.1 shows that the probes measure distinct, independent, temperatures.

Accordingly, these assumptions are considered to be reasonable. Next, it is assumed that fluid kinetic and potential energy changes are negligible, a widely held assumption for heat exchangers. This is an acceptable assumption for this apparatus due to the greater magnitude of energy changes in the fluids caused by temperature changes compared with changes in kinetic energy (due to fluid velocity variation) or potential energy (due to height or pressure variation). Finally, the LMTD method assumes fluid specific heat values and the overall heat transfer coefficient U_h are constant. Taking fluid properties at a T_M of 30°C and at the highest recorded column temperature of 150°C reveals little c_p variation. For the liquid, Paratherm, c_p varies between 1.74 and 2.08 kJ/kgK, while for the gas, nitrogen, c_p varies between 1.09 and 1.05 kJ/kgK. These variations are not considered to be significant for this analysis; however variation in U_h caused by other fluid property changes with temperature may potentially be significant. The Nitrogen density (using properties calculated at 20 bar) varies between 263 kg/m^3 at T_M and 52.5 kg/m^3 at 150°C, affecting the nature of the fluid flow within the column and therefore the convective heat transfer coefficient between gas and liquid. The liquid viscosity varies by one order of magnitude, additionally affecting the fluid interactions. Gas viscosity and liquid density do not exhibit significant changes over the same temperature range. Despite this potential variation in U_h caused by fluid property variations, this assumption is accepted so that the LMTD method may be used to evaluate the exchangers. It is a robust and straightforward method of heat exchanger analysis, and was considered superior to other options in this context even given this assumption. The ε-NTU method of heat exchanger analysis, a common alternative to the LMTD method, relies on the same assumptions regarding U_h and c_p (Incropera, 2007) and therefore provides no benefit over the LMTD method. For this reason, the LMTD method was preferred. If separate measurements of gas and liquid temperature could be made within the columns, a more precise piece-wise LMTD method could be employed which would have a more-constant U_h, however given the packing and temperature probe geometry this is not possible in the apparatus. More advanced methods of heat exchanger analysis either include specific geometries which do not encompass direct-contact exchangers, or require CFD which the author concluded would not produce confident results in this context without significant additional work.

The derivation of the LMTD method is not presented here and is widely available in literature such as Incropera (2007). Two equations, shown below, are utilised for the LMTD method.

$$q = U_h A \, \Delta T_{lm} \tag{7.1}$$

where q is the heat transfer rate, U_h is the overall heat transfer coefficient, A is the surface area of heat exchange, and ΔT_{lm} is the log-mean temperature difference, given as follows:

$$\Delta T_{lm} = \frac{\Delta T_1 - \Delta T_2}{\ln(\Delta T_1 / \Delta T_2)} \tag{7.2}$$

In the case of a counter-current heat exchanger, found in both apparatus columns and the heater block, the temperature differences are defined as:

$$\Delta T_1 = T_{h,1} - T_{c,1} = T_{h,i} - T_{c,o} \tag{7.3}$$

$$\Delta T_2 = T_{h,2} - T_{c,2} = T_{h,o} - T_{c,i} \tag{7.4}$$

where h and c refer to the hot and cold streams, 1 and 2 refer to ends of the exchanger, and i and o refer to inlet and outlet (Incropera, 2007). Substituting in the temperature probe locations found in the apparatus yields:

$$\begin{aligned} Top \quad Column: \quad & \Delta T_1 = TCB_G - TCB_L \\ & \Delta T_2 = TCT_G - TCT_L \\ Bottom \quad Column: \quad & \Delta T_1 = BCT_L - BCT_G \\ & \Delta T_2 = BCB_L - BCB_G \end{aligned} \tag{7.5}$$

where TCB and TCT refer to the 'top column top' and 'top column bottom' apparatus locations respectively, and BCT and BCB refer to the 'bottom column top' and 'bottom column bottom' locations respectively. Subscripts G and L refer to the gas and liquid respectively. Note that the hot fluid changes between the columns: in the bottom column, liquid which has just been heated enters the column, and is therefore the hot fluid, while in the top column gas which has just been heated in the bottom column enters the top column and is therefore the hot fluid. With ΔT_{lm} now fully defined, the remaining terms in Equation 7.1 can be addressed. The heat transfer rate q is defined in a similar manner to Equation 4.6 for an incompressible substance:

$$q = \dot{m} c_p \Delta T \tag{7.6}$$

where ΔT refers to the change in temperature across the heat exchanger of the fluid, and $\dot{m}$ and c_p are fluid mass-flow and specific heat. Either the gas or the liquid can be used for the calculation of U_h in principle, however the density and specific heat of the liquid are more stable than that of the gas across the temperature ranges found in the packed columns, and therefore are used for analysis. The final undefined variable in Equation 7.1 is A, the heat transfer area. It is defined as the specific surface area a of

the packing multiplied by the column internal volume V. This approximation was used in Chapter 4, and is based upon the assumption that the liquid fully wets out across the packing, and gas-liquid heat transfer takes place uniformly across the whole packing surface area.

In order to account for small variations in column performance over the course of a trial, a steady-state phase was established for each trial consisting of the time between two speed increases before the flooding point and the flooding point. In practice, the apparatus was left for about 45 minutes after each gas volume flow-rate increase before flow-rate was increased again, so this steady state period is about 90 minutes for most trials. In all cases, the author avoided including operation during the start-up phase or after flooding as part of steady state operation. For each data point in the steady-state phase, the LMTD and U_h value of each column were calculated, where U_h is found by rearranging the previously discussed equations:

$$U_h = \frac{\dot{m} c_p \Delta T}{a V \Delta T_{lm}} \tag{7.7}$$

U_h was then averaged over the steady-state time period for each trial, and this value used to represent the trial. A plot of U_h against system pressure is shown in Figure 7.5, noting that each experimental trial represents one operating pressure. The magnitude of U_h shown in this figure was substantially less than originally envisioned for the experimental apparatus, with an average value of 5.86 ± 0.17 W/m^2K for the bottom column and 1.77 ± 0.17 W/m^2K for the top column. These values would be expected of heat transfer between gases in free convection (Engineers Edge, 2000), but are well below what would be expected of the forced flow and boundary surface conditions found within the columns. At a minimum, it was hoped that these values would meet or exceed U_h values found in high pressure gas and liquid shell and tube heat exchangers, 200 to 400 W/m^2K. The low experimental U_h values are likely due to the fact that relative to the heat transfer surface area, the heat transfer power was small. There are several possible explanations for this situation, the first of which is that the column is oversized, either in diameter or length, for this application. Although experimental results do not yield data which can be used to judge the suitability of column diameter, Figure 7.9 provides insight into the length of the columns. At 300mm and 900mm column displacements discontinuities in the column temperature profiles are evident, potentially indicating that the remaining near-ambient temperature sections of the columns are not performing useful heat exchange. In the bottom column this accounts for 300mm of un-used column length, while in the top column it ac-

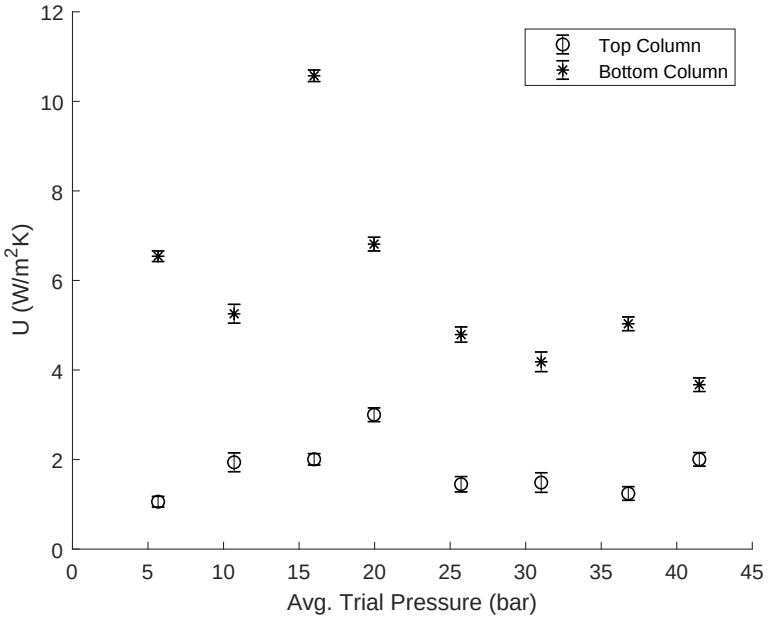

Figure 7.5: Overall heat transfer coefficient U_h for experimental trials against trial pressure. Experimental uncertainty is shown using error bars.

counts for 800mm of un-used column. Recalculating U_h for both columns removing the unused sections of column yields marginally improved heat transfer coefficients of $7.33 W/m^2K$ for the bottom column, and $3.8 W/m^2K$ for the top column. Although these values are improvements on earlier calculations, they are still far below expected values. Another explanation for low values of U_h is the low pressure at which the apparatus was operated at relative to its design parameters, the density of N_2 nearly quadruples between the max pressure of 42.5 bar used here and the design pressure of 200 bar. This density increase would increase the gas mass-flow for a given pumping rate, increasing the ability of the gas to absorb heat from the liquid and therefore the heat transfer rate q. According to Equation 7.6 U_h would be expected to increase linearly to changes in N_2 density (if $\rho\dot{V}$ is substituted for $\dot{m}$), however it is difficult to confidently predict if this change in U_h would occur owing to N_2 flow rate adjustments which would likely be needed to account for increased flooding effects at higher pressures.

The experimental uncertainty of U_h was determined using the root mean squares error propagation method as discussed by Pintar (2001). Uncertainty primarily originates in random error from the RTD temperature probes; the manufacturer specifies a tolerance of $\pm 0.80°C$ for the temperature range found within the columns. This exper-

imental error propagates through the calculation of column ΔT_{lm} and ΔT, affecting U_h. Examining the remaining variables for the calculation of U_h in Equation 7.7, c_p (specific heat), a (packing specific surface area), and V (column volume) are considered to be exact values for the purpose of this analysis, while liquid mass-flow rate $\dot{m}$ requires further scrutiny. Liquid mass-flow from the positive-displacement pump is calculated by dividing the mass displaced per stroke by the average stroke time:

$$\dot{m}_l = \frac{v \cdot \rho}{t} \tag{7.8}$$

where v is the internal volume of the liquid piston, ρ is the liquid density, and t is the time for one stroke, adjusted for turn-around time. v and ρ are known precisely enough to be considered exact for these calculations, while t was affected by measurement error. The linear actuator driving the liquid pump does not provide real time position data, so the time for one stroke was measured by several times, and an average of the measured values was taken and used throughout the trials. A tolerance of ± 0.30s is used to quantify error in measured stroke time, based upon average human reaction times (Jain et al., 2015). This error propagates to $\dot{m}$, which is then incorporated in the calculation of δU, the uncertainty in U_h. Notably this measured value was supported by a liquid temperature oscillation near the pump shown in Figure 7.4. The full derivation of error propagation of temperature and $\dot{m}$ measurements to produce an uncertainty value for U_h is not presented here owing to the length of these calcuations, however note in Figure 7.5 that this uncertainty is not constant across trials - it varies with the magnitude of measured temperatures.

Figure 7.5 shows no discernible relationship between apparatus pressure and U_h; an examination of Equation 7.7, which defines U_h, shows that a relationship is not directly expected. The terms of this equation are $\dot{m}$, c_p, a, V, ΔT and ΔT_{lm}. Liquid massflow was set to be constant throughout all trials, and no significant temperature variations were observed in the (constant volume) positive displacement liquid pump which could have caused variation in liquid density and therefore liquid massflow. Liquid specific heat has no significant variation with temperature in this range, and column internal volume V and packing specific surface area a are constant. Variations in ΔT and ΔT_{lm} as a result of pressure changes alone are unlikely, but are examined here for the sake of completeness.

Consider first ΔT, the liquid temperature change across each column. Figure 7.6 shows variations in ΔT of both fluids across the experimental trials, noting that only the liquid ΔT values are used in this analysis. No systematic change in any fluid ΔT

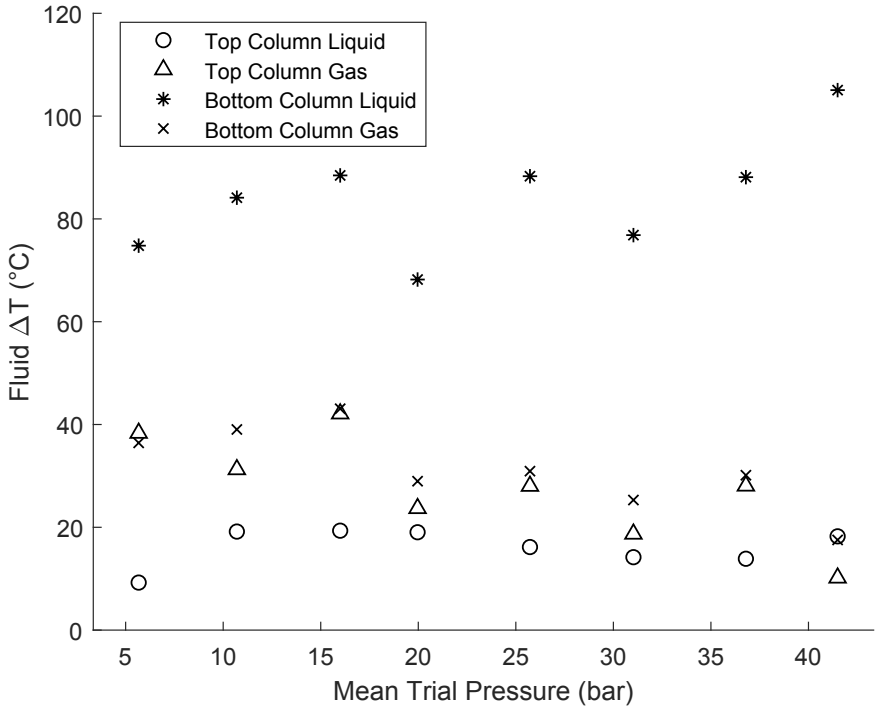

Figure 7.6: Gas and liquid temperature differences across both the top and bottom columns. Note that error bars reflecting measurement uncertainty have been omitted for clarity as uncertainty is much less than measured values.

with pressure is evident. The bottom column liquid ΔT is significantly greater than other values; this is due to the previously discussed positioning of the heater. Note that experimental uncertainty of measured temperatures has been omitted in Figure 7.6 for clarity and is omitted in subsequent figures for the same reason.

Although not used in the calculation of U_h, a brief examination of the gas ΔT values shown in Figure 7.6 reveals a considerably lower ΔT for the bottom column, and a slightly higher ΔT for the top column compared with liquid values. These differences are the result which fluid is considered to be the 'hot' fluid in each column. In the bottom column the hot fluid is the liquid because heat is transferred from the liquid to the gas; in the top column the hot fluid is the gas because heat is transferred from the gas to the liquid. As a result, the previously reported U_h values would likely be slightly higher for the top column if calculations were instead based upon the gas, which is the hot fluid for this column.

ΔT_{lm} is the final variable in Equation 7.7 to be examined for a relationship with operating pressure to attempt to explain the variations in U_h shown in Figure 7.5. It relies on two sets of temperature differences for each column, and each temperature

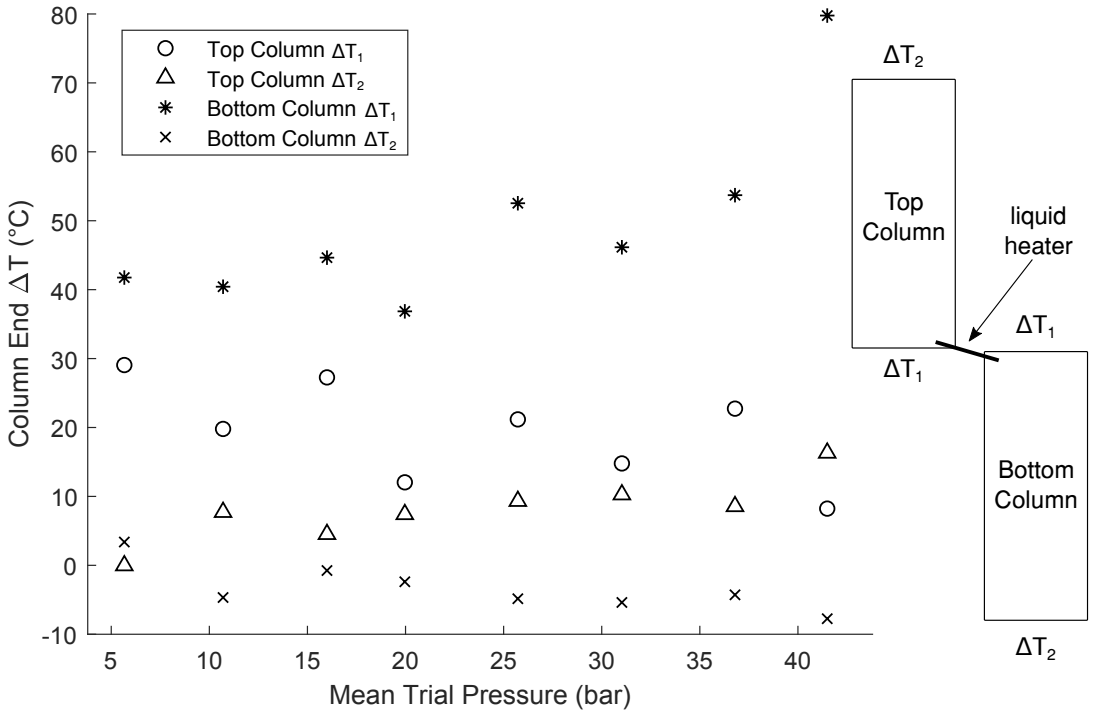

Figure 7.7: Temperature differences of fluids exiting and entering columns as used to calculate the LMTD. On the right, the location of the temperature differences is shown.

difference describes one end of the column. The convention for labelling the 'hot' and 'cold' fluid streams for these temperature differences are given in Equations 7.3 and 7.4. Figure 7.7 shows the variation in ΔT_1 and ΔT_2 across trials and the location of each ΔT in the apparatus. Similar to the previously discussed liquid temperature differences, the highest temperature differences used to calculated the LMTD occur between incoming and outgoing fluid streams just after the heater. The second highest temperature difference occurs between the incoming hot gas and outgoing liquid in the top column, while the ends of both columns at T_M show similar low temperature differences. No relationship between ΔT_1 or ΔT_2 and pressure was found, and therefore no relationship in the presented experimental data between ΔT_{lm} and pressure was found.

With no obvious relationship between U_h and system pressure determined by examining Equation 7.7, other variations in apparatus parameters were examined to determine whether they may have caused changes in U_h. The effect of pressure on the column flooding point is examined later in this chapter, and the experimental procedure to determine the flooding point may have affected the calculation of U_h. In order to find the flooding point, the gas volume flow-rate is increased at several points in

time throughout a trial until the column floods. Because the steady state analysis period used to determine U_h is the period of time encompassing two flow-rate increases before the flooding point, and because the flooding point varies significantly between trials, the gas volume flow-rate differs significantly between the trials. This relationship was examined by plotting U_h as a function of gas volume flow-rate for all trials and no trend was apparent, discounting the possibility of a relationship between gas $\dot{v}$ and U_h. As mentioned previously, liquid flow-rate was kept constant and the heater was set at the same operating temperature T_H across all trials. Experimental time before the flooding point was not constant between trials; the start-up phase did not vary however the number of gas volume-flow increases before flooding varied according to the closeness of the author's initial gas volume-flow guess to the flooding point. The initial gas volume-flow was meant to be two to three gas flow-rate increases below the flooding point, and the expected flooding point was predicted based upon results at the previous pressure setting. These predictions were closer in some trials than others, so some trials required more gas volume flow rate changes (and associated stabilisation time) than others. U_h was plotted as a function of experimental time before flooding to determine whether trial time differences explained variations in U_h, but no relationship was found and the plot is omitted as it does not meaningfully contribute to this analysis. ΔT and ΔT_{lm} were similarly compared with operational time before flooding, but no relationship was apparent. The author therefore concludes that the variations in U_h found in the presented experimental trials are likely the result of random experimental variation: water-jacket mains water inlet temperature changes, varying amounts of liquid entrainment before flooding causing fluctuations in liquid $\dot{m}$ within the columns, and random variation in gas and liquid movement within the columns affecting measured temperatures. The last two effects merit further discussion.

Partial liquid entrainment occurs when the gas flow-rate in the columns is sufficiently high to slow liquid movement under the influence of gravity, but not high enough to cause full flooding conditions to develop. Its effects are not uniform across experimental trials, and is the result of the large incremental change in gas flow-rate necessitated by the experimental method to quantify column flooding point. Consider two experimental trials: In the first, no flooding metrics are visible so temperature profiles are constant, the gas flow-rate is increased, and the column decisively floods. In the second, the same initial conditions are apparent however upon increasing the gas flow-rate temperatures partially converge but full flooding conditions do not develop. The second condition requires a further gas flow-rate increase before flooding occurs,

so data where some temperature convergence is present is used to calculate U_h. The partial temperature convergences indicate liquid entrainment, which will reduce liquid $\dot{m}$ through the columns, even when liquid pump $\dot{m}$ is unchanged.

Random variation in gas and liquid movement within the columns affects temperature measurements of the liquid, which unlike the gas does not expand to fill the volume which contains it. The liquid randomly moves through the packing under the influence of gravity and establishes preferential flow paths. Once a flow path is established it is likely maintained unless disrupted, and flow paths are newly established in each trial. If a liquid flow were to establish a path substantially avoiding RTD probes in one trial and following them in another, two differing temperature profiles would result. Differing temperature profiles would cause differing U_h values to be calculated. It is difficult to prove this effect from the experimental data collected, it would be helpful to quantify this variation by conducting repeated trials under the same operational conditions and comparing the temperature variation between identically placed probes across the trials. Additionally, verification of liquid distributor performance (potentially using an ambient pressure clear column) would aid in identifying preferential liquid flow paths and potentially suggest improvements to liquid distributor design to avoid them.

The total range of calculated U_h values ($6\,W/m^2K$ for the top column and $2\,W/m^2K$ for the bottom) is narrow considering the magnitude of common values for high-pressure process heat exchangers of 200-400 W/m^2K. This suggests that the variations in U_h between trials presented here should not reduce confidence in the results. While the values of the overall heat transfer coefficient U_h were significantly less than originally anticipated, they nonetheless demonstrate that effective gas-liquid heat transfer took place within both experimental columns. Improvement of apparatus thermal characteristics in accordance with the first section of this chapter would likely significantly increase U_h.

7.3 Column Efficiency and Temperature Profiles

Although calculated overall heat transfer coefficient values were well below initial estimates, the preceding analysis suggests that this is the result of low pressure operation, poor heater performance, and high steady state losses, not a fundamental breakdown of gas-liquid heat transfer. All elevated temperatures present in the top column are a result of successful gas-liquid heat transfer in the bottom column, and the temperature profile developed in the bottom column similarly shows effective gas-liquid heat trans-

fer. Fluid output temperatures at the ends of the columns opposite the heater were both low, indicating successful heat transfer in both columns. Without substantial gas-liquid heat transfer, the bottom column would uniformly heat up and the top column would remain cold. The thermal power in each fluid flow calculated according to:

$$P = \dot{m} \cdot c_p \cdot \Delta T \tag{7.9}$$

where P is the thermal power, $\dot{m}$ and c_p are mass-flow rate and specific heat, and ΔT the change in fluid temperature across the column. Power was calculated for the liquid and gas in each column for each trial, yielding the following average values:

$$\begin{aligned} Top \quad Column: \quad & P_{T,L} = 0.19\ kW \\ & P_{T,G} = 0.14\ kW \\ Bottom \quad Column: \quad & P_{B,L} = 1.09\ kW \\ & P_{B,G} = 0.15\ kW \end{aligned}$$

These values are consistent with expected behaviour in a system with steady state losses and irreversibilities, and are worth briefly examining. $P_{B,L}$ is the power of the liquid flow entering the bottom column, it reflects 0.31kW of losses between the heater and the bottom column from the heater average output power of 1.4kW. $P_{B,G}$ shows 0.94 kW of loss between the liquid and gas flows, due to heat losses to the column and packing. $P_{T,G}$ shows 0.01 kW of loss as the gas travels from the bottom column to the top, as a result of heat loss to pipework. The bottom column heat transfer values follow expected behaviour; the liquid heat transfer rate is higher than that of the gas because the liquid is the hot driving fluid of the bottom column. The top column heat transfer rates appear to show non-physical results, as the heat transfer rate of the gas, which is the hot driving fluid for this column, is less than that of the liquid. The liquid cannot be heated at a greater rate than the rate at which the gas gives up its heat unless there are additional heat sources. The discrepant liquid heat transfer value is explained by examining the apparatus near the top column liquid output temperature probe used to calculated $P_{T,L}$. Inspection of thermal photography during apparatus operation revealed elevated temperatures in the liquid plate housing the probe consistent with temperatures observed in the top column liquid output, accounting for a higher than expected ΔT, and therefore power, of the liquid. Conducted heat from the heater block along the liquid pipework was responsible for heating the liquid plate.

Heat transfer efficiency is strongly influenced by the heat capacity rates of the fluids; heat capacity rate is defined as the product of the fluid mass-flow rate and fluid heat

capacity. Under highly efficient heat transfer conditions the heat capacity rates of both fluids are near equal, and all heat rejected from one fluid is absorbed at an equal rate by the other. In practice, thermal losses to the environment and thermal resistances to heat transfer occur, so although matching heat capacity rates is critical for efficient heat transfer, satisfying this requirement alone does not guarantee efficient heat transfer. It is common practice in heat exchanger design to ensure that the heat capacity rate of one fluid is significantly greater than the other to provide consistent exchanger output temperatures even under slightly varying mass flow-rates. This practice is not used in this apparatus owing to the paramount concern of heat exchange efficiency; variations in output temperature are tolerated in order to maximise efficiency. The present experimental apparatus was designed to allow for matching heat capacity rates of the gas and liquid operating at 200 bar, however at the 42.5 bar to which the apparatus was limited both the gas density and gas specific heat are significantly reduced when compared with conditions at 200 bar. The liquid density and specific heat are not significantly affected. As a result, for a fixed volume-flow rate, the heat capacity rate of the gas is significantly reduced at these lower pressures. Figure 7.8 shows the heat capacity rates of an experimental trial at 42.5 bar; note that the liquid heat capacity rate significantly exceeds that of the gas even though the heat capacity rate of the gas increases as gas volume-flow rate is increased. The gas volume-flow rate cannot be increased past the flooding point, so at these lower pressures the heat capacities can never approximate one another. Due to this mismatch, the gas cannot absorb or reject an equal amount of heat from the liquid, contributing to the low calculated efficiencies.

Heat transfer efficiency was calculated for the bottom column only due to the discussed inaccuracy in the calcuation of top column liquid heat transfer power. Defined as the cold fluid heat transfer rate divided by the hot fluid heat transfer rate, the efficiency was 13.9% averaged across all trials. Both efficiency and heat transfer magnitudes were below originally anticipated values due to high steady-state thermal losses. In considering column efficiency, the relative heat capacity of the fluids must also be considered to provide additional perspective. Similar to U_h, no trends were found in efficiency with varying pressures or experiment durations.

The next step in evaluating column heat transfer performance is to examine the temperature profiles within the columns, and compare them with profiles developed in models developed in Chapter 4. Figure 7.9 shows temperature distributions in both columns for the same 15 bar representative experimental trial discussed in Sections 7.1 and 7.2. Plotted points do not distinguish between gas and liquid temperatures except

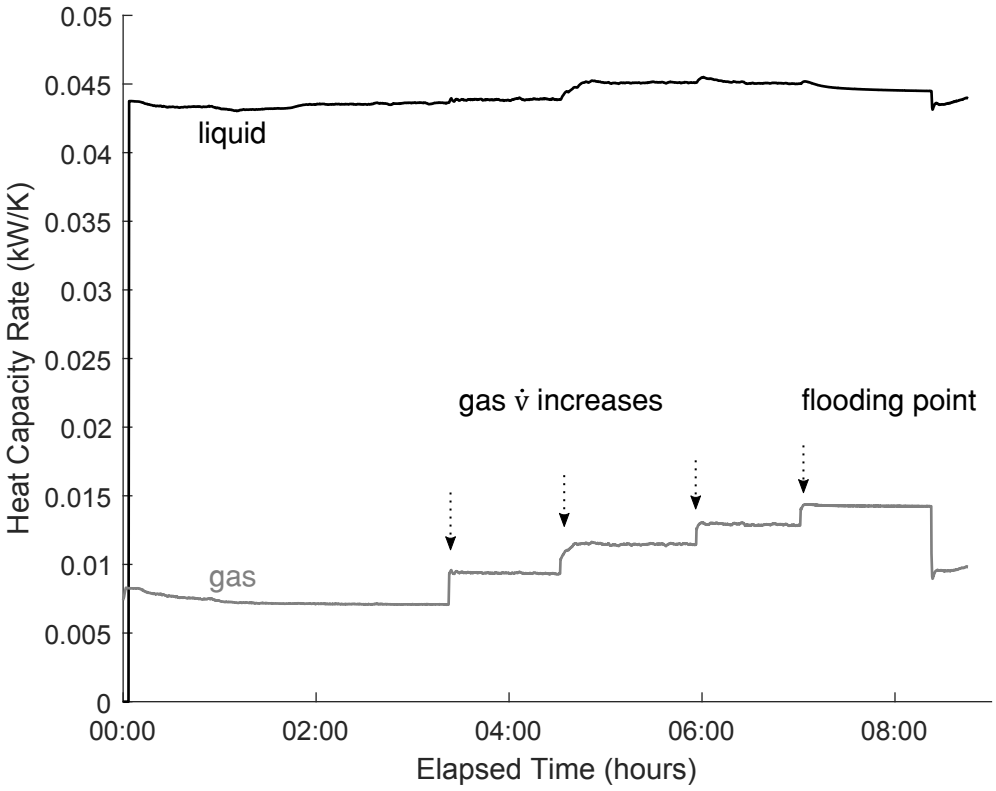

Figure 7.8: Comparison of gas and liquid heat capacity rates during a trial at 42.5 bar. Increases in gas heat capacity rate are due to increases in gas volume-flow.

where probes were able to independently measure the fluids in pipework, and arrows have been added showing pipework connections between columns and fluid flow direction. Both the top and bottom columns show approximately linear temperature profiles from high to low temperature.

In order to compare the experimental results with the finite volume heat transfer model set out in Chapter 4, each column was simulated using experimental conditions. The results of these simulations are plotted in Figure 7.9. The bottom column is simulated by assuming a T_H of the bottom column liquid inlet temperature and a T_M of its liquid outlet, while the top column is simulated assuming a T_H of the top column gas inlet and a T_M of the gas outlet. This model calculates packing, liquid, and gas temperatures individually, but packing and liquid values are very similar at each data point, so only the liquid and gas temperatures are plotted here. Visual inspection shows good model agreement with experimental results, showing a better fit to the bottom column temperatures than to the top. Note that the bottom column gas outlet temperature differs significantly from other bottom column temperatures indicating that measured column temperatures are dominated by the liquid. This follows logically as the liquid is the hot fluid in this column, driving the temperature profile within it. The top column has a more scattered temperature profile than the bottom, likely because the hot fluid is the gas; the velocity of which is more distributed across the column than the liquid. The top column liquid output temperature is similarly an outlier in this column indicating that the gas drives the temperature profile in the top column. Heat transfer rates of simulated columns agreed with experimentally calculated values within 15%, with the exception of the bottom column liquid rate. As discussed previously in this section, this heat transfer value was significantly affected by high steady state losses which were not incorporated into the model. Although no judgement can be made on model performance outwith the temperatures and pressure found across the trials in these experiments, the model did prove reliable in predicting experimental results and likely is a useful tool for future work in this area.

7.4 Flooding Point Estimation

The usefulness to the PHES project of the packed columns depends not only on their thermal performance, but also on their ability to operate across desired flow-rate ranges. Flooding is a phenomenon where gas forces liquid backwards in a packed column; as the gas becomes denser its molecules occupy a greater fraction of the column void,

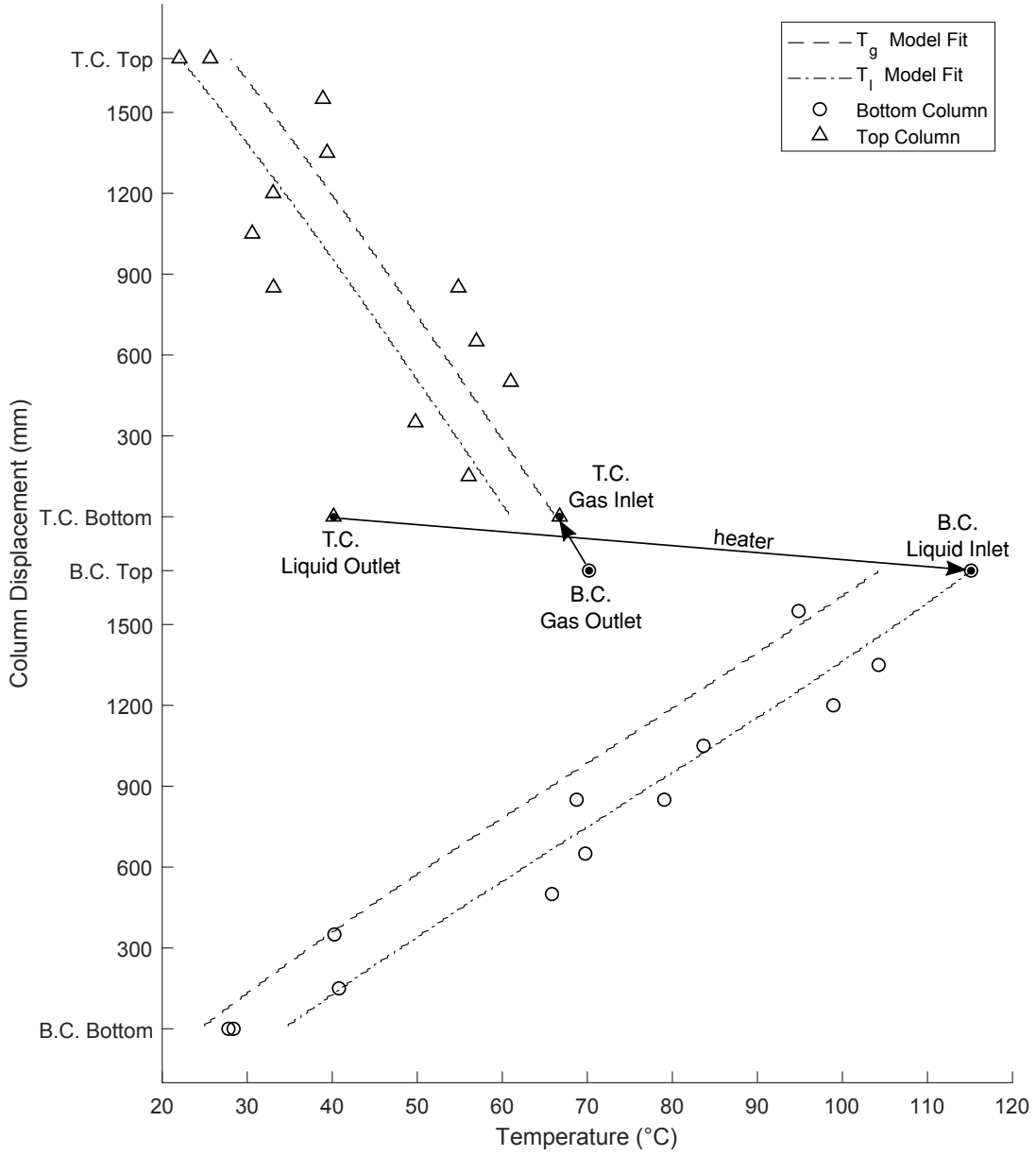

Figure 7.9: Temperature distribution within columns, with select points labelled and arrows indicating pipe connections between columns. A finite volume column model based upon fluid inlet temperatures is plotted for both columns.

increasing its propensity to affect liquid flow. Flooding causes a breakdown of packed column heat or mass transfer, and therefore must be avoided in normal operation. Flooding is the primary concern in the operation of direct-contact heat exchange in a packed column; although overall heat exchange coefficients tend to be high because there is only one heat exchange process rather than two to three in a conventional heat exchanger, fluid volume flow-rates can be limited due to flooding. Determination of the column flooding points across trials was made using the experimental procedures set out in Chapter 5. Although existing packed column models such as Stichlmair et al. (1989) can predict flooding, it is a useful quantity to characterise in this apparatus in order to verify the application of existing models at the elevated temperatures and pressures present in the experimental columns. Due to the restricted maximum operating pressure of the apparatus these results don't cover the full PHES operating range, however they allow the effects of increased system pressure to be explored. The onset of flooding is characterised by two metrics:

1. Breakdown in heat transfer within the columns visible in sudden temperature changes within the apparatus at the flooding point.

2. Development of a non-linear temperature profile due to the convergence of temperature values when flooding occurs.

The data sets recorded during experimental trials were analysed to determine the gas flow rate at which the onset of flooding was detected. A limitation in this experimental method is the incremental gas volume flow rate change; flow rates were increased in increments of 1.5L/min which was sufficiently large to obscure the precise onset of flooding in some cases. Given the 45 minute settling time, continuous variation was not practical. These incremental flow increases affect the precision of the reported data; potentially further trials could be conducted varying gas flow-rate with smaller incremental changes to quantify the flooding points more precisely.

Typical column conditions surrounding the flooding point are shown in Figure 7.10, revealing several interesting characteristics of column behaviour. First, note that the gas flow rate increase results in a transient spike in column temperatures in the top column, followed by a similar spike in the bottom column. These spikes are caused by the temporary interruption in gas flow caused by the gas pump linear actuator pausing to adjust speed; the time difference between the spike in the top column and the spike in the bottom column is about 60 seconds. The movement of the hot fluid in the top column (gas) is directly stopped then started while the hot fluid in the bottom

column (liquid) is only affected by the interruption in heat transfer, which is the likely cause of the time difference. The first flooding metric, sudden temperature changes within the columns, is most visible in the heater output and liquid input to the bottom column, labelled 'BCT liquid' in Figure 7.10. The sharp temperature rise is likely due to reduced liquid flow through the heater caused by flooding in the top column. Liquid is substantially entrained in the gas, blocking its downward flow, reducing the flow-rate through the heater and therefor increasing the outlet temperature.

The convergence of column temperatures is easily observable in the top and bottom columns, showing the occurrence of the second flooding metric. This temperature convergence is likely due to the columns filling with liquid, causing the collapse of the pre-flooding temperature profile. Within the column it is not known which fluid individual probes measure, likely some temperatures are closer to gas temperatures others are closer to liquid temperatures. Although the liquid distributor is intended to systematically spread the liquid across the whole cross sectional area of the column, preferential liquid paths undoubtedly develop and may concentrate around some RTD probes. Temperature convergence of the majority of probes is likely due to all probes measuring the same fluid, and, as the gas continues to move through the columns under flooding conditions, this fluid almost certainly is the liquid.

The flooding points of all experimental trials are presented in Figure 7.11 in which they are compared with the counter current gas liquid packed column flooding model proposed by Stichlmair et al. (1989) and discussed in Chapter 4. Results are presented with an experimental uncertainty of approximately ± 1.5 L/min, reflecting the incremental changes made to gas pump volume flow-rate. For each experimental trial, the average operational pressure during the steady state period is used to evaluate the Stichlmair model. Fluid properties are evaluated at an average column internal temperature of 80°C and the liquid volume fraction is estimated as 1.1% of column cross sectional area. While the model gives good agreement with experimental results at and above 25 bar, the model progressively deviates from experimentally determined values below this point. For pressure of 5-20 bar, the model predicts higher flooding points than found experimentally, giving an overly optimistic prediction of column performance. The higher pressure range is of greater interest for PHES development, so although the experimental results do not verify model performance at higher pressures than analysed here, they do suggest confidence in the model in predicting the onset of flooding.

The trend of measured flooding point shown in Figure 7.11 follows intuitively with

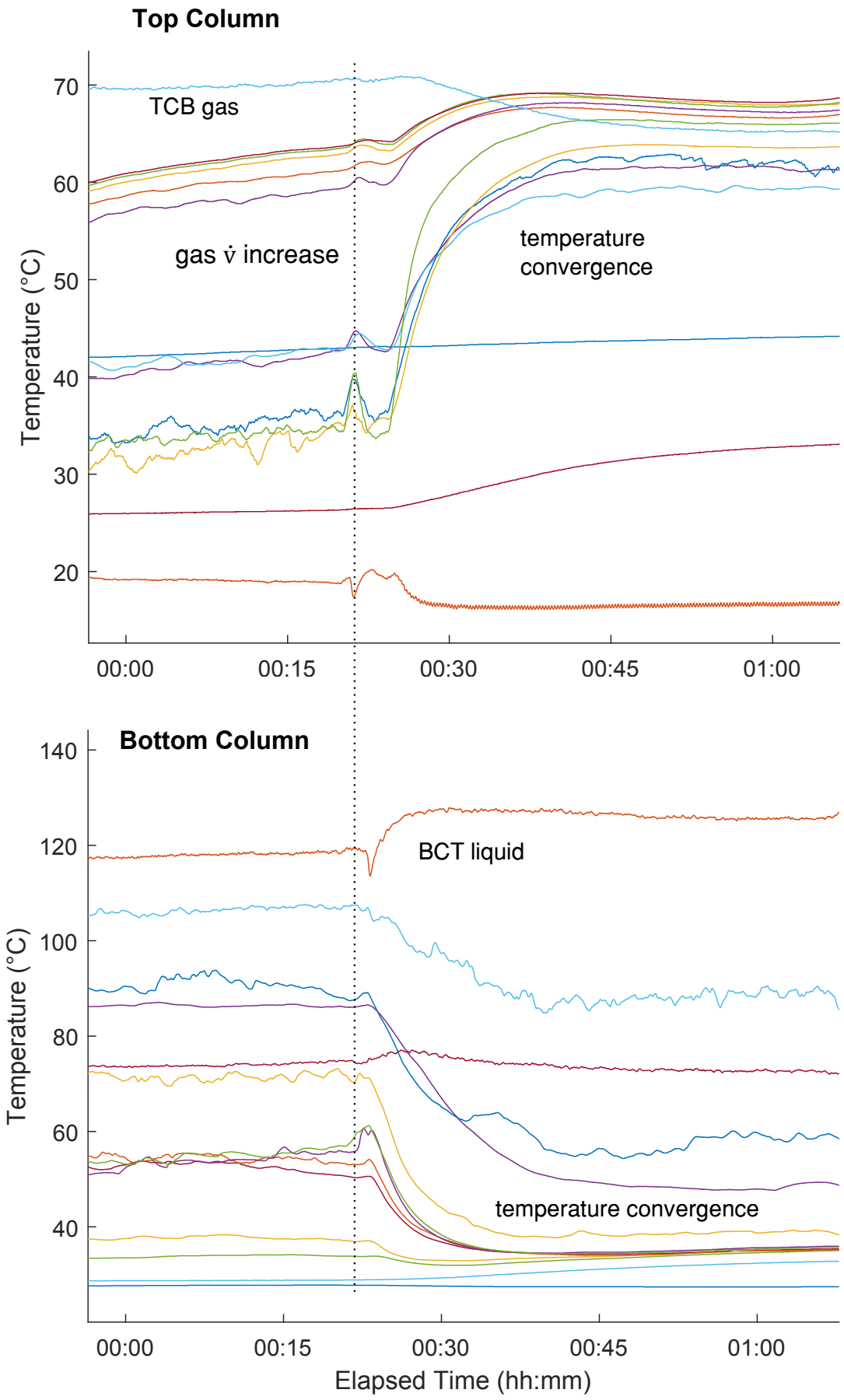

Figure 7.10: Column probe temperatures around the flooding point for the 15 bar representative trial. The gas volume flow-rate ($\dot{v}$) preceding the temperature convergence is the flooding point for this trial.

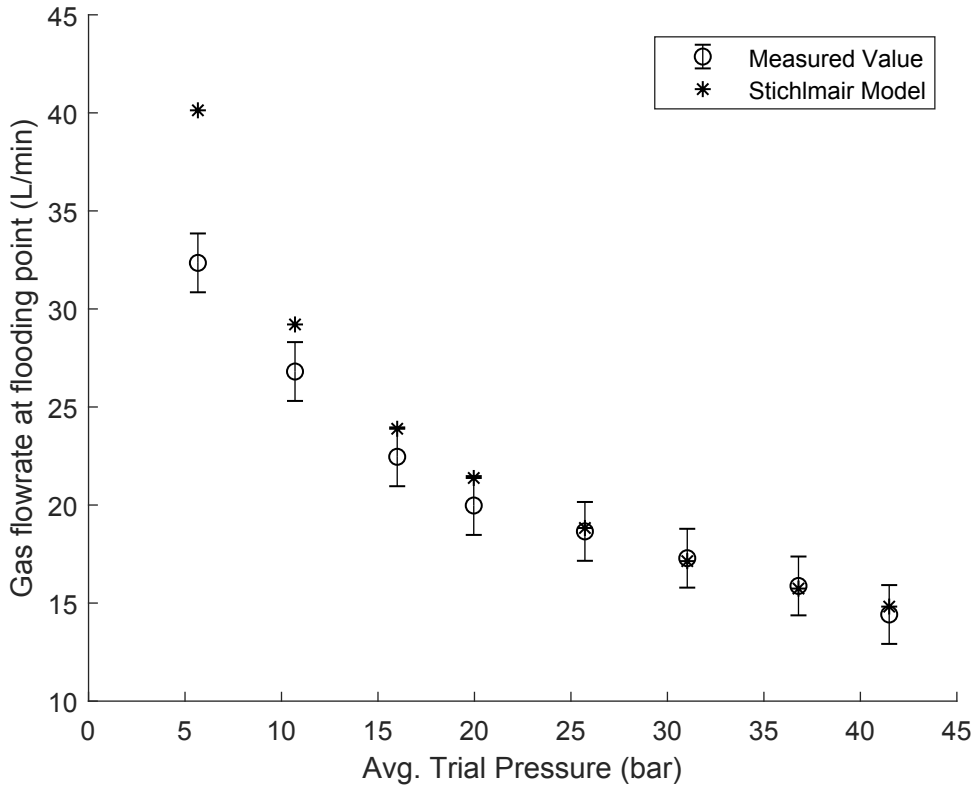

Figure 7.11: Gas flowrate at column flooding point plotted as a function of pressure, showing both experimental results and the model proposed by Stichlmair et al. (1989).

the change in gas properties as pressure increases. As pressure increases, the gas density increases, increasing the ability of the gas to entrain the liquid. Accordingly at higher pressures, the column is limited to lower gas flow-rates to avoid flooding. Given the considerable variation in column performance under differing conditions, it is impossible to make a judgement on the flooding point of a full scale packed column based on these experimental results, as they do not fulfil the homologous condition of identical temperature and pressures between pilot and full scale columns. The flooding model has been experimentally verified and sensible flooding point values have been found, but at reduced temperatures and pressures than had initially been specified. Further work is needed to expand the results of both U_h and flooding point to higher pressures and temperatures.

Chapter 8

Conclusions

This chapter summarises the results of both experiments and discusses the performance of the experimental apparatus and the models. Opportunities for further work concerning the packed-column experimental apparatus and the PHES system are discussed.

8.1 Apparatus Evaluation

The operational performance of the packed-column experimental apparatus is first considered. This apparatus was designed to demonstrate and quantify operation of pilot scale packed columns such that the performance of larger columns similar in nature could be confidently predicted. The experiments successfully demonstrated gas-liquid heat exchange in pilot packed columns at temperatures up to 120°C and pressures up to 42.5 bar showing that the heat exchanger envisioned for a full scale PHES plant is based upon a fundamentally sound principle. Demonstrated heat exchange efficiencies were notably less than anticipated, as heat exchange efficiency is strongly influenced by the degree to which the heat capacity rates of the gas and liquid match. When the heat capacity rates are equal, the heat exchange efficiency can be high as the a majority of the heat transferred from the liquid to the gas can be absorbed, and vice-versa in the subsequent column. At pressures up to 42.5 bar, the specific heat and density of the gas is significantly lower than at 200 bar, so for an equivalent volume-flow rate the gas has a much lower heat capacity rate at lower pressures. The experimental apparatus was designed for 200 bar operation, so at the gas mass-flow rates at 42.5 bar which do not cause flooding to occur, the heat capacity rate of the gas is notably lower than that of the liquid. Due to this mismatch, the gas cannot absorb or reject an equal amount of heat from the liquid, causing low efficiencies.

The pilot columns are scaled down versions of those which would be used in a PHES plant, and while geometric and packing scaling was carried out in accordance with established practice to predict full scale behaviour, the homologous condition between pilot and full scale column was not fulfilled. This condition specifies that the same fluids in the same proportions are used in both full and pilot scale columns at the same pressure and across the same temperature range. The reason that this condition is essential for accurate prediction of column behaviour is the highly specific nature of direct-contact gas-liquid interactions, and the wide variation in fluid density, specific heat, viscosity, and thermal conductivity with varying temperatures and (in the case of the gas) pressure. Homologous fluids and fluid proportions between pilot and full-scale columns were adhered to in the experiments, however the pressure and temperature equivalence were not. The experimental results therefore may not be used to confidently predict apparatus behaviour outside experimental temperatures and pressures. The results nonetheless provide value for the evaluation of column performance models and as a demonstration of packed columns applied to the problem of high pressure heat-transfer.

The piston-cylinder apparatus discussed in Chapter 3 is considered next, which had significantly narrower objectives than the packed-column apparatus. It was designed to demonstrate gas-liquid mixing within a linear, reciprocating cylinder using a novel mixing device. The efficacy of the mixing device was qualified using high-speed photography, and mixing was assessed by incrementally adding liquid and observing the effect upon the polytropic compression coefficient n. No systematic effect of the mixing device on polytropic coefficient was found suggesting that the novel mixing device was not effective, and high-speed photography supported this conclusion. The apparatus itself performed adequately, allowing the mixing device to be assessed and improvements to be suggested. Similar to the packed-column experiments, these experiments focused on heat transfer in gas-liquid interactions and were used to validate components of the PHES architecture. The piston-cylinder experiments focused on an early iteration of the PHES system, and when the design evolved to the next iteration the piston-cylinder concept was dropped.

Further work to improve the piston-cylinder experimental apparatus is not likely given the specialised nature of the process and the evolution in PHES design. If it were to be accomplished, improvements could be made in three areas: First, a new gas-liquid mixing device could be constructed, incorporating lessons learned from the current device tested. This would involve increasing circumferential mixer surface area

to assist with liquid droplet propagation from the bottom to the top of the cylinder. Second, a method of liquid injection could be added which would introduce the liquid via the central mixing device support rod, allowing for radial liquid propagation due to mixer rotational motion. Finally, the cylinder which currently acts as a large heat sink and potentially distorts experimental results could either be thermally decoupled from the experiment chamber, or externally insulated and heated.

8.2 Model Evaluation

The purpose of the packed-column experiments presented in this thesis are to validate two models; one to predict heat transfer within a packed column direct-contact heat exchanger, and another to predict when such an exchanger would exhibit flooding. As the piston-cylinder experiments were designed only to evaluate mixing-device performance, no model for its operation was proposed or validated. Both the packed-column heat transfer and packed-column flooding model were used to predict the ideal performance of the pilot columns, and both models were experimentally validated in the results presented in the previous chapters, albeit to differing degrees. The finite volume heat transfer model showed acceptable agreement with column temperature profiles and heat transfer rates discussed in Chapter 7. It therefore is likely a good predictor of column behaviour within the temperature and pressure ranges demonstrated. Due to significant variations in fluid properties from T_M to T_H and from p_L to p_H, the convective heat transfer coefficient between gas and liquid varies significantly across operating conditions. For this reason, the model cannot be considered validated outwith the conditions demonstrated by the current experiment; this is a fundamental difficulty in packed-column design.

The column flooding model, developed by Stichlmair et al. (1989), predicts the gas volume flow-rate at which a column will exhibit flooding known as the flooding point. This empirical model is based upon a wealth of prior packed column experimental literature, and includes specific adjustments for column conditions including fluid properties, geometry, and packing material. It does not explicitly call for column operating pressure in equations to solve for the flooding point, although the pressure is used in the calculation of fluid properties. Variations in flooding point with pressure in the Stichlmair model are therefore the result of variations in fluid properties with pressure, and do not account for the effect of elevated pressures on gas and liquid interactions. More recent work in the field has produced flooding models specifically

adjusted for higher pressure operation which account for buoyancy forces caused by elevated gas pressures, such as the model presented by Stockfleth and Brunner (2001). This model was not used in this analysis owing to the significant computational complexity it entailed, but it is notable that the Stichlmair model gave best agreement with experimental data at higher pressures, where the buoyancy forces it does not consider would be higher. It is likely that if experimental data were produced at higher pressures up to 200 bar there would be significant deviation from the Stichlmair model due to the greater magnitude of buoyancy forces, however for the purposes of these experiments it appears fit for purpose.

Evaluation of this model proved very sensitive to temperature and liquid volume-fraction, both parameters are difficult to conclusively measure in the columns in the apparatus. Temperature was set at 80°C, what was deemed an acceptable bulk temperature for all fluids within both columns. Liquid volume-fraction was estimated at 1.1% of cross-sectional area, similar to assumptions made in the finite volume heat transfer model based upon an assumed liquid film thickness and packing surface area. Slight adjustments to this value were made on the order of $\pm 0.1\%$ to adjust model results to match experimental data; this is considered acceptable practice as it tunes the model for future use. The model gave good agreement with experimental results for trials at 25 - 42.5 bar, and is a useful tool for confidently predicting column flooding point within this pressure range and within temperatures seen in experimental data. Outwith this range, further work is needed to produce confidence in the model for the temperature and pressures found in the PHES system.

8.3 Opportunities for Further Work

The primary shortcoming of the packed-column apparatus was poor performance of the heater, which prevented the apparatus from reaching its intended temperature T_H of 370°C. As discussed in Chapter 6 and, as experimental trials demonstrated, both the decision to place the heater on the liquid piping and the design of the heater resulted in a sub-optimal liquid temperature rise. The heater was not power limited, but its relatively low internal surface area and low convective heat transfer coefficient led to less heat transferred into the liquid than was intended. Placement of the heater between the two columns meant that liquid flow through the heater was driven solely by gravity, likely resulting in a partially full pipe with a slow, laminar flow. It is unlikely that the turbulator placed inside the heater had any turbulation effect on the liquid given these

low speeds. Had it been effective, it would have increased the convective heat transfer coefficient. While replacement of this heater with a larger version with a greater heat transfer surface area would partially solve the problem, a more straightforward addition to the apparatus to improve performance would be to add a heater on the gas pipe connecting the two columns. This would provide an independent heat source for the top column which does not rely on successful gas-liquid heat transfer in the bottom column, and would add more heat to the system to help offset steady state losses. At the gas flow-rates utilised in the apparatus the gas flow within the 25mm gas piping is turbulent, so a gas heater would have a much higher convective heat transfer coefficient than was present in the liquid heater.

Heat leakage from the gas and liquids into the pressure vessel components and the lab was noted and discussed in Chapter 7; these steady-state thermal losses incurred in column plates and the sensor blocks affected the ability of the apparatus to reach and maintain elevated temperatures. Even if an additional heater were to be added on the gas piping, addressing these sources of heat loss is critical as they would likely increase with increasing apparatus temperature. Partial apparatus disassembly would aid in assessing the condition of the internal insulation; if it has significantly degraded it would need to be replaced with a new type of insulation. Thermal conductivity testing on used insulation samples saturated with liquid would also inform work in this area. There are several locations within the apparatus where it was initially considered too difficult to insulate; the internal surfaces of the sensor blocks, and internal bores for temperature probes in the liquid plate are two examples. Even if insulating materials are not able to fit in these locations, a thermal break consisting of a less conductive material than carbon steel could be installed; for example, a stainless steel tube could be used to line the liquid bores and provide additional barriers to heat transfer.

Another aspect of packed-column apparatus performance which did not meet original expectations was the pressure range it was able to operate over. As discussed in Chapter 6, this was the result of insurance and regulatory concerns rather than physical limitations with apparatus hardware; all components met relevant safety factors for pressurised use. Extending apparatus operation to higher pressures would require replacement of the gas piston-cylinder pump assembly; fabrication and qualification of such an assembly would carry a moderate cost and a multi-month lead time. Installation of the replacement piston-cylinder would be non-trivial given the confined working environment, but likely feasible. This was not pursued in this thesis owing to cost and time concerns.

Gas and liquid pumps performed as expected during experimental trials with two relatively minor exceptions. First, during operation pump rod seals exhibited degradation due exposure to Paratherm HR and likely would have failed had the experiments continued for several months. The author investigated seal compatibility in the detailed design of the pumps, and although the liquid manufacturer had indicated that Viton, the seal material, was likely compatible with the liquid this proved not to be the case. A slow liquid leakage was observable from both pumps, however no significant apparatus gas pressure changes took place due to this leakage. Nevertheless these seals should be replaced before additional experimental trials are conducted. The second unexpected behaviour stemmed from the operation of the gas rectification manifold; check valves within this manifold exhibited chatter and produced loud noises and significant vibration during operation. The cause of this behaviour is thought to be the significant difference in fluid properties between nitrogen and the hydraulic oil for which the check valves were designed to operate. Although no negative experimental effects were observed, it is likely this effect shortened the life of the check valves.

Given additional time and resources, apparatus performance could be improved by expanding data collection to include differential pressure sensors across both columns. These additional measurements would allow for a pressure measurement of the flooding point, producing more confidence in the flooding values found in the preceding analysis based solely on temperature measurements. Dedicated gas and liquid flow-rate instrumentation would also increase confidence in flow-rates reported by the positive-displacement gas and liquid pumps; this would be especially helpful for the liquid as the liquid pump did not have real-time displacement feedback.

Verification of apparatus performance demonstrating cold exchanger operation would further extend the work presented here, and would fully validate the direct-contact heat exchanger concept for use within the PHES system. All work to date has focused on the hot heat exchanger owing to its higher and less well studied pressure regime. Given the lower pressures on the cold side of the Joule-Brayton cycle loop, a conventional heat exchanger might be appropriate for this process, but an extension of apparatus performance to examine cold behaviour would still be informative. Adapting the apparatus for cold operation was a design intent from apparatus conception, and would require a chiller, procurement of a cold heat exchange fluid (proposed to be 1-propanol), and potentially internal insulation upgrades.

Further work to examine liquid distributor design is also warranted, owing to the importance of uniform liquid distribution across the packing for good heat transfer.

Experimentally derived parameters such as U_h are dependent on the assumption of an even thin liquid film across the packing surface area; if improvements to the liquid distributor are not apparent in the event of poor distribution, quantification of this distribution would nonetheless aid calculations. One way to accomplish this would be to construct a clear column of identical diameter and packing to the pilot columns with a similar liquid distributor, and observe liquid distribution at ambient pressure. Such an experiment would not provide highly accurate results owing to fluid variations with temperature and pressure, but would likely still be instructive. Similar work could also be undertaken to instruct gas distributor design, likely using the same clear column and an opaque vapour.

The apparatus enhancements just described would go far in increasing the confidence in packed column performance for the PHES system. Operation between T_L and T_M at 20 bar and between T_M and T_H at 200 bar would satisfy the homologous scaling condition between the pilot columns in this apparatus and the full scale columns proposed for the PHES system. This would fully validate both the column flooding and finite volume models partially validated in this thesis, and allow for further development of PHES system architectures based upon experimentally verified data. The flooding point found at the temperature and pressure extremes will be critical to future development; if the flooding point of these configurations is too low, the columns will not be able to handle the necessary gas and liquid flows for PHES operation, necessitating larger full scale columns. As the purpose of incorporating direct-contact heat exchangers was a reduction in exchanger cost and complexity, if the flooding points are found to be much lower than originally anticipated the packed column design may need to be replaced with conventional heat exchangers. Column modelling to date has indicated that this is not a likely scenario, but only full demonstration will inspire confidence. Potentially, a CFD model could be built and validated using the data from such an expanded apparatus, providing further confidence in future models and contributing to the state of the art.

Following the acquisition of robust apparatus results across the whole temperature and pressure range, potentially incorporating some or all of the improvements suggested in this chapter, likely the next step for the apparatus is to be disassembled. The packed-columns portion of the apparatus would likely be incorporated into a pilot scale PHES plant, and the remainder re-purposed.

8.4 Advancement of PHES goals

The purpose of the work presented in this thesis is to advance the development of a PHES system, and the author worked closely with SynchroStor employees to ensure that the experiments conducted would positively contribute to system development. The development of any solution to a question so fundamental to our modern electricity grid as "How can electricity be stored for long durations in large quantities at low cost?" is by nature an iterative process: solutions are proposed, developed, and either discarded or kept depending on development. Three iterations of SynchroStor PHES development were described in the first chapter. In the first iteration, large, linear, slow-moving pistons were used to compress and expand a gas-liquid mixture which was made within the cylinder. This iteration was the impetus for the piston-cylinder experiments presented in Chapter 3; the author was attempting to develop a gas-liquid mixing device to fit within these cylinders to allow for the system to function. The construction and high-speed photography of the test apparatus partially led the PHES development team to abandon in-cylinder gas-liquid mixing; the tested mixing device was non-trivial to manufacture, was not an effective mixer, and proposed solutions would add additional complexity. Other developments also led to the decision to move to the next iteration in design, namely expected difficulties in scaling up the seals used in the large pistons and the suggestion that a gas-liquid direct-contact heat exchanger might supplement heat exchange within the cylinders.

Once direct-contact heat exchange was examined in detail, it was clear that the effort and complexity of in-cylinder gas-liquid mixing was not worth the benefit. A second system iteration then came about, where a packed-column gas-liquid heat exchanger would be used to exchange heat between the gaseous cycle working fluid and a liquid used to store heat or coolth. Existing literature on packed columns was almost entirely focused on mass-transfer applications, with most literature considering heat exchange as a side effect. Texts which were focused on heat-transfer applications of columns concentrated on phase change applications, the majority of which were undertaken at ambient pressure with air and water such as cooling towers and are therefore not relevant to this application.

Further confidence was needed regarding packed-column use for PHES applications; this lead the author to develop a finite volume heat transfer model to quantify packed column thermal performance, and to use a flooding model developed by Stichlmair et al. (1989) to predict column flooding points. Little published work was

available to determine convective heat transfer coefficients for use in the finite volume model; as a result there was significant uncertainty that the model would produce meaningful results. The author developed an experimental apparatus to verify both models and demonstrate direct-contact heat exchange; this work forms the majority of what has been presented. Preliminary results described in this thesis led SynchroStor to move past the packed-column direct-contact heat exchanger as a component in the PHES system. The over-riding reason for this decision is concerns over flooding; the heat transfer benefits of direct-contact heat exchange are countered by the difficulty in getting adequate gas flow through the exchanger to produce sufficient heat exchange without causing flooding. Although results presented up to 42.5 bar do not indicate that flooding will be an issue for 200 bar operation, this effect was considered to be too large an operational risk. Additionally, stringent material handling requirements and cost of the Paratherm HR thermal oil incentivised a different approach to heat exchange. SynchroStor therefore moved into the third iteration of system development based upon a different heat exchange technology, which is not discussed presently. Both experimental apparatus nonetheless provided valuable development information to the PHES project, and validated models for the unique conditions found within the proposed heat exchangers.

Appendix

Appendices

These appendices incorporate supplemental information relevant to the thesis. Appendix A1 documents pressure vessel certification performed by the author for several packed-column components by providing calculations for one part. Appendix A2 incorporates detailed manufacturing drawings for several packed-column components.

A.1 Pressure Vessel Certification

The document included in this section shows the process of ensuring that components fabricated used at high pressure comply with the European Pressure Equipment Directive (PED). Multiple design codes can be used to fulfil the requirements of this directive, with EN-13445 chosen for this application. EN-13445 is the unified European unfired pressure vessel design code, and encompasses design, material specifications, manufacture, and test. The documentation for the gas plate is included.

EN 13445:2014 Unfired Pressure Vessels

Adherence documentation – contact rig 1 part 2

Dan McKinley, University of Edinburgh, July 2018

The following documents the compliance of 'contact rig 1 part 2' (hereafter referred to as 'the part') with the normative clauses of EN 13445. The responsibility for this compliance rests with the Pumped Heat Energy Storage group at the University of Edinburgh (hereafter referred to as 'the manufacturer') because it designed the part, subcontracted its machining, performed additional machining, and intends to use the part within an experimental apparatus in pressure service.

Table of Contents:

EN 13445

EN 13445:2014 is a European Standard for Unfired Pressure Vessels which, when the normative clauses of the standard are complied with, satisfy safety requirements for the design of pressure vessels. The sections of the standard which apply to this part are:

- EN 13445-1 General
- EN 13445-2 Materials
- EN 13445-3 Design
- EN 13445-4 Fabrication
- EN 13445-5 Inspection and Testing

The normative clauses of this standard have been complied with for this part, and this compliance is documented in this section and in the appendices.

Part 1: General

This part of the standard defines terms and symbols and contains informative annexes on how to use the standard.

Part 2: Materials

Materials for pressure bearing parts shall meet the general requirements of 4.1, the special provisions of 4.2 if applicable, and shall be ordered complying with the technical delivery conditions of 4.3. The material chosen for this part was P355GH.

(4.1.2) A certificate of specific control is required if the Design by Analysis – Direct Route according to Annex B of EN 13445-3 is used. Such an inspection certificate (type 3.2) was provided with the material, fulfilling this requirement, and is included in Appendix C.

(4.1.4) The minimum elongation after fracture in any direction shall be ≥ 14% measured on a gauge length $L_O = 5.65\sqrt{S_O}$, where S_O is the original cross section. According to the inspection certificate 3.2 provided with the material, the minimum elongation after fracture meets this requirement.

(4.1.6) The material shall have a minimum impact energy measured on a Charpy-V-notch impact test of ≥ 27 J. The inspection certificate (type 3.2) specifies a minimum impact energy of 176 J at -50°C, the lower than the lowest foreseeable temperature of the part, fulfilling the requirement.

(4.2.1) Manufacturing processes, operating conditions, and lamellar tearing have been considered in specifying the material, fulfilling the provision.

(4.2.2) The material properties of P355GH at elevated temperatures are available in the European Standard for the material making this material a suitable choice for this application and fulfilling the provision.

(4.2.3) The prevention of brittle fracture has been considered in accordance with Annex B, and it has been determined that P355GH is suitable for use without detailed brittle fracture calculations because:

- The design temperature is above 50°C (B.5.1)
- The minimum impact energy is ≥ 27 J (B.5.2)
- The part pressure will never exceed 50% of design pressure at T < 20°C (B.5.4)

Therefore, the provision is fulfilled.

(4.3.1) The material was delivered in accordance with EN 10028-3:2009, complying with the technical delivery conditions.

Part 3: Design

(5.1) EN 13445-3 is only applicable when materials are not subject to localized corrosion in the presence of products which the vessel is to contain, and when all calculation temperatures are below the creep range. This part fulfils these criteria; it will not contain any corrosion causing products and its maximum allowable temperature, 370°C, is below the start of the creep range as defined by Section 18.4.3 of EN 13445-3 for ferritic steels as 380°C.

(5.3.4) The maximum allowable pressure of a vessel shall not be less than the differential pressure which will exist when the pressure relieving device starts to relieve. Therefore, the maximum allowable pressure of this part is 210 bar, the setting of the pressure relief valve which will be attached to it.

(5.4.1) Design by formulae (DBF) is the default method of design for EN 13445-3. Two other methods can be used to supplement or replace DBF

- Design by Analysis (DBA), either DBA – Direct Route in Annex B, or DBA – Stress Categories in Annex C
- Design by Experiment (DBE)

DBF is not applicable to this part due to the intricate and non-standard geometry; DBE is not applicable because it is a low volume part (qty. 4) and it is not economically viable to conduct the required material testing and destructive testing.

(5.4.2) Fulfilment of this requirement requires classification of the part into a testing group according to Table 6.6.1-1 from EN 13445-5. This table first requires the part material to be classified into a material group according to Table A-1 of EN 13445-2, which for P355GH is group 1.1. Accordingly, the testing group is 1b for this material as it contains no welds.

For testing group 1, the DBA requirements of Annex B and Annex C provide satisfactory designs for non-cyclic pressure loading, $n \leq 500$. Accordingly, the part will be limited to this number of cycles unless further analysis is carried out at a later date.

(5.4.6) DBA – direct route of Annex B is only applicable to testing group 1 parts. This part fulfils this requirement. Therefore, DBA according to Annex B is chosen as the design method.

Due to the length of DBA – Direct Route, it has been included in the separate Appendix A.

Part 4: Manufacture

(3.2) No special processes were specified in the manufacture of this part (welding, forming, or heat treatment), so no subcontractor form or welding documentation is necessary.

(5.4) All manufacturing drawings have tolerances specified which meet or exceed these standards, and those in (5.6).

(9.7) A visual inspection was performed on each part upon delivery from the subcontractor. The inspection verified: adherence to tolerances specified in the design drawing, placement of features, surface finish.

(9.8) The material designation P355GH will be placed upon the part.

Part 5: Inspection and testing

(5.2.2) The technical documentation of this part is as follows:

- *Manufacturer:* Pumped-Heat Energy Storage Project, The University of Edinburgh, Alrick Building, Edinburgh
- *Subcontractor:* Hughes Engineering Ltd., Craigton House, 133 Barfillan Dr., Glasgow
- *Max Pressure:* 210 bar
- *Design Pressure:* 200 bar
- *Min Pressure:* 1 bar
- *Test Pressure:* 300.3 bar
- *Capacity:* 2.775 L
- *Design Temperature:* 0°C - 370°C
- *Marking:* Stamped on outer round
- *Fluid Group:* Group 1 Liquid and Group 2 Gas
- *Allowed Number of Cycles:* less than 500

(5.2.3) All design and manufacturing drawings are included in Appendix D, fulfilling the requirement to include these drawings with compliance documentation.

(5.2.5) The results of design calculations are given in Appendix A, fulfilling the requirement to include these calculations with compliance documentation.

(5.2.6) The material certificates for this part are included in Appendix C, fulfilling the requirement to include these certificates with the compliance documentation.

(10.1) A final assessment was carried out in accordance with this clause, encompassing:

- A visual and dimensional inspection after delivery
- A documentation examination
- A proof test
- A post proof test examination

(10.2.3) Hydrostatic proof testing was completed in accordance with the requirements of this section and testing certificates are included in Appendix D.

(11.4) Marking of the part has been carried out in accordance with the requirements of this section.

UOE 07 2018 EN 13445 PS 200 TS 0 – 370 P355GH [SERIAL NO.]

(11.5) Declaration of compliance with this standard is given here.

MANUFACTURER'S DECLARATION OF COMPLIANCE FOR DESIGN, MANUFACTURE AND INSPECTION OF PRESSURE VESSEL		
Pressure Vessel	contact rig 1 part 2	
Description	Ø485x120mm plate of P355GH steel with a central bore for the passage of gas and liquid and a mounting face for contact rig 1 part 3.	
Vessel's manufacturer name	The University of Edinburgh	
General arrangement drawing No.	contact rig 1 part 2.pdf	
Serial Number(s)	E01,E02,E03,E04	
Year of manufacture	2017	
Volume (L)	2.775	
Maximum allowable pressure (bar)	210	
Maximum allowable temperature (°C)	370	
Minimum allowable temperature (°C)	0	
Contents	Group 1 Liquid, Group 2 Gas	
DESIGN		
Responsible Authority	The University of Edinburgh Pumped Heat Energy Storage Project G.180 Fleeming Jenkin Building EH9 3BF Edinburgh United Kingdom	
MANUFACTURE AND INSPECTION		
Responsible Authority	The University of Edinburgh Pumped Heat Energy Storage Project G.180 Fleeming Jenkin Building EH9 3BF Edinburgh United Kingdom	
VERSION OF EN 13445 USED		
Year of edition: 2014	Issue 4 (2017-07)	
The undersigned declares that the design, manufacture and inspection of this pressure vessel is in compliance with the requirements of EN 13445.		
Date: 23 August 2018	Name: Mr. Daniel McKinley	Position: PhD Student
Signature: 		
Date: 23 August 2018	Name: Prof. Win Rampen	Position: Chair of Energy Storage
Signature: 		

Appendix A – EN 13445:2014 Annex B

EN 13445:2014 Annex B Design by Analysis – Direct Route

(B.5.1) The general methodology of this design methods is a series of failure modes are considered, and for each failure mode there corresponds a single design check. The design check shall be carried out for both normal operating load cases, and special load cases such as testing.

For each design check a simple principle is stated. For each principle, one or more application rules are given, and the most relevant application rule should be selected.

For each design check/load case combination the fulfilment of the design check's principle is shown by:

- Specification of the design check/load case and corresponding actions;
- Determination of the actions' characteristic values or functions;
- Calculation of the actions' design values or design functions;
- Check of the fulfilment of the principle;
- Statement confirming whether or not the principle is fulfilled.

There are two load cases which must be considered for the part: operation and testing.

(B.6.1) Actions which act upon the part are classified as: permanent actions; temperature, pressure, and actions related to the deterministically; variable actions other than temperature and pressure; exceptional actions. The actions which act upon this part are given in the table below.

Action	Symbol	Characteristic Value	Description
Pressures and temperatures (Operation)	P_{sup}	210 bar	Reasonably foreseeable highest pressure
	T_{sup}	370°C	Reasonably foreseeable highest temperature
	P_{inf}	1 bar	Reasonably foreseeable lowest pressure
	T_{inf}	0°C	Reasonably foreseeable lowest temperature
Permanent	$G_{k,\,sup}$	2125000 N	Upper limit of total bolting force (nominal 1700000N)
	$G_{k,\,inf}$	1275000 N	Lower limit of total bolting force (nominal 1700000N)
Pressures and temperatures (Testing)	P_{sup}	300 bar	Reasonably foreseeable highest pressure
	T_{sup}	20°C	Reasonably foreseeable highest temperature
	P_{inf}	1 bar	Reasonably foreseeable lowest pressure
	T_{inf}	0°C	Reasonably foreseeable lowest temperature

These actions are modified in the design checks by multiplying them by a partial safety factor for actions γ_A, which account for uncertainty in the values.

(B.7.5) The design value of material strength parameter RM_d used in the design checks is given by $RM_d = RM/\gamma_R$, where γ_R is the partial safety factor for materials. Additionally, the

minimum specified material strength data from the relevant standard is used – not strength values from the inspection certificates.

The other material properties are given in Annex O and tabulated here, noting that the chosen reference temperature of 280°C is given by B.7.5.2

Property	Symbol	Value	Source
Yield Strength	R_{eH}	295 MPa	EN 10028-2
density (20°C)	ρ_{20}	7850 kg/m3	Table O-1
Poisson's ratio	v	0.3	O.3.5
modulus of elasticity	ET	193800 MPa	Table O-2
linear thermal expansion between 20C and T	$\beta_{20,280}$	13.387×10^{-6} / K	Table O-3
thermal conductivity	λ_{280}	48.82 W / (m*K)	Table O-4

(B.8.2) **Gross Plastic Deformation Design Check**

For each load case, the design value of actions or combinations of actions are carried by the design model with:

- Linear-elastic ideal-plastic constitutive law
- Tresca's yield condition and associated flow rule
- Proportional increase of all actions and a stress-free initial state
- Actions (pressure, temperature, forces) for both the testing and operation load cases
- Design material strength parameters and partial safety factors according to Table 1

Property	Load Case	Abbreviation	Value	Source
Material Strength Parameter (RM)	Operation	$R_{M,O}$	252 MPa	Table B.8-2
	Test	$R_{M,T}$	300 MPa	Table B.8-4
Partial Safety Factor (Material)	Operation	$\gamma_{R,O}$	1.25	Table B.8-2
	Test	$\gamma_{R,T}$	1.05	Table B.8-4
Partial Safety Factor (Pressure)	Operation	$\gamma_{P,O}$	1.2	Table B.8-1
	Test	$\gamma_{P,T}$	1.0	Table B.8-3
Partial Safety Factor (Permanent Action)	Operation	$\gamma_{G,O}$	1.2	Table B.8-1
	Test	$\gamma_{G,T}$	1.2	Table B.8-3

Table 1

The design model was created in Solidworks Simulation, and the relevant partial safety factors for all actions were multiplied by the actions to provides inputs to the model.

For the operating load case:

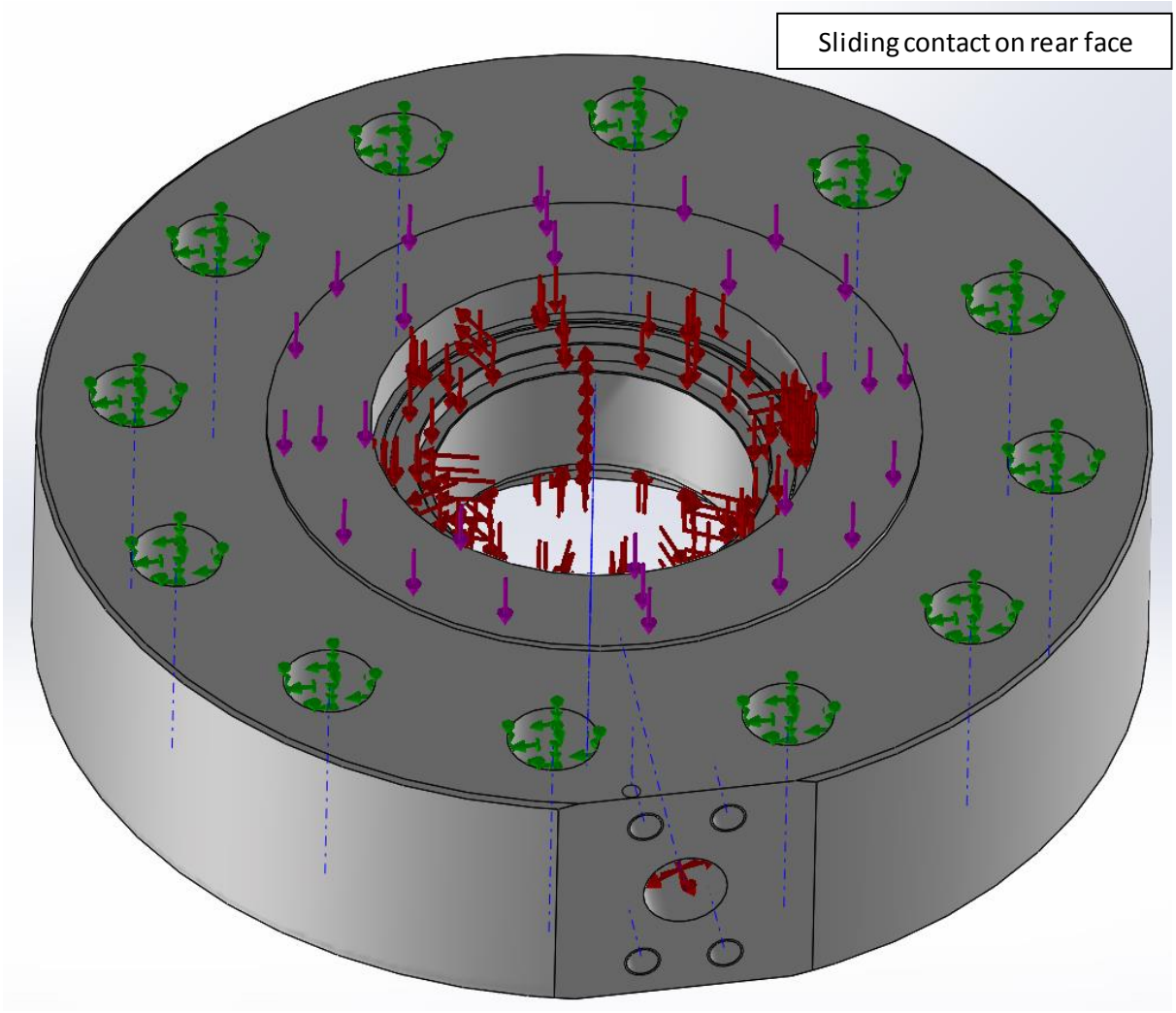

Figure 1: Operating load case model boundary conditions. Green indicates fixed geometry, purple the applied bolt force, and red internal pressure.

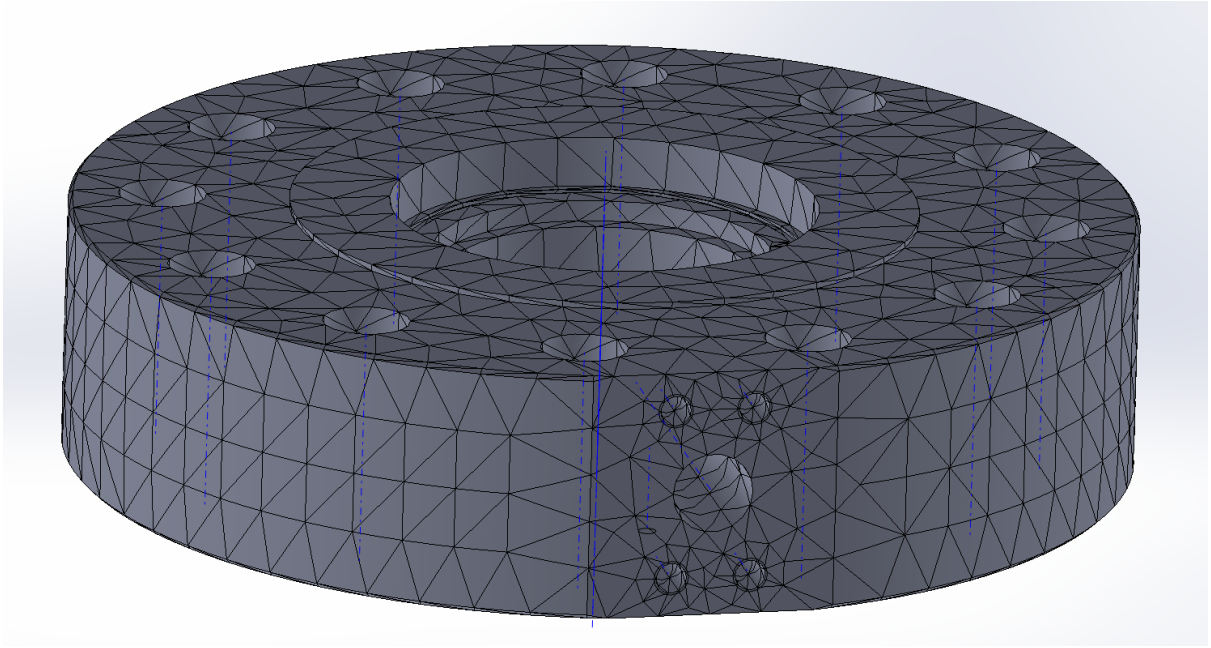

Figure 2: Mesh

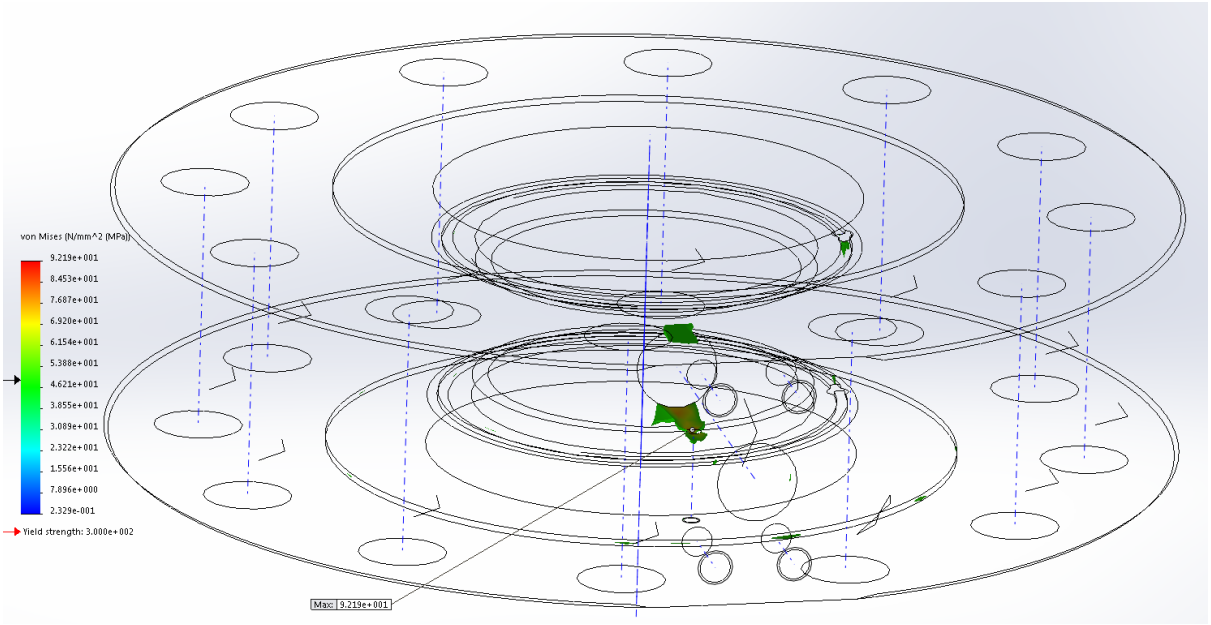

Figure 3: iso clipping of von Mises' stress greater than 46 MPa (max 92.19 MPa)

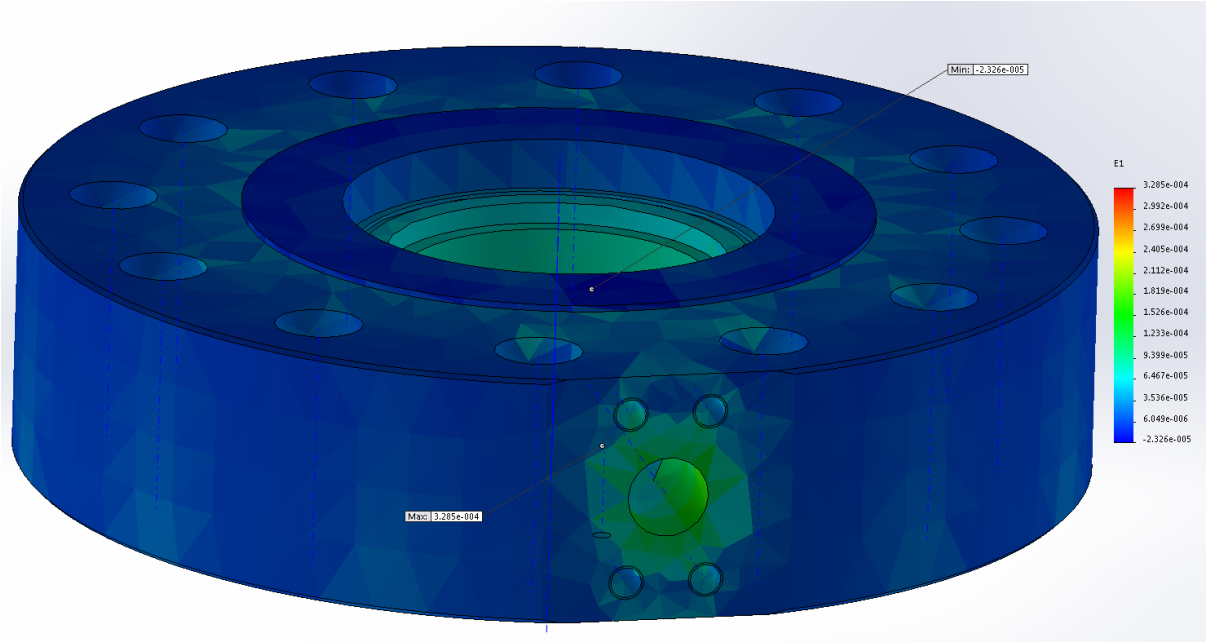

Figure 4: First Principal Strain (Max 3.285E-04, Min -2.326E-05)

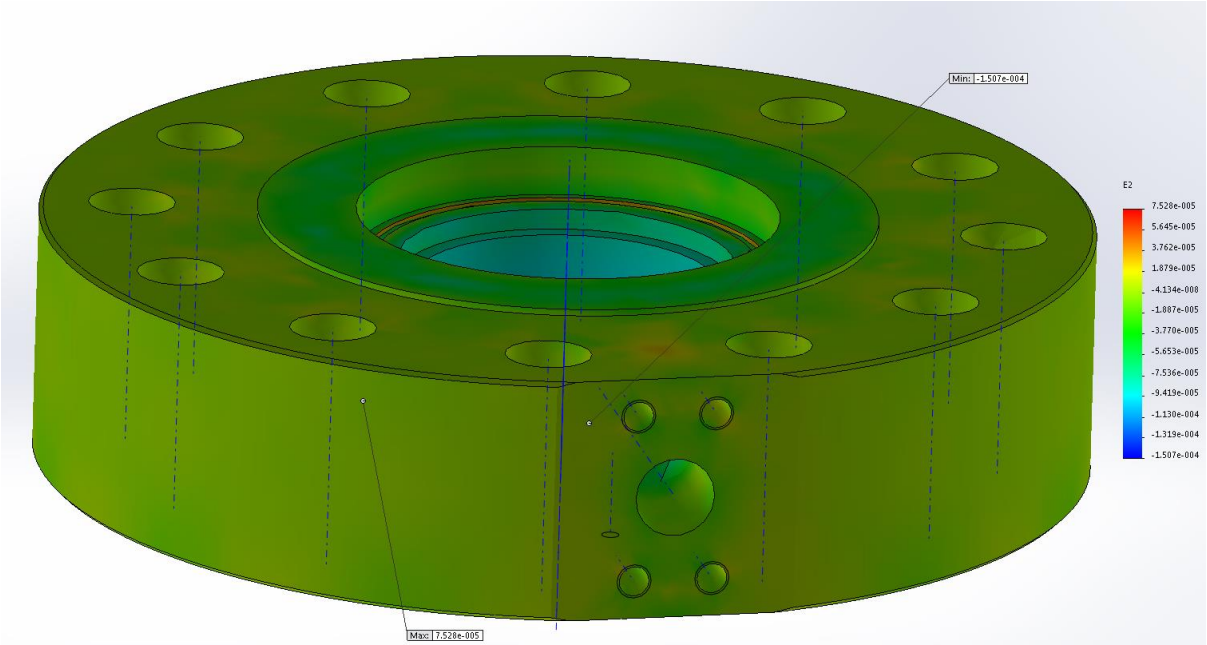

Figure 5: Second Principal Strain (Max 7.528E-05, Min -1.507E-04)

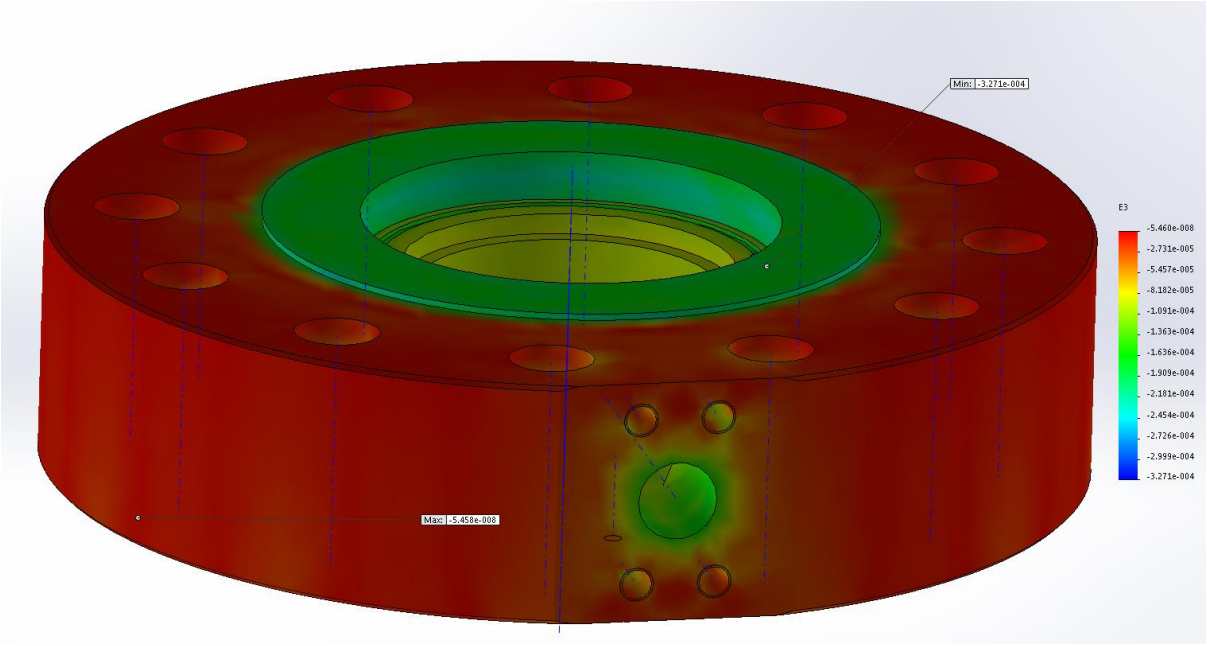

Figure 6:Third Principal Strain (Max -5.458E-08, Min -3.271E-04)

For the testing load case:

The boundary conditions are the same, with the exception that the internal pressure is 30 MPa, and the mesh is the same.

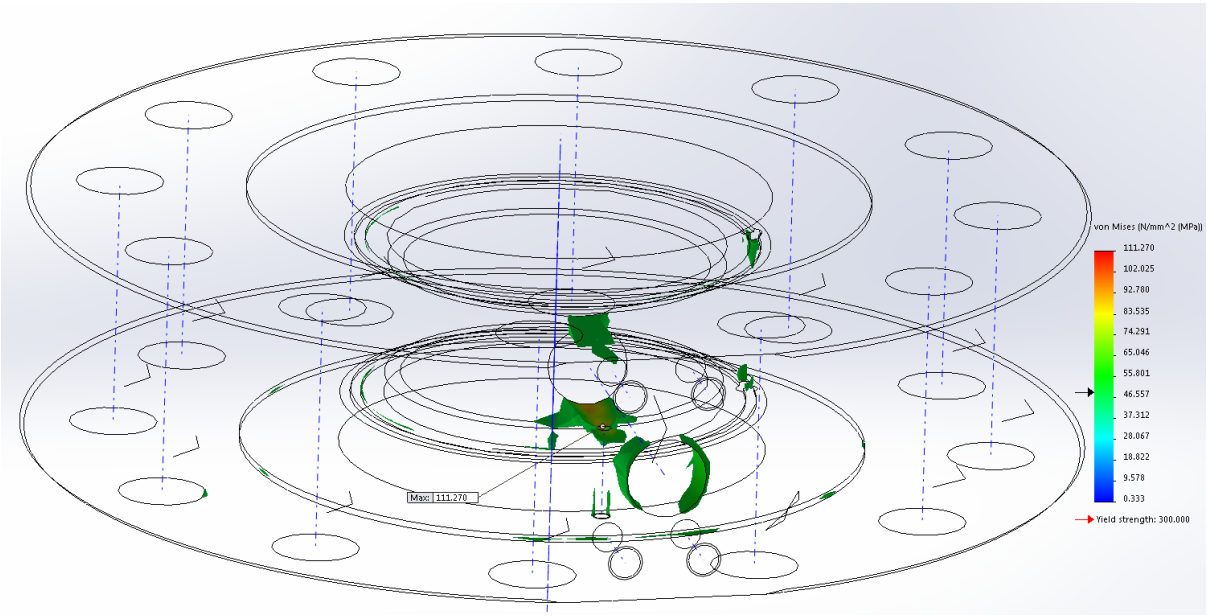

Figure 7: iso clipping of von Mises' stress greater than 46 MPa (max 111 MPa)

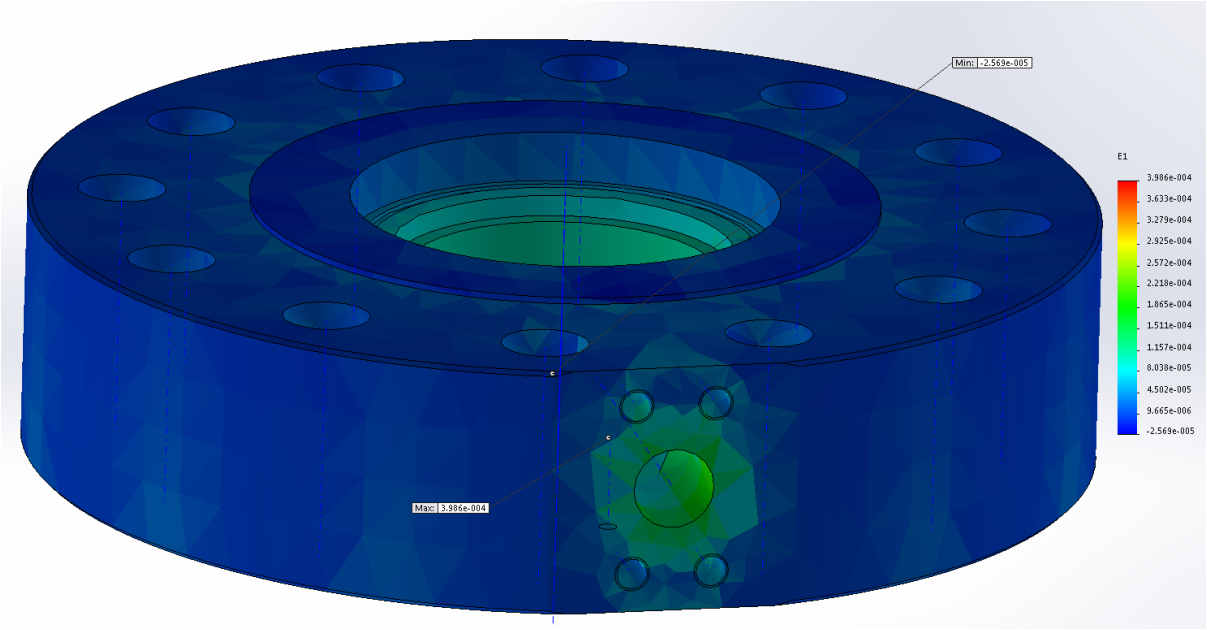

Figure 8: First Principal Strain (Max 3.986E-04, Min -2.569E-05)

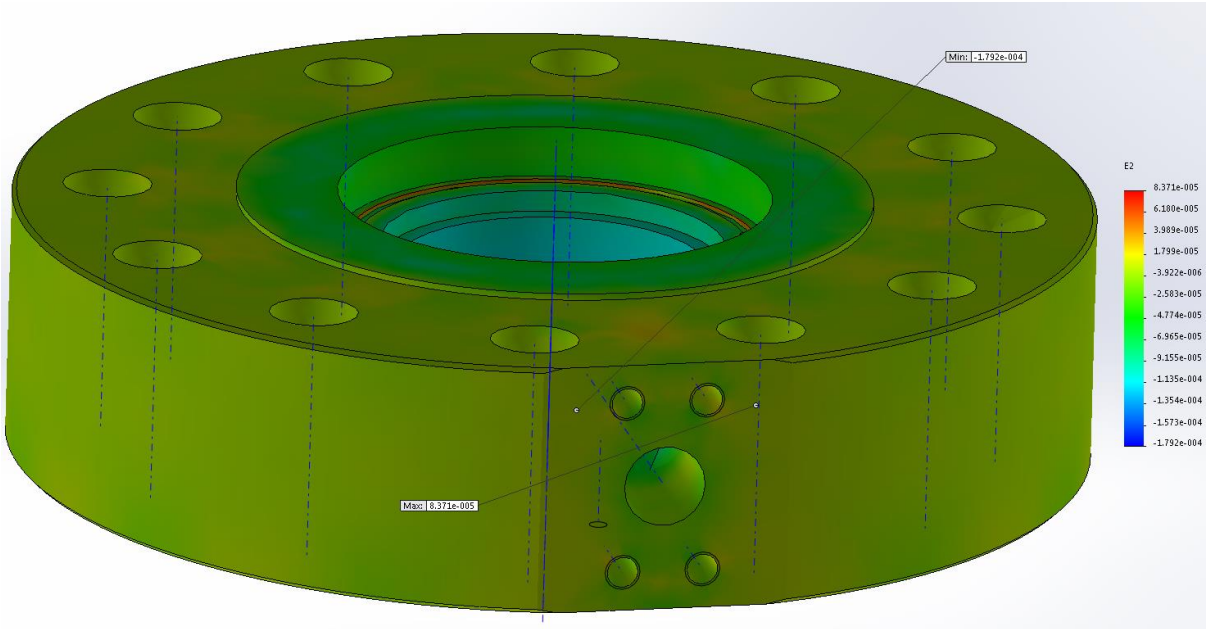

Figure 9: Second Principal Strain (Max 7.528E-05, Min -1.507E-04)

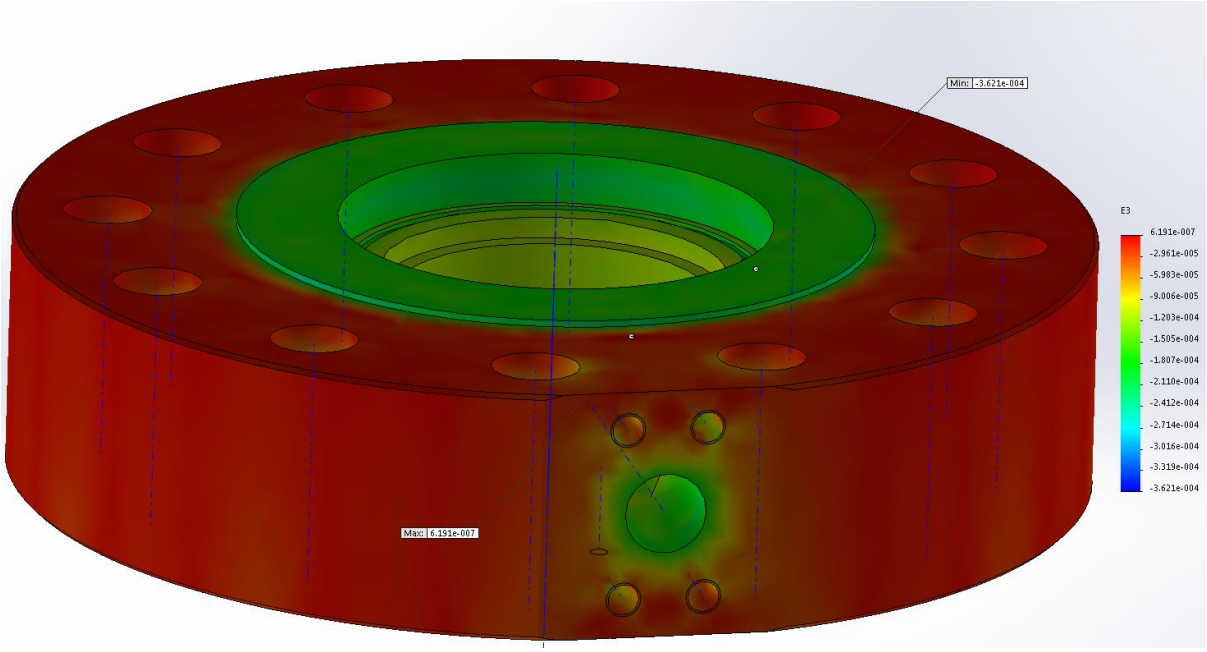

Figure 10: Third Principal Strain (Max -6.191E-07, Min -3.621E-04)

The principle is fulfilled because:

- the lower bound limit values of the combination of actions making up the operational load case are reached without violation of the 5% principal structural strain limit.
- the lower bound limit values of the combination of actions making up the operational load case are reached without violation of the 7% principal structural strain limit.

(B.8.3) **Progressive Plastic Deformation Design Check**

On repeated application of the action cycles, progressive plastic deformation shall not occur for:

- first order theory
- a linear-elastic ideal-plastic constitutive law
- von Mises' yield condition and associated flow rule

The principle is fulfilled (without specific proof) according to application rule 4 for load cases without thermal stresses for all action cycles within the range of actions allowed according to the Gross Plastic Deformation Design Check. This is allowable because:

- There are no stresses induced by prescribed displacements
- There are no thermal stresses because the part is free to expand and contract; and contact rig 1 part 2, to which the part is bolted, is made of the same material and subject to the same thermal loading.

(B.8.4) **Instability Design Check**

Buckling failure occurs when, because of a critical combination of magnitude and/or point of load application, together with the geometrical configuration of the machine member, the deflection of the member suddenly increases greatly with only a slight change in load. This non-linear response results in buckling failure if the buckled member is no longer capable of fulfilling its design function.

To satisfy this design check, a buckling FEA analysis was built in Solidworks Simulation encompassing:

- Pre-deformations according to the critical buckling shapes and deviations according to EN 13445-4:2014.
- Linear-elastic ideal-plastic constitutive law
- von Mises' yield condition and associated flow rule
- A maximum value of the principal structural strains of 5%
- Proportional increase of all actions and a stress-free initial state
- Partial safety factor of actions as specified in Gross Plastic Deformation (B.8.2)
- Design value of buckling strength and other material properties according to Table 2

Property	Load Case	Abbreviation	Value	Source
Material Strength Parameter	Operation	$R_{M,O}$	173.6 MPa	Table B.8-2
	Test	$R_{M,T}$	295.0 MPa	Table B.8-4
Partial Safety Factor (Buckling Strength)	Operation	$\gamma_{R,O}$	1.25	B.8.4.4
	Test	$\gamma_{R,T}$	1.1	B.8.4.5

Noting that although the part will be subject to a hydrostatic test in the test load condition, this alone does not fulfil the principle according to application rule 1 because the operation load case is not the subject of a test. Application rule 2 specifies that clause 8 'Shells under internal pressure' suffices as a stability check for pressure action, however the geometry of this part is not compatible with these design checks. Therefore, a Solidworks buckling analysis was conducted, the results of which are shown in Figure 11, which shows the resultant amplitude of buckling inducted deformations. Notably, these are very small values located in very thick-walled areas of the geometry, indicating that buckling is not a design concern.

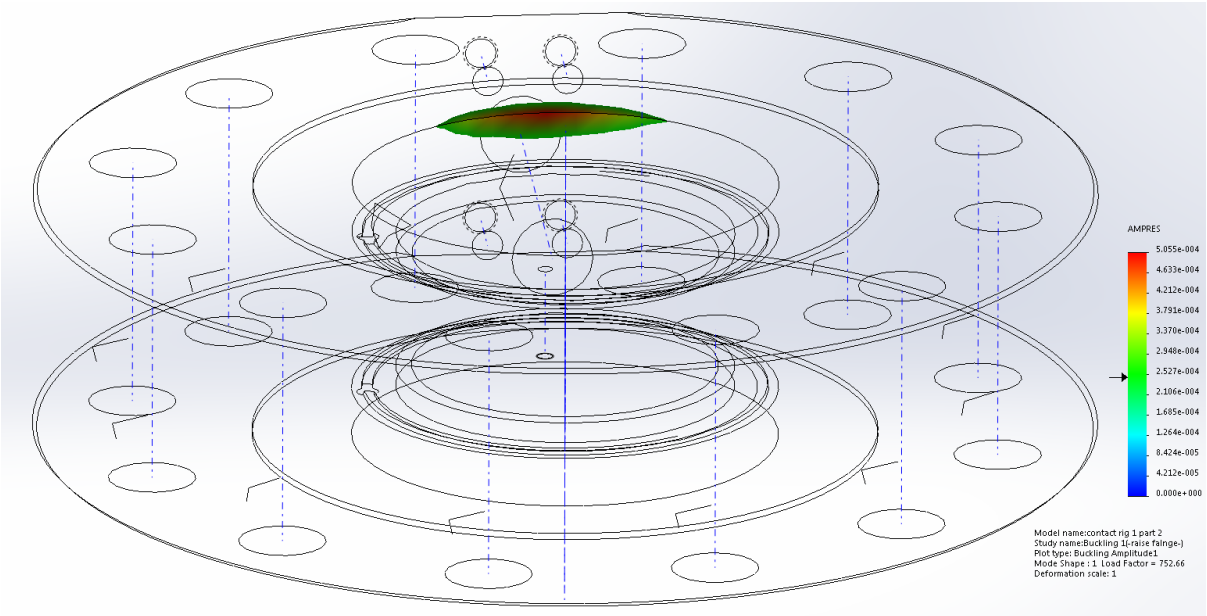

Figure 11: Buckling Resultant Amplitude displacement iso plot

Accordingly, the principle is fulfilled because:

- The hydrostatic test of the part under the test load case was completed without observation of deformation
- A Solidworks buckling analysis was completed according to the above specifications without showing significant displacement

(B.8.5) **Cyclic Fatigue Failure Design Check**

The principle of this design check is fulfilled by completing the requirements given in clause 18 of EN 13445-3, detailed assessment of fatigue life. However, clause 18 is intended for use on common geometry and is therefore difficult to accurately apply to this part. Solidworks fatigue modelling allows the gross plastic deformation operating condition load case to be fully cycled and produce results on expected cyclic damage and predicted life. Noting that the gross plastic deformation operating load case has partial safety factors applied, this analysis is inherently conservative.

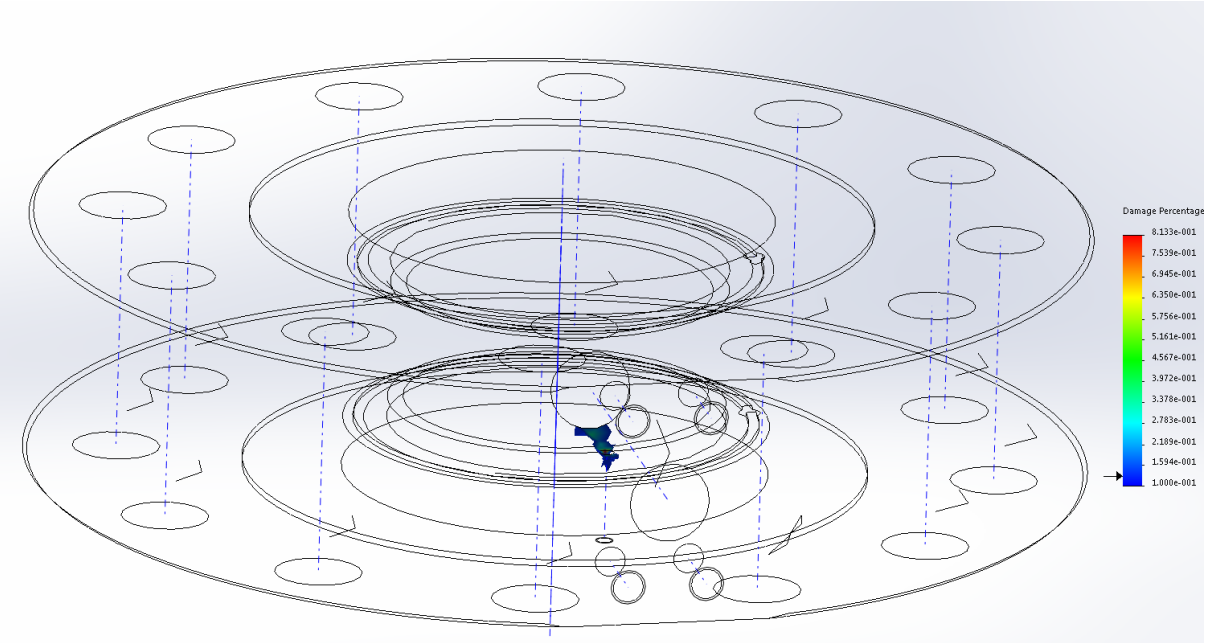

Figure 12: Damage percentage after 1000 full pressure cycles, Max 0.8%

This model fulfils the principle of this design check on the basis:

- The majority of predicted fatigue damage is not on a critical joint or fitting
- The fatigue analysis includes full cyclic loading of the bolting force, which will not be the case in normal operation as the bolts will be appropriately preloaded to prevent cyclic stresses
- The expected service life is expected to be much less than the predicted material life

(B.8.6) **Static Equilibrium Design Check**

The principle of this design check is that the effect of destabilising actions shall be smaller than the design effect of the stabilising actions. Notably:

- Partial safety factors shall be as used in Gross Plastic Deformation (B.8.2) design test
- Stabilising actions shall be represented by lower design values, while destabilising actions by upper design values

Destabilising effects include: internal pressure, which is attempting to separate the part from the parts above it and below it, and self-weight. Stabilising effects include the clamping force of the M39 bolts.

The only foreseeable condition in which the part is not in static equilibrium is if the bolts attaching the part to flanges above and below it fail, allowing the internal pressure to separate the part the parts above and below it. Earlier design checks verified the part material integrity with respect to plastic deformation and buckling, so dynamic situations resulting from these failure modes are not considered.

Flange bolting calculations according to EN 1591-1 were carried out and are documented separately which ensure that the bolts are sufficiently preloaded to meet a leak tightness criterion and prevent the system departing from static equilibrium.

Therefore, the principle is fulfilled.

Because all design checks have been satisfied, the part meets the requirements of Annex B – Design By Analysis, Direct Route.

Appendix B – Proof Test Certificates

Proof Test Report

Overview:

Vessel Manufacturer:	The University of Edinburgh. Machining subcontracted to Hughes Engineering Limited, Glasgow
Vessel ID:	Contact rig 1 part 2 (sensor block plate), E02
Date:	13 July 2018
Location:	Pumped Heat Energy Storage Lab, University of Edinburgh, Edinburgh
Test Pressure:	310 bar
Medium:	Hydraulic Oil
Holding Time:	30 minutes
Test Gauge:	0-700 bar, serial no. 105497-06

Remarks:

No signs of general plastic yielding

No signs of local deformations

No leaks observed from the pressure envelope.

Conclusion:

The pressure vessel meets the acceptance criteria for hydrostatic proof testing according to EN 13445-5:2014.

Inspector:	Mr. Daniel McKinley
Signature of Inspector:	
Verified by:	Prof. Win Rampen
Signature of Verifier:	
Date:	13 July 2018

A.2 Packed-Column Apparatus Design Drawings

Manufacturing drawings for key packed-column components are included in this section. Part nomeclature varied slightly throughout the project, so for clarity drawing names are referenced with part names in the following table . This is also the order in which the drawings are presented.

Drawing Name	Part Name	Qty. Produced
heating block 1 part 1	heater	1
contact rig 1 part 2	gas plate	4
contact rig 1 part 3	sensor block	4
contact rig 1 part 15	liquid plate	4
contact rig 1 part 20	spacer plate	2
heat exchange pipe	column	2

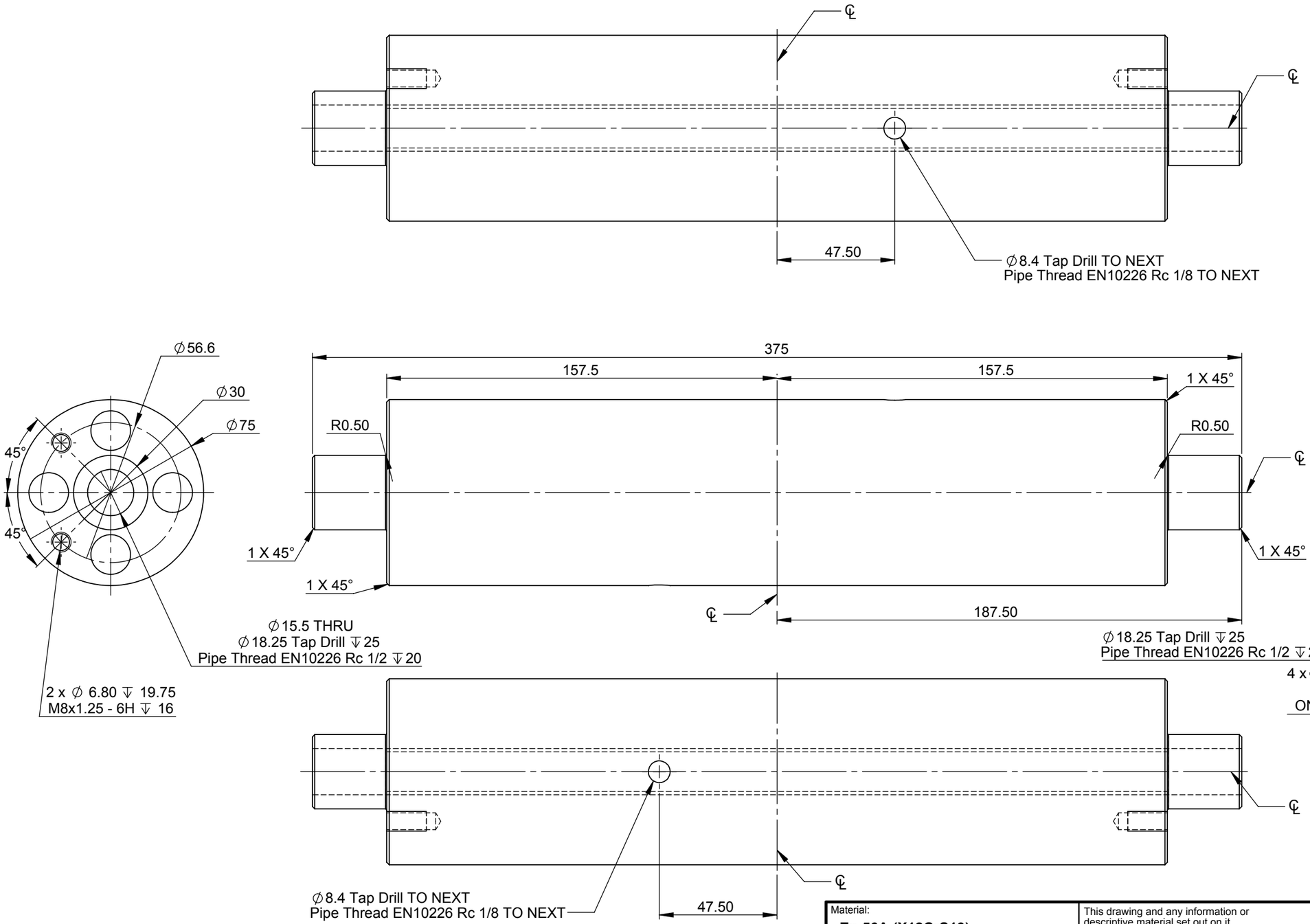

Material: **En 56A (X12CrS13)**	This drawing and any information or descriptive material set out on it are the confidential and copyright property of The University of Edinburgh. © and MUST NOT BE DISCLOSED, COPIED, LOANED in whole or part or used for any purpose without the written permission of The University of Edinburgh.	Description: **Heating block**	
Finish:			
Unless Otherwise Stated: 0 ± 1 Angular Tol.: **0.1°** 0.0 ± 0.1 Surface Finish: **0.8µm** 0.00 ± 0.0 All Dimensions: **mm**	Certification Required: EN 13445:2014	Drawn by: **DAN MCKINLEY**	Drawn Date: **14/07/17**
Drawing Scale: **1:1.7**	**Company Confidential**	Checked/Approved by: **WIN RAMPEN**	Checked/Approved Date: **18/07/17**
Approx Weight: **8306.79** g	Legal Owner: THE UNIVERSITY of EDINBURGH Pumped-Heat Energy Storage Project The King's Buildings, EH9 3JL Edinburgh	Part Number: **Heating block 1 part 1**	
Projection Method: **THIRD ANGLE** Sheet Size: **A3**		Drawing Number:	Sheet: **1 of 1** Revision:

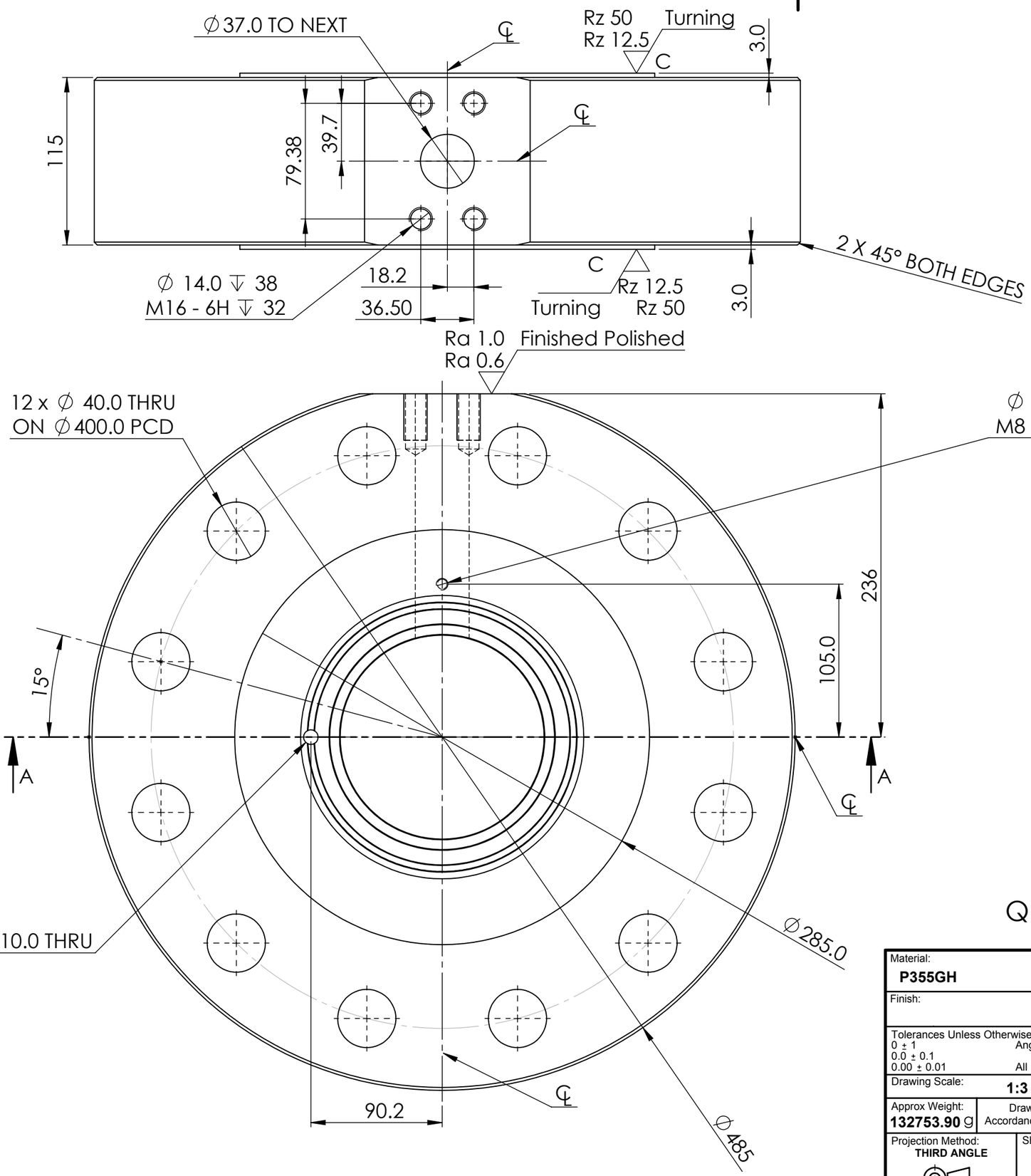

QUANTITY 4

Material: **P355GH**	This drawing and any information or descriptive material set out on it are the confidential and copyright property of The University of Edinburgh. © and MUST NOT BE DISCLOSED, COPIED, LOANED in whole or part or used for any purpose without the written permission of The University of Edinburgh.	Description: **Gas sandwich plate**	
Finish:			
Tolerances Unless Otherwise Stated: 0 ± 1 Angular Tol.: **0.1°** 0.0 ± 0.1 0.00 ± 0.01 All Dimensions: **mm**	Certification Required: EN 10204:2004 TYPE 3.1	Drawn by: **DAN MCKINLEY**	Drawn Date: **12/07/17**
Drawing Scale: **1:3**	**Company Confidential**	Checked/Approved by: **WIN RAMPEN**	Checked/Approved Date: **19/07/17**
Approx Weight: **132753.90** g; Drawing Produced In Accordance With ISO Standard	Legal Owner: THE UNIVERSITY of EDINBURGH	Part Number: **contact rig 1 part 2**	
Projection Method: **THIRD ANGLE**; Sheet Size: **A3**	Pumped-Heat Energy Storage Project The King's Buildings, EH9 3JL Edinburgh	Drawing Number:	Sheet: **1 of 3**; Revision:

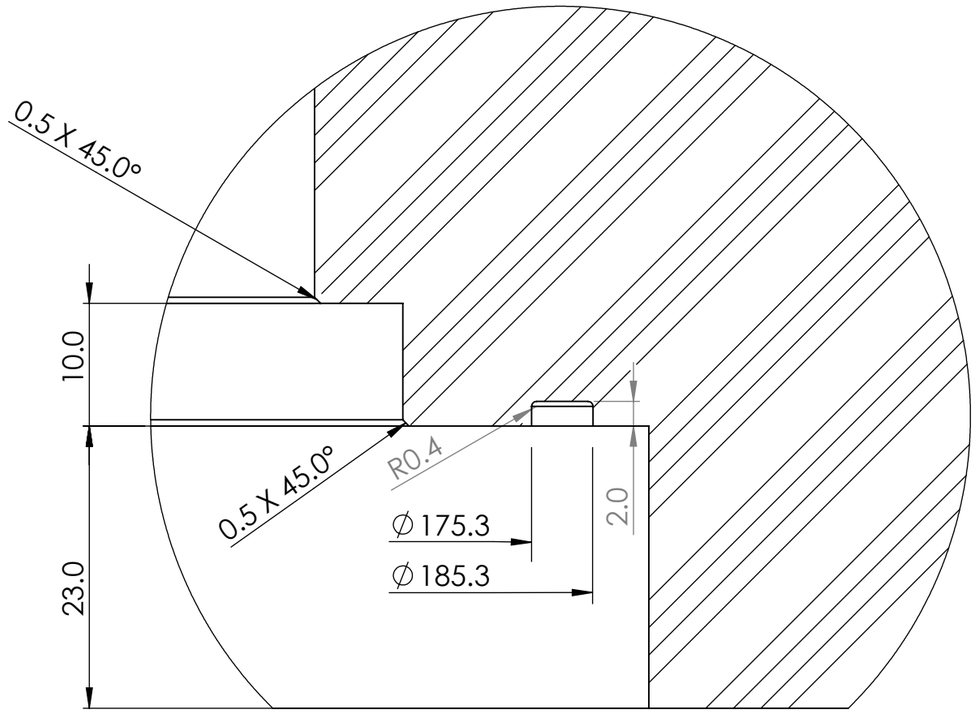

DETAIL B
SCALE 2 : 1

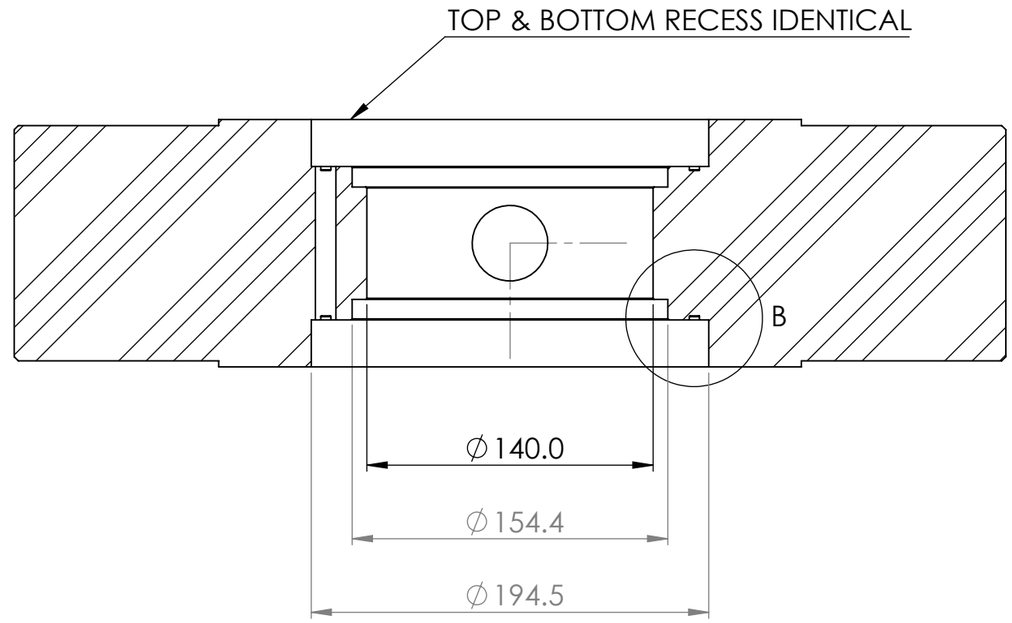

SECTION A-A

Material: **P355GH**	This drawing and any information or descriptive material set out on it are the confidential and copyright property of The University of Edinburgh. © and MUST NOT BE DISCLOSED, COPIED, LOANED in whole or part or used for any purpose without the written permission of The University of Edinburgh.	Description: **Gas sandwich plate**	
Finish:			
Tolerances Unless Otherwise Stated: 0 ± 1 / 0.0 ± 0.1 / 0.00 ± 0.01 — Angular Tol.: **0.1°** — All Dimensions: **mm**	Certification Required: EN 10204:2004 TYPE 3.1	Drawn by: **DAN MCKINLEY**	Drawn Date: **12/07/17**
Drawing Scale: **1:3**	**Company Confidential**	Checked/Approved by: **WIN RAMPEN**	Checked/Approved Date: **19/07/17**
Approx Weight: **132753.90 g** — Drawing Produced In Accordance With ISO Standard	Legal Owner: THE UNIVERSITY of EDINBURGH — Pumped-Heat Energy Storage Project, The King's Buildings, EH9 3JL Edinburgh	Part Number: **contact rig 1 part 2**	
Projection Method: **THIRD ANGLE** — Sheet Size: **A3**		Drawing Number:	Sheet: **2 of 3** — Revision:

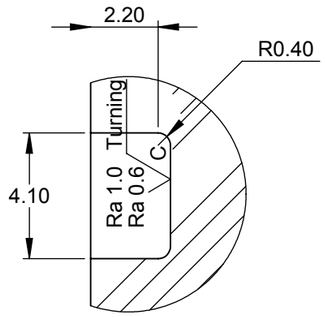

DETAIL B
SCALE 5 : 1

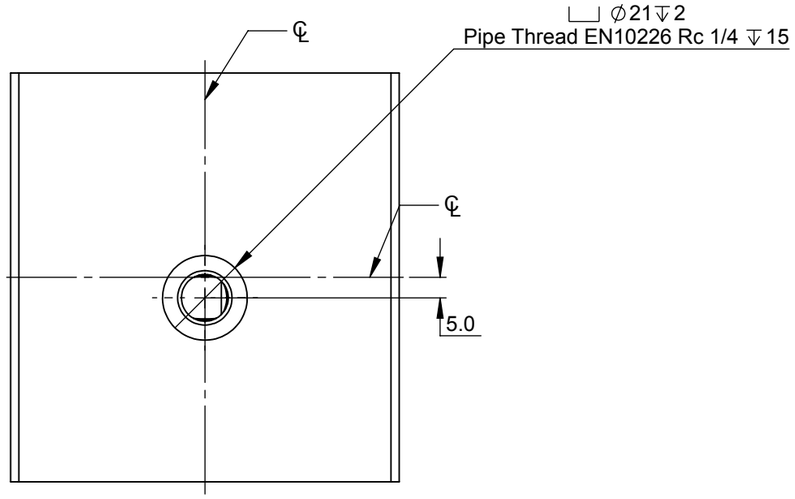

SECTION A-A

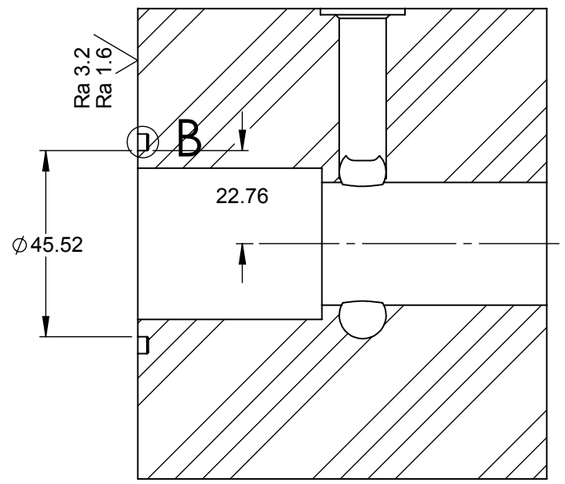

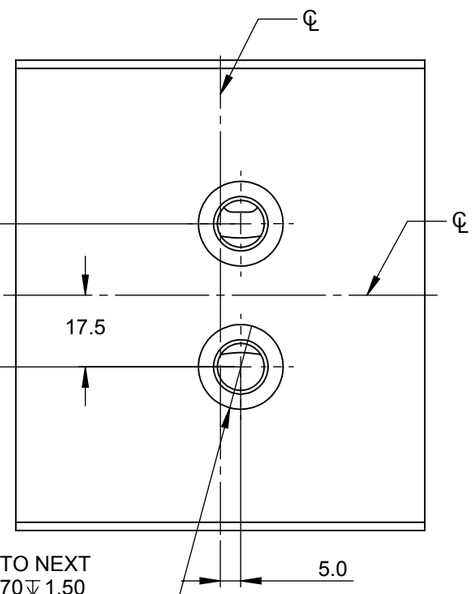

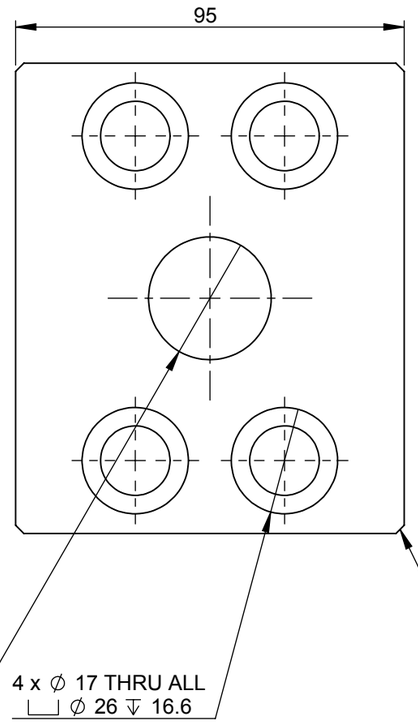

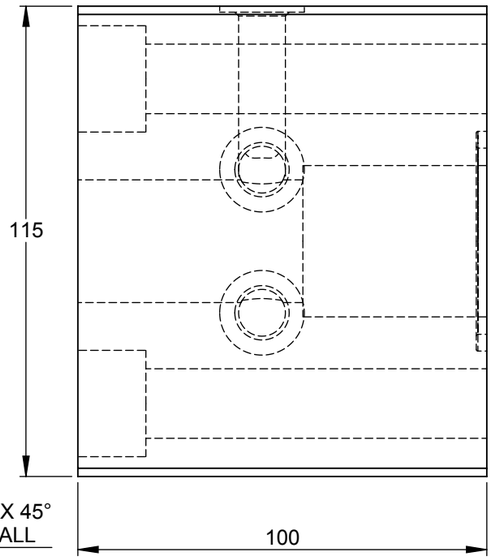

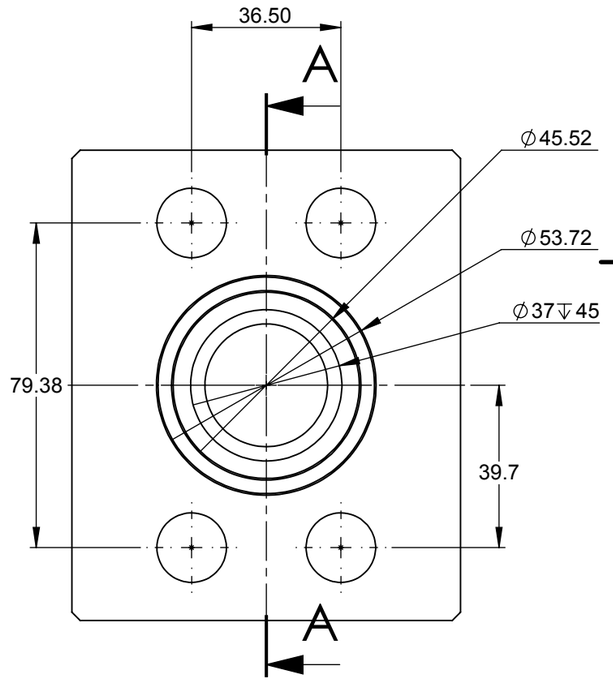

QUANTITY 4

Material: **P355NL2** Finish:	This drawing and any information or descriptive material set out on it are the confidential and copyright property of The University of Edinburgh. © and MUST NOT BE DISCLOSED, COPIED, LOANED in whole or part or used for any purpose without the written permission of The University of Edinburgh.	Description: **Gas outlet sensor block**	
Unless Otherwise Stated: 0 ± 1 0.0 ± 0.1 0.00 ± 0.0 Angular Tol.: **0.1 °** Surface Finish: **0.8µm** All Dimensions: **mm**	Certification Required: EN 10204:2004 TYPE 3.1	Drawn by: **DAN MCKINLEY**	Drawn Date: **22/06/2017**
Drawing Scale: **1:1.5**	**Company Confidential**	Checked/Approved by: **WIN RAMPEN**	Checked/Approved Date: **19/07/17**
Approx Weight: **6838.41** g Drawing Produced In Accordance With ISO Standard	Legal Owner: THE UNIVERSITY of EDINBURGH Pumped-Heat Energy Storage Project The King's Buildings, EH9 3JL Edinburgh	Part Number: **contact rig 1 part 3**	
Projection Method: **THIRD ANGLE** Sheet Size: **A3**		Drawing Number:	Sheet: **1 of 2** Revision: **C**

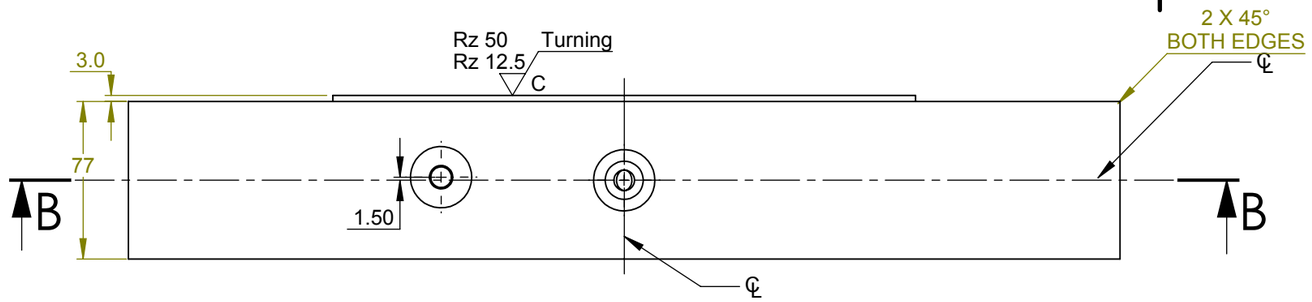

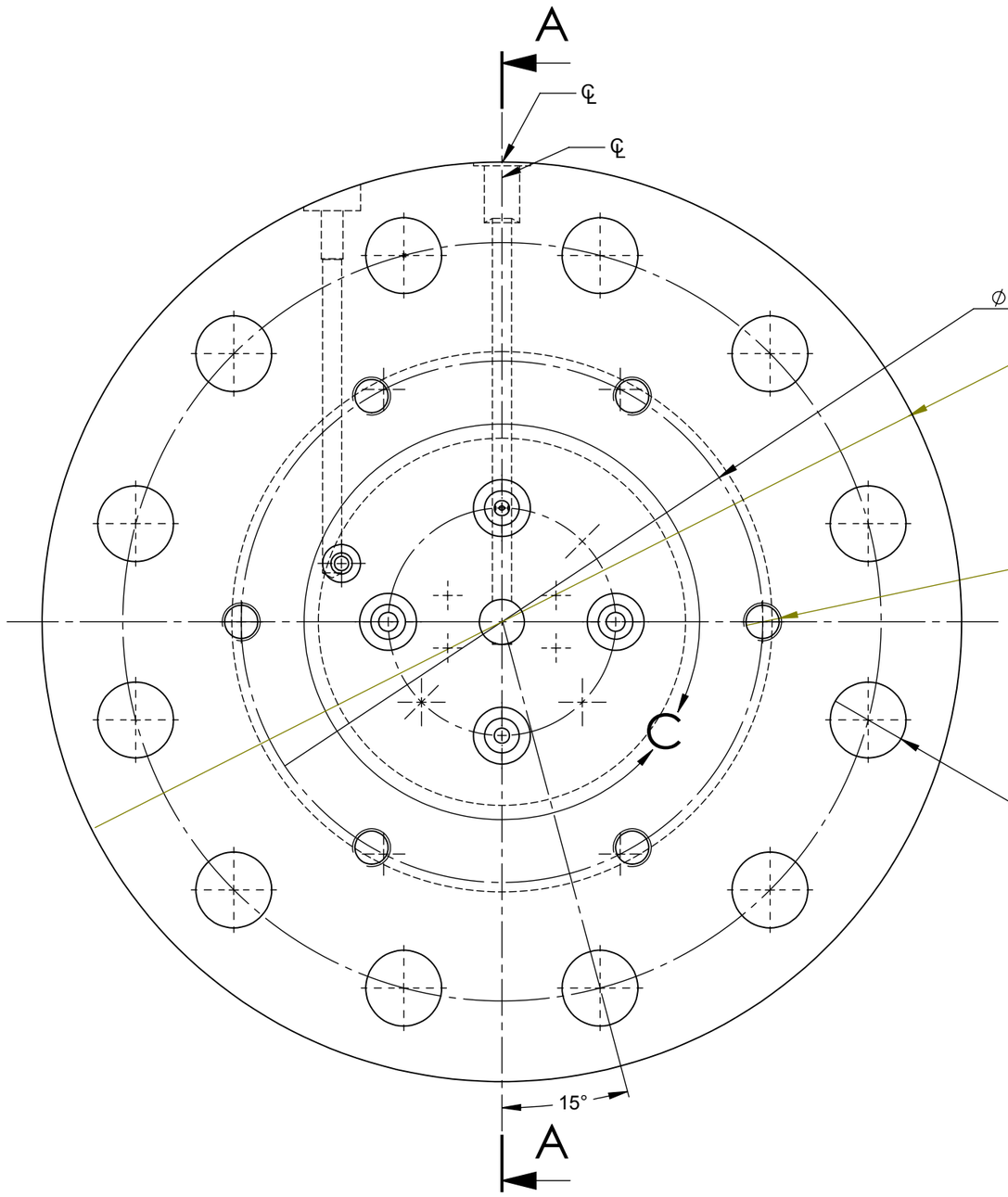

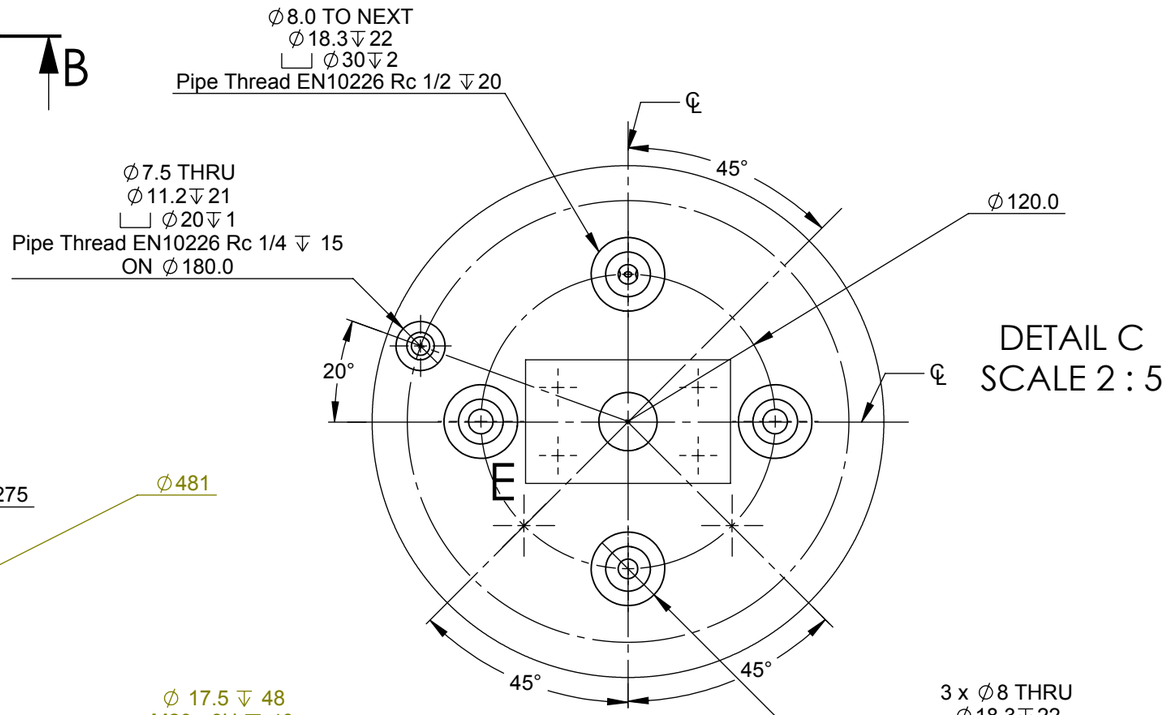

DETAIL C
SCALE 2 : 5

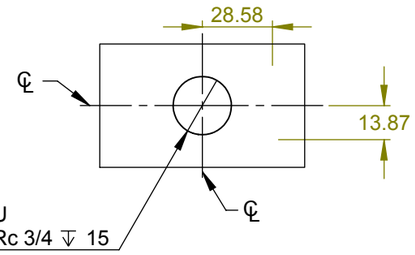

DETAIL E
SCALE 2 : 5

QUANTITY 4

Material: **P355GH**		This drawing and any information or descriptive material set out on it are the confidential and copyright property of The University of Edinburgh. © and MUST NOT BE DISCLOSED, COPIED, LOANED in whole or part or used for any purpose without the written permission of The University of Edinburgh.	Description: **Tube end cap**
Finish:			
Tolerances Unless Otherwise Stated: 0 ± 1 (Angular Tol.: **0.1°**) 0.0 ± 0.1 0.00 ± 0.01 (All Dimensions: **mm**)		Certification Required: EN 10204:2004 TYPE 3.1	Drawn by: **DAN MCKINLEY** / Drawn Date: **27/06/17**
Drawing Scale: **1:3**		**Company Confidential**	Checked/Approved by: **WIN RAMPEN** / Checked/Approved Date: **19/07/17**
Approx Weight: **100699.52** g	Drawing Produced In Accordance With ISO Standard	Legal Owner: THE UNIVERSITY of EDINBURGH	Part Number: **contact rig 1 part 15**
Projection Method: **THIRD ANGLE**	Sheet Size: **A3**	Pumped-Heat Energy Storage Project, The King's Buildings, EH9 3JL Edinburgh	Drawing Number: / Sheet: **1 of 3** / Revision:

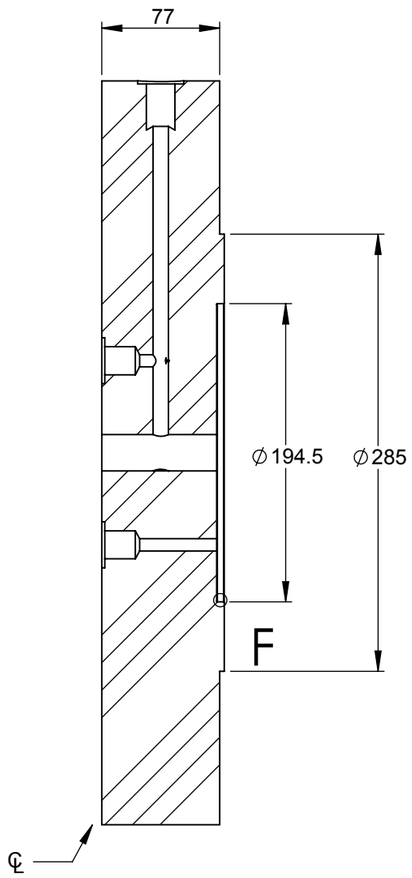

SECTION A-A

DETAIL F
SCALE 5 : 1

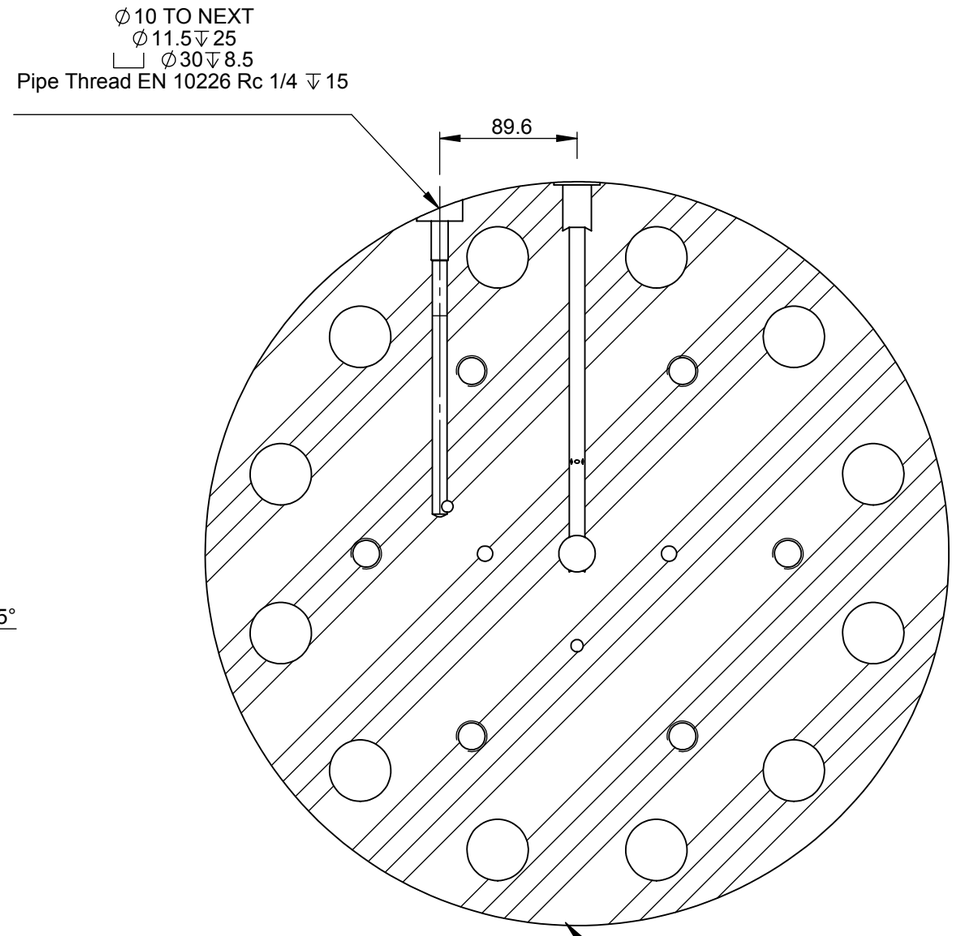

SECTION B-B

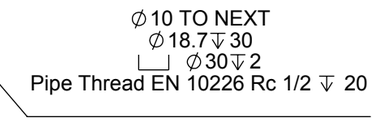

Material: **P355GH**		This drawing and any information or descriptive material set out on it are the confidential and copyright property of The University of Edinburgh. © and MUST NOT BE DISCLOSED, COPIED, LOANED in whole or part or used for any purpose without the written permission of The University of Edinburgh.	Description: **Tube end cap**
Finish:			
Tolerances Unless Otherwise Stated: 0 ± 1, 0.0 ± 0.1, 0.00 ± 0.01	Angular Tol.: **0.1°** All Dimensions: **mm**	Certification Required: EN 10204:2004 TYPE 3.1	Drawn by: **DAN MCKINLEY** / Drawn Date: **27/06/17**
Drawing Scale: **1:4**		**Company Confidential**	Checked/Approved by: **WIN RAMPEN** / Checked/Approved Date: **19/07/17**
Approx Weight: **100699.52** g	Drawing Produced In Accordance With ISO Standard	Legal Owner: THE UNIVERSITY of EDINBURGH	Part Number: **contact rig 1 part 15**
Projection Method: **THIRD ANGLE**	Sheet Size: **A3**	Pumped-Heat Energy Storage Project, The King's Buildings, EH9 3JL Edinburgh	Drawing Number: / Sheet: **2 of 3** / Revision:

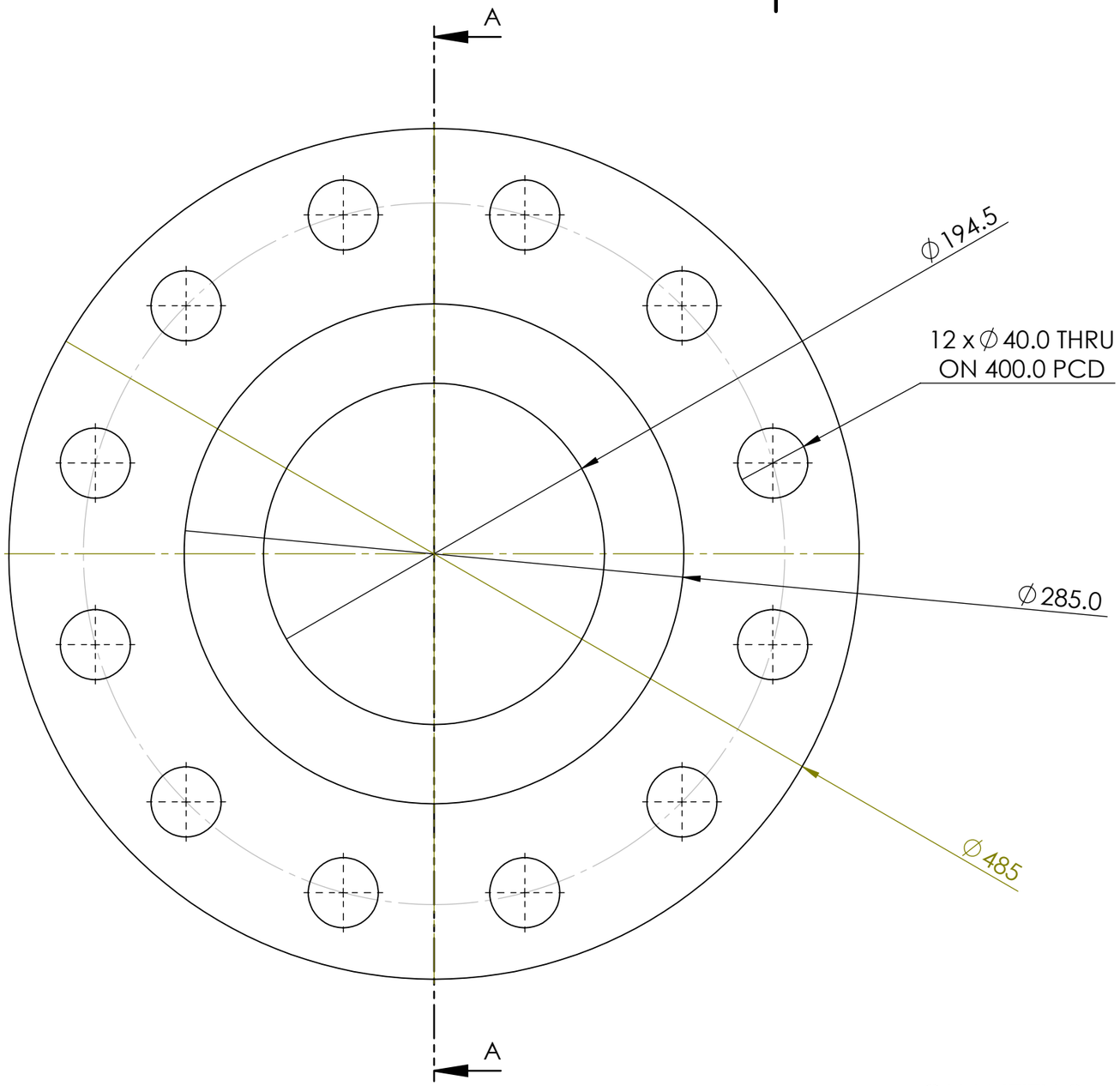

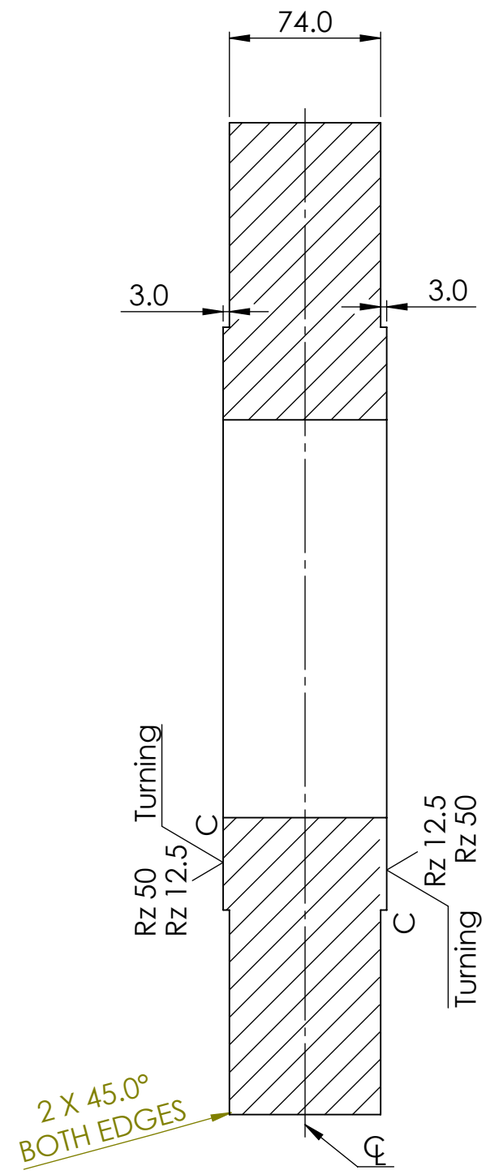

SECTION A-A

QUANTITY 2

Material: **P355GH**		This drawing and any information or descriptive material set out on it are the confidential and copyright property of The University of Edinburgh. © and MUST NOT BE DISCLOSED, COPIED, LOANED in whole or part or used for any purpose without the written permission of The University of Edinburgh.	Description: **column sump spacer plate**
Finish:			
Tolerances Unless Otherwise Stated: 0 ± 1 Angular Tol.: **0.1°** 0.0 ± 0.1 0.00 ± 0.01 All Dimensions: **mm**		Certification Required: EN 10204:2004 TYPE 3.1	Drawn by: **DAN MCKINLEY** / Drawn Date: **12/07/17**
Drawing Scale: **1:3**		**Company Confidential**	Checked/Approved by: **WIN RAMPEN** / Checked/Approved Date: **19/07/17**
Approx Weight: **82904.45** g	Drawing Produced In Accordance With ISO Standard	Legal Owner: THE UNIVERSITY of EDINBURGH	Part Number: **contact rig 1 part 20**
Projection Method: **THIRD ANGLE**	Sheet Size: **A3**	Pumped-Heat Energy Storage Project The King's Buildings, EH9 3JL Edinburgh	Drawing Number: / Sheet: **1 of 1** / Revision:

MODEL No: SW61580
SEAL KIT No:

STANDARD FLANGES TO EN1092-1
SIZE: DN200 PN250
SEALED WITH GASKET

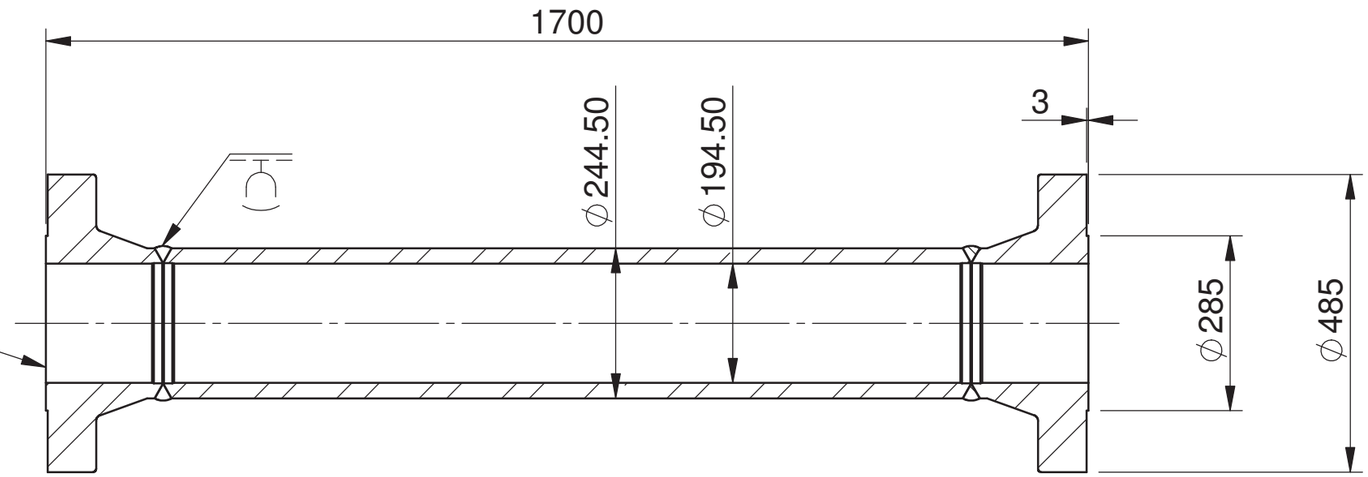

SECTION A-A

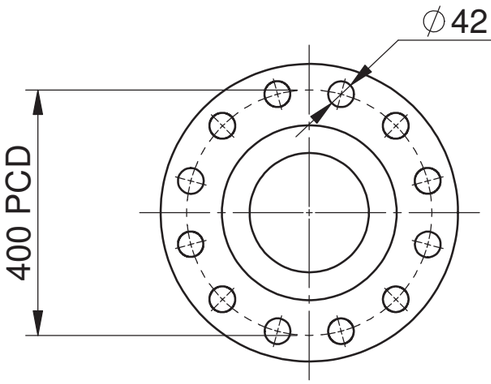

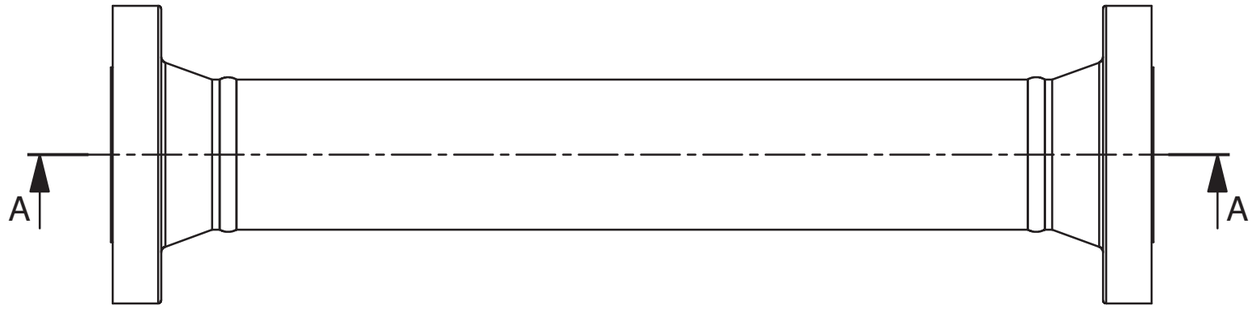

USED ON HYSTAT JOB REF : 104025

DESIGN CODE:	PD5500:2015	CERTIFICATION REQUIRED	
THIRD PARTY APPROVAL STATUS:	LLOYDS REGISTER	LEVEL 1 : BSEN10204:2004 TYPE 3.2	☐
MATERIAL: CYLINDER	EN10216-3 P355N	LEVEL 3 : BSEN10204:2004 TYPE 3.1	☒
END CAPS	ASTM A350 LF2	ATEX	☐
PISTON	N/A	FORM X	☐

SPECIFICATION			DESIGN TEMPERATURE:	-50 TO +400ºC
CAPACITY:	50	LITRES	FLUID/S:	VARIOUS
OPERATING PRESSURE:	200	BARG	ENVIRONMENT:	INDUSTRIAL
DESIGN PRESSURE:	200	BARG	SEALS:	J WALKER METAFLEX
TEST PRESSURE:	286	BARG	BURST DISC:	

CE
PED 2014/68/EU

REV	DESCRIPTION	DRN	DATE
A	WAS -120 + LENGTH WAS 2000	DM	10/05/17

ALL DIMENSIONS IN MM UNLESS STATED

GENERAL TOLERANCES
O/D : -0 / +2MM
LENGTH : ± 3MM

3RD ANGLE ORTHO

HYSTAT Piston Accumulators
SPA FIELDS INDUSTRIAL ESTATE,
NEW STREET, SLAITHWAITE,
HUDDERSFIELD, WEST YORKSHIRE,
ENGLAND, HD7 5BB.
TEL : +44 (0) 1484 845740
FAX : +44 (0) 1484 842254
E-MAIL : info@hystat.co.uk
WEB : www.hystat.co.uk

TITLE / MODEL No	HEAT EXCHANGE PIPE SW61580				
DRN	DM	DATE	20/12/16	CALCULATIONS	CS104025
CHKD	AB	DATE	20/12/16		
A3	SCALE 1:10	MASS	394.10 KG	DRG No	SW61580
				REV	A

A.3 Shell and Tube Heat Exchanger Design

The full output from UniSim Shell & Tube Heat Exchanger design software is included in this section. This design was carried out to assess the feasibility of this type of heat exchanger for the proposed 633 kW PHES pilot plant, and found to be too large and costly for this plant.

```
--------------------------------------------------------------------------------
 UniSim Shell-Tube Exchanger Modeler              (UniSim STE R440 Build
 18-03-2015)

     DESIGN
 File: C:\...\ownCloud\ownCloud\GL Contactor Rig\Modeling\UniSim HX
 Design\HX_final.STEI
 Run: 18-Sep-2019 13:19

--------------------------------------------------------------------------------

    THIS PROGRAM CONTAINS THE FOLLOWING PACKAGES:


    STE    440.0  UniSim Shell-Tube Exchanger Modeler

    PPP    440.0  Physical Property Package

    HTPST2 440.0  HEAT TRANSFER AND PRESSURE DROP PACKAGE

***   MESSAGES OUTPUT ***

** WARNING P11 *  Stream 1 item 303.1  :  Reference Pressure : bar
Input value (  200.00 ) is above expected range ( 0.00100  /   150.00 )

********************************************************************************

*** WARNING *** The following input item(s) are beyond the expected range:
204.3  (1)  Inlet pressure            200.0 bar           (0.010 / 150.0)

********************************************************************************

*** WARNING *** The correlations for RODbaffles have been supplied by Phillips
Petroleum Company to enable users to design or check exchangers with
RODbaffles. However, the use of the correlations does not grant any licence
under any Phillips patent.

********************************************************************************

*** WARNING *** The front end head type specified is not usually suitable for
pressures greater than about 150 bar. You may like to consider a D type.

********************************************************************************

Review of Results of Thermal Calculations
*****************************************

No warning messages generated.

End of Review of Thermal Calculations
********************************************************************************

- - - - - - - - - - - - - - - - RESULTS SUMMARY - - - - - - - - - - - - - - - -
|                                                                              |
| Area Ratio (Actual/Required) 1.0622   Duty Ratio (Actual/Specified)  1.0000  |
| Area Ratio (Clean)           1.0622   Heat load      kW               1501.7 |
| Effective  MTD     C   8.24           Heat transfer area   m2     469.41    |
|  One pass  MTD         8.24                                                  |
|                                          Shellside   Tubeside     Overall    |
| Heat Transfer Coeff.    W/m2 K (Clean)     1000.00     778.67      412.24    |
|  (based on tube o.d.)          (Dirty)     1000.00     778.67      412.24    |
| Pressure Drop       (Actual/Specified)       0.104      0.079                |
|    Fraction of Actual Loss in Nozzles        1.000      1.000                |
|                                                                              |
| Resistances:   (Shellside/Tubeside/Wall)    0.001000 / 0.001284 / 0.000142   |
|      m2 K/W  Fouling: (Shell/Tube/Total)           0 /        0 /         0  |
|           Total Fouling for Area Ratio=1                           0.000151  |
|      (Scale Tubeside Resistance by 0.779 to get value based on i.d.)         |
 - - - - - - - - - - - - - - - - - - - - - - - - - - - - - - - - - - - - - - -
```

| I=input T=tube-layout
----------EXCHANGER SPECIFICATION----------| C=calc. D=default R=revised
| U=unset W=warning E=error

|INPUT ITEM No's

- - - - - - - - - - - - - - - DESIGN CONSTRAINTS - - - - - - - - - - - - - - -

Max.No.shells in series		5	I	Min.No.tubeside passes		1	D	103.2	107.5
Max.No.shells in parallel		5	I	Max.No.tubeside passes		16	D	103.3	107.4
Min.shell diameter	mm	254.0	D	Min.tube length	mm	1219.2	D	116.3	107.2
Max.shell diameter	mm	2540.0	D	Max.tube length	mm	6096.0	D	103.1	107.1
Shell diam.increments		DEFAULT	D	Tube len.increment	mm	1219.2	D	108.6	107.3
Shell dia.increment	mm		U					116.4	
Rows per seal-strip			U	Max.baffle pitch	mm	152.4	D	107.6	104.3

- - - - - - - - - - - - - - - BASIC GEOMETRY - - - - - - - - - - - - - - -

Front end head type		TEMA A	I	Orientation		HORIZONTAL	C	102.2	102.5
Shell type		TEMA E	I	Hot side		HOT TUBESIDE	I	102.3	102.6
Rear end head type		TEMA L	D	No.exchangers in parallel		1	R	102.4	103.3
Shell internal diam.	mm	1117.6	D	No.exchangers in series		1	R	103.1	103.2
Tubeplate thickness	mm	303.0	C	No.of tubeside passes		1	C	108.4	106.4
Shell thickness	mm	12.7	C	Normal/full bundle		NORMAL	I	108.5	105.6
Countercurrent in 1st pass		YES	I	Tubes in window		YES	D	103.4	103.6
Pass partition layout		H-BANDED	I	Nozzles on opposite sides		YES	D	110.6	103.5
Bundle-band orientn.		*	D	Tube alignment(inter-pass)		YES	D	115.3	116.1
Layout symmetry		CASE 1	D	Area fraction submerged			U	116.5	115.4

- - - - - - - - - - - - - - - BUNDLE SIZE - - - - - - - - - - - - - - -

Effective tube count		1456	C	First row to shell	mm	27.1	C	106.5	109.1
Bundle-shell diam.clear.mm		12.7	C	Last row to shell	mm	23.7	C	108.1	109.2
Pairs of sealing-strips		0	U	No. of blocked-off tubes		0		106.6	145.1

- - - - - - - - - - - - - - - TUBES - - - - - - - - - - - - - - -

Tube type		PLAIN	I					105.1	
Outside diameter	mm	19.0	D	Tube pitch	mm	25.4	D	105.2	105.4
Wall thickness	mm	2.1	D	Tube pattern (angle)		90	D	105.3	105.5
Tube length (straight)	mm	6096.0	C	Eff. straight length	mm	5387.0	C	106.1	
Dist.after blank.baffle	mm	403.0	C					109.4	

- - - - - - - - - - - BAFFLES AND INTERMEDIATE SUPPORTS - - - - - - - - - - -

Baffle type		ROD BAFFLES	I	Number of baffles		36	C	104.1	104.6
Baffle pitch	mm	152.4	D	Diam.clearance-tube	mm		U	104.3	108.3
Baffle thickness	mm		U	Dia.clearance-shell	mm	6.3	C	104.5	108.2
Baffle cut (percent)		0	C	Cut orientation		*	C	104.2	104.4
Baffle cut (area percent)			U					107	

Intm.supports(inlet)		0	D	Support/blanking baffle		NORMAL	I	113.1 109.3
Intm.supports/baffle		0	D	Long.baffle.leakage	%		U	113.2 112.3
Intm.supports(return)		0	D	Special support at nozzle		NO	D	113.3 118.2
U-bend extra supports		0	D	Int.sup(central nozz.)		0	D	112.6 112.5
- - - - - - - - - - - - - - - DESIGN AND MATERIALS - - - - - - - - - - - - - - -								
Shell-design T	C	486.63	C	Shell-design P (abs)	bar	16.45	D	114.1 114.2
Tubes-design T	C	534.63	C	Tubes-design P (abs)	bar	240.0	D	114.3 114.4
TEMA Class		TEMA B	I	Eff.crossflow fraction			U	114.5 113.6
ExchangerMetal	316 Stainless		I					141.1 142..
Thermal Con.	W/m K	16.84	C	Tube density	kg/m3	8020	C	141.3 141.4
Young's mod.	MN/m2	180491	C	Axial stress	MN/m2	0	D	141.5 141.6
- - - - - - - - - - - - - - - EXCHANGER INFORMATION - - - - - - - - - - - - - - -								
Exchanger weight(dry)	kg	47801	C	Weight of bundle	kg	10738	C	
(Full of water)	kg	54988	C					
- NOZZLES -								
		-----SHELLSIDE-----			-----TUBESIDE-----								
Nozzle function		Inlet	Outlet	Interm	Inlet	Outlet	Interm	DDD	DDD	131.1 121.1
Nozzle type		PLAIN	PLAIN	PLAIN	PLAIN	PLAIN	PLAIN	DDD	DDD	131.4 121.4
No.in parallel		1	1	1	1	1	1	DDC	CCC	130.. 120..
Orientation		Bottom	Top	Top	Top	Bottom	Bottom	CCC	CCC	131.6 121.6
Inside diameter	mm	40.89	40.89		50.50	40.89		CCU	CCU	131.3 121.3
Nominal Pipe Size	inches							UUU	UUU	132.4 122.4
Wall Thickness	mm							UUU	UUU	132.3 122.3
- - NOZZLE RESULTS - - -										
Pressure loss	bar	0.0078	0.0153		0.0187	0.0231				
Pressure loss % of total		7.512	14.65		5.943	7.328				
Velocity (Nozzle)	m/s	0.961	1.317		6.138	7.131				
Rho-v-sq.(Nozzle)	kg/m s2	892.3	1223		3515	9614				
" (Shell in/out)	kg/m s2									
"(Bundle in/out)	kg/m s2	823.4	578.5							
Max Rho-v-sq.for Design								UUU	UUU	132.1 122.1

- - - - - - - - - - - - - - - - - - PROCESS SUMMARY - - - - - - - - - - - - - - - - - -

		- HOT TUBESIDE -		- COLD SHELLSIDE -				
		Inlet	Outlet	Inlet	Outlet			
Temperature	C	400.00	60.00	20.00	360.00	IR	IR	204.1/2
Quality(vap mass frac)		1.000	1.000	0	0	II	II	202.3/4
Pressure	bar	200.0	196.0	13.00	12.00	WD	ID	204.3/6
Pressure loss	bar	0.315		0.104		C	C	
Allowed		4.000		1.000		I	I	204.4
Mass Flow	kg/h	13536		9326		I	C	202.2
Fouling Rest.	m2 K/W	0		0		D	D	204.5
Heat load	kW	1502		1502				
- - PROCESS METHODS - -								
Heat balance: revise		HEAT LOAD		HEAT LOAD		C	C	205.2
Liquid h.t.coef.	W/m2 K	500.0		1000		I	I	206.1

2-phase.h.t.c.	W/m2 K	500.0	500.0	I	I	206.2
Vapour h.t.coef.	W/m2 K	1000	500.0	I	I	206.3
Liquid h.t.coef.scaling		1.000	1.000	D	D	206.4
2-phaseh.t.coef.scaling		1.000	1.000	D	D	206.5
Vapour h.t.coef.scaling		1.000	1.000	D	D	206.6
Pressure drop scaling		1.000	1.000	D	D	207.5
Vap.shear enhancement		YES	*	D		210.1
Wet wall desuperheat.		NO	*	I		210.2
Colburn-Hougen method		NO	*	D		210.4
Boiling curve		*	+CORRECTIONS		D	210.5
Refce. heat flux	W/m2		0	U	C	211.1
Boiling curve expo.			0	U	C	211.2
Refce. temp. diff.	C		1.000	U	C	211.6
Subcooled boiling		IGNORED	IGNORED		I	211.4
Post dryout ht.trans.		*	NO		R	211.5
No.points on curve		11	11	C	C	205.4
Fit to ht.load curve		BEST FIT	BEST FIT	I	I	205.5
Gravity pressure changes		NO GRAV.	NO GRAV.	D	D	205.6
- DESIGN CONSTRAINTS -						
Max.HeatFlux	W/m2			U	U	207.1
Nozzles press.drop	%	15.00	15.00	D	D	207.2
Min.velocity	m/s	0.0000100		D		207.3
Max.velocity	m/s	100.0		D		207.4

- - - - - - - - - - - - OUTPUT/CALCULATION OPTIONS - - - - - - - - - - - - -

Units of output	SI	I	Tube Layout Data	IGNORE	D	010.1 020.3
Physical property	FILE	D	Vibration check	NONE	D	010.2 013.1
Summary ouput	YES	D	Pressure drop details	NO	D	011.1 013.2
Exchanger and process output	YES	D	Inter-shell Conditions	NO	D	011.2 013.5
Shell integration output	NO	D	Shellside flow distibution	NO	D	011.3 013.4
Calculated stream curves	NO	D	General interface output	YES	I	013.6 012.1
Local temp. cross (design)	YES	D				020.1
Basis for design	MINIMUM COST	D	Highest area ratio	1.250	D	020.4 020.5

*** STREAM HEAT LOAD CURVES USED BY STE ***

Cold Shellside Stream: Pressure dependence ignored
Flow = 9326. kg/h 2.591 kg/s
Hot Tubeside Stream: Pressure dependence ignored
Flow = 13536. kg/h 3.760 kg/s

Point	Pressure bar	Pr.change bar	Temperature C	Enthalpy kJ/kg	Quality	--- Heat Load --- kW	fraction
Cold	(Cold) Stream 2						
Inlet	13.00	0.00000	20.00	-97.7	0.0000	0.0	0.0000
1	12.98	-0.01500	20.00	-97.7	0.0000	0.0	0.0000
2	13.00	0.00000	71.72	-39.7	0.0000	150.2	0.1000
3	13.00	0.00000	115.61	18.2	0.0000	300.3	0.2000
4	13.00	0.00000	154.54	76.2	0.0000	450.5	0.3000
5	13.00	0.00000	189.94	134.2	0.0000	600.7	0.4000
6	13.00	0.00000	222.66	192.1	0.0000	750.9	0.5000
7	13.00	0.00000	253.23	250.1	0.0000	901.0	0.6000
8	13.00	0.00000	282.03	308.1	0.0000	1051.2	0.7000
9	13.00	0.00000	309.33	366.0	0.0000	1201.4	0.8000
10	13.00	0.00000	335.28	424.0	0.0000	1351.5	0.9000
11	12.01	-0.98500	360.00	482.0	0.0000	1501.7	1.0000
Outlet	12.00	-1.00000	360.00	482.0	0.0000	1501.7	1.0000
Hot	(Hot) Stream 1						
Inlet	200.00	0.00000	400.00	407.6	1.0000	0.0	0.0000
1	199.94	-0.06000	400.00	407.6	1.0000	0.0	0.0000
2	200.00	0.00000	365.32	367.7	1.0000	-150.2	0.1000
3	200.00	0.00000	330.64	327.7	1.0000	-300.3	0.2000
4	200.00	0.00000	295.99	287.8	1.0000	-450.5	0.3000
5	200.00	0.00000	261.42	247.9	1.0000	-600.7	0.4000
6	200.00	0.00000	226.98	207.9	1.0000	-750.9	0.5000
7	200.00	0.00000	192.73	168.0	1.0000	-901.0	0.6000
8	200.00	0.00000	158.78	128.0	1.0000	-1051.2	0.7000
9	200.00	0.00000	125.23	88.1	1.0000	-1201.4	0.8000
10	200.00	0.00000	92.24	48.2	1.0000	-1351.5	0.9000
11	196.06	-3.94000	60.00	8.2	1.0000	-1501.7	1.0000
Outlet	196.00	-4.00000	60.00	8.2	1.0000	-1501.7	1.0000

SUMMARY OF ALTERNATIVE DESIGNS WHOSE COST RATIO IS NOT MORE THAN 1.250

SHELLS IN PARA -PASSES	SHELL DIAM. MM	TUBE LENGTH MM	NUM.OF TUBES	--- BAFFLES --- NUM SEAL MM	PITCH MM	/CUT STR- O/O	NUM ---------- NOZZLE DIAMETERS SHELL SIDE IPS	IN MM	/ OUT MM	/ INTER MM	TUBE SIDE IN MM	/ OUT MM	/ INTER MM	PRESSURE DROPS OVER SHELL / TUBE BAR	COST RATIO ITEM/ CHOSEN
1* 1- 1	1117.6	6096.0	1456	36/	152.4/	0. 0		40.9/	40.9/	0.0	50.5/	40.9/	0.0	0.104/ 0.315	1.062 1.00
1* 1- 1	1295.4	4876.8	1968	28/	152.4/	0. 0		40.9/	40.9/	0.0	50.5/	40.9/	0.0	0.104/ 0.315	1.098 1.15
2* 1- 1	787.4	6096.0	709	36/	152.4/	0. 0		26.6/	40.9/	0.0	40.9/	26.6/	0.0	0.066/ 0.267	1.052 1.13
2* 1- 1	889.0	4876.8	910	28/	152.4/	0. 0		26.6/	40.9/	0.0	40.9/	26.6/	0.0	0.066/ 0.267	1.043 1.25
1* 1- 2	THERE IS AN EFFECTIVE TEMPERATURE CROSS IN THE 1 ST SHELL														
1* 1- 4	FAILURE OF THE TEMPERATURE CALCULATION IN THE 1 ST SHELL - CHECK THAT THE UNIT IS FEASIBLE														
1* 1- 6	FAILURE OF THE TEMPERATURE CALCULATION IN THE 1 ST SHELL - CHECK THAT THE UNIT IS FEASIBLE														
1* 1- 8	FAILURE OF THE TEMPERATURE CALCULATION IN THE 1 ST SHELL - CHECK THAT THE UNIT IS FEASIBLE														
1* 1-10	FAILURE OF THE TEMPERATURE CALCULATION IN THE 1 ST SHELL - CHECK THAT THE UNIT IS FEASIBLE														
1* 1-12	FAILURE OF THE TEMPERATURE CALCULATION IN THE 1 ST SHELL - CHECK THAT THE UNIT IS FEASIBLE														
1* 1-14	FAILURE OF THE TEMPERATURE CALCULATION IN THE 1 ST SHELL - CHECK THAT THE UNIT IS FEASIBLE														
1* 1-16	FAILURE OF THE TEMPERATURE CALCULATION IN THE 1 ST SHELL - CHECK THAT THE UNIT IS FEASIBLE														
1* 2- 1	787.4	6096.0	709	36/	152.4/	0. 0		40.9/	50.5/	50.5	62.7/				

```
      40.9/  62.7   0.099/  0.283 1.052  1.13
255   1* 2- 1  889.0  4876.8    910  28/  152.4/ 0.   0   40.9/  50.5/  50.5   62.7/
      40.9/  62.7   0.099/  0.282 1.043  1.25
256   1* 2- 2     THERE IS AN EFFECTIVE TEMPERATURE CROSS IN THE 1 ST SHELL
257
258   1* 2- 4     FAILURE OF THE TEMPERATURE CALCULATION IN THE 1 ST SHELL - CHECK THAT
      THE UNIT IS FEASIBLE
259   1* 2- 6     FAILURE OF THE TEMPERATURE CALCULATION IN THE 1 ST SHELL - CHECK THAT
      THE UNIT IS FEASIBLE
260   1* 2- 8     FAILURE OF THE TEMPERATURE CALCULATION IN THE 1 ST SHELL - CHECK THAT
      THE UNIT IS FEASIBLE
261   1* 2-10     FAILURE OF THE TEMPERATURE CALCULATION IN THE 1 ST SHELL - CHECK THAT
      THE UNIT IS FEASIBLE
262   1* 2-12     FAILURE OF THE TEMPERATURE CALCULATION IN THE 1 ST SHELL - CHECK THAT
      THE UNIT IS FEASIBLE
263
264   1* 2-14     FAILURE OF THE TEMPERATURE CALCULATION IN THE 1 ST SHELL - CHECK THAT
      THE UNIT IS FEASIBLE
265   1* 2-16     FAILURE OF THE TEMPERATURE CALCULATION IN THE 1 ST SHELL - CHECK THAT
      THE UNIT IS FEASIBLE
266   1* 3- 2     THERE IS AN EFFECTIVE TEMPERATURE CROSS IN THE 1 ST SHELL
267   1* 3- 4     FAILURE OF THE TEMPERATURE CALCULATION IN THE 1 ST SHELL - CHECK THAT
      THE UNIT IS FEASIBLE
268   1* 3- 6     FAILURE OF THE TEMPERATURE CALCULATION IN THE 1 ST SHELL - CHECK THAT
      THE UNIT IS FEASIBLE
269
270   1* 3- 8     FAILURE OF THE TEMPERATURE CALCULATION IN THE 1 ST SHELL - CHECK THAT
      THE UNIT IS FEASIBLE
271   1* 3-10     FAILURE OF THE TEMPERATURE CALCULATION IN THE 1 ST SHELL - CHECK THAT
      THE UNIT IS FEASIBLE
272   1* 3-12     FAILURE OF THE TEMPERATURE CALCULATION IN THE 1 ST SHELL - CHECK THAT
      THE UNIT IS FEASIBLE
273   1* 3-14     FAILURE OF THE TEMPERATURE CALCULATION IN THE 1 ST SHELL - CHECK THAT
      THE UNIT IS FEASIBLE
274   1* 3-16     FAILURE OF THE TEMPERATURE CALCULATION IN THE 1 ST SHELL - CHECK THAT
      THE UNIT IS FEASIBLE
275
276   1* 4- 2     THERE IS AN EFFECTIVE TEMPERATURE CROSS IN THE 1 ST SHELL
277   1* 4- 4     FAILURE OF THE TEMPERATURE CALCULATION IN THE 1 ST SHELL - CHECK THAT
      THE UNIT IS FEASIBLE
278   1* 4- 6     FAILURE OF THE TEMPERATURE CALCULATION IN THE 1 ST SHELL - CHECK THAT
      THE UNIT IS FEASIBLE
279   1* 4- 8     FAILURE OF THE TEMPERATURE CALCULATION IN THE 1 ST SHELL - CHECK THAT
      THE UNIT IS FEASIBLE
280   1* 4-10     FAILURE OF THE TEMPERATURE CALCULATION IN THE 1 ST SHELL - CHECK THAT
      THE UNIT IS FEASIBLE
281
282   1* 4-12     FAILURE OF THE TEMPERATURE CALCULATION IN THE 1 ST SHELL - CHECK THAT
      THE UNIT IS FEASIBLE
283   1* 4-14     FAILURE OF THE TEMPERATURE CALCULATION IN THE 1 ST SHELL - CHECK THAT
      THE UNIT IS FEASIBLE
284   1* 4-16     FAILURE OF THE TEMPERATURE CALCULATION IN THE 1 ST SHELL - CHECK THAT
      THE UNIT IS FEASIBLE
285   1* 5- 2     THERE IS AN EFFECTIVE TEMPERATURE CROSS IN THE 1 ST SHELL
286   1* 5- 4     FAILURE OF THE TEMPERATURE CALCULATION IN THE 1 ST SHELL - CHECK THAT
      THE UNIT IS FEASIBLE
287
288   1* 5- 6     FAILURE OF THE TEMPERATURE CALCULATION IN THE 1 ST SHELL - CHECK THAT
      THE UNIT IS FEASIBLE
289   1* 5- 8     FAILURE OF THE TEMPERATURE CALCULATION IN THE 1 ST SHELL - CHECK THAT
      THE UNIT IS FEASIBLE
290   1* 5-10     FAILURE OF THE TEMPERATURE CALCULATION IN THE 1 ST SHELL - CHECK THAT
      THE UNIT IS FEASIBLE
291   1* 5-12     FAILURE OF THE TEMPERATURE CALCULATION IN THE 1 ST SHELL - CHECK THAT
      THE UNIT IS FEASIBLE
292   1* 5-14     FAILURE OF THE TEMPERATURE CALCULATION IN THE 1 ST SHELL - CHECK THAT
      THE UNIT IS FEASIBLE
293
294                          SUMMARY OF ALTERNATIVE DESIGNS WHOSE COST RATIO IS NOT
                             MORE THAN 1.250
295
296   SHELLS   SHELL   TUBE  NUM.OF --- BAFFLES --- NUM ----------- NOZZLE DIAMETERS
      ---------- PRESSURE  DROPS OVER   COST
```

```
297   IN PARA  DIAM.  LENGTH  TUBES                SEAL---- SHELL SIDE ---- ---- TUBE
      SIDE -----                SURF.  RATIO
298   *SERIES                      NUM/ PITCH /CUT STR-  IN  /  OUT / INTER   IN  /  OUT
      / INTER  SHELL /  TUBE  RATIO  ITEM/
299   -PASSES   MM      MM               MM   O/O IPS   MM     MM     MM     MM
      MM     MM         BAR            CHOSEN
300
301    1* 5-16     FAILURE OF THE TEMPERATURE CALCULATION IN THE 1 ST SHELL - CHECK THAT
       THE UNIT IS FEASIBLE
302
303
304   TEMA Style Summary
305    1 Diam/Length(mm) 1117.6/ 6096.0 TypeAEL , HORIZONTAL    1 Exchgrs connected 1
       series x  1 para. Selection Basis: COST
306    2 Surface areas   m2 - total     531.19 - /shell     531.19   - heat transfer
       469.41            STE cost     10429
307
308                                      COLD SHELLSIDE          HOT TUBESIDE
309                                     INLET     OUTLET       INLET     OUTLET
310      *FLOWRATES*            UNITS   (Cold) Stream 2         (Hot) Stream 1
         *CLEARANCES ETC.*
311    3 Total Fluid Flowing     kg/h            9326.2             13536.0         1
       Tube/Baffle  (Diametric) mm    0.00000
312    4 Total Vapour + Gas      kg/h         0.0        0.0     13536.0    13536.0  2
       Bundle/Shell (Diametric) mm     12.700
313    5 Total Liquid            kg/h      9326.2     9326.2         0.0        0.0  3
       Baffle/Shell (Diametric) mm    6.35000
314    6 Steam/Water             kg/h               0.0                 0.0         4
       Baffle Thickness         mm    0.00000
315    7 Non-Condensables        kg/h               0.0                 0.0
316    8 Condensed/Evaporated    kg/h               0.0                 0.0
       *PERCENTAGE OF TOTAL PRESSURE DROP*
317                                                                              5
      Shell X-Flow   0.0  Tube Straight  0.0
318      *LIQUID PROPERTIES*
         6       Window   0.0       Return    0.0
319    9 Density                 kg/m3      967.0      705.5         0.0        0.0
       7       Ends     0.0
320   10 Viscosity         centipoise     2.9687     0.1356      0.0000     0.0000
       8       Nozzle  ****       Nozzle   ****
321   11 Specific Heat        kJ/kg K     1.0123     2.4036      0.0000     0.0000
322   12 Conductivity           W/m K     0.1936     0.0901      0.0000     0.0000
       *DIMENSIONLESS NUMBERS*  Shell   Tube
323   13 Molecular Weight                166.00     166.00        0.00       0.00   9
       Reynolds In  Gas/Vapour      0.   6297.
324
      10          Out Gas/Vapour      0.   9020.
325      *VAPOUR PROPERTIES*
         11          In  Liquid         29.      0.
326   14 Density                kg/m3     0.0000     0.0000     93.2957   192.9066
       12          Out Liquid        643.      0.
327   15 Viscosity         centipoise     0.0000     0.0000      0.0352     0.0246  13
       Prandtl  In  Gas/Vapour  0.0000  0.7674
328   16 Specific Heat        kJ/kg K     0.0000     0.0000      1.1520     1.2578
       14          Out Gas/Vapour  0.0000  0.7976
329   17 Conductivity           W/m K     0.0000     0.0000      0.0528     0.0388
       15          In  Liquid      15.521   0.000
330   18 Molecular weight                  0.00       0.00       28.01      28.01
       16          Out Liquid       3.618   0.000
331
332      *2-PHASE PROPERTIES*
333   19 Latent heat            kJ/kg       0.00       0.00        0.00       0.00
334
      *HEAT LOADS*          Shell     Tube
335      *TEMPERATURES AND PRESSURES*                                             19
         Gas/Vapour      kW          0.     1502.
336   20 Stream                     C      20.00     360.00      400.00      60.00  20
       Cond./Evap.     kW         0.        0.
337   21 Bulk Average / Skin        C     198.61     202.01      207.06     202.59  21
       Liquid          kW      1502.        0.
338   22 Pressure In/Out           bar     13.000 /   12.896     200.000 /  199.685
339                                                                              22
      Wet Wall Desuperheat. N/A: HTC Fact. NO
```

```
340    23 DP Calc./Estimated       bar     0.1043 /   1.0000      0.3150 /   4.0000  23
       Vap.Shear Enhancement N/A: User HTC YES
341       (Frictional/Accelerational)      0.0000 /   0.0000      0.0001 /   0.0000
342       (Nozzles+Turns/Gravitational)    0.1043 /   0.0000      0.3149 /   0.0000
343        *HT. TRANS. COEFF/RESIST*
           *Veloc./Momentum Flux     m/s  /   kg/m s2
344    24 Stream                W/m2 K      1000. / .0010000        779. / .0012842  24
       Shell-Nozzle Inlet    0.96  /     892.3
345    25 Fouling               W/m2 K         0. / .0000000          0. / .0000000
       25             Outlet    1.32  /    1222.9
346    26 Wall                  W/m2 K                 7067. / .0001415
       26              Inter    0.00  /       0.0
347    27 Overall Clean         W/m2 K                  412. / .0024257
       27     X-Flow Highest    0.00  /       0.0
348    28 Overall Dirty         W/m2 K                  412. / .0024257
       28     Window Highest    0.01  /       0.0
349                                                                          29
      Tube -Nozzle Inlet    6.14  /    3515.0
350    29 Total Heat Duty           kW                    1501.71
       30             Outlet    7.13  /    9613.8
351    30 Eff. Wtd. MTD./1 Pass MTD   C                 8.24 /     8.24
       31              Inter    0.00  /       0.0
352    31 Area Ratio - Actual/Reqd.                        1.0622                   32
       Tube       Highest    0.16  /       2.4
353
354       *TUBE DETAILS*             *NOZZLE DETAILS   mm *   *BAFFLE DETAILS*
          *LAYOUTS*
355    32 Number of Tube Passes    1 Imping. Prot. - NONE     Segmental Type RODBAFF 33
       Lowest  Row C/L Height   mm     -535.10
356    33 Type-PLAIN / Number   1456 Diameters  Shell   Tube  Cut   (Percent)   0.0  34
       Highest Row C/L Height   mm      531.70
357    34 OD/ID mm   19.050 / 14.834 Inlet    40.89    50.50  Cut/NozC/L(Deg)     0  35
       Shell/Top of Tube Bundle mm       27.10
358    35 Length nominal mm  6096.00 Outlet   40.89    40.89  Number             36  36
       Total Number Baffle Overlap Rows     44
359    36 Length Effect. mm  5387.00 Inter     0.00     0.00  Pitch    mm    152.40  36
       Total Number Tube Rows in Windows     0
360    37 Pitch mm (90 deg)    25.40 No. Sealing Strips    0  Endspace-Front   0.00  38
       Number of Tubes Submerged          1456
361    38 Weight kg   Bundle/Dry/Wet   10738/  47801/  54988  Endspace-Rear    0.00  39 Th
       Cond 316 Stainless      W/m K  16.84
362
363
```

Bibliography

American Electric Power. Transmission Facts, 2011. URL https://web.archive.org/web/20110701133947/http://www.aep.com/about/transmission/docs/transmission-facts.pdf.

Ametherm Inc. Four Most Common Types of Temperature Sensor, Dec. 2015. URL https://www.ametherm.com/blog/thermistors/temperature-sensor-types.

M. J. Baker, S. Daniels, P. G. Young, and G. R. Tabor. Investigation of flow through a computationally generated packed column using CFD and additive layer manufacturing. *Computers and Chemical Engineering*, 67:159, 2014. ISSN 0098-1354. URL http://dx.doi.org/10.1016/j.compchemeng.2014.04.005.

A. R. Balakrishnan and D. C. T. Pei. Heat Transfer in Gas-Solid Packed Bed Systems. 1. A Critical Review. *Industrial & Engineering Chemistry Process Design and Development*, 18(1):30–40, Jan. 1979. ISSN 0196-4305. doi: 10.1021/i260069a003. URL https://doi.org/10.1021/i260069a003.

Beacon Power. Frequency Regulation and Flywheels - Fact Sheet, Mar. 2010. URL https://web.archive.org/web/20100331042630/http://www.beaconpower.com/files/Flywheel_FR-Fact-Sheet.pdf.

BEIS. Energy Trends: Renewables - GOV.UK, Feb. 2018. URL https://www.gov.uk/government/statistics/energy-trends-section-6-renewables.

C. Borgnakke and R. E. Sonntag. The air-standard refigeration cycle. In *Fundamentals of Thermodynamics*, page 418. Wiley, Singapore, 8th edition, 2014a. ISBN 978-1-118-32177-5 978-1-118-13199-2. URL https://www.dawsonera.com/readonline/9781118507032. OCLC: 859529056.

C. Borgnakke and R. E. Sonntag. Power and Refrigeration Systems - Gaseous Working Fluids. In *Fundamentals of Thermodynamics*, pages 401–408. Wiley, Singapore, 8th edition, 2014b. ISBN 978-1-118-32177-5 978-1-118-13199-2. URL https://www.dawsonera.com/readonline/9781118507032. OCLC: 859529056.

D. Bowman. Exploding tyre causes death, 2018. URL https://www.etyres.co.uk/news/exploding-tyre-causes-death-6734.html.

N. P. Brandon, J. S. Edge, M. Aunedi, P. G. Bruce, B. K. Chakrabarti, T. Esterle, J. W. Somerville, Y. L. Ding, C. Fu, and P. S. Grant. UK research needs in grid scale energy storage technologies. *EnergySuperStore.org*, 2016.

P. Breeze. Hydrogen Energy Storage. In P. Breeze, editor, *Power System Energy Storage Technologies*, pages 69–77. Academic Press, Jan. 2018. ISBN 978-0-12-812902-9. URL http://www.sciencedirect.com/science/article/pii/B9780128129029000080.

P. Brown. Mitsubishi Installs 50mw Energy Storage System to Japanese Power Company, Mar. 2016. URL https://electronics360.globalspec.com/article/6402/mitsubishi-installs-50mw-energy-storage-system-to-japanese-power-company.

D. Bucker. EWE plans to build the world´s largest battery, June 2017. URL https://www.ewe.com/en/media/press-releases/2017/06/ewe-plans-to-build-the-worlds-largest-battery-ewe-ag.

M. Burke. Malta raises $26m and forms new company committed to building the future of grid-scale energy storage: Electro-thermal energy storage system incubated at X, Alphabet's Moonshot Factory, collects and stores inexpensive and abundant energy from the grid and dispatches it as electricity on demand. *PR Newswire; New York*, Dec. 2018. URL http://search.proquest.com/docview/2158224110/citation/9A2B85D6C06D435CPQ/1.

E. Butterman. George Brayton, Apr. 2012. URL https://www.asme.org/engineering-topics/articles/automotive/george-brayton.

J. Cahill. Early Detection of Distillation Column Flooding Conditions, Aug. 2012. URL https://www.emersonautomationexperts.com/2012/measurement/pressure/early-detection-of-distillation-column-flooding-conditions/.

Y. A. Cengel and M. A. Boles. *Thermodynamics: an Engineering Approach*. McGraw-Hill, New York, 2011. ISBN 978-0-07-352932-5 978-0-07-736674-2 978-0-07-098669-5. OCLC: 755937100.

Centaur Media. Team connects first grid-scale pumped heat energy storage system, Jan. 2019. URL https://www.theengineer.co.uk/grid-scale-pumped-heat-energy-storage/.

J. M. Coulson. *Chemical Engineering Design*, volume 6. Butterworth Heinemann, Oxford, third edition edition, 1999. ISBN 978-0-7506-4142-5.

T. R. G. Davenne, S. D. Garvey, B. Cardenas, and J. P. Rouse. Stability of packed bed thermoclines. *Journal of Energy Storage*, 19:192–200, Oct. 2018. ISSN 2352-152X. doi: 10.1016/j.est.2018.07.015. URL http://www.sciencedirect.com/science/article/pii/S2352152X17306254.

N. Davey. The History of the Gas Turbine. In *The Gas Turbine*. Van Nostrand Co., New York, 1914. URL https://catalog.hathitrust.org/Record/002023268.

Delphi Technologies. 350 Bar GDi System, 2019. URL https://www.delphi.com/featured-technologies/350-bar-gdi-system-low-particulate-emissions.

T. Desrues, J. Ruer, P. Marty, and J. Fourmigué. A thermal energy storage process for large scale electric applications. *Applied Thermal Engineering*, 30(5):425–432, Apr. 2010. ISSN 13594311. doi: 10.1016/j.applthermaleng.2009.10.002. URL http://linkinghub.elsevier.com/retrieve/pii/S1359431109002932.

I. Dincer and M. Rosen. *Thermal energy storage: systems and applications*. Wiley, Hoboken, N.J, 2nd ed edition, 2011. ISBN 978-0-470-74706-3.

P. N. Dwivedi and S. N. Upadhyay. Particle-Fluid Mass Transfer in Fixed and Fluidized Beds. *Industrial & Engineering Chemistry Process Design and Development*, 16(2):157–165, Apr. 1977. ISSN 0196-4305. doi: 10.1021/i260062a001. URL https://doi.org/10.1021/i260062a001.

J. C. Elgin and F. B. Weiss. Liquid Holdup and Flooding in Packed Towers. *Industrial & Engineering Chemistry*, 31(4):435–445, Apr. 1939. ISSN 0019-7866. doi: 10.1021/ie50352a010. URL https://doi.org/10.1021/ie50352a010.

B. Elmegaard and W. Brix. Efficiency of Compressed Air Energy Storage. *The 24th International Conference on Efficiency, Cost, Optimization, Simulation and Environmental Impact of Energy Systems*, page 13, 2011.

Engineering ToolBox. Plastics - Thermal Conductivity Coefficients, 2011. URL https://www.engineeringtoolbox.com/thermal-conductivity-plastics-d_1786.html.

Engineers Edge. Convective Heat Transfer Coefficients Table Chart, 2000. URL https://www.engineersedge.com/heat_transfer/convective_heat_transfer_coefficients__13378.htm.

European Committee for Standardization. EN 13445-2:2014 Unfired Pressure Vessels Part 2 Materials, 2014. URL https://bsol.bsigroup.com/Bibliographic/BibliographicInfoData/000000000030339205.

Evaporator Dryer Technologies, Inc. High Pressure Atomizing Nozzles, 2016. URL http://www.evapdryertech.com/atomizing.html.

J. Flaig. Renewables underground – solution to energy's biggest problem could be right beneath our feet. *IMechE*, May 2019. URL https://www.imeche.org/news/news-article/feature-renewables-underground-why-the-solution-to-energy%27s-biggest-problem-could-be-right-beneath-our-feet.

R. Gaiser. General Compression - What We Do, Mar. 2016. URL https://web.archive.org/web/20160310004811/http://www.generalcompression.com/index.php/who.

P. Gardner, G. Sharp, and P. Ramirez. The Benefits of Pumped Storage Hydro to the UK. Technical report, Scottish Renewables, June 2016. URL http://www.british-hydro.org/downloads/TypesofHydro/Pumped%20Storage%20report.pdf.

S. D. Garvey, A. J. Pimm, J. A. Buck, S. Woolhead, K. W. Liew, B. Kantharaj, J. E. Garvey, and B. D. Brewster. Analysis of a wind turbine power transmission system with intrinsic energy storage capability. *Wind Engineering*, 39(2):149–173, 2015. URL http://journals.sagepub.com/doi/pdf/10.1260/0309-524X.39.2.149.

S. George. UK's largest battery storage facility comes online in Hertfordshire, 2018. URL https://www.edie.net/news/8/UK-s-largest-battery-storage-facility-comes-online-in-Hertfordshire/.

N. A. H. Hairul, A. M. Shariff, and M. A. Bustam. Process behaviour in a packed absorption column for high pressure CO2 absorption from natural gas using PZ+AMP blended solution. *Fuel Processing Technology*, 157:20–28, Mar. 2017. ISSN 0378-3820. URL https://doi.org/10.1016/j.fuproc.2016.11.008.

S. S. Halkarni, A. Sridharan, and S. V. Prabhu. Estimation of volumetric heat transfer coefficient in randomly packed beds of uniform sized spheres with water as working medium. *International Journal of Thermal Sciences*, 110:340–355, Dec. 2016. ISSN 1290-0729. doi: 10.1016/j.ijthermalsci.2016.07.012. URL http://www.sciencedirect.com/science/article/pii/S1290072916302502.

J. S. Howes and J. Macnaghten. Apparatus for use as a heat pump, Mar. 2007. URL https://patents.google.com/patent/WO2006100486A9/.

G. F. Hundy, A. R. Trott, and T. C. Welch. Chapter 2 - The Refrigeration Cycle. In G. F. Hundy, A. R. Trott, and T. C. Welch, editors, *Refrigeration, Air Conditioning and Heat Pumps (Fifth Edition)*, pages 19–39. Butterworth-Heinemann, Jan. 2016. ISBN 978-0-08-100647-4. doi: 10.1016/B978-0-08-100647-4.00002-4. URL http://www.sciencedirect.com/science/article/pii/B9780081006474000024.

F. P. Incropera, editor. *Introduction to Heat Transfer*. Wiley, Hobokenm, NJ, 5th edition, 2007. ISBN 978-0-471-45727-5.

Industrial Measurement Systems. Ultrasonic Thermometry, 2019. URL https://imsysinc.com/Knowledgebase/ultratherm.htm.

IRENA. Electricity Storage and Renewables: Costs and Markets to 2030. *International Renewable Energy Agency*, page 55, Oct. 2017. URL www.irena.org.

A. Jain, R. Bansal, A. Kumar, and K. Singh. A comparative study of visual and auditory reaction times on the basis of gender and physical activity levels of medical first year students. *International Journal of Applied and Basic Medical Research*, 5(2):124–127, 2015. ISSN 2229-516X. doi: 10.4103/2229-516X.157168. URL https://www.ncbi.nlm.nih.gov/pmc/articles/PMC4456887/.

B. Jiang, Z. Wang, X. Fu, and Y. Wang. Experimental Study on Heat Transfer of Heated Falling Film Under Gas–Liquid Cross-Flow Condition. *Heat Transfer Engineering*, 35(1):34–42, Jan. 2014. ISSN 0145-7632. doi: 10.1080/01457632.2013.810087. URL https://doi.org/10.1080/01457632.2013.810087.

V. Jiřičný, V. Staněk, P. Svoboda, and J. Ondráček. Experimental Study of the Flooding and Appearance of a Bubble Bed on Top of a Countercurrent Packed-Bed Column. *Industrial & Engineering Chemistry Research*, 40(1):407–412, Jan. 2001. ISSN 0888-5885. doi: 10.1021/ie000269r. URL https://doi.org/10.1021/ie000269r.

R. E. Johnstone. *Pilot plants, models and scale-up methods in chemical engineering*. McGraw-Hill series in chemical engineering. McGraw-Hill, New York, 1957.

R. Karwa. One-Dimensional Steady State Heat Conduction. In R. Karwa, editor, *Heat and Mass Transfer*, pages 7–116. Springer Singapore, Singapore, 2017. ISBN 978-981-10-1557-1. doi: 10.1007/978-981-10-1557-1_2. URL https://doi.org/10.1007/978-981-10-1557-1_2.

N. Kolev. *Packed Bed Columns*. Elsevier, 2006. ISBN 978-0-444-52829-2. doi: 10.1016/B978-0-444-52829-2.X5000-6. URL https://linkinghub.elsevier.com/retrieve/pii/B9780444528292X50006.

I. Kolin. Nine Ericsson's engines. In *The Evolution of the Heat Engine*, pages 56–63. Moriya Press, River Falls, WI, 1998. ISBN 978-0-9652455-2-4.

H. Krehenwinkel and H. Knapp. Pressure drop and flooding in packed columns operating at high pressures. *Chemical Engineering & Technology*, 10(1):231–242, 1987. ISSN 1521-4125. doi: 10.1002/ceat.270100128. URL https://onlinelibrary.wiley.com/doi/abs/10.1002/ceat.270100128.

D. MacKay. *Sustainable Energy - Without the Hot Air*. UIT Cambridge, Cambridge, reprinted edition, 2010. ISBN 978-0-9544529-3-3. URL https://www.withouthotair.com/.

J. MacNaghten. Isentropic receives Carbon Trust Applied Research Grant News, Mar. 2010. URL https://web.archive.org/web/20100303025527/http://www.isentropic.co.uk/index.php?mact=News,cntnt01,detail,0&cntnt01articleid=2&cntnt01returnid=52.

J. MacNaghten and J. S. Howes. Apparatus for use as a heat pump, Mar. 2007. URL https://patents.google.com/patent/WO2006100486A9/en.

M. Mancheva. Japan's HEPCO, SEI kick off 15-MW battery system verification, Jan. 2016. URL http://renewablesnow.com/news/japans-hepco-sei-kick-off-15-mw-battery-system-verification-507909/.

N. Massey. Energy Storage Hits the Rails Out West, Mar. 2014. URL https://www.scientificamerican.com/article/energy-storage-hits-the-rails-out-west/.

T. McBride, A. Bell, and D. Kpshire. ICAES Innovation: Foam-Based Heat Exchange. *ICAES*, SustainX:4, 2013.

J. C. Middleton. Chapter 15 - Gas liquid dispersion and mixing. In N. Harnby, M. F. Edwards, and A. W. Nienow, editors, *Mixing in the Process Industries*, pages 322–363. Butterworth-Heinemann, Oxford, Jan. 1992. ISBN 978-0-7506-3760-2. doi: 10.1016/B978-075063760-2/50036-6. URL http://www.sciencedirect.com/science/article/pii/B9780750637602500366.

S. Z. Mikhail and W. R. Kimel. Densities and Viscosities of 1-Propanol-Water Mixtures. *Journal of Chemical & Engineering Data*, 8(3):323–328, July 1963. ISSN 0021-9568. doi: 10.1021/je60018a014. URL https://doi.org/10.1021/je60018a014.

T. Miyahara, K. Ogawa, Y. Nagano, A. Hirade, and T. Takahashi. Flow dynamics in low height packed column having large fractional void space. *Chemical Engineering Science*, 47(13):3323–3330, Sept. 1992. ISSN 0009-2509. doi: 10.1016/0009-2509(92)85041-9. URL http://www.sciencedirect.com/science/article/pii/0009250992850419.

National Grid plc. FES in 5 - Future Energy Scenarios, July 2018. URL http://fes.nationalgrid.com/fes-document/.

NIST. Thermophysical Properties of Fluid Systems, 2018. URL https://webbook.nist.gov/chemistry/fluid/.

Omega Engineering. Non-contact thermometers - Types and terms, 2018. URL https://www.omega.co.uk/literature/transactions/volume1/thermometers2.html.

Paratherm. Paratherm™ HR Synthetic-Aromatic Heat Transfer Fluid Typical Properties, 2018. URL https://www.paratherm.com/heat-transfer-fluids/paratherm-hr-synthetic-aromatic-heat-transfer-fluid/.

G. Parkinson. Tesla big battery goes the full discharge for first time, Dec. 2017. URL https://reneweconomy.com.au/tesla-big-battery-goes-full-discharge-100mw-first-time-37826/.

H. Paus. A Ten-Mile Storage Battery. *Popular Science Monthly*, (July 1930):60, 1930. URL https://books.google.co.uk/books?id=sigDAAAAMBAJ&lpg=PA60&dq=1930%20plane%20%22Popular&pg=PA60#v=onepage&q&f=true.

R. Petela. Exergetic analysis of atomization process of liquid. *Fuel*, 63(3):419–422, Mar. 1984. ISSN 0016-2361. doi: 10.1016/0016-2361(84)90022-X. URL http://www.sciencedirect.com/science/article/pii/001623618490022X.

A. Pimm and S. D. Garvey. Chapter 7 - Underwater Compressed Air Energy Storage. In T. M. Letcher, editor, *Storing Energy*, pages 135–154. Elsevier, Oxford, Jan. 2016. ISBN 978-0-12-803440-8. doi: 10.1016/B978-0-12-803440-8.00007-5. URL http://www.sciencedirect.com/science/article/pii/B9780128034408000075.

A. Pintar. Error Analysis. In *Error Analysis in Chemical Engineering*. Michigan Technological University, Sept. 2001. URL http://pages.mtu.edu/~fmorriso/Pintar_Error_Analysis_or_UO_Lab.pdf.

M. Porta and J. M. Last. Student's T test. In *A Dictionary of Public Health*. Oxford University Press, May 2018. ISBN 978-0-19-184438-6. URL http://www.oxfordreference.com/view/10.1093/acref/9780191844386.001.0001/acref-9780191844386-e-4319.

Robert Currie, B. Elrick, M. Ioannidi, and C. Nicolson. Introduction to Integrating Renewable Energy, 2002. URL http://www.esru.strath.ac.uk/EandE/Web_sites/01-02/RE_info/integration.htm.

M. Roberts, F. Chen, and O. Saygi-Arslan. Brayton refrigeration cycles for small-scale LNG. *Gas Processing*, (July/August 2015):27–32, 2015. URL http://www.airproducts.com/~/media/downloads/article/L/lng-braytonrefrig-cycle-article.pdf.

R. Robinson. ETI invest £14m in energy storage breakthrough with Isentropic, June 2012. URL https://web.archive.org/web/20130924164327/http://www.eti.co.uk/news/article/eti_invest_14m_in_energy_storage_breakthrough_with_isentropic.

W. Roetzel and B. Spang. Typical Values of Overall Heat Transfer Coefficients. In *VDI Heat Atlas*, pages 75–78. Springer Berlin Heidelberg, Berlin, Heidelberg, 2010. ISBN 978-3-540-77876-9. URL http://link.springer.com/10.1007/978-3-540-77877-6_6.

M. Scervini. Thermocouple Drift, Aug. 2009. URL https://www.msm.cam.ac.uk/utc/thermocouple/pages/Drift.html.

R. K. Shah and D. P. Sekulić. Classification of Heat Exchangers. In *Fundamentals of Heat Exchanger Design*. John Wiley & Sons, 2003. ISBN 978-0-471-32171-2. URL https://app.knovel.com/hotlink/pdf/id:kt008IZ7D3/fundamentals-heat-exchanger/direct-contact-heat-exchangers.

R. Singh, R. P. Saini, and J. S. Saini. Nusselt number and friction factor correlations for packed bed solar energy storage system having large sized elements of different shapes. *Solar Energy*, 80(7):760–771, July 2006. ISSN 0038-092X. doi:

10.1016/j.solener.2005.07.001. URL http://www.sciencedirect.com/science/article/pii/S0038092X05002318.

J. Stichlmair, J. L. Bravo, and J. R. Fair. General model for prediction of pressure drop and capacity of countercurrent gas/liquid packed columns. *Gas Separation & Purification*, 3(1):19–28, Mar. 1989. ISSN 0950-4214. doi: 10.1016/0950-4214(89)80016-7. URL http://www.sciencedirect.com/science/article/pii/0950421489800167.

H. Stiesdal. Grid Scale Battery, Jan. 2019. URL https://www.stiesdal.com/material/2019/02/Stiesdal-GridScale-01.01.19.pdf.

R. Stockfleth and G. Brunner. Holdup, Pressure Drop, and Flooding in Packed Countercurrent Columns for the Gas Extraction. *Industrial & Engineering Chemistry Research*, 40(1):347–356, Jan. 2001. ISSN 0888-5885. doi: 10.1021/ie000466q. URL https://doi.org/10.1021/ie000466q.

J. W. Tester, E. Drake, M. Driscoll, M. Golay, and W. Peters, editors. *Sustainable energy: choosing among options*. MIT Press, Cambridge, MA, 2nd ed edition, 2012. ISBN 978-0-262-01747-3.

United Nations Framework Convention on Climate Change. Paris Agreement, 2016. URL http://unfccc.int/files/home/application/pdf/paris_agreement.pdf.

J. C. van Miltenburg and G. J. K. van den Berg. Heat Capacities and Derived Thermodynamic Functions of 1-Propanol between 10 K and 350 K and of 1-Pentanol between 85 K and 370 K. *Journal of Chemical & Engineering Data*, 49 (3):735–739, May 2004. ISSN 0021-9568. doi: 10.1021/je0499768. URL https://doi.org/10.1021/je0499768.

M. Wilkins. *The History of Foreign Investment in the United States to 1914*. Harvard University Press, 1989. ISBN 978-0-674-39666-1. Google-Books-ID: eZkaMjTzBdcC. p308.

WindTP. Wind Driven Thermal Pumping, 2019. URL http://www.wind-tp.com/.

B. Wischenewski. Calculation of thermodynamic state variables of nitrogen, 2016. URL http://www.peacesoftware.de/einigewerte/stickstoff_e.html.

World Nuclear Association. Nuclear Power in the United Kingdom, Dec. 2017. URL http://www.world-nuclear.org/information-library/country-profiles/countries-t-z/united-kingdom.aspx.

M. Zhang, H. Dong, and Z. Geng. Computational study of flow and heat transfer in fixed beds with cylindrical particles for low tube to particle diameter ratios. *Chemical Engineering Research and Design*, 132:149–161, Apr. 2018. ISSN 0263-8762. doi: 10.1016/j.cherd.2018.01.006. URL http://www.sciencedirect.com/science/article/pii/S026387621830008X.